Diffusion in supramolecular gels for drug delivery

A thesis submitted to The University of Manchester
for the degree of Doctor of Philosophy
in the Faculty of Biology, Medicine and Health

2025

Riccardo Morbidini

SCHOOL OF HEALTH SCIENCES
DIVISION OF PHARMACY AND OPTOMETRY

Contents

Total Word Count: 39670 words

List of Abbreviations

AFM Atomic force microscopy.

API Active Pharmaceutical Ingredient.

AUC Area Under the Curve.

DDS Drug delivery system.

DLS Dynamic Light Scattering.

DOX Doxorubicin.

DS Dielectric Spectroscopy.

ECM Extra Cellular Matrix.

FCS Fluorescent Correlation Spectroscopy.

FmocFF N-fluorenylmethoxycarbonyl-diphenylalanine.

FRAP Fluorescence Recovery After Photobleaching.

FWHM Full Width at Half Maximum.

GdL Glucono-δ lactone.

HA Hyaluronic acid.

HB Hydrogen Bond.

HPLC High Performance Liquid Chromatography.

HWHM Half Width at Half Maximum.

IBU Ibuprofen sodium.

ILL Institut Laue-Langevin.

IM Intramuscular.

INS Insulin.

IV Intravenous.

LMWG Low molecular weigth gelator.

LYS Lysozyme.

MD Molecular Dynamics.

mRNA messenger ribonucleic acid.

MSD Mean square displacement.

MSDM Multi-scale diffusion models.

NBS Neutron Backscattering.

NIST National Institute of Standards and Technology.

NSE Neutron Spin Echo.

PA polarization analysis.

PCA Principal Component Analysis.

PCM Paracetamol.

PEG Poly-ethylene glycol.

PFGNMR Pulse-Field Gradient Nuclear Magnetic Resonance.

pI Isoelectric point.

PVA Poly-vinyl alcohol.

QENS Quasi-Elastic Neutron Scattering.

SANS Small angle neutron scattering.

SAXS Small angle x-ray scattering.

SC Subcutaneous.

SCISSOR Subcutaneous Injection Site SimulaTOR.

SEM Scanning electron microscopy.

SPT Single-Particle Tracking.

STD Saturation Transfer Difference.

TEM Transmission electron microscopy.

THF Tetrahydrofuran.

ToF Time-of-Flight.

UV Ultra Violet.

XPCS X-ray Photon Correlation Spectroscopy.

List of Figures

List of Tables

Abstract

The administration of biologics and chemotherapeutics often requires subcutaneous injection, posing challenges for sustained and localized delivery. Supramolecular hydrogels offer a promising solution, combining biocompatibility, tunability, and injectability for controlled release. This thesis investigates microscopic and macroscopic factors influencing drug diffusion using Quasi-Elastic Neutron Scattering (QENS) to probe drug mobility within supramolecular gels at atomistic length scales and sub-nanosecond timescales.

Chapter 3 analyzes the diffusion of three drugs—ibuprofen sodium, insulin, and lysozyme—in dipeptide-based hydrogels (FmocFF). These drugs, chosen for their increasing molecular size, enable a systematic study of size-dependent diffusion. QENS probes both short-timescale dynamics and solvent-gel interactions, while in vitro studies with the Subcutaneous Injection Site SimulatOR (SCISSOR) reveal bulk diffusion behavior. Results show that steric confinement and surface erosion dominate release, masking hydrodynamic effects observed at the nanoscale, highlighting the importance of integrating molecular-level insights. Chapter 4 focuses on Doxorubicin (DOX) within electrostatically modified β-sheet-forming hydrogels. Non-covalent interactions, especially cation–π interactions, significantly slow diffusion. QENS data align with long-term release results, emphasizing the role of drug–fiber interactions and the tunability of these peptide hydrogels for studying transport across scales. Chapter 5 explores water–ethanol mixtures, revealing non-linear phase behavior and possible molecular clustering. Neutron spectroscopy with polarization analysis decouples self- and collective motions, showing increased rigidity of the water network with rising ethanol content. Chapter 6 extends this to solute effects, including a bis-urea gel and paracetamol. While the gel network does not alter solvent dynamics, paracetamol significantly perturbs them. These findings underscore the complex interplay between solute, solvent, and gel. Overall, this work highlights diffusion in gels as a multi-scale process. Integrating QENS with conventional methods lays the groundwork for predictive models of therapeutic release.

Declaration

No portion of the work referred to in the thesis has been submitted in support of an application for another degree or qualification of this or any other university or other institute of learning.

Copyright statement

Rationale for journal format

The decision to write this thesis in the journal format stems from the nature of the findings obtained throughout my research. Each chapter of this thesis corresponds to a standalone story, providing a focused exploration of different aspects of the overarching research theme. The thesis is organized around the following papers:

1. **Morbidini R.**, Edkins R. M., Carrascosa J., Czakkel O., Hanafy D. I., Kalaria D. R., Seydel T. and Edkins K.* Comparing Microscopic and Macroscopic Diffusion in Drug Delivery: a Study of Small Drug and Protein Dynamics in a Supramolecular Peptide Hydrogel.
   (Submitted to *Advanced Healthcare Material*)

2. **Morbidini R.**, Zoghi N., Sarter M., Saiani A., Seydel T., and Edkins K.* Electrostatic Tuning of Doxorubicin Diffusion: Molecular-Level Insights into Long-Term Drug Release in Supramolecular Peptide Hydrogel.
   (Completed drafting)

3. **Morbidini, R.**, Edkins, R. M., Devonport, M., Nilsen, G., Seydel, T., and Edkins, K.* (2023). Molecular structural dynamics in water–ethanol mixtures: Spectroscopy with polarized neutrons simultaneously accessing collective and self-diffusion. *The Journal of Chemical Physics*, 159(22).
   (*Published*)

4. **Morbidini, R.**, Edkins, R. M., Nemkovski, K., Nilsen, G., Seydel, T., and Edkins, K.*. Perturbation of Water-Ethanol Solvent Structural Relaxation by a Bis-Urea Supramolecular Gel and Paracetamol. *The Journal of Chemical Physics* 162.11 (2025)

The journal format not only aligns with the PhD strategy but also enhances the accessibility and impact of the research outcomes by making them readily available to the academic community.

Preface

The research for this project is carried out within the InnovaXN H2020 MSCA COFUND programme, bringing together the expertise of large-scale neutron and x-rays facilities with the R&D needs of European industry. Contextually this PhD studentship (XN2020-ILL21 www.innovaxn.eu) is made by the collaboration of *University of Manchester* (supervised by Prof.Katharina Edkins and Prof.Jayne Lawrence), *Institut Laue Langevin* (Grenoble, FR) (supervised by Dr.Tilo Seydel), and *AstraZeneca* (supervised by Dr.Dhaval Kalaria)

This project has received funding from the European Union's Horizon 2020 research and innovation programme under the Marie Skłodowska-Curie grant agreement No 847439.

Blank page

Chapter 1

Introduction

1.1 Towards a novel drug delivery platform

The rapid evolution of therapeutic approaches continuously demand innovative and ad hoc drug delivery strategies.[1] To navigate this multifaceted field, drug delivery can be conceptualized as a three-legged table, supported by three fundamental pillars: drug design, efficacy in treating the disease and patient adherence to the therapy. Each pillar is indispensable for achieving therapeutic success (Fig.1.1). Let's consider as an example small molecule drugs, the most simple yet widespread class of therapeutics. These low molecular weight compounds ($<$ 900 daltons) owe their success to several attributes: ease of synthesis, chemical stability, and ability to cross biological barriers, enabling oral administration.[2] Furthermore, their manageable production costs and straightforward development pathways have solidified their role in addressing broad therapeutic needs.[3] However, small molecule drugs are often limited by poor aqueous solubility and lack of specificity, leading to off-target effects and systemic toxicity, particularly in oncology.[4, 5] Hence, in the frame of a drug delivery as a table, small molecule drugs are particularly advantageous

Figure 1.1: Schematic representation of a drug delivery strategy depicted as a table, with each leg symbolizing an essential element for overall stability.

in terms of formulation simplicity and patient compliance, largely due to their suitability for oral administration. However, their limited specificity and associated side effects represent significant weaknesses that undermine the overall stability of an effective drug delivery strategy (Fig.1.1).

These limitations become evident when small molecule drugs are compared to biologics, a class of therapeutics derived from living organisms. The advent of biologics has revolutionized treatment paradigms, analogous to the shift from fuel-powered to electric cars, by enabling highly specific targeting of previously intractable diseases.[6] For instance, protein-based biologics like insulin have transformed diabetes management by mimicking natural hormones to regulate blood sugar levels. Similarly, monoclonal antibodies have revolutionized autoimmune disease treatment; in rheumatoid arthritis, they selectively target inflammatory pathways to alleviate symptoms and slow disease progression.[7] More recently, the success of nucleic acid-based therapies (exemplified by mRNA vaccines)[8] and semaglutide-based drugs[9] (named *Breakthrough of the Year* by *Science* in 2020 and 2023, respectively) highlights the potential of biologics to address global health crises, such as the COVID-19 pandemic and obesity, with unprecedented speed and effectiveness. Their increased size and complexity, central to their therapeutic efficacy, also contribute to the significantly higher production costs compared to small molecule drugs. However, these costs are gradually being reduced through advances in biotechnology, particularly with the development of biosimilars (i.e. compounds designed to replicate biologics at a lower cost) making them more accessible in the long run.[10] Therefore, the most pressing challenge associated with biologics lie in the optimization of their pharmacokinetics (Absorption, Distribution, Metabolism, Excretion) profiles.[11] The primary limitations occur in the first two stages of administration, as biologics have poor membrane permeability and are susceptible to rapid proteolytic degradation in the gastrointestinal tract. These factors prevent oral administration, which is the most convenient route for ensuring patient adherence to therapy. While advances in oral delivery methods for biologics,[12, 13] and alternative routes of administration (intranasal, pulmonary, transdermal)[14] are constantly being explored, current

technologies still struggle with the persistent issue of low bioavailability (i.e. the proportion of an administered drug that reaches systemic circulation in its active form).[14, 15] As a result, parenteral administration remains the preferred route for most biologic and other therapeutics, such as oncology drugs, where maximizing bioavailability and ensuring predictable release profiles is crucial. This modality of administration encompasses several routes, including intravenous (IV), intramuscular (IM), and subcutaneous (SC) injections, each with shared characteristics and distinct differences that influence their application in therapy.[16] Intravenous administration is the most direct method, delivering drugs directly into the bloodstream, ensuring rapid onset of action and precise control over dosing. Intramuscular injection, by contrast, involves depositing the drug into muscle tissue, allowing for slower and more sustained absorption compared to IV administration. However, both routes represent invasive and painful approaches, often requiring trained professionals to avoid post-injection side effects. Subcutaneous administration consists in delivering the drug into the hypodermis, offering a balance between high bioavailability and ease of administration and it is particularly suitable for self-administration of biologics, such as insulin or monoclonal antibodies. However, the tolerability of SC injection is often challenged by the need to deliver high doses in small volumes, requiring greater injection pressures. This can compromise patient comfort, as the process becomes more painful.[17] Moreover, while SC injection ensures gradual absorption, its pharmacokinetic profile is often poorly predictable, making it challenging to tailor the therapeutic response to the specific need for either rapid or sustained action.[16] As a result, injected therapeutics often have a reduced half-life, necessitating frequent administrations and diminishing patient compliance. In drug delivery, three main strategies are commonly employed to address these challenges: modifying the drug itself, altering its surrounding environment, or introducing an interface between the drug and its environment through a delivery system.[2] To achieve greater control over pharmacokinetic parameters, the latter approach is most frequently adopted. Among these systems, micelles, nanoparticles, and liposomes offer drug protection and enhanced targeting.[18, 19] However, it is through the use of

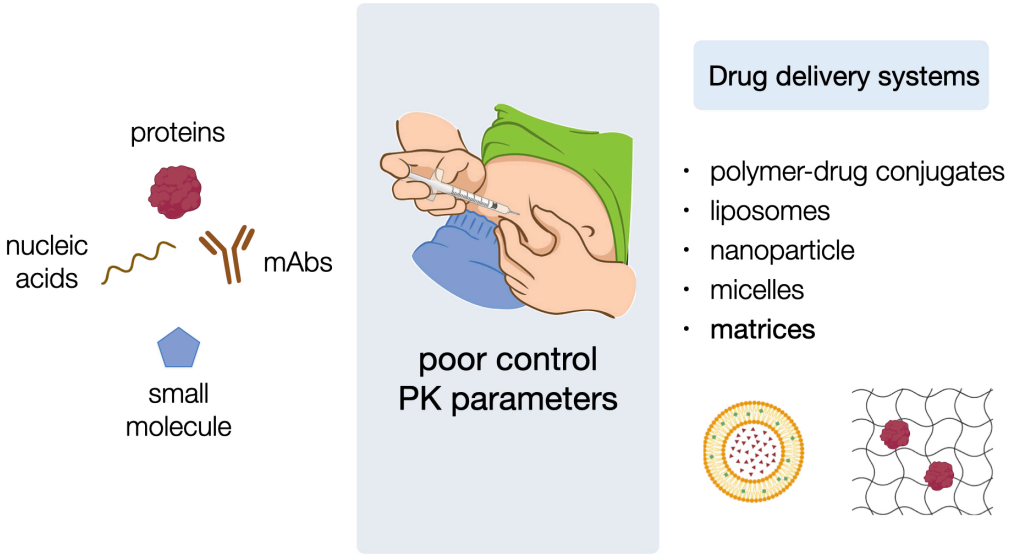

Figure 1.2: Drug delivery systems (DDSs) to improve control over release and half-life of biologics and small molecules.

matrix-based systems for encapsulating the drug that precise control over its release can be achieved.[2, 20] In this kind of the need to limit drug loading to maintain systems stability leads to frequent administration. Additionally, the increased viscosity of the formulation and the potential matrix toxicity poses significant challenges in developing patient-friendly matrix-based delivery systems. Matrix-based drug delivery systems have been extensively studied for their potential to enhance patient compliance during injection. While patient adherence might seem the least important leg of the table of Fig.1.1 it is crucial for the stability of a drug delivery strategy.[20] Among the various systems designed to address these challenges, gels represent a promising class of materials due to their unique structural and mechanical properties.

1.2 Gels

A gel is a system of two-coherent interpenetrating phases, consisting of a three-dimensional continuous solid network that retains a significant liquid fraction, commonly via surface tension.[21] This unique structure allows gels to exhibit properties ranging from soft and weak to hard and tough, behaving like solids despite being predominantly liquid by mass (often more than 99%). Given their dual nature, gels are ubiquitous in everyday life applications: in food (e.g. gelatin),[22] in moisture absorption (e.q. silica gels);[23] and extending to the cellular level, where cells themselves exhibit gel-like properties.[24] This widespread presence has led the concept of gels to permeate everyday language, further complicating efforts to define them, a challenge famously summarized by Dr. Dorothy Jordan Lloyd's remark: 'Gels are easier to recognize than define'.[25]

Gels can be classified in various ways, reflecting differences in their composition, structure, and the mechanisms through which they form (Table 1.1). One key classification criterion is solvent type. Hydrogels are gels in which water serves as the liquid phase, and these are particularly valued in biomed-

Table 1.1: Classification of gels based on various criteria.

Classification	**Name**
Solvent	Hydrogels Organogels
Origin	Natural Synthetic
Cross-linking	Physical Chemical
Particle size	Macrogels Microgels Nanogels
Polymer type	Macromolecular Supramolecular

ical applications for their biocompatibility and soft, tissue-like properties.[26] Organogels, which use organic solvents instead of water, are commonly employed in applications where hydrophobic drugs or cosmetic agents need to be delivered.[27, 28] Hydroalcoholic gels incorporate both water and alcohol, often used in topical formulations, including hand sanitizers.[29]

Another major classification considers the origin of the gel materials. Natural gels, derived from biological sources like gelatin or collagen, offer the advantage of biodegradability and are often used in food and pharmaceutical industry. For instance, Hyaluronic acid hydrogels are widely used in tissue engineering and cosmetic applications due to their moisture retention capability,[30] while agarose hydrogels are commonly utilized in molecular biology for gel electrophoresis.[31] In contrast, synthetic gels are engineered through polymer chemistry, offering more consistency and greater control over their mechanical properties, which makes them ideal for industrial applications or for contexts where precise design is required. Polyethylene glycol (PEG)-based gels exemplify materials engineered for precise design, where molecular weight, cross-linking density, and functionalization can be finely controlled. This tunability allows for consistent mechanical and biochemical properties, making them ideal for biomedical and industrial applications requiring high reproducibility and specificity.[32, 33]

Gels can also be categorized based on their cross-linking mechanism.[34] Physical gels form networks through non-covalent interactions such as hydrogen bonds, ionic bonds, or van der Waals forces. These gels are generally reversible and can respond to external stimuli like temperature or pH. Chemical gels, on the other hand, are formed through covalent bonds, making them more stable and permanent, which is ideal for applications requiring long-term durability and strength.

The classification can also be made based on the size of the gel's structural elements (e.g. pore sizes, fibres thickness etc.).[35] Macrogels (> 100 μm) are typically used in bulk materials where fine-scale interaction is not required such has wound dressing or tissue engineering.[35] Microgels (ranging from 100 nm to 100 μm) are often utilized as stimuli-responsive carriers for controlled

drug release in precision therapies,[36] whereas nanogels (< 100 nm) are ideal for targeted delivery to biological barriers as their small size enhances bioavailability, cellular uptake, and penetration of biological barriers.[37] Notably, these classifications are not mutually exclusive and single gel can belong to multiple categories simultaneously. For instance, hyaluronic acid hydrogels are natural, physically or chemically cross-linked hydrogels; agarose hydrogels are natural, physically cross-linked; and PEG hydrogels are synthetic and may be physically or chemically cross-linked, depending on their synthesis method.
A final distinction can be made depending on the nature of the network formation. Macromolecular gels are based on one-dimensional fibers formed by covalently bonded polymer chains, resulting in a more rigid and permanent structures.[38] These gels typically exhibit high mechanical stability and strength, making them suitable for structural or load-bearing applications. Supramolecular gels, by contrast, rely on a different mechanism of network formation, that will be explored in more detail in the following section.

1.2.1 Supramolecular gels

Supramolecular gels form through the non-covalent self-assembly of low-molecular-weight gelator (LMWG) molecules into one-dimensional structures, creating a dynamic and reversible network (Fig. 1.3).[21, 39–49] The self-assembly process that leads to the formation of supramolecular gels typically begins with an environmental trigger, such as changes in temperature,[50] pH,[51] ionic strength,[42] enzymatic activity,[52] light exposure,[53] or mechanical mixing.[54] This trigger initiates the one-dimensional crystallization of LMWG molecules dissolved at very low concentrations (less than 1 wt.%) in a solvent (either organic or not)[45] (Fig. 1.3a). Such process typically ranges from minutes to hours, depending on the gelator chemistry and specific environmental conditions.[55, 56] Intermolecular forces such as hydrogen bonding, π-π stacking, van der Waals interactions, hydrophobic effects, and electrostatic interactions drive this aggregation (Fig. 1.3b) by energy minimization.Following this initial strand formation, the molecules undergo lateral assembly, resulting in bundled fibers

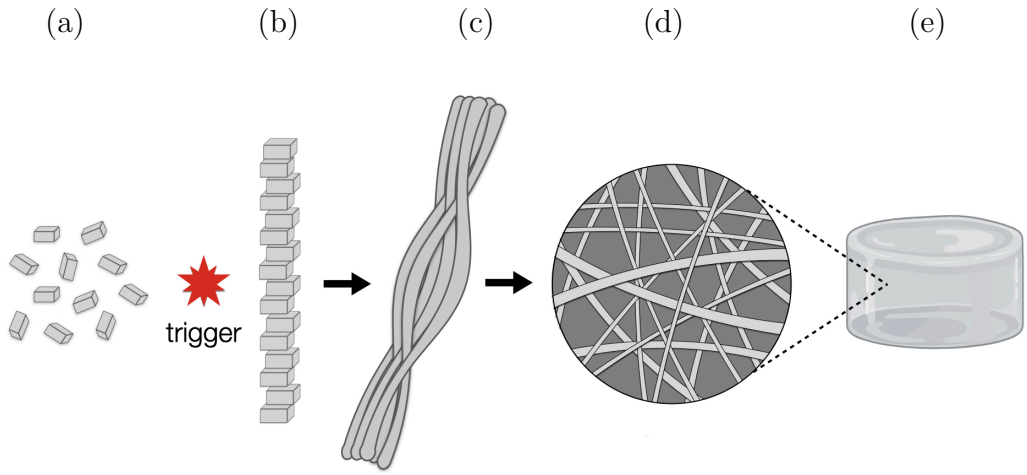

Figure 1.3: Supramolecular self-assembly. (a) LMWG dissolved in solution; (b) 1D aggregation triggered by external stimuli; (c) lateral association forming fiber bundles; (d) fiber entanglement; and (e) self-supporting macroscopic gel.

that adopt diverse morphologies, including ribbons, rods, tapes, helices, or sheets. These fibers eventually entangle to form a three-dimensional, continuous network capable of supporting a macroscopic gel structure (Fig. 1.3c-e). While this simplified representation suggests that supramolecular gels might be easily reproducible, their final form remains highly sensitive to various factors. Batch-to-batch variability is significant, with the kinetics of gelation influenced by parameters such as the choice of solvent, gelator concentration, container geometry, temperature, solubilization method, and the rate at which environmental changes are applied.[57, 58] Understanding the variability in gel formation necessitates the use of different techniques to probe the structure of supramolecular gels across different length scales. Assessing the gel state often begins with the simple yet qualitative vial inversion test, where the arrest of liquid flow indicates gelation.[21] While this test provides a quick, preliminary measure of gelation, it fails to provide quantitative insights into critical param-

eters such as viscoelastic properties, network architecture, and fiber morphology. A comprehensive review of structural characterization methods is beyond the scope of this thesis and has been detailed elsewhere.[47, 59] In this context, three representative methods to monitor the progression of self-assembly at different scales are briefly reported.

Structural characterization

Rheometry is a key technique for quantifying the viscoelastic properties of gels by measuring their mechanical response (deformation or flow, ε_0) to an applied stress (σ_0): $\sigma_0 = G\varepsilon_0$ Here, the complex modulus, $G = G' + iG''$, is decomposed into the elastic storage modulus (G') and the viscous loss modulus (G'').[60] A defining feature of a gel is a storage modulus (G') exceeding the loss modulus (G'') by at least an order of magnitude.[21] This corresponds to a small phase shift (δ), where strain lags only slightly behind stress, and a low loss tangent ($\tan\delta = G''/G' < 0.1$), reflecting the predominance of elastic (solid-like) behavior. This behavior remains consistent up to a critical value of applied stress, known as the yield stress. Beyond this threshold, G' undergoes a sharp drop, indicating the breakdown of the gel network and the onset of liquid flow. The magnitude of G' provides indirect insight into the gel's structural characteristics, such as the concentration of gel fibers and the density of crosslinks, both of which contribute to the material's mechanical strength. Additionally, the evaluation of G' is particularly useful when the gel is used as a matrix for encapsulating solutes. Any changes in the storage modulus may indirectly signal an interaction between the solute and the gel fibers, potentially affecting the stability of the gel network.[61]

Microscopy techniques provide direct visualization of gel networks, shedding light on fiber morphology, pore size, and crosslink distribution. Electron microscopy, including transmission (TEM) and scanning (SEM), offers nanoscale resolution for structural characterization. TEM reveals internal fiber details with resolutions below 1 nm, while SEM captures three-dimensional surface architectures with resolutions in the range of 1–20 nm.[62] Despite their strengths, sample dehydration during imaging can introduce artifacts, necessitating spe-

cialized approaches such as vitrification in cryo-electron microscopy to preserve the hydrated state. Atomic force microscopy (AFM) complements electron microscopy by imaging fibers in their native state, even in liquid environments. AFM also provides nanoscale resolution, but artifacts from tip-sample interactions can affect accuracy.[63, 64] While microscopy reveals intricate details of gel architecture, its findings are often validated with complementary techniques like scattering methods.[65]

Small-angle X-ray scattering (SAXS) and small-angle neutron scattering (SANS) are powerful methods for probing gel structures at scales between 1 and 100 nm.[66, 67] Unlike microscopy, these techniques provide averaged data on fiber shapes, dimensions, and dispersion throughout the bulk sample, revealing structural heterogeneity. Often combined due to the complementary information they provide through different interactions with matter, SAXS and SANS each offer practical advantages: SAXS excels in detecting heavy elements (e.g., metals, ions) and electron-dense regions and it is widely favoured for its accessibility and versatility. On the other hand, SANS allows for contrast variation, making it particularly useful for studying the effect of the solvent or specific components within complex systems.[68–70] Although small-angle scattering requires fitting data to theoretical models for interpretation, it provides a critical complement to microscopy by offering a broader, statistically representative view of fibre structure.

Properties

Supramolecular gels exhibit distinctive properties that set them apart from other gel types:[41]

- **design flexibility** Supramolecular gels offer an extensive toolbox for researchers, with a variety of possible combinations between LMWG, solvents and gelation triggers. This versatility allows for the design of gels with tailored properties for specific application;[42]
- **self-healing:** many supramolecular gels possess inherent self-healing properties due to the reversible nature of their non-covalent interac-

tions. When damaged, these gels can autonomously repair their structure, restoring their original properties;[71]

- **biodegradability** many LMWG used are designed to be biocompatible and biodegradable. The non-covalent nature of the interactions holding the gel network together often allows for easier breakdown;

- **reversibility and stimuli responsiveness:** supramolecular gels can undergo reversible gel-to-sol transitions in response to various stimuli, such as temperature or pH but also common mixing. This responsiveness arises from the dynamic nature of the non-covalent interactions forming the gel network;[46, 72]

- **tunability:** the properties of supramolecular gels can be finely tuned through subtle modifications of the LMWG structure. Small changes in the molecular design can lead to significant alterations in the self-assembly process, resulting in diverse final structures and macroscopic properties.[73]

This responsive and flexible nature of supramolecular gels makes them suitable for different applications spanning from sensing,[74] catalysis,[75] water purification,[76] art conservation.[77] Moreover, this class of materials are particularly attractive for biomedical applications[45, 78] such as wound dressing,[79] tissue regeneration,[80] biologics storage alternative to cold chain[81] and cell culture.[82] Among biomedical applications, supramolecular gels have also gained considerable attention for drug delivery, which will be discussed in the following section.

1.2.2 Gels for drug delivery

Gels have emerged as promising matrix-based systems for drug delivery, offering an effective solution to the challenge of achieving a controlled drug release profile.[83, 84] They offer high biocompatibility especially when the solvent involved is water (hydrogels) or the polymer is natural in origin or mimic the

tissue composition.[85] For instance, cellulose-based hydrogels are widely applied in drug delivery systems, addressing needs ranging from wound healing to post-stroke treatments.[86] Other works have demonstrated the potential of hyaluronic acid-based hydrogel for the localized and controlled release of anti-bacterial and anti-inflammatory drugs.[87] Chitosan-based hydrogels have proven to increase mucosal bioadhesivity, thereby enhancing drug retention at the target site and making them particularly suitable for oral, ocular, and nasal drug delivery routes.[88] Indeed, different routes of administration are currently in use for hydrogels, and depending on the site of action, gel properties such as stiffness or mesh size can be adapted accordingly. For example, the rheological nature of gels and their ability to retain shape make them optimal for depot subdermal implants.[89] These devices, used for purposes such as birth control, rely on the geometry of the implant to dictate the release rate, with any breakage due to external stress potentially causing uneven release or, in the worst case, dose dumping.[90] The higher storage modulus of gels and their ability to maintain shape under stress can prevent such breakages, ensuring an unaffected release profile. Indeed, two of the most successful hydrogel-based products currently on the market — INFUSE, which releases a human bone protein for the treatment of long bone fracture and spinal fusion via a collagen hydrogel network,[91] and VANTAS, used for prostate cancer treatment via a synthetic polymer—are both based on surgical implants.[92] Implantable devices are often necessary for treating diseases in deep tissues where biological barriers hinder drug permeability.[93] Subcutaneous injection of polymeric hydrogels offers a less invasive alternative while maintaining controlled drug diffusion, but it also presents the challenge of increased formulation viscosity at the injection site. Supramolecular gels offer several advantages for drug delivery, which have been extensively reviewed and updated in recent studies.[45, 94–99] With their self-healing and shear-thinning properties, can be administered in either gel or sol states, reducing the discomfort typically associated with injecting highly viscous formulations. Their stimuli-responsive behavior can be leveraged to optimize drug release, as seen in pH-sensitive systems where the acidic microenvironment of tumor sites triggers targeted

release.[100] Additionally, the biodegradability of these gels is complemented by the biocompatible nature of their LMWGs, which are often composed of peptides or amino acid derivatives.[94, 101] This feature ensures better clearance of the gel scaffold after fulfilling its therapeutic role. A recent and promising innovation in supramolecular gel systems is the development of self-delivery systems, where the requirement for an external vehicle is bypassed. In this approach, a drug molecule itself is converted into a LMWG, often through enzyme-cleavable functionalities that trigger gelation.[102–104] This strategy improves bioavailability of poorly soluble hydrophobic drugs while enabling high drug loading and customizable designs tailored to specific disease states.

1.3 Diffusion in gels

(Note: This section is partially adapted from a tutorial review titled *Comprehensive multiscale analysis for diffusion in gels*, of which I am co-author. The review will be soon submitted to *Chemical Society Review*)

1.3.1 Drug release mechanisms

The control over the dynamics of encapsulated drug in hydrogel is often regarded has highly dependent on the network density. Acting as a sieve, the gel matrix restricts particle movement by increasing their free path, leading to a sustained release profile. A key parameter for characterizing this process is the mesh size (ξ), defined as the average free space between the entangled gel fibers.[105] Although accurately determining mesh size is challenging due to its variability (spanning up to two orders of magnitude within the sub-micrometer range) this parameter enables a classification of release mechanisms when compared to the radius of the drug molecules (r_{drug}). As reported in Fig.1.4, three main scenarios can be identified:

- $r_{drug} < \xi$: this is the case of many small molecule drugs, that are almost free to diffuse through the matrix resulting on fast release;
- $r_{drug} \sim \xi$: for drugs with sizes comparable with the mesh size the release mechanism is hindered by the steric obstacle of gel fibres resulting in a slower release;
- $r_{drug} > \xi$: in this extreme case drug compounds can be permanently trapped in the network and their release has to be mediated by other mechanism than simple diffusion like hydrogel swelling, deformation or gel erosion (bulk or surface)

Regardless of the release mechanism, achieving a truly prolonged drug release remains challenging. Diffusion-controlled systems often exhibit the least sustained profiles, with drug half-life (i.e. the time needed for 50% of the drug

to be released) typically extending to about one day. In contrast, systems relying on drug release via matrix degradation can achieve significantly longer half-lives, often lasting up to approximately two weeks.[105] To further slow drug release, introducing diffusion barriers to impede molecular transport has emerged alongside other strategies, including promoting covalent drug-polymer interactions, leveraging electrostatic and hydrophobic interactions, and inducing stimuli-responsive swelling to modulate mesh size. These approaches aim to enhance control over release profiles and adapt them to specific therapeutic requirements.[106] However, this schematic model may oversimplify a process like diffusion that, even in the pure solution, shows a complex multi-scale na-

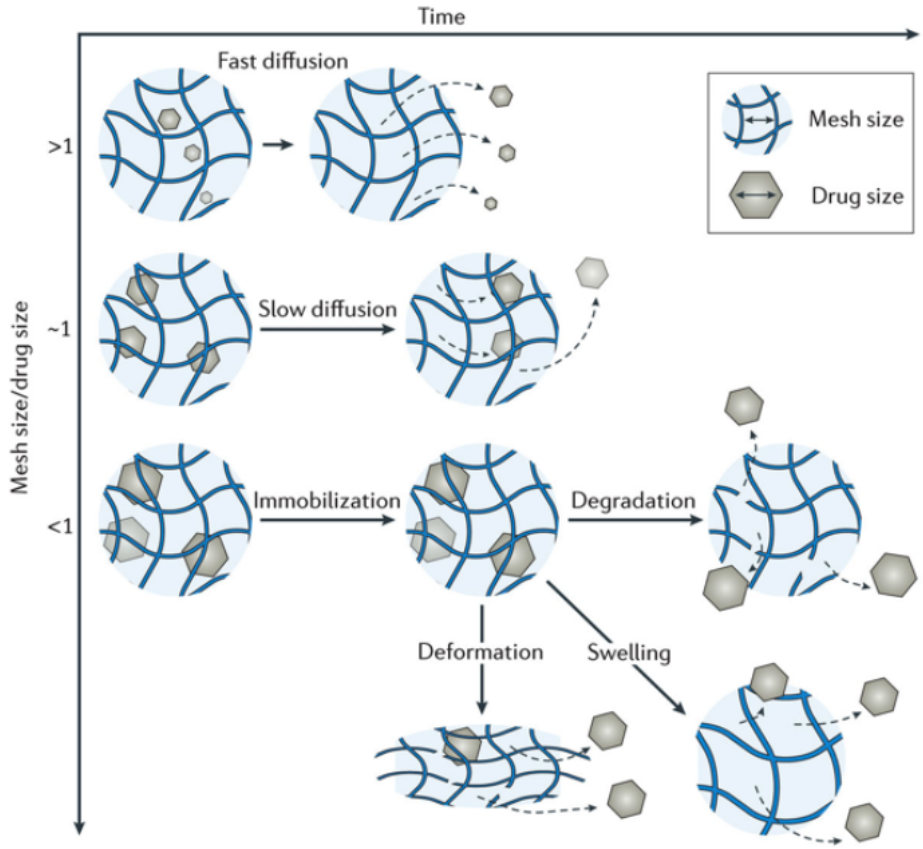

Figure 1.4: Drug release mechanisms based on the ratio ξ/r_{drug}. Reprinted with permission from Ref.[105] Copyright 2016, Macmillan Publishers Limited.

ture. In the context of gels, many factors influencing diffusion at the molecular level are often overlooked in studies that focus solely on parameters like release half-life or drug release amounts. It is unclear from the schematic model at what point a drug molecule transitions from fast diffusion to slow diffusion, or whether this transition is solely dependent on the drug molecular size. Therefore, understanding the fundamentals of the diffusion process is essential to explain why diffusion-based mechanisms may be too slow or too fast in certain systems, as it ultimately determines drug bioavailability. This understanding serves as a crucial first step toward improving the design of materials for enhanced performance and controlled release.

1.3.2 Fundamentals of diffusion

Fick's law

The theoretical framework for diffusion was first established by Fick (1855) who observed that mass transfer arises from the collective movement of randomly dispersing particles, flowing from regions of higher concentration to those of lower concentration.[107, 108] This fundamental concept translates into the first Fick's law that relates the concentration profile C to the mass flux $\vec{J}$ (the rate at which particles diffuse through a unit area per unit time):[109]

$$\vec{J} = -D\frac{\partial C}{\partial x} \tag{1.1}$$

Here $\partial C/\partial x$ is the concentration gradient along the direction x, perpendicular to the area under consideration, with the negative sign representing that the flux occurs from regions of higher to lower concentration in a steady-state regime. The parameter D, known as the diffusion coefficient, has dimension of $(\text{length})^2 \times (\text{time})^{-1}$, and it quantifies the spread of a substance over a surface. The temporal evolution of the concentration profile is described by Fick's second law, derived from eq.1.1 by imposing the principle of mass conservation:[109]

$$\frac{\partial C(x,t)}{\partial t} = D\frac{\partial^2 C(x,t)}{\partial x^2} \tag{1.2}$$

Hence, the diffusive process can be mathematically described as the tendency of the system to return to an equilibrium state characterized by a uniform concentration of particles, which represents the state of maximum entropy and a thermal equilibrium.[110, 111] It is important to note that this description applies to substances diffusing in isotropic media, such as pure solutions.[112, 113] Under these conditions, D can be treated as a scalar quantity, assuming its invariance across all points and directions. This ideal case fails to accurately describe more heterogeneous structures, such as polymer solution or gels. In such systems, D may depend on the concentration of the diffusing substance C as well as the time scale, resulting in a diffusion coefficient that varies across space and time, expressed as $D(\vec{x}, t)$. In anisotropic cases, the flow of the substance at any given point is not necessarily oriented perpendicular to the area it crosses. Instead, the direction of flow changes continuously. This behavior is addressed by modifying Eq. 1.1, where the diffusion coefficient is represented as a tensor, accounting for variations in directionality

$$\begin{aligned} -J_x &= D_{11}\frac{\partial C}{\partial x} + D_{12}\frac{\partial C}{\partial y} + D_{13}\frac{\partial C}{\partial z}, \\ -J_y &= D_{21}\frac{\partial C}{\partial x} + D_{22}\frac{\partial C}{\partial y} + D_{23}\frac{\partial C}{\partial z}, \\ -J_z &= D_{31}\frac{\partial C}{\partial x} + D_{32}\frac{\partial C}{\partial y} + D_{33}\frac{\partial C}{\partial z}. \end{aligned} \tag{1.3}$$

This means that in anisotropic systems, where preferential directions exist, the flux along one direction is influenced not only by the concentration gradient in that direction but also by gradients in the other two directions. For instance, the term $\mathrm{D}_{32}\partial C/\partial y$ represents the contribution to the flux in the z-direction (J_z) arising from the concentration gradient in the y-direction. Representing the diffusion coefficient as a tensor has been crucial in mapping the anisotropy in white brain environment (cellular membranes, axonal packing)[114] or to simulate the diffusion of non-spherical nanoparticles in fluids.[115]

Stokes-Einstein equation

Usually related to transport phenomena on systems out of equilibrium (as a heterogeneous molecule distribution), the concept of a diffusion coefficient occurs even at equilibrium when the net movement is zero, but particles keep moving in no preferential direction. Historically, different approaches were adopted to describe the random movement of particles, i.e. Brownian motion. Despite the diversity in complexity, these approaches converge to a common description based on macroscopic parameters like temperature, particle size, and liquid viscosity. Brownian motion, driven by random thermal fluctuations, is best described by the mean square displacement (MSD), i.e. using the average spread of a particle over time rather than individual particle trajectories. Following the random walker formalism, with particle assumed to move randomly and independently with successive steps of equal length, the MSD is given by

$$\langle \Delta \vec{x}^2 \rangle = 2nDt \tag{1.4}$$

where n is the dimensionality, t is the time and D is the diffusion coefficient represented by the slope of the linear growth. Although this method describes the MSD as driven by the solvent molecules it fails to model their opposition to motion due to friction.[116] This feature was included by the Langevin's approach who assumed that the particle dynamic is the net result of viscous drag forces and an average fluctuating force due to random impact ("kicks") of the solvent molecule.[117] The idea of encoding all the random kicks of the solvent molecules in an average "noise", i.e. reducing the number of degrees of freedom, converges in the following modification of the deterministic Newton's law:

$$m\frac{d^2\vec{x}}{dt^2} = -\gamma\frac{d\vec{x}}{dt} + \langle \vec{F}(t) \rangle \tag{1.5}$$

where m is the mass of the colloidal particle, γ is the friction and $\langle \vec{F}(t) \rangle$ is the average fluctuating force. By solving this equation one gets to the MSD now

accounting for the effect of the surrounding medium:

$$\langle \Delta \vec{x}^2(t) \rangle = 2\frac{k_B T}{\gamma}\left[t + \frac{\gamma}{m}e^{-\frac{\gamma}{m}t}\right] \tag{1.6}$$

This expression suggests that two main contributions influence Brownian motion, at two different time scales. For very short times $t \ll \gamma/m$, the exponential term can be expanded leading to

$$\langle \Delta \vec{x}^2 \rangle = \frac{k_B T}{m}t^2 \tag{1.7}$$

meaning that in this shortest time regime the Brownian particle falls in the ballistic regime where inertia dominates over the friction and random thermal forces. At a longer observation time $t \gg \gamma/m$ a simple diffusive regime for the particle is observed and the MSD becomes linear with t:

$$\langle \Delta \vec{x}^2 \rangle = 2\frac{k_B T}{\gamma}t \tag{1.8}$$

This finding for MSD suggests that, even assuming homogeneous medium, the diffusive behaviour is strongly affected by the observation time, leading to a short- and long-range diffusion following two distinct trends (Fig.1.5a-b). Combining Eq.1.4 and Eq.1.7 yields a significant relation defining the diffusion coefficient:

$$D\gamma = k_B T \tag{1.9}$$

This result is an expression of the fluctuation-dissipation theorem,[118] which relates fluctuations of particle position at equilibrium, expressed through the thermal energy of fluid molecules, to the dissipation that returns the system to thermal equilibrium due to friction. Using the Stokes' law $\gamma = 6\pi\eta R$ for a spherical particle of radius R moving in a homogeneous material with dynamic viscosity η gets to the Stokes-Einstein relation which gives an expression for the self-diffusion coefficient or the synonymous tracer diffusion D:

$$\mathrm{D} = \frac{\mathrm{k_B T}}{6\pi\eta \mathrm{R}} \tag{1.10}$$

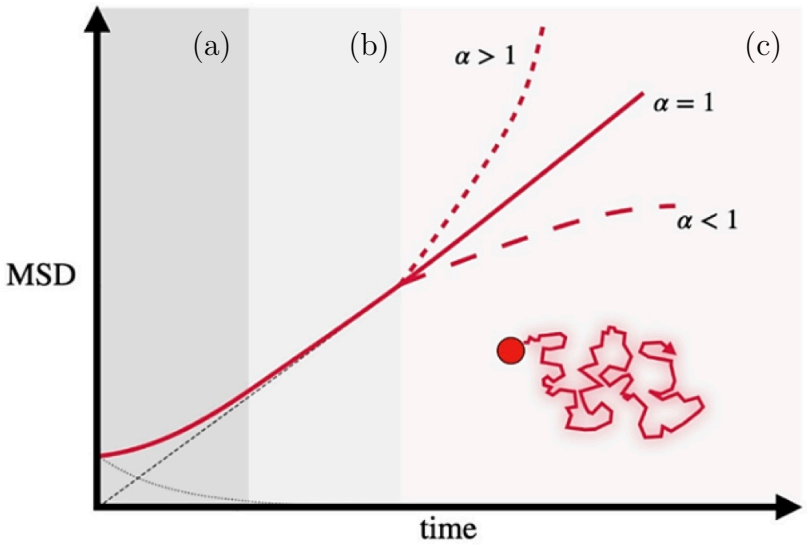

Figure 1.5: Schematic of the ensemble-averaged mean-squared displacement (MSD, $\langle x^2 \rangle$) as a function of time for a Brownian particle. Both axes are linear. The scaling exponent α is defined by the relation MSD$\sim t^{\alpha}$, where α characterizes the diffusive regime. (a) At short times, the Brownian particle is in the ballistic regime ($\alpha = 2$), as described by Eq.1.7. (b) At intermediate times, it transitions into normal diffusion ($\alpha = 1$) according to Eq.1.8. (c) At longer times, interactions with other particles or confinement effects can alter the motion, leading to anomalous diffusion: subdiffusion ($\alpha < 1$) or superdiffusion ($\alpha > 1$).

This relation relies on several approximations since it describes a free diffusion of a spherical particle without spatial restriction. No external or intermolecular interactions are considered by assuming a dilute system where the only forces are thermal motion and friction of a fluid with a constant viscosity (Newtonian fluid). In polymer solutions or gels, where viscosity depends on shear rate (non-Newtonian fluid), Eq.1.10 often explicitly accounts for the shear-frequency dependence of viscosity within the framework of generalized Stokes-Einstein equations.[119, 120] Strictly speaking as soon as a second particle is introduced in the system intermolecular interaction should be taken into account.[121] Their effect is two-fold: through a long range influence on the solvent flow field (hydrodynamic interactions) and through direct inter-

actions due to their surface charge or excluded volume. One way to describe how all these contributions are encompassed in the diffusion equation is to use the formalism of Smoluchowski[122] and Einstein[123] who followed a probabilistic approach instead of following the single particle trajectory as in Langevin's work. The Smoluchowski equation describes the time evolution of the conditional probability density function $P(\vec{r_0}, t_0|\vec{r}, t)$ which gives the probability to find a particle at position $\vec{r}$ and time t if it was at position $\vec{r_0}$ at time t_0 in the presence of an external intermolecular potential $V(\vec{r})$:

$$\frac{\partial}{\partial t}P(\vec{r_0}, t_0|\vec{r}, t) = D\frac{\partial}{\partial r}\Big[\frac{\partial}{\partial r}P(\vec{r_0}, t_0|\vec{r}, t) + \frac{\partial V(\vec{r})}{\partial r}\frac{P(\vec{r_0}, t_0|\vec{r}, t)}{k_B T}\Big] \tag{1.11}$$

Considering a diluted system, with a low particle concentration and a small particle size/mean free path ratio, this second term on the right hand side can be neglected and the Smoluchowski equation converges to Fick's law (while it becomes relevant for strongly interacting solutes or at high concentrations). The solution of this equation allows one to link the self diffusion of a Brownian particle to the concentration-driven Fickian diffusion. With the condition that at time $t = t_0$, the diffusing particle is at $\vec{r_0}$, $P(\vec{r_0}, t|\vec{r_0}, t) = \delta(\vec{r} - \vec{r_0})$, the time evolution of the probability function reads as:

$$P(\vec{r_0}, t_0|\vec{r}, t) = \frac{P(\vec{r_0}, t_0|\vec{r_0}, t_0)}{\sqrt{(4\pi D t)^3}}\exp\Big(-\frac{r^2}{4Dt}\Big) \tag{1.12}$$

In a uniform solution or suspension, Brownian motion does not cause any net change in the concentration with time in any part of the solution. But if the particle distribution is not uniform, then Brownian motion tends to equalize it (Fig.1.6). As such the diffusion coefficient in Fick's law can be interpreted as the average value of an ensemble of Brownian particles.

Self, collective and mutual diffusion

Another way to interpret the concept of probability density function is through the formalism proposed by Van Hove which relates particle displacements to measurable correlation functions depending on a point of observation in space $\vec{r}$

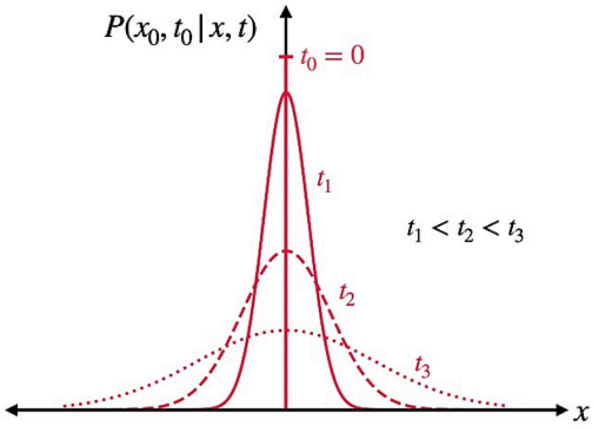

Figure 1.6: Spatial and time dependence of the probability density function $P(x_0, t|x, t)$ of a Brownian particle.

and time t, for many-particle systems consisting of N particles.[126, 127] Here the key quantity is the dynamic correlation function $G(\vec{r}, t)$ which can be expressed by the combination of a self-term (Eq.1.13) and a pair-term (Eq.1.14)

$$G_{\text{self}}(\vec{r}, t) = \frac{1}{N} \sum_{j=1}^{N} \langle \delta(\vec{r} - |\vec{R}_j(t) - \vec{R}_j(0)|) \rangle \tag{1.13}$$

$$G_{\text{pair}}(\vec{r}, t) = \frac{1}{N} \sum_{i,j=1}^{N} \langle \delta(\vec{r} - |\vec{R}_j(t) - \vec{R}_i(0)|) \rangle \tag{1.14}$$

therein the j^{th} particle position at time t, $\vec{R}_j(t)$, is related to the position of the same j^{th} particle at time $t = 0$, $\vec{R}_j(0)$, in the case of the self-term and to the position of a different particle, $\vec{R}_i(0)$ ($i^{th} = j^{th}$), in the case of the pair-term (with the angular brackets representing the ensemble average, Fig.1.7a,b). The observed Van Hove functions show that atomic correlations have a role in diffusion processes even without considering mixing due to concentration gradients. Therefore the diffusion coefficient at equilibrium is not only a single

particle process but it is sensitive on how surrounding particles are distributed and on the kind of interaction that occurs (hydrogen bonds, Van der Waals forces etc.). Depending on the type of correlation function measured, different types of diffusion can be identified: *self-diffusion* is derived from the self-term of the Van Hove correlation function, reflecting the motion of individual particles, while *collective diffusion* comes from the pair-term, which captures particle interactions and how they influence each other's trajectories. Since the term collective diffusion might conflict with the typically used mutual diffusion for reasons of clarity, we herein refer to *mutual diffusion* when describing macroscopic and concentration-driven diffusion for mixing species

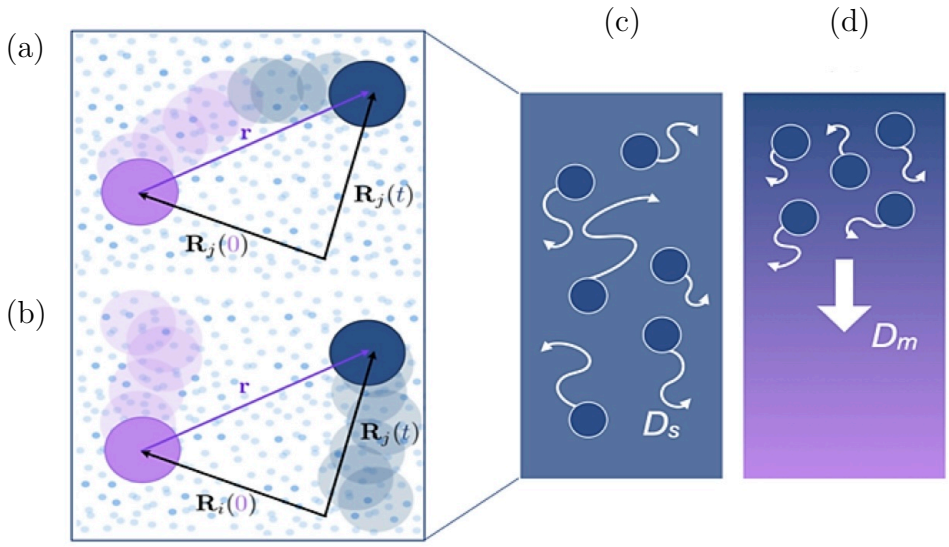

Figure 1.7: Differences between self, collective and mutual diffusion. The self-term (a) of the Van Hove correlation function describes the position correlation of a particle with itself at two time points (self-diffusion) while the pair-term (b) correlates the position of a particle at time t with that of another particle at a different time (collective diffusion). Adapted from Ref.,[124] Copyright © 2019, Cambridge University Press. Schematic presentation of the difference between self-diffusion (c) and mutual diffusion (d). For self-diffusion D_s, the uniform background indicates system equilibrium. For mutual diffusion D_m, the gradient colour of the background reflects a concentration gradient in the sample. Adapted from Ref.[125]

in systems out of equilibrium,[109, 128] keeping the term "collective" diffusion for the description of molecular density fluctuations at equilibrium (i.e. not driven by concentration gradients) derived from the Van Hove correlation functions (Eq.1.14). These three terms are linked depending on the observational time and length scale.[126, 129–131] At distances comparable to the particle size, the influence of surrounding particles at equilibrium is negligible, and collective diffusion approaches self-diffusion. In contrast, at larger distances where solute concentration gradients become significant, collective diffusion transitions toward mutual diffusion. As these gradients evolve over longer time and length scales, macroscopic or bulk diffusion is characterized by the mutual diffusion coefficient (D_m).[132]

Anomalous diffusion

Brownian diffusion is described with a linear time dependence of the mean square displacement and it is based on the assumption of a Gaussian probability distribution of the displacements. According to the central limit theorem for a sufficiently long elapsed time every random distribution of following steps ultimately tends to a Gaussian behaviour.[133, 134] However, for many physical environments like polymer solutions, biological cells or porous media, subsequent steps might present a non-zero correlation meaning that the systems keep "memory" of the previous state. This memory between following steps lead to a deviation from the normally distributed displacements and hence deviation from a simple diffusion. From a mathematical point of view this *anomalous diffusion* is encoded in the generalized Langevin equation,[135, 136] with the formalism of fractional derivatives, leading to a power law dependence of the mean square displacement introduced in Eq.1.4:[133, 137]

$$\langle \Delta r^2 \rangle = 6D(t)t^{\alpha} \tag{1.15}$$

where $D(t)$ is the diffusion coefficient, t is the lag time, and α is a parameter accounting for the degree of deviation from Brownian diffusion. Fig.1.5c shows three types of diffusion that can be identified: normal or Brownian ($\alpha = 1$),

sub-diffusion ($\alpha < 1$), and super-diffusion ($\alpha > 1$). In general, any deviation from normal Brownian motion is considered anomalous diffusion, where MSD is not linearly correlated to time.[138] Anomalous diffusion can be caused by molecular crowding,[139, 140] the restriction of diffusion,[141] or internal mobility of polymer chains.[142]

As already observed, anomalous diffusion can occur in some complex systems with anisotropic confinement, such as brain tissue,[143] where diffusion may be sub-diffusive in one dimension but normal in others, and in carbon nanotubes,[144] where molecules diffuse along the tube's axis but are restricted orthogonally. In the formalism of a diluted colloidal suspension used to obtain the Stokes-Einstein law, it has already been shown that the MSD is composed by a short term behaviour which increases with t^2 and a linear behaviour at longer elapsed time (Eq.1.6). If, as it is in many real cases, the suspension is not infinitely diluted there will be a characteristic time when the particle-particle interaction becomes effective.[145] When particles come close, their movement slows down due to the caging effect of nearby particles, resulting in sub-diffusion. An example of this heterogeneous MSD profile is given for proteins in solution where a short time regime mediated by hydrodynamic interactions couples with direct interactions after a specific lag time, and hence directly relates to macromolecular crowding. The lag time for the case of a protein of radius 2.5 nm in water near ambient temperature can be on the order of 100 ns. On a longer observation timescale this effect is averaged out and diffusion becomes simple diffusion in the long-time limit.[145] It is intuitive to associate sub-diffusion with molecular motion hindered by physical obstacles, such as crowding or confinement.[146] However, super-diffusion has been reported, for instance, in the case of ibuprofen migrating through a polymeric gel, where interactions with anionic fibers enhance mobility;[147] in this context, the diffusion is marked by a non-uniform distribution of step sizes, influenced by cycles of temporary binding and release due to transient hydrogen bonds between the drug and the gel network.

Therefore to observe hints of anomalous diffusion, it is crucial to match the timescale when the physical origin of the deviation from a simple Brown-

ian motion becomes effective, and hence selecting the experimental technique to probe diffusion accordingly is essential. As it is shown Fig.1.5a, ballistic diffusion ("free flight") is present in the very first step of diffusion prior to collisions of the diffusing particle with surrounding solvent molecules, where the hypothesis of a decoupled timescale between fast solvent and slow solute does not hold.[148]

Although non-Gaussian probability distribution is a widespread issue, a general interpretation of its origin is still pursued starting from a quantitative assessment of the self part of the Van Hove distribution $G_s(\vec{r}, t)$ for different elapsed times. For non-Gaussian distribution $G_s(\vec{r}, t)$ a central portion of the curve can be well approximated with a symmetrical bell shape curve with its own width, and deviations are observed in the tail of the distribution. Wang et al.[149] modeled this deviation with a single exponential decay in the case of lipid vesicles diffusing in a solution of aligned F-actin filaments. By decoupling the average diffusivity into a Gaussian and non-Gaussian diffusion coefficient, they have shown that the main differences in the liposome diffusivity, perpendicular and parallel to the filaments, arises from the contribution of the tails of the distribution. Their hypothesis is that the non-Gaussianity is due to the coupling between liposome and filaments diffusivity within a comparable time scale. Foreman et al. analysed the tail of the distribution with a term α_2 coming from a series expansion of $G_s(\vec{r}, t)$ which is a hallmark of non-Gaussianity for $\alpha_2 > 0$ (where $\alpha_2 = 0$ stands for Gaussian behaviour). It has been shown that larger deviation from Gaussian dynamics of probe particles in an unentangled polymer solution is more pronounced in case of larger particles.[150] These two examples suggest how different physical reasons underpin the non-Gaussian behaviour of complex systems.

Factors affecting diffusion in gels

The diffusion of solutes within gels differs significantly from the behavior of free colloidal particles in a continuous fluid of known viscosity. This difference arises primarily from the sample-spanning network that defines the gel's structure and imparts its viscoelastic properties.[151] This network im-

poses a combination of constraints on solute dynamics, that can be broadly classified into **steric** and **non-steric** interactions. Steric interactions result from the spatial restrictions imposed by direct confinement the gel network (Fig.1.8a).[152–154] These constraints limit the solute's free path, with the degree of restriction determined by the relative size of the solute and the gel's mesh size (Fig.1.4).[105, 155–157] The heterogeneity of gels, determined by a distribution of pore and fibre sizes,[158, 159] create regions with differing degrees of confinement: solutes near the fibres experience greater confinement, while others in the inner regions of the pores exhibit a more bulk-like behavior. Non-steric interactions encompass all indirect effects on solute diffusion arising from the gel's surface chemistry. These effects can be significant, as the total fibre surface of a bulk gel composed of nanostructures is exceptionally large (Fig.1.8b-d).[160] Key contributions include hydrophobic[161, 162] and electrostatic interactions,[163–165] as well as hydrodynamic effects due to variations in solvent viscosity induced by fiber chemistry.[166] Importantly, the temporal scale at which solute diffusion is analyzed regulates the interplay between steric and non-steric factors. Adapting concepts from colloidal physics,[148] two diffusion regimes can be distinguished. In the short-time regime, solutes move over distances comparable to their size. Here, hydrodynamic interactions dominate over steric hindrance plays a minor role because boundaries too far. Short-time diffusion can thus be approximated as free movement in a locally homogeneous medium, with hydrodynamic interaction altering the effective solvent viscosity. Conversely, in the long-time domain, solutes travel longer distances and more likely approaching the physical boundaries that extend their diffusion paths and slow their overall mobility.[167] In this regime, hydrodynamic interactions provide a subtle background influence that is often masked by the stronger effects of fiber confinement. Nevertheless, these interactions remain important and can influence the overall dynamics. For instance, a study combining experiments and simulations in a polymeric gel showed that including hydrodynamic interactions in the simulation model improved its alignment with experimental data, emphasizing the relevance of these interactions despite confinement.[168]

1.3.3 Empirical models for diffusion in gels

Building on the theoretical framework of diffusion, empirical models provide a practical approach to describe and predict diffusion in complex systems like gels. Mathematical solutions to Equation 1.2 are typically derived under assumptions of infinite media or specific boundary conditions defined by simplified geometries such as plane sheets, cylinders, or spheres.[109] However, for describing and predicting solute diffusion in real systems like gels, phenomeno-

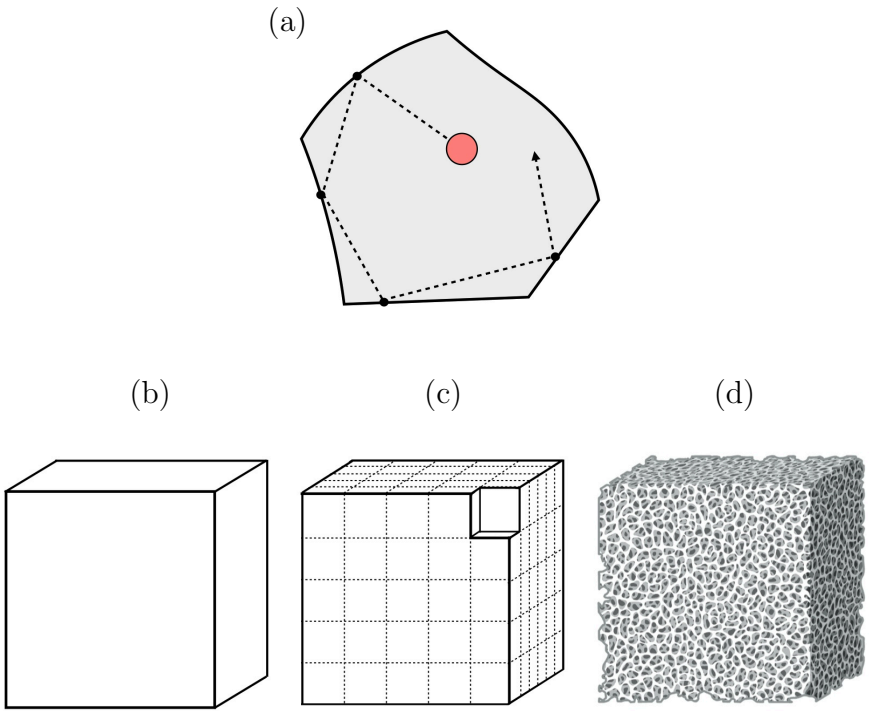

Figure 1.8: Schematic representation showing (a) Steric hindrance encountered by a spherical molecule as it diffuses over distances constrained by surrounding boundaries. (b)-(c) Surface area amplification at the nanoscale: a cubic volume of 1 cm^3 subdivided into units of 1 nm^3 results in a total surface area increase by a factor of 10^7. (d) For a macroscopic gel sample composed of entangled nanofibers, this scaling provides an estimate of the extensive surface area available for interaction with the liquid phase.

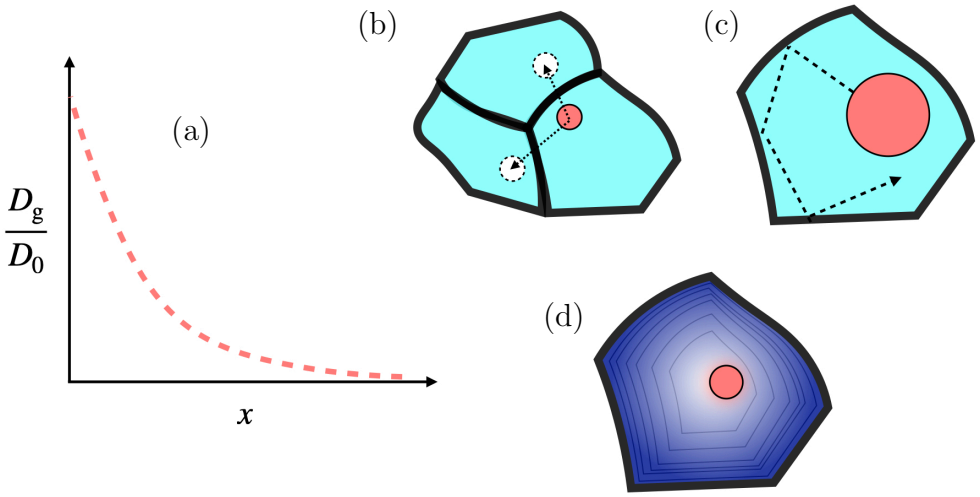

Figure 1.9: (a) This schematic diagram illustrates the common trend of spherical molecule's diffusion within gel networks according to the three different theories. The variable x in linear scale represents factors that hinder diffusion in gels, such as the size of the diffusing molecule, the fibre density, and the interaction with the gel matrix.(b) Free-volume theory describing the molecule jumping between the free volume of neighbouring pores (c) obstruction theory showing a rigid network hindering large molecule (d) hydrodynamic theory showing increase drag to the solvent introduced by the presence of the polymer.

logical corrections to the theoretical values are often employed. Empirical models for gel diffusion coefficient D_g generally consists in scaling reference diffusion coefficients (D_0, such as for solutes in bulk water) with exponential decay functions (Fig.1.9a).[85, 169–172] The exponential factors account for the reduction in diffusion rates caused by the gel matrix and distinguish one model from another. Conceptually, these factors can be grouped into three classes of theories: free-volume, obstruction and hydrodynamic. Out of these, the first two conceptualize the schematic regimes of fast and slow diffusion depicted in Fig.1.4. The **free-volume theory** is mostly applied when the solute size is smaller than the dimension of the pore in the gel network.[173] and

it describes the diffusion of molecules as proceeding through jumps between transient voids formed in the solvent space by the redistribution of the free volume within the liquid (Fig.1.9b).[174] The main factor hindering diffusion in the model originally proposed by Yasuda et al.[175] and then developed by Lustig and Peppas[176, 177] is the probability of finding a hole free-volume adjacent to the molecule:

$$\frac{D_g}{D_0} = P_0 \cdot \exp\left[-\frac{V_s}{V_{fvw}}\left(\frac{\phi_p}{1-\phi_p}\right)\right] \tag{1.16}$$

where D_g is the diffusion coefficient in the gel, D_0 is the diffusion coefficient in the bulk solvent, V_s is the volume of the solute, V_{fvw} is the solvent free volume, and ϕ_p is the polymer volume fraction in the gel. The probability of finding an opening between the polymer chains, P_0, modulated the overall diffusion process.

The **obstruction theory** describes the gel network as a matrix of immobile, impermeable fibers that restrict solute diffusion by acting as a sieve, where the polymer chains increase the solute's path length and thus slow diffusion (Fig.1.9c).[178–180] Hence, the factor hindering diffusion here is primarily the polymer chain, acting as a sieve, that increase the free path of the solute thus resulting in a slower diffusion. Among the models derived from this theory, the one proposed by Ogston has shown the best agreement with experimental data.[172, 181] This model considers the polymer network as randomly oriented straight fibers, where the diffusion of molecules depends on the ratio of their size to the available space within the polymeric structure. This relationship is described mathematically as:

$$\frac{D_g}{D_0} = \exp\left(-\pi\left[\frac{r_s + r_f}{\xi + 2r_f}\right]^2\right) \tag{1.17}$$

where r_s is the solute radius, r_f is the hydrated radius of the gel fibres and ξ is the mesh size. It has been recently shown that the agreement with the experimental data can vary depending on the definition of the mesh size ξ, either as the correlation length (the segment of the polymer chain between entanglement points that remains unaffected by other chains) or as the mesh

radius (defined as the end-to-end distance between cross-linking points within the network).[172] The obstruction model has proven effective for describing the diffusion of hard spheres that do not chemically interact with rigid polymer fibers.[172] The **hydrodynamic theory** describes the increase of the frictional drag ($\gamma = 6\pi\eta R$) of the Stokes Einstein equation (Eq.1.10) due to the presence of the fibres (Fig.1.9d).[171, 182] Cukier's formulation[183] describes this increase hindrance as a function of drug size, mesh size and a constant of proportionality incorporating polymer-solvent interactions κ:

$$\frac{D}{D_0} = \exp\left(-\kappa\frac{r_\mathrm{s}}{\xi}\right) \tag{1.18}$$

The most advanced approach in the development of empirical models for diffusion in hydrogels consists in multiscale diffusion models (MSDM), that aim to provide a comprehensive description by integrating different theoretical frameworks and accounting for their dominance across various length scales. A notable contribution in this regard is the work of Axpe et al.,[184] which combines free-volume (Eq. 1.16) and obstruction (Eq. 1.17) theories while minimizing the reliance on empirical parameters:

$$\frac{D_\mathrm{g}}{D_0} = A \cdot \exp\left[-\frac{V_\mathrm{s}}{V_\mathrm{fvw}}\left(\frac{\phi_\mathrm{p}}{1-\phi_\mathrm{p}}\right)\right] + (1-A)\cdot\exp\left(-\pi\left[\frac{r_\mathrm{s}+r_\mathrm{f}}{\xi+2r_\mathrm{f}}\right]^2\right) \tag{1.19}$$

where A is a weighting factor that balances the contributions of the two mechanisms by normalizing the total probability. This model was validated through a meta-analysis of 66 different combinations of solute sizes (dextrans) and hydrogel types, including PEG- and alginate-based systems, demonstrating its potential to predict the transition between diffusion regimes for pharmaceutically relevant solute sizes. However, its applicability is limited by the exclusion of critical drug-polymer interactions, such as hydrophobic, cation-π, and electrostatic effects, which can further reduce diffusion by up to 25%.[185] Incorporating these interactions would compromise the model's generality, as it would necessitate a shift toward highly system-dependent frameworks, thus reducing its broad applicability.[184] In conclusion, despite their utility in in-

cluding the factors influencing diffusion in hydrogels within a mathematical formalism, these empirical models retain significant limitations that hinder their predictive power. Moreover, the experimental techniques used to validate these models vary widely, from macroscopic approaches like drug release across membranes and slabs to microscopic methods such as fluorescent imaging or spectroscopy. These techniques probe different diffusion phenomena, ranging from concentration-driven gradients to self-diffusion, and span various timescales, often considering steric and non-steric effects indiscriminately. In addition to that, while these models were primarily designed for the diffusion of hard spheres in polymeric and inert gels, their applicability to supramolecular gels remains uncertain. The heterogeneous and flexible nature of supramolecular gels, combined with limited control over polymerization degree, poses additional challenges for adapting these models to such complex systems.[156, 158]

1.3.4 Experimental methods to probe diffusion

Bulk diffusion

The simplest setup to probe drug diffusion at long time scale consists of exposing the drug-loaded gel (source) to a large receptor buffer (sink), allowing the solute to diffuse via concentration gradient of Fick's law (Fig.1.10a).[186–188] Several physicochemical parameters influence the drug release at long time scale; pH affects drug solubility and the solute's interaction with the polymer network via changes in electrostatic properties; temperature influences the gel's stability and swelling behavior; agitation speed can accelerate solute migration or disrupt the hydrogel scaffold; not sufficiently large buffer volume can affect the concentration gradient. Methods to probe drug concentration profiles over time in the buffer, range from simple and accessible techniques to those requiring higher sensitivity and specificity. UV-Vis absorption spectroscopy is commonly used but has limitations in sensitivity at low concentrations and lacks specificity for distinguishing multiple components (see Chapter 2). To overcome these limitations, UV-Vis spectroscopy is often

combined with High-Performance Liquid Chromatography (HPLC), which separates species and enhances detection even at low concentrations.[189] Given the sensitivity of these experiments to external factors like pH, temperature, and agitation, as well as the long acquisition times (hours to days), efforts have been made to standardize experimental setups. In fact, the heterogeneity of these setups directly impacts mathematical modeling of drug release kinetics, which remains highly system-specific. This is evident in the commonly used Korsmeyer-Peppas equation:[190]

$$\frac{M_t}{M_\infty} = k \cdot t^n \tag{1.20}$$

that describes the amount of drug released at a certain time M_t over the total mass released M_∞ in terms of a kinetic constant k and a diffusivity exponent n, a parameter describing the release mechanism. For $n = 0.5$, Eq.1.20 reduces

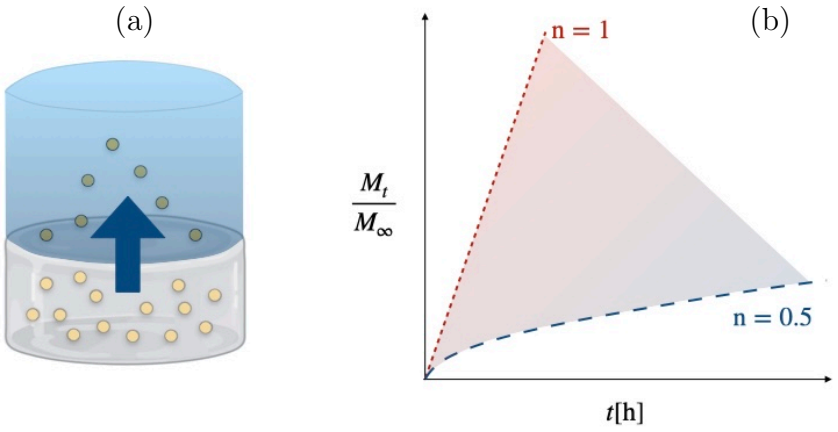

Figure 1.10: (a) General sketch of drug release experiment, with a solute entrapped in a gel layer flowing by concentration gradients to a buffer. (b) Korsmeyer-Peppas equation profiles at different n values, ranging from diffusion-controlled mechanisms (Higuchi equation, $n = 0.5$) to zero-order kinetics ($n = 1$). Intermediate values reflect the transition from diffusion-controlled release to gel erosion or swelling mechanisms

Table 1.2: Comparison of relevant methods for probing solute diffusion in gels.

Method	**Time Scale**	**Length Scale**
UV-vis, HPLC	hours - days	mm
FRAP	s - min	μm
FCS	μs - ms	μm
SPT	ms - s	nm
(PFG)-NMR	ms - s	μm - mm
QENS	ps - ns	Å- nm

to the Higuchi equation, representing purely diffusion-driven release, typically applicable for small solutes relative to mesh size.[191] When n ranges between 0.5 and 1 (constant amount of drug released over time, zero order kinetics) (Fig.1.10b), the release mechanism transitions between diffusion control and processes such as gel swelling or surface erosion, which are challenging to disentangle. Despite improvements and standardization of experimental setups, probing bulk diffusion at long timescales inherently fails to capture the complexities at smaller scales. As discussed in the previous sections, the longer the time scale measured, the more entangled steric and non-steric interactions become, making it difficult to accurately describe self-diffusion and resulting in a diffusion coefficient that combines various contributions.

Molecular level diffusion

Fluorescent labelling An intuitive method to visualize molecular diffusion is to use the fluorescent properties of molecules or attach fluorescent labels to them. Techniques based on this principle include Fluorescence Correlation Spectroscopy (FCS), Fluorescence Recovery After Photobleaching (FRAP), and Single-Particle Tracking (SPT).

FCS, for instance, is based on confocal fluorescence microscopy to monitor fluctuations in fluorescence intensity caused by molecules diffusing through a small observation volume.[192] In this technique, the fluorescence intensity at a given time, $I_{\mathrm{f}}(t)$, is compared to the intensity at a later time, $I_{\mathrm{f}}(t+\tau)$.

By analyzing the relationship between these two intensity measurements over increasing lag times (τ) yields the autocorrelation function, $G(\tau)$, expressed as:[193]

$$G(t,\tau) = \frac{\langle I_{\mathrm{f}}(t) I_{\mathrm{f}}(t+\tau)\rangle}{\langle I_{\mathrm{f}}(t)\rangle^2} \tag{1.21}$$

At $\tau = 0$, the autocorrelation function reaches its maximum, $G(t,0)$, which is inversely proportional to the average number of molecules within the confocal volume. As τ increases, the autocorrelation function decays, typically following a single exponential process: $G(t,\tau) \sim G(t,0) \times \exp(-t/\tau_{\mathrm{D}})$, where τ_{D} represents the relaxation time. When diffusion is slow, $I(t)$ and $I(t+\tau)$ remain similar in magnitude since molecules do not diffuse out of the focal volume during short lag times. Therefore, longer correlation times correspond to longer relaxation times, which indicate lower self-diffusion coefficients, as $D_{\mathrm{self}} \sim \tau_{\mathrm{D}}^{-1}$. Formally, the autocorrelation function in Eq.1.21 is similar to that used in other techniques to probe molecular diffusion such as Dynamic Light Scattering (DLS) or X-ray Photon Correlation Spectroscopy (XPCS). However, FCS is particularly advantageous for studying diffusion in gels. Unlike DLS, FCS is not affected by multiple scattering in opaque or turbid samples being more selective to fluorescent probes,[194] and it avoids sample damage due to intense radiation, as in XPCS.[195] Moreover, FCS requires minimal sample quantities, functioning effectively with highly dilute solutions at nanomolar to micromolar concentrations. By focusing on a femtoliter-scale observation volume, FCS enables precise analysis of molecular motion and interactions within complex biological environments,[196] over timescales ranging from microseconds to milliseconds.[140] At this scale, steric confinement within a fiber network plays a critical role in diffusion, as demonstrated by Fatin-Rouge et al., who used FCS to study rhodamine 6G-labeled nanoparticles in agarose gels.[197] Their findings highlight FCS's ability to measure diffusion regimes governed by the solute-to-mesh size ratio, enabling the detection of anomalous diffusion of larger molecules.

FRAP offers an alternative approach for determining the diffusion and transient binding of a fluorescent probe molecule in biological tissues or soft materi-

als.[198] In a typical FRAP experiment, a high-intensity laser beam irreversibly photobleaches fluorophores in a defined region of the sample, reducing fluorescence intensity in that area.[199] Recovery occurs as unbleached fluorescent molecules diffuse into, and bleached molecules exit, the region. The recovery rate, tracked via fluorescence intensity over time, reveals diffusion rates and binding interactions.[200] FRAP typically measures diffusion at micrometer and second scales, much longer than FCS, thus including the study of solute-fibre interaction, as well as direct confinement effects within gel networks. Among the parameters extracted from the fit of experimental data, the bound vs. free fraction, residence time at binding sites, and immobile fraction offer unique insights into the dynamics within gel networks.[201] For instance, Cinar et al. used FRAP to investigate the mobility of doxorubicin, a fluorescent anticancer drug, in a peptide amphiphile supramolecular gel.[202] They found that drug mobility was influenced by gelator concentration, with up to 50% of the drug becoming immobilized at higher concentrations.(Further details on the mathematical and computational interpretation of FRAP data are available in the review by Lorén et al.[198] Both FCS and FRAP have inherent limitations. The use of fluorescent labels can alter the mobility of molecules by changing their size and shape, which may affect the accuracy of diffusion measurements. In addition, both techniques are susceptible to light-induced damage: FCS can cause photo-damage to the solute or diffusion medium, particularly at high laser powers, while FRAP's photobleaching process can also affect the sample, especially in biological contexts. Furthermore, when both diffusion and binding occur simultaneously, the standard models for both methods may not accurately describe the recovery or correlation data, requiring more complex fitting models to obtain reliable results.[198]

SPT is a fluorescence microscopy method that adopts a different approach compared to FCS or FRAP. Instead of analyzing average intensity fluctuations within a small volume, SPT uses high-sensitivity cameras to detect and localize single emitters in real time, directly tracking individual molecules or particles, visualizing their trajectories (a process analogous to molecular dynamics simulations,[173] but achieved through experimental observation).[203] By

repeatedly imaging the same molecule across consecutive frames, SPT reconstructs its path through space while simultaneously quantifying parameters like diffusion coefficients, confinement zones, or directional motion. As with other labeling methods, the relative size of the labels compared to the parent molecules can introduce artifacts in describing the parent dynamics. Achieving sustained intensity over time (up to several minutes) with optimal spatial accuracy (1–50 nm) depends on photon acquisition, which is influenced by the fluorescence quality of the tag and the microscope resolution. Smaller tags, such as organic dyes (1–2 nm) or quantum dots (5–8 nm), minimize perturbation to system mobility when attached to lipids, proteins, or DNA. In contrast, larger emitters like gold nanoparticles (> 40 nm) provide brighter and more photostable signals over extended periods. SPT is uniquely suited to directly quantify anomalous transport by mapping heterogeneous environments, such as crowded media, membranes, and gel networks.[204, 205] Burla et al. used SPT to investigate tracer diffusion in hyaluronan hydrogel networks, showing how crosslinking affects nutrient and growth factor transport.[206] They described sub-diffusion as resulting from enhanced viscous drag in loosely crosslinked networks and from steric hindrance in more rigid, less transient fibers. SPT also contributes to understanding ergodicity-breaking systems. The ergodic hypothesis assumes equivalence between time-averaged and ensemble-averaged measurements. By comparing single-particle trajectories averaged over time with ensemble techniques, SPT can reveal deviations from ergodicity.[150, 207] This is particularly relevant in systems like gels, where anisotropic phase space and heterogeneous dynamics can cause underestimation of global properties, such as diffusion coefficients or mean square displacement, when inferred from local single-particle analyses.

Nuclear Magnetic resonance (NMR) NMR offers a suite of techniques capable of probing molecular dynamics in gels across a broad spectrum of timescales, ranging from rapid solvent diffusion to slower interactions with gel fibers and network relaxation.[208] NMR operates on the principle that certain atomic nuclei possess intrinsic nuclear spin, which allows them to behave

like magnets when placed in a strong external magnetic field.[209] In this field, the nuclei align either with the field (lower energy state) or against it (higher energy state), creating two distinct energy levels. The application of radiofrequency pulses induces transitions between these energy levels, and upon its removal, the excited nuclei relax back to their ground state, emitting energy that can be analyzed as a measurable signal and converted into the characteristic NMR spectrum. The relaxation process, that can be studied in a non-invasive and non-destructive way, is significantly influenced by the chemical environment. Specifically NMR relaxometry can measure: a) the spin-lattice relaxation time T_1 which reflects the energy transfer from nuclear spins to their surrounding environment (the "lattice") and is sensitive to slow molecular motions (ms-s); b) the spin-spin relaxation time T_2 which reflects the loss in magnetization due to the interactions with the nearby excited nuclei resulting in a faster molecular motions ranging from μs to ms. Jadwiga Tritt-Goc's group has extensively employed NMR relaxometry to study solvent-gelator interactions, uncovering how gel structure significantly influence solvent mobility.[166, 210–212] NMR can be used to evaluate the ability of fiber surfaces to bind solvent molecules at the interface[213] or to promote interactions with guest molecules.[214] In this context, saturation transfer difference NMR (STD-NMR) has been utilized to probe the surface chemistry of gel fibers, revealing characteristics such as surface charge and ion-binding properties, which are influenced by preparation methods and gel composition.[215] In another study, Segarra-Maset et al. used STD-NMR to identify an affinity between dopamine and an hydrogel surface,[216] highlighting how solute-fiber interactions can be highly specific and selective.

Building on the basics of the method, Pulsed Field Gradient NMR (PFG-NMR) extend the NMR capabilities for quantitatively measuring molecular self-diffusion.[217–219] In a standard PFG-NMR experiment, two magnetic field gradient pulses are applied alongside 90° and 180° radiofrequency pulses. The first gradient pulse alters the alignment of nuclear spins, effectively encoding their positions, while the second gradient pulse aims to reverse this process and restore the original magnetization. However, because diffusion occurs between

these two pulses, not all magnetization can be perfectly refocused, leading to a reduction in signal intensity. This loss of signal is measured as a function of the strength of the magnetic field gradient and is used to calculate the diffusion coefficient. The relationship between signal attenuation and diffusion can be expressed by the Stejskal-Tanner equation:[218]

$$I_{\mathrm{G}} = I_{\mathrm{G}=0} \cdot \exp\left[-(\gamma\delta G)^2 \left(\Delta - \frac{\delta}{3}\right) \cdot D\right] \tag{1.22}$$

where I_{G} is the signal intensity at a specific gradient strength, $I_{\mathrm{G}=0}$ is the signal intensity when no gradient is applied, γ is the gyromagnetic ratio, δ is the duration of magnetic field-gradient pulse, G is the magnetic field gradient, and Δ is the diffusion time and D is the self-diffusion coefficient. The length scale probed depend on the gradient G strength and duration while the time scale is given by the interval between two pulses Δ leading to values from μm to mm and ms-s.[219] making this method ideal for investigating molecular-level solute dynamics in polymeric hydrogels.[220] This method has been employed to determine the diffusion coefficients of large molecules, such as insulin and lysozyme, in dextran hydrogel finding an agreement with drug release profiles.[221] However, although this technique provides a microscopic validation to drug release studies by probing a wide spatial and temporal range, it cannot unambiguously separate the contributions of steric and non-steric effect to solute diffusion withing the gel scaffold.

Quasi-Elastic Neutron Scattering (QENS)

In this thesis, QENS will be a central method for studying the diffusion of drug molecules within supramolecular gels. A more detailed discussion of the theoretical principles, experimental setup, and specific data analysis approaches will be presented in Chapter 3.

Quasi-elastic neutron scattering (QENS) is an experimental technique widely employed to study atomic fluctuations, molecular reorientations, and collective and self-dynamics by analyzing small energy and momentum transfers in neutrons after their interaction with atomic nuclei.[222, 223] QENS operates on the picosecond (10^{-12} s) to nanosecond (10^{-9} s) timescale and probes spatial lengths ranging from 1 to 500 Å, depending on the specific instrument configuration. This makes it uniquely suited to exploring diffusion regimes that are largely inaccessible to other experimental methods. Indeed, QENS enables direct experimental validation of phenomena that are otherwise only accessible through molecular dynamics simulations.[224, 225] Due to the specificity of neutron interaction with matter, QENS is particularly sensitive to light elements but it can have drastic differences among distinct isotopes, as it is the case of the high sensitivity of hydrogen (^{1}H) with respect to deuterium (^{2}H). This allows for the measurement of diffusion in a wide range of systems, from soft matter to condensed matter, without the need for tracers or labels that could alter the system's intrinsic properties.[225] Furthermore, unlike other scattering probes such as X-rays, neutrons do not cause radiation damage, making them ideal for studying biological systems in their native state. For instance, QENS has been successfully employed to investigate the dynamic behavior of lipid membranes interacting with the SARS-CoV-2 peptide, providing valuable insights into the mechanism of membrane fusion, a key process for viral entry and infection.[226] Similarly, QENS has proven effective in examining crowding effects in solutions of monoclonal antibodies, revealing how the macromolecular environment alters protein dynamics and interactions, an important factor in the formulation and stability of biopharmaceuticals.[227] In addition, the

technique has been employed to explore the intracellular dynamics of water in various human cancer cells compared to their healthy counterparts.[228] In the context of gels, QENS provides a unique perspective as it can probe the dynamics of network,[229, 230] or solvent[231–233] It has been shown that by varying the solvent's isotopic composition, QENS can selectively probe the dynamics of either water or polymer in poly(vinyl alcohol) (PVA) swollen hydrogels, allowing for the study of matrix-solvent interactions.[229] Although only a few studies have focused on solute diffusion in gels,[234] QENS holds significant potential for investigating the Brownian motion of solutes, such as drug molecules, in these media. However, the mesh size of typical gel networks is often two or more orders of magnitude larger than the length scales probed by QENS, meaning that confinement effects are less pronounced in gels compared to systems like

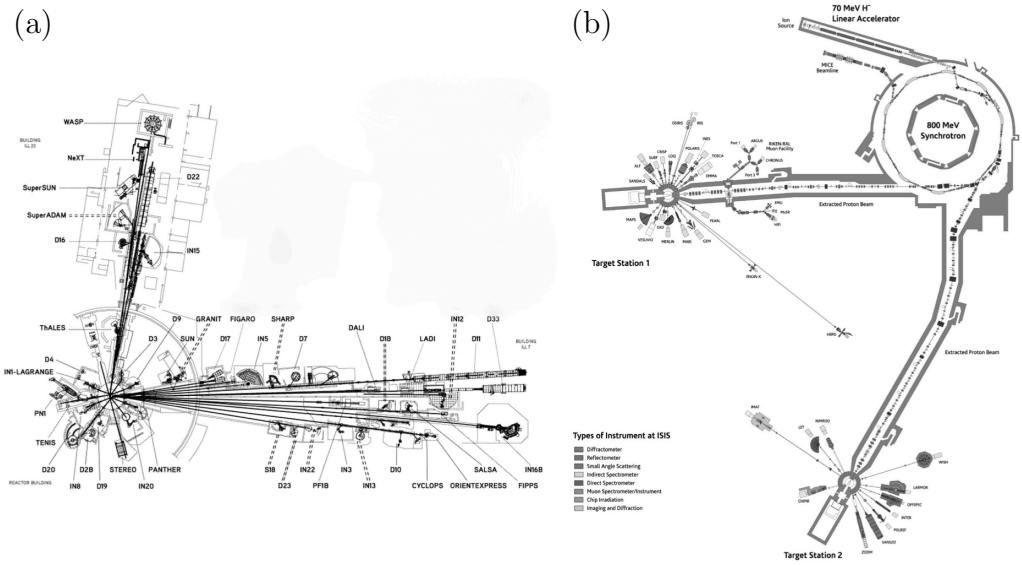

Figure 1.11: Neutron facilities.(a) Institut Max Von Laue-Paul Langevin (Grenoble, France) where neutron are produced via nuclear fission in a reactor and delivered as a continuous flux. Image taken from https://www.ill.eu/(b) ISIS spallation neutron and muon source at Harwell (Oxford, United Kingdom) where neutrons are emitted in pulses from an excited heavy nucleus bombarded by accelerated protons. Image taken from https://www.isis.stfc.ac.uk/

carbon nanotubes,[235] porous materials such as zeolites,[224, 236] or endofullerene cages that trap single atoms,[237] where confinement occurs at the atomic scale. Although gels provide lower degree of confinement than the physical systems above mentioned on the timescales accessible by QENS, this technique is a powerful tool for investigating the influence of fiber surfaces on solute dynamics. This is particularly evident in a series of studies where QENS was used to investigate the picosecond self-diffusion of solvent and drugs on a bis-urea supramolecular gel.[234, 238] These studies revealed that the self-diffusion of a water-ethanol mixture is faster in the gel than in the respective pure solution, with the effect being more pronounced in less concentrated gels. This increase in diffusion was attributed to a reduction in local viscosity caused by the breaking of hydrogen bonds near the hydrophobic surface of the gel fibers.[238] Conversely, the same system examined by PFG-NMR shows the opposite trend, with slower diffusion in the gel, underscoring the importance of the probed time scale in minimizing the influence of steric confinement. Moreover, even the self-diffusion of non-steroidal anti-inflammatory drugs, such as paracetamol and ibuprofen sodium, was found to be faster in the gel than in pure solution.[234] These findings demonstrate that QENS can effectively probe hydrodynamic interactions and surface effects on small diffusing molecules, even when direct fiber confinement is negligible due to the relatively small displacement scale compared to the mesh size. As will be elaborated in the following chapters, QENS also comes with its limitations. Pre-experiment, access to neutron facilities (Fig.1.11) can be competitive, with limited available beamtime and the need for meticulous planning. Post-experiment, data interpretation poses challenges, as the nanoscale phenomena observed are often influenced by overlapping random processes, making it difficult to assign specific causes to small energy differences derived from ensemble-averaged data.[239, 240]

1.4 Hypothesis and aim

Gels, which exhibit intermediate properties between liquids and solids, have emerged as promising vehicles for drug delivery in the pharmaceutical field, particularly for achieving the sustained release of therapeutic agents. Among these, supramolecular gels offer enhanced stimuli−responsiveness and greater tunability compared to conventional macromolecular gels. Despite these promises, drug release studies in supramolecular gels are often treated as if they involve a mere solvent system with the network providing only steric hindrance to diffusion. This representation has led to experimental approaches that predominantly utilize bulk techniques focused on diffusion driven by concentration gradients. In such methods non-steric factors like gel fiber chemistry, solvent structural relaxation, and network dynamics are masked by the dominant influence of steric confinement. Consequently, the theoretical frameworks that arise from these studies are typically based on highly system-specific phenomenological observations leading to empirical scaling of diffusion coefficient obtained with Fick's laws.

The project hypothesis is that a fundamental understanding of the principles governing diffusion at the microscopic scale is essential for developing a predictive approach to interpret drug release at the macroscopic scale. This hypothesis stems from the counterintuitive observation of faster drug diffusion probed with QENS in a bis-urea-based supramolecular gel, driven by gel surface chemistry and directly linked to the molecular structure and assembly of LMWG.[234, 238]

Building on these observations, this project aims to investigate drug diffusion in supramolecular gels by strategically examining the extremes of the diffusion timescale spectrum to decouple the factors influencing diffusion (Fig.1.12). The primary focus is on microscopic phenomena, where non-steric effects are likely to emerge. Quasi-elastic neutron scattering (QENS) will serve as the fundamental technique, uniquely giving access to molecule-size displacements

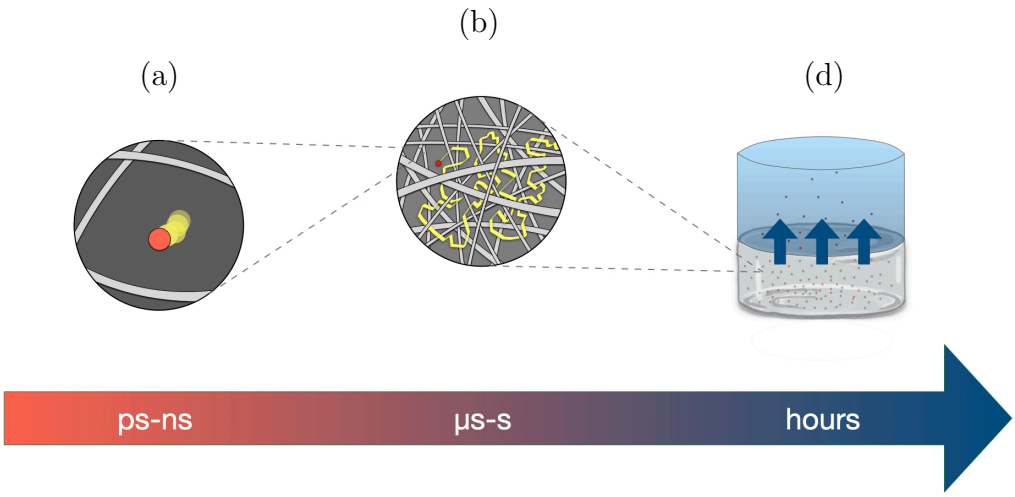

Figure 1.12: Schematic overview of a spherical molecule's diffusion within and from the gel matrix at different timescales.(a) $ps-ns$: non-steric hydrodynamic effect; (b) $\mu s-s$: direct confinement due to fibre network; (c) $hours$: combined impact of both effects at longer timescale.

without direct interference from direct fibre confinement, enabling the study of ensemble-average Brownian motion within the gel's pores. QENS data will be complemented by UV-Vis studies conducted in a subcutaneous injection site simulator (SCISSOR), an in vitro model designed to mimic subcutaneous injection. This bottom-up approach seeks to establish a novel framework for understanding drug diffusion in supramolecular gels, bridging the gap between theoretical and practical applications in drug delivery. The project's aims are structured around three core objectives:

- **Drug Size Across Scales:** Investigate the diffusion of various drugs, ranging from small molecules (Ibuprofen sodium) to biologics (Insulin and Lysozyme), within a single peptide hydrogel (FmocFF gel). This approach keeps the gel constant while varying solute size, to understand how molecular weight and geometry influence diffusion at both short and

long timescales.

- **Molecular-level Drug Diffusion in Tunable Hydrogels:** Examine the diffusion of a single drug (Doxorubicin) in a series of amphiphilic octa-peptide hydrogels derived from modifications of the F8 sequence, integrating existing UV-Vis studies with QENS measurements.
- **Diffusion from the Solvent Perspective:** Use the novel polarization analysis option implemented on QENS spectrometer to examine solvent (water-ethanol mixture) structural dynamics as influenced by the drug (Paracetamol) and the gel network (bis-urea)

Specifically, the bis-urea gel was selected due to the availability of prior QENS data under standard conditions;[234] the FmocFF gel enables extension of this approach to a distinct gel class, while the F8-based peptide family allows systematic investigation of surface modifications, leveraging its amphiphilic nature to better disentangle hydrophobic and hydrophilic effects—and was chosen over FmocFF due to existing diffusion data and its tunable sequence design. Due to the complexity of the task, this study does not aim to directly characterize the structural features of the gels, and therefore relies on the use of well-characterized gels from the literature. Instead, it seeks to indirectly probe the effects of specific molecular assemblies and surface chemistry through the dynamics of probe solutes.

Note: throughout this thesis, the term *microscopic* is used in contrast to macroscopic to describe molecular-level diffusion phenomena, rather than to specify a precise spatial regime (e.g., μm). While microscopic might conventionally imply intermediate length scales (such as region (b) in Fig.1.12), in this context it refers to short-timescale, local dynamics typically occurring on the picosecond to nanosecond range, where hydrodynamic effects dominate. To facilitate clarity, the terminology of *short*, *intermediate*, and *long* timescales is used consistently to distinguish the relevant regimes in solute diffusion through gels: short refers to picoseconds to nanoseconds, intermediate to the microsecond-to-second range where confinement effects emerge, and

long to macroscopic timescales spanning minutes to hours, where multiple effects are coupled. These definitions are specific to the framework of this thesis and aim to streamline discussion across different dynamical regimes.

Bibliography

[1] Qian Chen, Zhen Yang, Haoyu Liu, Jingyuan Man, Ayodele Olaolu Oladejo, Sally Ibrahim, Shengyi Wang, and Baocheng Hao. Novel drug delivery systems: An important direction for drug innovation research and development. *Pharmaceutics*, 16(5):674, 2024.

[2] Ava M Vargason, Aaron C Anselmo, and Samir Mitragotri. The evolution of commercial drug delivery technologies. *Nature biomedical engineering*, 5(9):951–967, 2021.

[3] Swen Hoelder, Paul A Clarke, and Paul Workman. Discovery of small molecule cancer drugs: successes, challenges and opportunities. *Molecular oncology*, 6(2):155–176, 2012.

[4] Caroline F Thorn, Connie Oshiro, Sharon Marsh, Tina Hernandez-Boussard, Howard McLeod, Teri E Klein, and Russ B Altman. Doxorubicin pathways: pharmacodynamics and adverse effects. *Pharmacogenetics and genomics*, 21(7):440–446, 2011.

[5] Erica Gornstein and Thomas L Schwarz. The paradox of paclitaxel neurotoxicity: Mechanisms and unanswered questions. *Neuropharmacology*, 76:175–183, 2014.

[6] Huy X Ngo and Sylvie Garneau-Tsodikova. What are the drugs of the future? *MedChemComm*, 9(5):757–758, 2018.

[7] Michael S Kinch, Zachary Kraft, and Tyler Schwartz. Monoclonal antibodies: Trends in therapeutic success and commercial focus. *Drug Discovery Today*, 28(1):103415, 2023.

[8] T Thanh Le, Zacharias Andreadakis, Arun Kumar, R Gómez Román, Stig Tollefsen, Melanie Saville, Stephen Mayhew, et al. The covid-19 vaccine development landscape. *Nat Rev Drug Discov*, 19(5):305–306, 2020.

[9] Jeffrey M Friedman. The discovery and development of glp-1 based drugs that have revolutionized the treatment of obesity. *Proceedings of the National Academy of Sciences*, 121(39):e2415550121, 2024.

[10] Dzintars Gotham, Melissa J Barber, and Andrew Hill. Production costs and potential prices for biosimilars of human insulin and insulin analogues. *BMJ global health*, 3(5):e000850, 2018.

[11] Xin Xu and Yulia Vugmeyster. Challenges and opportunities in absorption, distribution, metabolism, and excretion studies of therapeutic biologics. *The AAPS journal*, 14:781–791, 2012.

[12] Julia Mantaj and Driton Vllasaliu. Recent advances in the oral delivery of biologics. *Pharm J*, 304(7933):2–7, 2020.

[13] Solene Masloh, Maxime Culot, Fabien Gosselet, Anne Chevrel, Leonardo Scapozza, and Magali Zeisser Labouebe. Challenges and opportunities in the oral delivery of recombinant biologics. *Pharmaceutics*, 15(5):1415, 2023.

[14] Nataša Škalko-Basnet. Biologics: the role of delivery systems in improved therapy. *Biologics: Targets and Therapy*, pages 107–114, 2014.

[15] Michael R Turner and Sathy V Balu-Iyer. Challenges and opportunities for the subcutaneous delivery of therapeutic proteins. *Journal of pharmaceutical sciences*, 107(5):1247–1260, 2018.

[16] Lorenzo Tomasini, Marianne Ferrere, and Julien Nicolas. Subcutaneous drug delivery from nanoscale systems. *Nature Reviews Bioengineering*, pages 1–20, 2024.

[17] Russell P Watt, Hetal Khatri, and Andrew RG Dibble. Injectability as a function of viscosity and dosing materials for subcutaneous administration. *International Journal of Pharmaceutics*, 554:376–386, 2019.

[18] Shradha Dattani, Xiaoling Li, Charina Lampa, David Lechuga-Ballesteros, Amanda Barriscale, Behzad Damadzadeh, and Bhaskara R Jasti. A comparative study on micelles, liposomes and solid lipid nanoparticles for paclitaxel delivery. *International Journal of Pharmaceutics*, 631:122464, 2023.

[19] Shivakalyani Adepu and Seeram Ramakrishna. Controlled drug delivery systems: current status and future directions. *Molecules*, 26(19):5905, 2021.

[20] Tsvetelina H Baryakova, Brett H Pogostin, Robert Langer, and Kevin J McHugh. Overcoming barriers to patient adherence: the case for developing innovative drug delivery systems. *Nature Reviews Drug Discovery*, 22(5):387–409, 2023.

[21] Jonathan W Steed. Anion-tuned supramolecular gels: a natural evolution from urea supramolecular chemistry. *Chemical Society Reviews*, 39(10):3686–3699, 2010.

[22] Soumya Banerjee and Suvendu Bhattacharya. Food gels: gelling process and new applications. *Critical reviews in food science and nutrition*, 52(4):334–346, 2012.

[23] Ming Dai, Fei Zhao, Juanjuan Fan, Qing Li, Ya Yang, Zhuangjun Fan, Shengjie Ling, Haipeng Yu, Shouxin Liu, Jian Li, et al. A nanostructured moisture-absorbing gel for fast and large-scale passive dehumidification. *Advanced Materials*, 34(17):2200865, 2022.

[24] Gerald H Pollack. Is the cell a gel—and why does it matter? *The Japanese journal of physiology*, 51(6):649–660, 2001.

[25] D Jordon Lloyd. The problem of gel structure. *Colloid chemistry*, 1:767–782, 1926.

[26] Pablo Sánchez-Cid, Mercedes Jiménez-Rosado, Alberto Romero, and Víctor Pérez-Puyana. Novel trends in hydrogel development for biomedical applications: A review. *Polymers*, 14(15):3023, 2022.

[27] Maya Davidovich-Pinhas. Oleogels: a promising tool for delivery of hydrophobic bioactive molecules, 2016.

[28] Mariia A Kuzina, Dmitrii D Kartsev, Alexander V Stratonovich, and Pavel A Levkin. Organogels versus hydrogels: advantages, challenges, and applications. *Advanced Functional Materials*, 33(27):2301421, 2023.

[29] Carla Villa and Eleonora Russo. Hydrogels in hand sanitizers. *Materials*, 14(7):1577, 2021.

[30] Iris L Kim, Robert L Mauck, and Jason A Burdick. Hydrogel design for cartilage tissue engineering: a case study with hyaluronic acid. *Biomaterials*, 32(34):8771–8782, 2011.

[31] Pei Yun Lee, John Costumbrado, Chih-Yuan Hsu, and Yong Hoon Kim. Agarose gel electrophoresis for the separation of dna fragments. *Journal of visualized experiments: JoVE*, (62):3923, 2012.

[32] Chien-Chi Lin and Kristi S Anseth. Peg hydrogels for the controlled release of biomolecules in regenerative medicine. *Pharmaceutical research*, 26:631–643, 2009.

[33] Anisha A D'souza and Ranjita Shegokar. Polyethylene glycol (peg): a versatile polymer for pharmaceutical applications. *Expert opinion on drug delivery*, 13(9):1257–1275, 2016.

[34] Jaya Maitra, Vivek Kumar Shukla, et al. Cross-linking in hydrogels-a review. *Am. J. Polym. Sci*, 4(2):25–31, 2014.

[35] Caroline SA de Lima, Tatiana S Balogh, Justine PRO Varca, Gustavo HC Varca, Ademar B Lugão, Luis A. Camacho-Cruz, Emilio Bucio, and Slawomir S Kadlubowski. An updated review of macro, micro, and nanostructured hydrogels for biomedical and pharmaceutical applications. *Pharmaceutics*, 12(10):970, 2020.

[36] V Castro Lopez, J Hadgraft, and MJ Snowden. The use of colloidal microgels as a (trans) dermal drug delivery system. *International journal of pharmaceutics*, 292(1-2):137–147, 2005.

[37] Hui Zhang, Yingjie Zhai, Juan Wang, and Guangxi Zhai. New progress and prospects: The application of nanogel in drug delivery. *Materials Science and Engineering: C*, 60:560–568, 2016.

[38] Mariana Chelu and Adina Magdalena Musuc. Polymer gels: Classification and recent developments in biomedical applications. *Gels*, 9(2):161, 2023.

[39] Pierre Terech and Richard G Weiss. Low molecular mass gelators of organic liquids and the properties of their gels. *Chemical reviews*, 97(8):3133–3160, 1997.

[40] Lara A Estroff and Andrew D Hamilton. Water gelation by small organic molecules. *Chemical reviews*, 104(3):1201–1218, 2004.

[41] Neralagatta M Sangeetha and Uday Maitra. Supramolecular gels: Functions and uses. *Chemical Society Reviews*, 34(10):821–836, 2005.

[42] Gareth O Lloyd and Jonathan W Steed. Anion-tuning of supramolecular gel properties. *Nature chemistry*, 1(6):437–442, 2009.

[43] Marc-Oliver M Piepenbrock, Gareth O Lloyd, Nigel Clarke, and Jonathan W Steed. Metal-and anion-binding supramolecular gels. *Chemical reviews*, 110(4):1960–2004, 2010.

[44] Kenji Hanabusa and Masahiro Suzuki. Development of low-molecular-weight gelators and polymer-based gelators. *Polymer journal*, 46(11):776–782, 2014.

[45] Kathryn J Skilling, Francesca Citossi, Tracey D Bradshaw, Marianne Ashford, Barrie Kellam, and Maria Marlow. Insights into low molecular mass organic gelators: a focus on drug delivery and tissue engineering applications. *Soft matter*, 10(2):237–256, 2014.

[46] Christopher D Jones and Jonathan W Steed. Gels with sense: supramolecular materials that respond to heat, light and sound. *Chemical Society Reviews*, 45(23):6546–6596, 2016.

[47] Emily R Draper and Dave J Adams. Low-molecular-weight gels: the state of the art. *Chem*, 3(3):390–410, 2017.

[48] Phillip RA Chivers and David K Smith. Shaping and structuring supramolecular gels. *Nature Reviews Materials*, 4(7):463–478, 2019.

[49] David K Smith. Supramolecular gels–a panorama of low-molecular-weight gelators from ancient origins to next-generation technologies. *Soft Matter*, 2024.

[50] Sijie Xian and Matthew J Webber. Temperature-responsive supramolecular hydrogels. *Journal of Materials Chemistry B*, 8(40):9197–9211, 2020.

[51] Carlo Diaferia, Elisabetta Rosa, Giancarlo Morelli, and Antonella Accardo. Fmoc-diphenylalanine hydrogels: Optimization of preparation methods and structural insights. *Pharmaceuticals*, 15(9):1048, 2022.

[52] Zhimou Yang, Gaolin Liang, and Bing Xu. Enzymatic control of the self-assembly of small molecules: a new way to generate supramolecular hydrogels. *Soft Matter*, 3(5):515–520, 2007.

[53] Fan Xu and Ben L Feringa. Photoresponsive supramolecular polymers: From light-controlled small molecules to smart materials. *Advanced Materials*, 35(10):2204413, 2023.

[54] Ruben Van Lommel, Julie Van Hooste, Johannes Vandaele, Gert Steurs, Tom Van der Donck, Frank De Proft, Susana Rocha, Dimitrios Sakellariou, Mercedes Alonso, and Wim M De Borggraeve. Does supramolecular gelation require an external trigger? *Gels*, 8(12):813, 2022.

[55] Mari C Mañas-Torres, Cristina Gila-Vilchez, Juan A González-Vera, Francisco Conejero-Lara, Victor Blanco, Juan Manuel Cuerva, Modesto T Lopez-Lopez, Angel Orte, and Luis Álvarez de Cienfuegos. In situ real-time monitoring of the mechanism of self-assembly of short peptide supramolecular polymers. *Materials Chemistry Frontiers*, 5(14):5452–5462, 2021.

[56] Shinya Kimura, Kurea Adachi, Yoshiki Ishii, Tomoki Komiyama, Takuho Saito, Naofumi Nakayama, Masashi Yokoya, Hikaru Takaya, Shiki Yagai, Shinnosuke Kawai, et al. Molecular-level insights into the supramolecular gelation mechanism of urea derivative. *Nature Communications*, 16(1):3758, 2025.

[57] Dave J Adams. Personal perspective on understanding low molecular weight gels. *Journal of the American Chemical Society*, 144(25):11047–11053, 2022.

[58] Emily R Draper and Dave J Adams. Controlling supramolecular gels. *Nature Materials*, 23(1):13–15, 2024.

[59] Guocan Yu, Xuzhou Yan, Chengyou Han, and Feihe Huang. Characterization of supramolecular gels. *Chemical Society Reviews*, 42(16):6697–6722, 2013.

[60] Alexander Ya Malkin, Svetlana R Derkach, and Valery G Kulichikhin. Rheology of gels and yielding liquids. *Gels*, 9(9):715, 2023.

[61] Ranjoo Choe and Seok Il Yun. Fmoc-diphenylalanine-based hydrogels as a potential carrier for drug delivery. *e-Polymers*, 20(1):458–468, 2020.

[62] P Eaton, P Quaresma, C Soares, C Neves, MP De Almeida, E Pereira, and P West. A direct comparison of experimental methods to measure dimensions of synthetic nanoparticles. *Ultramicroscopy*, 182:179–190, 2017.

[63] B Drake, CB Prater, AL Weisenhorn, SAC Gould, TR Albrecht, CF Quate, DS Cannell, HG Hansma, and PK Hansma. Imaging crystals, polymers, and processes in water with the atomic force microscope. *Science*, 243(4898):1586–1589, 1989.

[64] Kavit HS Main, James I Provan, Philip J Haynes, Geoffrey Wells, John A Hartley, and Alice LB Pyne. Atomic force microscopy—a tool for structural and translational dna research. *APL bioengineering*, 5(3), 2021.

[65] Connor RM MacDonald and Emily R Draper. Applications of microscopy and small angle scattering techniques for the characterisation of supramolecular gels. *Beilstein Journal of Organic Chemistry*, 20(1):2608–2634, 2024.

[66] Cy M Jeffries, Jan Ilavsky, Anne Martel, Stephan Hinrichs, Andreas Meyer, Jan Skov Pedersen, Anna V Sokolova, and Dmitri I Svergun. Small-angle x-ray and neutron scattering. *Nature Reviews Methods Primers*, 1(1):70, 2021.

[67] Daniel McDowall, Dave J Adams, and Annela M Seddon. Using small angle scattering to understand low molecular weight gels. *Soft Matter*, 18(8):1577–1590, 2022.

[68] Mitsuhiro Shibayama. Small-angle neutron scattering on polymer gels: phase behavior, inhomogeneities and deformation mechanisms. *Polymer journal*, 43(1):18–34, 2011.

[69] Jean-Baptiste Guilbaud and Alberto Saiani. Using small angle scattering (sas) to structurally characterise peptide and protein self-assembled materials. *Chemical Society Reviews*, 40(3):1200–1210, 2011.

[70] Emily R Draper, Bart Dietrich, Kate McAulay, Christopher Brasnett, Haleh Abdizadeh, Ilias Patmanidis, Siewert J Marrink, Hao Su, Honggang Cui, Ralf Schweins, et al. Using small-angle scattering and contrast matching to understand molecular packing in low molecular weight gels. *Matter*, 2(3):764–778, 2020.

[71] Uttam Kumar Das, Subhabrata Banerjee, and Parthasarathi Dastidar. Remarkable shape-sustaining, load-bearing, and self-healing properties displayed by a supramolecular gel derived from a bis-pyridyl-bis-amide of l-phenyl alanine. *Chemistry–An Asian Journal*, 9(9):2475–2482, 2014.

[72] Michael C Koetting, Jonathan T Peters, Stephanie D Steichen, and Nicholas A Peppas. Stimulus-responsive hydrogels: Theory, modern advances, and applications. *Materials Science and Engineering: R: Reports*, 93:1–49, 2015.

[73] Emily R Cross, Sophie M Coulter, Ana M Fuentes-Caparrós, Kate McAulay, Ralf Schweins, Garry Laverty, and Dave J Adams. Tuning the antimicrobial activity of low molecular weight hydrogels using dopamine autoxidation. *Chemical Communications*, 56(58):8135–8138, 2020.

[74] Xinhua Cao, Aiping Gao, Ji-ting Hou, and Tao Yi. Fluorescent supramolecular self-assembly gels and their application as sensors: A review. *Coordination Chemistry Reviews*, 434:213792, 2021.

[75] Arnab Dawn. Supramolecular gel as the template for catalysis, inorganic superstructure, and pharmaceutical crystallization. *International Journal of Molecular Sciences*, 20(3):781, 2019.

[76] Zenab Darban, Syed Shahabuddin, Rama Gaur, Irfan Ahmad, and Nanthini Sridewi. Hydrogel-based adsorbent material for the effective re-

moval of heavy metals from wastewater: a comprehensive review. *Gels*, 8(5):263, 2022.

[77] Emiliano Carretti, Massimo Bonini, Luigi Dei, Barbara H Berrie, Lora V Angelova, Piero Baglioni, and Richard G Weiss. New frontiers in materials science for art conservation: responsive gels and beyond. *Accounts of chemical research*, 43(6):751–760, 2010.

[78] Huan Cao, Lixia Duan, Yan Zhang, Jun Cao, and Kun Zhang. Current hydrogel advances in physicochemical and biological response-driven biomedical application diversity. *Signal transduction and targeted therapy*, 6(1):426, 2021.

[79] SO Blacklow, Jianyu Li, Benjamin R Freedman, Mahdi Zeidi, Chen Chen, and David J Mooney. Bioinspired mechanically active adhesive dressings to accelerate wound closure. *Science advances*, 5(7):eaaw3963, 2019.

[80] Pascal Bertsch, Mani Diba, David J Mooney, and Sander CG Leeuwenburgh. Self-healing injectable hydrogels for tissue regeneration. *Chemical Reviews*, 123(2):834–873, 2022.

[81] Simona Bianco, Muhammad Hasan, Ashfaq Ahmad, Sarah-Jane Richards, Bart Dietrich, Matthew Wallace, Qiao Tang, Andrew J Smith, Matthew I Gibson, and Dave J Adams. Mechanical release of homogenous proteins from supramolecular gels. *Nature*, 631(8021):544–548, 2024.

[82] Junzhe Lou and David J Mooney. Chemical strategies to engineer hydrogels for cell culture. *Nature Reviews Chemistry*, 6(10):726–744, 2022.

[83] Ferdinand Brandl, Fritz Kastner, Ruth M Gschwind, Torsten Blunk, Jörg Teßmar, and Achim Göpferich. Hydrogel-based drug delivery systems: Comparison of drug diffusivity and release kinetics. *Journal of Controlled Release*, 142(2):221–228, 2010.

[84] Shazia Mansoor, Pierre PD Kondiah, and Yahya E Choonara. Advanced hydrogels for the controlled delivery of insulin. *Pharmaceutics*, 13(12):2113, 2021.

[85] Nikolas A Peppas, P Bures, WS Leobandung, and H Ichikawa. Hydrogels in pharmaceutical formulations. *European journal of pharmaceutics and biopharmaceutics*, 50(1):27–46, 2000.

[86] Diana Elena Ciolacu, Raluca Nicu, and Florin Ciolacu. Cellulose-based hydrogels as sustained drug-delivery systems. *Materials*, 13(22):5270, 2020.

[87] Yi Luo, Kelly R Kirker, and Glenn D Prestwich. Cross-linked hyaluronic acid hydrogel films: new biomaterials for drug delivery. *Journal of controlled release*, 69(1):169–184, 2000.

[88] Fatemeh Ahmadi, Zahra Oveisi, S Mohammadi Samani, and Zohreh Amoozgar. Chitosan based hydrogels: characteristics and pharmaceutical applications. *Research in pharmaceutical sciences*, 10(1):1–16, 2015.

[89] Nirmala Musmade, Anil Jadhav, Priyanka Moin, Suvarna Patil, and Akhilesh Gupta. An overview of in situ gel forming implants: current approach towards alternative drug delivery system. *J Biol Chem Chron*, 5:14–21, 2019.

[90] Abel Santos, Moom Sinn Aw, Manpreet Bariana, Tushar Kumeria, Ye Wang, and Dusan Losic. Drug-releasing implants: current progress, challenges and perspectives. *Journal of Materials Chemistry B*, 2(37):6157–6182, 2014.

[91] PC Bessa, M Casal, and RL Reis. Bone morphogenetic proteins in tissue engineering: the road from laboratory to clinic, part ii (bmp delivery). *Journal of tissue engineering and regenerative medicine*, 2(2-3):81–96, 2008.

[92] Peter N Schlegel and Histrelin Study Group. Efficacy and safety of histrelin subdermal implant in patients with advanced prostate cancer. *The Journal of urology*, 175(4):1353–1358, 2006.

[93] Francois Xavier Rwandamuriye, Cameron W Evans, Ben Wylie, Marck Norret, Breana Vitali, Diwei Ho, Dat Nguyen, Ellise A Roper, Tao Wang, Matt S Hepburn, et al. A surgically optimized intraoperative poly (i: C)-releasing hydrogel prevents cancer recurrence. *Cell Reports Medicine*, 4(7), 2023.

[94] Carlos BP Oliveira, Valéria Gomes, Paula MT Ferreira, José A Martins, and Peter J Jervis. Peptide-based supramolecular hydrogels as drug delivery agents: recent advances. *Gels*, 8(11):706, 2022.

[95] Carlos BP Oliveira, André Carvalho, Renato B Pereira, David M Pereira, Loic Hilliou, Peter J Jervis, José A Martins, and Paula MT Ferreira. New supramolecular hydrogels based on diastereomeric dehydrotripeptide mixtures for potential drug delivery applications. *Gels*, 10(10):629, 2024.

[96] Trideva K Sastri, Vishal N Gupta, Souvik Chakraborty, Sharadha Madhusudhan, Hitesh Kumar, Pallavi Chand, Vikas Jain, Balamuralidhara Veeranna, and Devegowda V Gowda. Novel gels: an emerging approach for delivering of therapeutic molecules and recent trends. *Gels*, 8(5):316, 2022.

[97] Joanna Skopinska-Wisniewska, Silvia De la Flor, and Justyna Kozlowska. From supramolecular hydrogels to multifunctional carriers for biologically active substances. *International Journal of Molecular Sciences*, 22(14):7402, 2021.

[98] Mafalda Rodrigues, Ana C Calpena, David B Amabilino, María Luisa Garduño-Ramírez, and Lluïsa Pérez-García. Supramolecular gels based on a gemini imidazolium amphiphile as molecular material for drug delivery. *Journal of Materials Chemistry B*, 2(33):5419–5429, 2014.

[99] Sophie M Coulter, Sreekanth Pentlavalli, Yuming An, Lalitkumar K Vora, Emily R Cross, Jessica V Moore, Han Sun, Ralf Schweins, Helen O McCarthy, and Garry Laverty. In situ forming, enzyme-responsive peptoid-peptide hydrogels: An advanced long-acting injectable drug delivery system. *Journal of the American Chemical Society*, 146(31):21401–21416, 2024.

[100] Jie Zhu, Rui Gao, Zhongshi Wang, Zhiming Cheng, Zhonghua Xu, Zaiyang Liu, Yiqun Wu, Min Wang, and Yuan Zhang. Sustained and targeted delivery of self-assembled doxorubicin nonapeptides using ph-responsive hydrogels for osteosarcoma chemotherapy. *Pharmaceutics*, 15(2):668, 2023.

[101] Yi Li, Feihu Wang, and Honggang Cui. Peptide-based supramolecular hydrogels for delivery of biologics. *Bioengineering & translational medicine*, 1(3):306–322, 2016.

[102] Parthasarathi Dastidar, Rajdip Roy, Rumana Parveen, and Koushik Sarkar. Supramolecular synthon approach in designing molecular gels for advanced therapeutics. *Advanced Therapeutics*, 2(1):1800061, 2019.

[103] Xiaoyi Feng, Yuning Luo, Fangjie Li, Xueting Jian, and Yang Liu. Development of natural-drugs-based low-molecular-weight supramolecular gels. *Gels*, 7(3):105, 2021.

[104] Zhimou Yang, Gaolin Liang, and Bing Xu. Enzymatic hydrogelation of small molecules. *Accounts of chemical research*, 41(2):315–326, 2008.

[105] Jianyu Li and David J Mooney. Designing hydrogels for controlled drug delivery. *Nature Reviews Materials*, 1(12):1–17, 2016.

[106] Sam Sutton, Neil L Campbell, Andrew I Cooper, Mark Kirkland, William J Frith, and Dave J Adams. Controlled release from modified amino acid hydrogels governed by molecular size or network dynamics. *Langmuir*, 25(17):10285–10291, 2009.

[107] Adolph Fick. V. on liquid diffusion. *The London, Edinburgh, and Dublin Philosophical Magazine and Journal of Science*, 10(63):30–39, 1855.

[108] You-Yeon Won and Doraiswami Ramkrishna. Revised formulation of fick's, fourier's, and newton's laws for spatially varying linear transport coefficients. *ACS omega*, 4(6):11215–11222, 2019.

[109] John Crank. *The mathematics of diffusion*. Oxford university press, 1979.

[110] E Bringuier. From mechanical motion to brownian motion, thermodynamics and particle transport theory. *European journal of physics*, 29(6):1243, 2008.

[111] Nico Roos. Entropic forces in brownian motion. *American Journal of Physics*, 82(12):1161–1166, 2014.

[112] Edward Lansing Cussler. *Diffusion: mass transfer in fluid systems*. Cambridge university press, 2009.

[113] Tobias Titze, Alexander Lauerer, Lars Heinke, Christian Chmelik, Nils ER Zimmermann, Frerich J Keil, Douglas M Ruthven, and Jörg Kärger. Transport in nanoporous materials including mofs: the applicability of fick's laws. *Angewandte Chemie International Edition*, 54(48):14580–14583, 2015.

[114] Lauren J O'Donnell and Carl-Fredrik Westin. An introduction to diffusion tensor image analysis. *Neurosurgery Clinics*, 22(2):185–196, 2011.

[115] Zi-Tong Zhang, Xin Zhao, and Bing-Yang Cao. Diffusion tensors of arbitrary-shaped nanoparticles in fluid by molecular dynamics simulation. *Scientific Reports*, 9(1):18943, 2019.

[116] Alfred Rudin and Phillip Choi. *The elements of polymer science and engineering*. Academic press, 2012.

[117] Paul Langevin et al. Sur la théorie du mouvement brownien. *CR Acad. Sci. Paris*, 146(530-533):530, 1908.

[118] Rep Kubo. The fluctuation-dissipation theorem. *Reports on progress in physics*, 29(1):255, 1966.

[119] Robert Zwanzig. *Nonequilibrium statistical mechanics*. Oxford university press, 2001.

[120] Arkady L Kholodenko and Jack F Douglas. Generalized stokes-einstein equation for spherical particle suspensions. *Physical Review E*, 51(2):1081, 1995.

[121] GK406082 Batchelor. Brownian diffusion of particles with hydrodynamic interaction. *Journal of Fluid Mechanics*, 74(1):1–29, 1976.

[122] Marian V Smoluchowski. Über brownsche molekularbewegung unter einwirkung äußerer kräfte und deren zusammenhang mit der verallgemeinerten diffusionsgleichung. *Annalen der Physik*, 353(24):1103–1112, 1916.

[123] Albert Einstein. Über die von der molekularkinetischen theorie der wärme geforderte bewegung von in ruhenden flüssigkeiten suspendierten teilchen. *Annalen der physik*, 4, 1905.

[124] Marcus Hennig. *Dynamics of Globular Proteins in Crowded Electrolyte Solutions. Studied by Neutron Scattering*. PhD thesis, Universität Tübingen, 2011.

[125] Julie Fisher. *Modern NMR techniques for synthetic chemistry*. CRC Press, 2014.

[126] George H Vineyard. Scattering of slow neutrons by a liquid. *Physical Review*, 110(5):999, 1958.

[127] Léon Van Hove. Correlations in space and time and born approximation scattering in systems of interacting particles. *Physical Review*, 95(1):249, 1954.

[128] Marc-André Gagnon and Michel Lafleur. Comparison between nuclear magnetic resonance profiling and the source/sink approach for characterizing drug diffusion in hydrogel matrices. *Pharmaceutical development and technology*, 16(6):651–656, 2011.

[129] S Longeville, W Doster, and G Kali. Myoglobin in crowded solutions: structure and diffusion. *Chemical Physics*, 292(2-3):413–424, 2003.

[130] Wolfgang Doster and Stéphane Longeville. Microscopic diffusion and hydrodynamic interactions of hemoglobin in red blood cells. *Biophysical journal*, 93(4):1360–1368, 2007.

[131] Marc-André Gagnon and Michel Lafleur. Self-diffusion and mutual diffusion of small molecules in high-set curdlan hydrogels studied by 31p nmr. *The Journal of Physical Chemistry B*, 113(27):9084–9091, 2009.

[132] Ana CF Ribeiro and Miguel A Esteso. Transport properties for pharmaceutical controlled-release systems: a brief review of the importance of their study in biological systems. *Biomolecules*, 8(4):178, 2018.

[133] Ralf Metzler and Joseph Klafter. The random walk's guide to anomalous diffusion: a fractional dynamics approach. *Physics reports*, 339(1):1–77, 2000.

[134] Joseph Klafter and Igor M Sokolov. Anomalous diffusion spreads its wings. *Physics world*, 18(8):29, 2005.

[135] Josep M Porra, Ke-Gang Wang, and Jaume Masoliver. Generalized langevin equations: Anomalous diffusion and probability distributions. *Physical Review E*, 53(6):5872, 1996.

[136] V Kobelev and E Romanov. Fractional langevin equation to describe anomalous diffusion. *Progress of Theoretical Physics Supplement*, 139:470–476, 2000.

[137] Hisham Al-Obaidi and Alexander T Florence. Nanoparticle delivery and particle diffusion in confined and complex environments. *Journal of Drug Delivery Science and Technology*, 30:266–277, 2015.

[138] Stefano Bo, Falko Schmidt, Ralf Eichhorn, and Giovanni Volpe. Measurement of anomalous diffusion using recurrent neural networks. *Physical Review E*, 100(1):010102, 2019.

[139] Daniel S Banks and Cécile Fradin. Anomalous diffusion of proteins due to molecular crowding. *Biophysical journal*, 89(5):2960–2971, 2005.

[140] Nina Kristine Reitan, Aphirak Juthajan, Tore Lindmo, and Catharina de Lange Davies. Macromolecular diffusion in the extracellular matrix measured by fluorescence correlation spectroscopy. *Journal of Biomedical Optics*, 13(5):054040–054040, 2008.

[141] Michael J Saxton. Single-particle tracking: effects of corrals. *Biophysical Journal*, 69(2):389–398, 1995.

[142] Roman Shusterman, Tatyana Gavrinyov, and Oleg Krichevsky. Internal dynamics of superhelical dna. *Physical review letters*, 100(9):098102, 2008.

[143] Eugene B Postnikov, Anastasia I Lavrova, and Dmitry E Postnov. Transport in the brain extracellular space: Diffusion, but which kind? *International Journal of Molecular Sciences*, 23(20):12401, 2022.

[144] M Dvoyashkin, A Wang, A Katihar, J Zang, GI Yucelen, S Nair, DS Sholl, CR Bowers, and S Vasenkov. Signatures of normal and anomalous diffusion in nanotube systems by nmr. *Microporous and mesoporous materials*, 178:119–122, 2013.

[145] Marco Grimaldo, Felix Roosen-Runge, Fajun Zhang, Frank Schreiber, and Tilo Seydel. Dynamics of proteins in solution. *Quarterly Reviews of Biophysics*, 52:e7, 2019.

[146] Soichiro Yamada, Denis Wirtz, and Scot C Kuo. Mechanics of living cells measured by laser tracking microrheology. *Biophysical journal*, 78(4):1736–1747, 2000.

[147] Franca Castiglione, Mosè Casalegno, Monica Ferro, Filippo Rossi, Guido Raos, and Andrea Mele. Evidence of superdiffusive nanoscale motion in anionic polymeric hydrogels: Analysis of pgse-nmr data and comparison with drug release properties. *Journal of Controlled Release*, 305:110–119, 2019.

[148] Gerhard Nägele. On the dynamics and structure of charge-stabilized suspensions. *Physics Reports*, 272(5-6):215–372, 1996.

[149] Bo Wang, James Kuo, Sung Chul Bae, and Steve Granick. When brownian diffusion is not gaussian. *Nature materials*, 11(6):481–485, 2012.

[150] Kathryn Foreman and Khanh-Hoa Tran-Ba. Single-particle tracking in poly (ethylene glycol) diacrylate: probe size effect on the diffusion behaviors of nanoparticles in unentangled polymer solutions. *The Journal of Physical Chemistry B*, 127(31):7091–7102, 2023.

[151] Adolfo J Banchio, Gerhard Nägele, and Johan Bergenholtz. Viscoelasticity and generalized stokes–einstein relations of colloidal dispersions. *The Journal of chemical physics*, 111(18):8721–8740, 1999.

[152] Lei Liu, Pusheng Li, and Sanford A Asher. Entropic trapping of macromolecules by mesoscopic periodic voids in a polymer hydrogel. *Nature*, 397(6715):141–144, 1999.

[153] P Sekhar Burada, Peter Hänggi, Fabio Marchesoni, Gerhard Schmid, and Peter Talkner. Diffusion in confined geometries. *ChemPhysChem*, 10(1):45–54, 2009.

[154] Susanne R Veith, Eric Hughes, Gilles Vuataz, and Sotiris E Pratsinis. Restricted diffusion in silica particles measured by pulsed field gradient nmr. *Journal of colloid and interface science*, 274(1):216–228, 2004.

[155] Emmabeth Parrish, Matthew A Caporizzo, and Russell J Composto. Network confinement and heterogeneity slows nanoparticle diffusion in polymer gels. *The Journal of Chemical Physics*, 146(20), 2017.

[156] Matthew Wallace, Dave J Adams, and Jonathan A Iggo. Analysis of the mesh size in a supramolecular hydrogel by pfg-nmr spectroscopy. *Soft Matter*, 9(22):5483–5491, 2013.

[157] Paige J Moncure, Zoe C Simon, Jill E Millstone, and Jennifer E Laaser. Relationship between gel mesh and particle size in determining nanoparticle diffusion in hydrogel nanocomposites. *The Journal of Physical Chemistry B*, 126(22):4132–4142, 2022.

[158] Yuji Matsumoto, Atsuomi Shundo, Masashi Ohno, Nobutomo Tsuruzoe, Masahiro Goto, and Keiji Tanaka. Mesoscopic heterogeneity in pore size of supramolecular networks. *Langmuir*, 34(25):7503–7508, 2018.

[159] Edgar Fuentes, Kamila Boháčová, Ana M Fuentes-Caparrós, Ralf Schweins, Emily R Draper, Dave J Adams, Silvia Pujals, and Lorenzo Albertazzi. Paint-ing fluorenylmethoxycarbonyl (fmoc)-diphenylalanine hydrogels. *Chemistry–A European Journal*, 26(44):9869–9873, 2020.

[160] Maria Pozzi, Sarodi Jonak Dutta, Mia Kuntze, Jeannette Bading, Johanna S Rußbult, Cornelius Fabig, Malte Langfeldt, Florian Schulz, Patricia Horcajada, and Wolfgang J Parak. Visualization of the high surface-to-volume ratio of nanomaterials and its consequences. *Journal of chemical education*, 101(8):3146–3155, 2024.

[161] Adam A Dinerman, Joseph Cappello, Mohamed El-Sayed, Stephen W Hoag, and Hamidreza Ghandehari. Influence of solute charge and hydrophobicity on partitioning and diffusion in a genetically engineered silk-elastin-like protein polymer hydrogel. *Macromolecular bioscience*, 10(10):1235–1247, 2010.

[162] Peter H Santschi, Wei-Chun Chin, Antonietta Quigg, Chen Xu, Manoj Kamalanathan, Peng Lin, and Ruei-Feng Shiu. Marine gel interactions with hydrophilic and hydrophobic pollutants. *Gels*, 7(3):83, 2021.

[163] Naoki Hirota, Yasuhiro Kumaki, Tetsuharu Narita, Jian Ping Gong, and Yoshihito Osada. Effect of charge on protein diffusion in hydrogels. *The Journal of Physical Chemistry B*, 104(42):9898–9903, 2000.

[164] Nicolas Fatin-Rouge, Antoine Milon, Jacques Buffle, Richard R Goulet, and Andre Tessier. Diffusion and partitioning of solutes in agarose hydrogels: the relative influence of electrostatic and specific interactions. *The Journal of Physical Chemistry B*, 107(44):12126–12137, 2003.

[165] Johann Hansing, Joseph R Duke III, Emily B Fryman, Jason E DeRouchey, and Roland R Netz. Particle diffusion in polymeric hydrogels with mixed attractive and repulsive interactions. *Nano letters*, 18(8):5248–5256, 2018.

[166] Joanna Kowalczuk, Adam Rachocki, Michał Bielejewski, and Jadwiga Tritt-Goc. Effect of gel matrix confinement on the solvent dynamics in supramolecular gels. *Journal of colloid and interface science*, 472:60–68, 2016.

[167] Malgorzata Anna Wisniewska and John Georg Seland. Investigating structure-dependent diffusion in hydrogels using spatially resolved nmr spectroscopy. *Journal of colloid and interface science*, 533:671–677, 2019.

[168] Johann Hansing and Roland R Netz. Hydrodynamic effects on particle diffusion in polymeric hydrogels with steric and electrostatic particle–gel interactions. *Macromolecules*, 51(19):7608–7620, 2018.

[169] Alan H Muhr and John MV Blanshard. Diffusion in gels. *Polymer*, 23(7):1012–1026, 1982.

[170] Laurent Masaro and XX Zhu. Physical models of diffusion for polymer solutions, gels and solids. *Progress in polymer science*, 24(5):731–775, 1999.

[171] Brian Amsden. Solute diffusion within hydrogels. mechanisms and models. *Macromolecules*, 31(23):8382–8395, 1998.

[172] Brian G Amsden. Hydrogel mesh size and its impact on predictions of mathematical models of the solute diffusion coefficient. *Macromolecules*, 55(18):8399–8408, 2022.

[173] Manuel Quesada-Pérez and Alberto Martín-Molina. Solute diffusion in gels: Thirty years of simulations. *Advances in Colloid and Interface Science*, 287:102320, 2021.

[174] Morrel H Cohen and David Turnbull. Molecular transport in liquids and glasses. *The Journal of Chemical Physics*, 31(5):1164–1169, 1959.

[175] H Yasuda, LD Ikenberry, and CE Lamaze. Permeability of solutes through hydrated polymer membranes. part ii. permeability of water soluble organic solutes. *Die Makromolekulare Chemie: Macromolecular Chemistry and Physics*, 125(1):108–118, 1969.

[176] Nikolaos A Peppas et al. *Hydrogels in medicine and pharmacy*, volume 1. CRC press Boca Raton, FL, 1986.

[177] Nikolaos A Peppas and Shelia L Wright. Solute diffusion in poly (vinyl alcohol)/poly (acrylic acid) interpenetrating networks. *Macromolecules*, 29(27):8798–8804, 1996.

[178] JS Mackie and P Meares. The diffusion of electrolytes in a cation-exchange resin membrane i. theoretical. *Proceedings of the Royal Society of London. Series A. Mathematical and Physical Sciences*, 232(1191):498–509, 1955.

[179] Yuhang Zhou, Junjie Li, Ying Zhang, Dianyu Dong, Ershuai Zhang, Feng Ji, Zhihui Qin, Jun Yang, and Fanglian Yao. Establishment of

a physical model for solute diffusion in hydrogel: understanding the diffusion of proteins in poly (sulfobetaine methacrylate) hydrogel. *The Journal of Physical Chemistry B*, 121(4):800–814, 2017.

[180] Kavindya K Senanayake, Ehsan Akbari Fakhrabadi, Matthew W Liberatore, and Ashis Mukhopadhyay. Diffusion of nanoparticles in entangled poly (vinyl alcohol) solutions and gels. *Macromolecules*, 52(3):787–795, 2019.

[181] AG Ogston. The spaces in a uniform random suspension of fibres. *Transactions of the Faraday Society*, 54:1754–1757, 1958.

[182] Manuel Quesada-Pérez, José-Alberto Maroto-Centeno, Maria del Mar Ramos-Tejada, and Alberto Martín-Molina. Coarse-grained simulations of solute diffusion in crosslinked flexible hydrogels. *Macromolecules*, 55(5):1495–1504, 2022.

[183] RI Cukier. Diffusion of brownian spheres in semidilute polymer solutions. *Macromolecules*, 17(2):252–255, 1984.

[184] Eneko Axpe, Doreen Chan, Giovanni S Offeddu, Yin Chang, David Merida, Hector Lopez Hernandez, and Eric A Appel. A multiscale model for solute diffusion in hydrogels. *Macromolecules*, 52(18):6889–6897, 2019.

[185] Silviya P Zustiak, Hacene Boukari, and Jennie B Leach. Solute diffusion and interactions in cross-linked poly (ethylene glycol) hydrogels studied by fluorescence correlation spectroscopy. *Soft matter*, 6(15):3609–3618, 2010.

[186] Göran Frenning and Maria Strømme. Drug release modeled by dissolution, diffusion, and immobilization. *International journal of pharmaceutics*, 250(1):137–145, 2003.

[187] Susan D'Souza. A review of in vitro drug release test methods for nano-sized dosage forms. *Advances in pharmaceutics*, 2014(1):304757, 2014.

[188] Margaux Vigata, Christoph Meinert, Dietmar W Hutmacher, and Nathalie Bock. Hydrogels as drug delivery systems: A review of current characterization and evaluation techniques. *Pharmaceutics*, 12(12):1188, 2020.

[189] Sudipta Ganguly and Alekha K Dash. A novel in situ gel for sustained drug delivery and targeting. *International journal of pharmaceutics*, 276(1-2):83–92, 2004.

[190] Philip L Ritger and Nikolaos A Peppas. A simple equation for description of solute release i. fickian and non-fickian release from non-swellable devices in the form of slabs, spheres, cylinders or discs. *Journal of controlled release*, 5(1):23–36, 1987.

[191] Juergen Siepmann and Nicholas A Peppas. Higuchi equation: Derivation, applications, use and misuse. *International journal of pharmaceutics*, 418(1):6–12, 2011.

[192] Michael Gösch and Rudolf Rigler. Fluorescence correlation spectroscopy of molecular motions and kinetics. *Advanced Drug Delivery Reviews*, 57(1):169–190, 2005.

[193] Lan Yu, Yunze Lei, Ying Ma, Min Liu, Juanjuan Zheng, Dan Dan, and Peng Gao. A comprehensive review of fluorescence correlation spectroscopy. *Frontiers in physics*, 9:644450, 2021.

[194] Fan Zhang, Andrew J Allen, Lyle E Levine, Jan Ilavsky, and Gabrielle G Long. Ultra-small-angle x-ray scattering—x-ray photon correlation spectroscopy: A new measurement technique for in-situ studies of equilibrium and nonequilibrium dynamics. *Metallurgical and Materials Transactions A*, 43:1445–1453, 2012.

[195] Robert L Leheny. Xpcs: Nanoscale motion and rheology. *Current opinion in colloid & interface science*, 17(1):3–12, 2012.

[196] Inka Negwer, Andreas Best, Meike Schinnerer, Olga Schäfer, Leon Capeloa, Manfred Wagner, Manfred Schmidt, Volker Mailänder, Mark Helm, Matthias Barz, et al. Monitoring drug nanocarriers in human blood by near-infrared fluorescence correlation spectroscopy. *Nature Communications*, 9(1):5306, 2018.

[197] Nicolas Fatin-Rouge, Konstantin Starchev, and Jacques Buffle. Size effects on diffusion processes within agarose gels. *Biophysical journal*, 86(5):2710–2719, 2004.

[198] Niklas Lorén, Joel Hagman, Jenny K Jonasson, Hendrik Deschout, Diana Bernin, Francesca Cella-Zanacchi, Alberto Diaspro, James G McNally, Marcel Ameloot, Nick Smisdom, et al. Fluorescence recovery after photobleaching in material and life sciences: putting theory into practice. *Quarterly reviews of biophysics*, 48(3):323–387, 2015.

[199] Hendrik Deschout, Koen Raemdonck, Jo Demeester, Stefaan C De Smedt, and Kevin Braeckmans. Frap in pharmaceutical research: practical guidelines and applications in drug delivery. *Pharmaceutical research*, 31:255–270, 2014.

[200] Tom KL Meyvis, Stefaan C De Smedt, Patrick Van Oostveldt, and Joseph Demeester. Fluorescence recovery after photobleaching: a versatile tool for mobility and interaction measurements in pharmaceutical research. *Pharmaceutical research*, 16:1153–1162, 1999.

[201] Sophie R Van Tomme, Bruno G De Geest, Kevin Braeckmans, Stefaan C De Smedt, Florence Siepmann, Juergen Siepmann, Cornelus F van Nostrum, and Wim E Hennink. Mobility of model proteins in hydrogels composed of oppositely charged dextran microspheres studied by protein release and fluorescence recovery after photobleaching. *Journal of controlled release*, 110(1):67–78, 2005.

[202] Goksu Cinar, Ayse Ozdemir, Seren Hamsici, Gokhan Gunay, Aykutlu Dana, Ayse B Tekinay, and Mustafa O Guler. Local delivery of doxoru-

bicin through supramolecular peptide amphiphile nanofiber gels. *Biomaterials science*, 5(1):67–76, 2017.

[203] Carlo Manzo and Maria F Garcia-Parajo. A review of progress in single particle tracking: from methods to biophysical insights. *Reports on progress in physics*, 78(12):124601, 2015.

[204] Koen JA Martens, John Van Duynhoven, and Johannes Hohlbein. Spatiotemporal heterogeneity of κ-carrageenan gels investigated via single-particle-tracking fluorescence microscopy. *Langmuir*, 36(20):5502–5509, 2020.

[205] Katie A Rose, Mehdi Molaei, Michael J Boyle, Daeyeon Lee, John C Crocker, and Russell J Composto. Particle tracking of nanoparticles in soft matter. *Journal of Applied Physics*, 127(19), 2020.

[206] Federica Burla, Tatjana Sentjabrskaja, Galja Pletikapic, Joey Van Beugen, and Gijsje H Koenderink. Particle diffusion in extracellular hydrogels. *Soft Matter*, 16(5):1366–1376, 2020.

[207] Andrey G Cherstvy, Samudrajit Thapa, Caroline E Wagner, and Ralf Metzler. Non-gaussian, non-ergodic, and non-fickian diffusion of tracers in mucin hydrogels. *Soft Matter*, 15(12):2526–2551, 2019.

[208] Yury E Shapiro. Structure and dynamics of hydrogels and organogels: An nmr spectroscopy approach. *Progress in Polymer Science*, 36(9):1184–1253, 2011.

[209] Ioannis P Gerothanassis, Anastassios Troganis, Vassiliki Exarchou, and Klimentini Barbarossou. Nuclear magnetic resonance (nmr) spectroscopy: basic principles and phenomena, and their applications to chemistry, biology and medicine. *Chemistry Education Research and Practice*, 3(2):229–252, 2002.

[210] Michal Bielejewski and Jadwiga Tritt-Goc. Evidence of solvent- gelator interaction in sugar-based organogel studied by field-cycling nmr relaxometry. *Langmuir*, 26(22):17459–17464, 2010.

[211] Jadwiga Tritt-Goc, Adam Rachocki, and Michał Bielejewski. The solvent dynamics at pore surfaces in molecular gels studied by field-cycling magnetic resonance relaxometry. *Soft Matter*, 10(39):7810–7818, 2014.

[212] Joanna Kowalczuk, Michał Bielejewski, Andrzej Łapinski, Roman Luboradzki, and Jadwiga Tritt-Goc. The solvent–gelator interaction as the origin of different diffusivity behavior of diols in gels formed with sugar-based low-molecular-mass gelator. *The Journal of Physical Chemistry B*, 118(14):4005–4015, 2014.

[213] Valeria Gabrielli, Agne Kuraite, Marcelo Alves da Silva, Karen J Edler, Jesús Angulo, Ridvan Nepravishta, Juan C Muñoz-García, and Yaroslav Z Khimyak. Spin diffusion transfer difference (sdtd) nmr: An advanced method for the characterisation of water structuration within particle networks. *Journal of Colloid and Interface Science*, 594:217–227, 2021.

[214] Aldino Viegas, João Manso, Franklin L Nobrega, and Eurico J Cabrita. Saturation-transfer difference (std) nmr: a simple and fast method for ligand screening and characterization of protein binding. *Journal of chemical Education*, 88(7):990–994, 2011.

[215] Matthew Wallace, Jonathan A Iggo, and Dave J Adams. Probing the surface chemistry of self-assembled peptide hydrogels using solution-state nmr spectroscopy. *Soft Matter*, 13(8):1716–1727, 2017.

[216] María D Segarra-Maset, Beatriu Escuder, and Juan F Miravet. Selective interaction of dopamine with the self-assembled fibrillar network of a molecular hydrogel revealed by std-nmr. *Chemistry–A European Journal*, 21(40):13925–13929, 2015.

[217] Erwin L Hahn. Spin echoes. *Physical review*, 80(4):580, 1950.

[218] Edward O Stejskal and John E Tanner. Spin diffusion measurements: spin echoes in the presence of a time-dependent field gradient. *The journal of chemical physics*, 42(1):288–292, 1965.

[219] William S Price. Pulsed-field gradient nuclear magnetic resonance as a tool for studying translational diffusion: Part 1. basic theory. *Concepts in Magnetic Resonance: An Educational Journal*, 9(5):299–336, 1997.

[220] S Matsukawa, H Yasunaga, C Zhao, S Kuroki, H Kurosu, and I Ando. Diffusion processes in polymer gels as studied by pulsed field-gradient spin-echo nmr spectroscopy. *Progress in Polymer Science*, 24(7):995–1044, 1999.

[221] Yukiko ASO, Sumie Yoshioka, and Shigeo KOJiMA. Determination of the diffusion coefficient of insulin and lysozyme in crosslinked dextran hydrogels by pulsed-field-gradient nmr. *Chemical and pharmaceutical bulletin*, 46(11):1836–1839, 1998.

[222] Marc Bée. *Quasielastic neutron scattering*. Adam Hilger; Bristol (UK), 1988.

[223] Mark TF Telling. *A practical guide to quasi-elastic neutron scattering*. Royal Society of Chemistry, 2020.

[224] Hervé Jobic and Doros N Theodorou. Quasi-elastic neutron scattering and molecular dynamics simulation as complementary techniques for studying diffusion in zeolites. *Microporous and mesoporous materials*, 102(1-3):21–50, 2007.

[225] Victoria García Sakai and Arantxa Arbe. Quasielastic neutron scattering in soft matter. *Current Opinion in Colloid & Interface Science*, 14(6):381–390, 2009.

[226] Andreas Santamaria, Krishna C Batchu, Olga Matsarskaia, Sylvain F Prévost, Daniela Russo, Francesca Natali, Tilo Seydel, Ingo Hoffmann,

Valérie Laux, Michael Haertlein, et al. Strikingly different roles of sars-cov-2 fusion peptides uncovered by neutron scattering. *Journal of the American Chemical Society*, 144(7):2968–2979, 2022.

[227] Marco Grimaldo, Hender Lopez, Christian Beck, Felix Roosen-Runge, Martine Moulin, Juliette M Devos, Valerie Laux, Michael Hartlein, Stefano Da Vela, Ralf Schweins, et al. Protein short-time diffusion in a naturally crowded environment. *The journal of physical chemistry letters*, 10(8):1709–1715, 2019.

[228] MPM Marques, ALM Batista de Carvalho, CB Martins, JD Silva, M Sarter, V García Sakai, JR Stewart, and LAE Batista de Carvalho. Cellular dynamics as a marker of normal-to-cancer transition in human cells. *Scientific Reports*, 13(1):21079, 2023.

[229] Gaio Paradossi, Ivana Finelli, Francesca Natali, Mark TF Telling, and Ester Chiessi. Polymer and water dynamics in poly (vinyl alcohol)/poly (methacrylate) networks. a molecular dynamics simulation and incoherent neutron scattering investigation. *Polymers*, 3(4):1805–1832, 2011.

[230] Toshiji Kanaya, Nobuaki Takahashi, Hiroki Takeshita, Masatoshi Ohkura, Koji Nishida, and Keisuke Kaji. Structure and dynamics of poly (vinyl alcohol) gels in mixtures of dimethyl sulfoxide and water. *Polymer journal*, 44(1):83–94, 2012.

[231] Sylvie Spagnoli, Isabelle Morfin, Miguel A Gonzalez, Pierre Carcabal, and Marie Plazanet. Solvent contribution to the stability of a physical gel characterized by quasi-elastic neutron scattering. *Langmuir*, 31(8):2554–2560, 2015.

[232] Noriko Onoda-Yamamuro, Yasuhiro Inamura, and Osamu Yamamuro. Quasielastic neutron scattering study on thermal gelation in aqueous solution of agarose. *Gels*, 9(11):879, 2023.

[233] Francesca Cavalieri, Ester Chiessi, Raffaella Villa, Lucia Vigano, Nadia Zaffaroni, Mark F Telling, and Gaio Paradossi. Novel pva-based hydrogel

microparticles for doxorubicin delivery. *Biomacromolecules*, 9(7):1967–1973, 2008.

[234] Robert M Edkins, Markus Appel, Tilo Seydel, and Katharina Edkins. The modifying effect of supramolecular gel fibres on the diffusion of paracetamol and ibuprofen sodium on the picosecond timescale. *Phys. Chem. Chem. Phys.*, 22(19):10838–10844, 2020.

[235] Giuseppe Briganti, GIOVANNA Rogati, Alexandra Parmentier, M Maccarini, and F De Luca. Neutron scattering observation of quasi-free rotations of water confined in carbon nanotubes. *Scientific reports*, 7(1):45021, 2017.

[236] Alexander J O'Malley, Iain Hitchcock, Misbah Sarwar, Ian P Silverwood, Sheena Hindocha, C Richard A Catlow, Andrew PE York, and PJ Collier. Ammonia mobility in chabazite: insight into the diffusion component of the nh 3-scr process. *Physical Chemistry Chemical Physics*, 18(26):17159–17168, 2016.

[237] George Razvan Bacanu, Tanzeeha Jafari, Mohamed Aouane, Jyrki Rantaharju, Mark Walkey, Gabriela Hoffman, Anna Shugai, Urmas Nagel, Monica Jiménez-Ruiz, Anthony J Horsewill, et al. Experimental determination of the interaction potential between a helium atom and the interior surface of a c60 fullerene molecule. *The Journal of Chemical Physics*, 155(14), 2021.

[238] Tilo Seydel, Robert M Edkins, Christopher D Jones, Jonathan A Foster, Robert Bewley, Juan A Aguilar, and Katharina Edkins. Increased rate of solvent diffusion in a prototypical supramolecular gel measured on the picosecond timescale. *Chemical Communications*, 54(49):6340–6343, 2018.

[239] Aline Cisse, Tatsuhito Matsuo, Marie Plazanet, Francesca Natali, Michael Marek Koza, Jacques Ollivier, Dominique J Bicout, and Judith Peters. The dynamical matryoshka model: 2. modeling of local lipid

dynamics at the sub-nanosecond timescale in phospholipid membranes. *Biochimica et Biophysica Acta (BBA)-Biomembranes*, 1864(9):183950, 2022.

[240] Maksim S Plekhanov, Sabrina LJ Thoma, Andreas Magerl, Markus Appel, and Mirijam Zobel. Quasi-elastic neutron scattering of citrate-capped iron oxide nanoparticles: Distinguishing between ligand, water, and magnetic dynamics. *The Journal of Physical Chemistry C*, 128(28):11661–11671, 2024.

Blank page

Chapter 2

Materials and Methods

2.1 Supramolecular gels

2.1.1 FmocFF hydrogel

The N-fluorenylmethoxycarbonyl-diphenylalanine (Fmoc-Phe-Phe-OH or FmocFF) is a LMWG recognized for its ability to form stable gels at very low concentration (0.22–2.14 wt%), both in aqueous or organic solvents. This gelation is driven by non-covalent interactions triggered by pH changes.[1–5] Structurally, FmocFF consists of two phenylalanine (FF) residues functionalized at the N-terminus with a fluorenylmethoxycarbonyl (Fmoc) group, which promotes self-assembly through π-π stacking of fluorenyl groups, hydrogen bonding between peptide backbones, and hydrophobic interactions among phenylalanine side chains (Fig.2.1a). The model architecture, proposed by Smith et al.,[1] features nanocylindrical fibers formed by anti-parallel β-sheets, where peptides are interlocked via $\pi - \pi$ stacking of the Fmoc moieties (Fig. 2.1b). FmocFF is particularly responsive to pH changes.[3] At high pH (>10), where the molecule is predominantly in its ionized state, self-assembly is largely inhibited. Self-assembly begins when the pH decreases to the first pK_a range (10.2–9.5). Further pH reduction leads to fiber de-ionization and lateral packing into flat ribbons, eventually forming a three-dimensional gel network comprising liquid and solid phases (Fig. 2.1c-d). Thanks to its biocompatibility, high water retention, pH responsiveness, and thixotropic behavior, FmocFF emerges as a promising material for drug delivery.[4, 6] Its pH sensitivity enables stimuli-controlled release, as small pH changes can modulate gel stability and drug release rates.[4] Additionally, its thixotropic nature allows the gel to liquefy under shear (e.g., during injection) and rapidly reform post-administration, enabling minimally invasive delivery with controlled release profiles.[7] The FmocFF self-assembly can be achieved via three main methods:[4] pH-switch,[1, 8] solvent-switch[9, 10] and catalytic method.[11] The method used to induce gelation significantly influences the assembly process and the resulting gel properties.[12] In this study, we utilize the pH-switch method. This method was chosen because it relies on environmentally responsive pH changes rather than the addition of

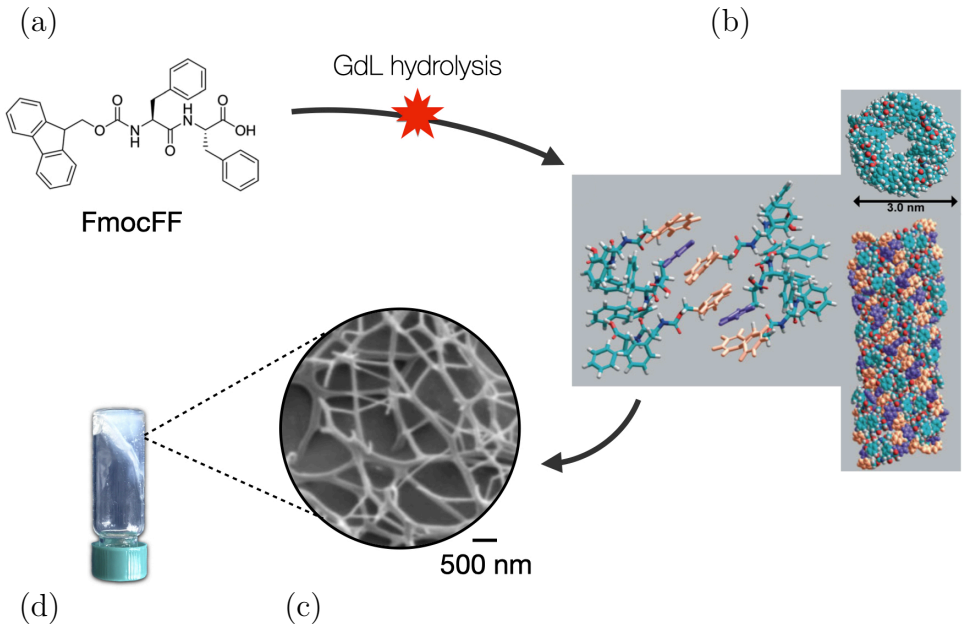

Figure 2.1: (a) Molecular structure of FmocFF LMWG;(b) Model of the self-assembly process triggered by pH change, illustrating the π-stacking of FmocFF, with fluorenyl group (orange) and phenyl group (purple) decorating the nano-cylindrical fibril. Adapted with permission from Ref.[1] Copyright 2008 Wiley; (c) Cryo-SEM image showing the entangled fibrous network characteristic of the gel structure. Adapted with permission from Ref.[1] Copyright 2008 Wiley (d) Bulk gel exhibiting self-supportive properties, as demonstrated by its resistance to flow during the vial inversion test

organic solvents or catalysts which are less suitable for drug delivery purposes; additionally, it offers greater control and flexibility over the gelation process, allowing for a more gradual assembly ($\sim$18 h compared to $\sim$5 min).[4] At high pH, the peptide is fully solubilized due to the deprotonation of the C-terminal carboxylic acid. As the pH gradually decreases, the C-terminal carboxylic acid becomes protonated, driving the self-assembly process until gelation occurs. Specifically, we adopt the protocol established by Adams et al.,[8] in which the pH is lowered through the slow hydrolysis of glucono-δ-lactone (GdL). GdL releases gluconic acid in aqueous solution, resulting in a gradual and consistent decrease in pH, leading to uniform gel formation over approximately 18

hours. This controlled pH reduction method offers significant advantages over abrupt pH-switch techniques, such as the dropwise addition of HCl, which often produces turbid and inhomogeneous gels within seconds. In contrast, the slow hydrolysis of GdL ensures reproducibility and structural homogeneity, yielding translucent and uniform gels.

Preparation procedure FmocFF (98% purity) was purchased from Bachem. Sodium deuteroxide solution (40 wt.% in D_2O, 99.5 atom% D), glucono-δ-lactone (GdL), ibuprofen sodium (IBU), lysozyme from chicken egg white (LYS), and recombinant human insulin (INS) (both as lyophilized powders) were obtained from Sigma Aldrich. All chemicals were used without further purification. Initially, 5 mg of FmocFF gelator (0.5 wt.%) was dissolved in 1 ml aqueous NaOH solution at pH around 10.4; this high pH needed for the deprotonation of the C-terminal carboxylic acid of FmocFF, was achieved with one mole equivalent of NaOH (0.1M). Once the FmocFF was added, the solution has been through cycles of vortexing and sonication to ensure complete dissolution of the solid gelator. Following dissolution, 6.4 mg of GdL was introduced to the solution. After the addition of GdL, the drug compounds dissolved in H_2O were introduced to the solution to achieve a final concentration of 5 wt.% for ibuprofen sodium and 2.4 wt.% for insulin and lysozyme. The lower concentration for the two proteins is due to a balance between ensuring a sufficient signal for QENS measurement and maintaining gel stability.

2.1.2 β-sheet forming modified peptides hydrogels

Inspired by the foundational studies of Zhang and co-workers,[15, 16] the family of β-sheet forming peptides, designed by Saiani's group,[13, 14, 17–21] expand and showcase the potential of peptide-based hydrogels. These LMWG are short (8 amino acids long) peptides consisting of alternating hydrophobic (phenylalanine: F) and hydrophilic (lysine: K and glutamic acid: E) residues (Fig.2.2a). Under suitable conditions, such as achieving the critical gelation concentration and adjusting environmental factors like pH or ionic strength, these pep-

tides self-assemble in water into anti-parallel β-sheet rich fibres with all the phenyl rings on one side and the polar moeities on the opposite side. This amphiphatic nature drives the formation of stable fibrillar networks, as the hydrophobic faces of two β-sheets align to minimize water exposure, leading to the development of a stable, interconnected three-dimensional network. Alongside their long-term stability and high reproducibility, these gels exhibit remarkable thixotropic properties, enabling them to restore their structure after mechanical disruption. This capability makes them particularly suitable for advanced formulations, including injectable and sprayable hydrogels tailored for biomedical applications.[22] A key advantage of this hydrogel system is its modularity, enabling straightforward surface modifications. For exam-

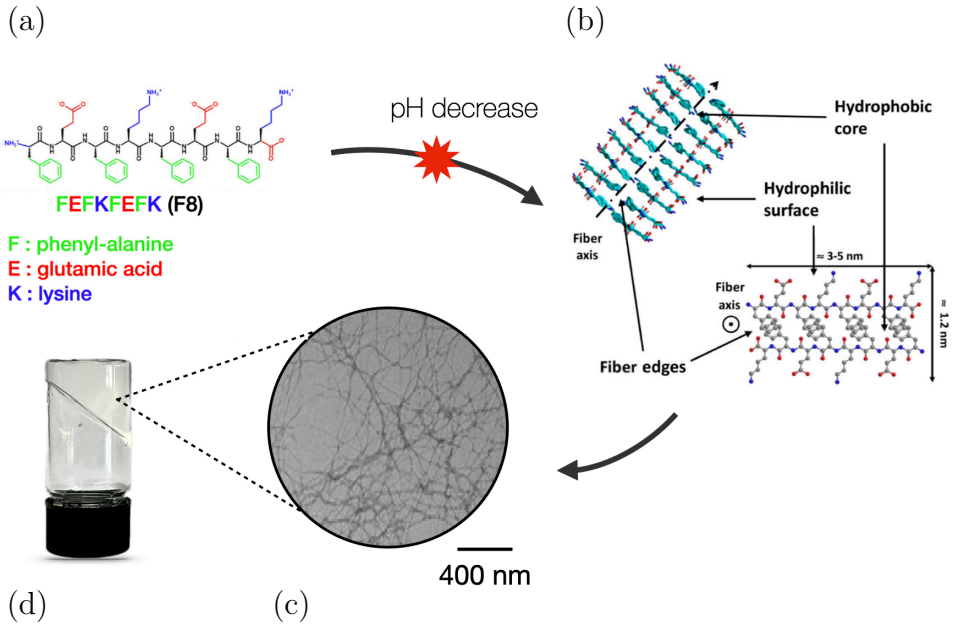

Figure 2.2: (a) Molecular structure of FEFKFEFK (F8) LMWG; (b) Structural organization of the β-sheet-rich fibre structural organization featuring a hydrophobic core and a hydrophilic surface. Adapted with permission from Ref.[13] Copyright 2022 The Authors. (c) TEM image showing the gel network. Adapted with permission from Ref.[14] . Copyright 2020 American Chemical Society (d) Bulk gel exhibiting self-supportive properties, as demonstrated by its resistance to flow during the vial inversion test

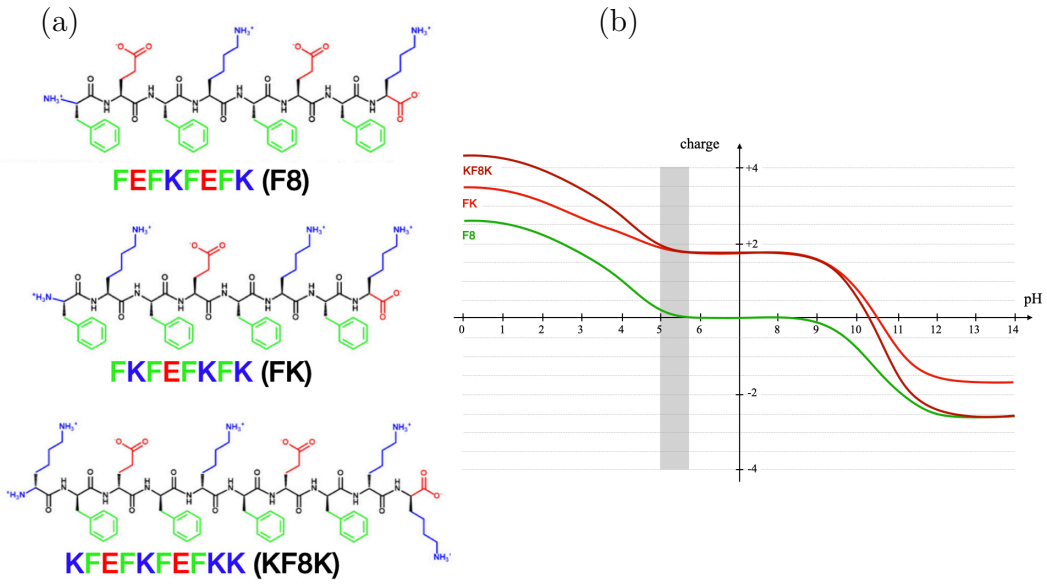

Figure 2.3: (a) Molecular structures of F8, FK and KF8K LMWG. Adapted with permission from Ref.[13] Copyright 2022 The Authors. (b) Peptide charge as a function of pH. Curves sourced from the ThermoFisher Scientific website.

ple, electrostatic tuning can be easily applied,[13, 14] showcasing the potential of supramolecular gels for tailored functionalization. This versatility is particularly valuable for drug delivery applications, where the gel's surface properties play a crucial role in controlling drug release kinetics.[13, 23–25] In this study, the peptide sequences are derived from the octapeptide FEFKFEFK (F8).[17] The FKFEFKFK (FK) sequence replaces the P2 glutamic acid at the peptide's C-terminus with lysine,[13] while the KFEFKFEFKK (KF8K) sequence introduces two additional lysines at both ends—one aligned with the phenyl rings and the other with the polar lysines (Fig.4.1a).[14] Such modifications lead to peptides with distinct fiber edge characteristics: in F8 and FK gels, the hydrophobic regions are exposed at the fiber edges, while in KF8K gels, the hydrophobic core is shielded by the extra lysines. For a broad pH range, including those used in this study, both FK and KF8K sequences carry a +2 charge, whereas F8 remains neutral (Fig.4.1b).

Preparation procedure Peptide powders were purchased from LifeTein® LLC (US) as HCl salts with over 95% purity and stored at -20°C. Doxorubicin hydrochloride (DOX, purity 95%) was obtained from Fluorochem (UK), while all other solvents and reagents were purchased from Sigma-Aldrich. Following the previously outlined method,[13, 14] peptide hydrogels (both unloaded and DOX-loaded) were prepared by dissolving peptide powder and/or DOX in deuterium oxide (D_2O) (used instead of H_2O to suppress solvent signal in QENS experiment). The pH was then adjusted to 5–5.7 through incremental additions of 50 mM NaOD (replacing NaOH). After each NaOD addition, samples were vortexed, and gentle centrifugation was used to remove any trapped air bubbles. Final concentrations were set at 14 mM for the peptide and 5 wt.% for DOX (86 mM instead of 240 μM) and samples were then stored overnight at 4 °C before use. The higher amount of drug loaded is due to the requested signal for QENS for small drugs.

2.1.3 Bis-urea gel

The bis-urea gelator is a low molecular weight gelator (LMWG) known for its robust self-assembly capabilities and versatility in various solvents. Its molecular structure features bis-urea motifs, which promote strong hydrogen bonding interactions (Fig. 2.4(a)). The synthesis of the bis-urea LMWG follows a straightforward procedure described by Lloyd et al:[26] (S)-1-phenylethyl isocyanate (2.1 g, 13.6 mmol) was dissolved in 150 mL of dry chloroform ($CHCl_3$) in a three-necked round-bottomed flask fitted with a condenser and maintained under nitrogen flow. Ethylenediamine (0.408 g, 0.454 mL, 6-8 mmol) was added dropwise to the solution, which was then refluxed for 24 hours under nitrogen. The resulting white precipitate was filtered using a Büchner funnel, yielding 1.96 g of the product (81%, 5.5 mmol) (note: the gelator synthesis has been made by Shereen Habib). The bis-urea gelator demonstrates remarkable versatility, gelling various solvent systems at low concentrations (as low as 0.05 wt.%). In highly hydrophobic solvents like Toluene, gelation is facilitated by the addition of a small volume of polar co-solvent,

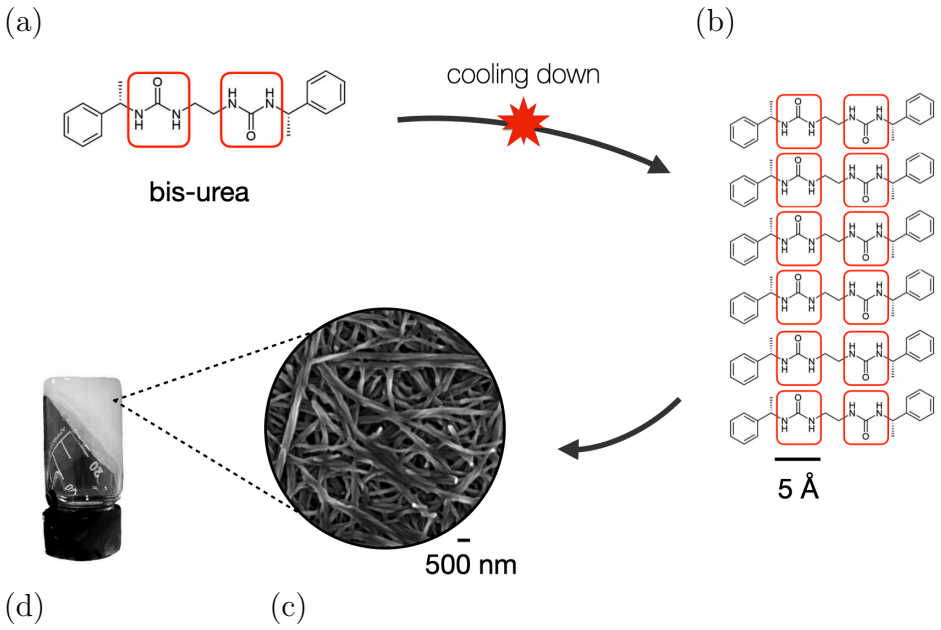

Figure 2.4: (a) Molecular structure of bis-urea LMWG (urea moieties undergoing hydrogen bonds assembly highlighted in red);(b) Schematic of the one-dimensional self-assembly process driven by hydrogen bonding of the urea moieties;(c) SEM image of dried bis urea gel, showing the gel network. Adapted from Ref.[28] with permission from the Royal Society of Chemistry. (d) Bulk gel exhibiting self-supportive properties, as demonstrated by its resistance to flow during the vial inversion test (note: sample is opaque to visible light).

such as DMSO.[27] In polar solvents like water, dissolution of the gelator requires ethanol as a co-solvent. A mixture of water and ethanol (7:3 v/v) forms a reliable gel at 0.3–0.5 wt.% gelator concentration following a heating and cooling procedure. The non-covalent interactions within the gelator structure grant the gel complete thermoreversibility. The bis-urea gelator forms a gel through a hierarchical self-assembly process driven by strong unidirectional hydrogen bonding. The gelator molecules align into α-tape motifs resembling velcro-like hook-and-loop fasteners.[26, 28] This interaction promotes the formation of one-dimensional (1D) polymer fibrils, which further aggregate into fibers (10–50 nm width). Fibre entanglement and solvent retention result in a three-dimensional network structure that gives rise to the macroscopic gel

(Fig.2.4(b–d)). The hydrophobic phenyl rings on the outer surfaces of the fibrils disrupt water/ethanol hydrogen bonding near the fibers, reducing local viscosity. This reduction has been hypothesized to enhance picosecond self-diffusion rates of both solvent molecules and incorporated drugs.

Preparation Procedure A 7:3 v/v water/ethanol solvent mixture was prepared by mixing the two components until homogeneity. Accurately weighed gelator (0.006 g for 0.3 wt.% or 0.010 g for 0.5 wt.%) was suspended in 2.0 mL of the solvent mixture. The suspension was heated with a heat gun up to $\sim 70°C$, dissolving most of the gelator. Remaining larger particles were dispersed using sonication, followed by further heating until a clear solution was obtained. For drug-loaded gels, paracetamol (5 wt.%) was added to the suspension before the heating/cooling cycle. Reference solvent samples were prepared following the same heating/sonication protocol to account for solvent evaporation and any changes in solvent ratios.

2.2 Quasi-Elastic Neutron Scattering (QENS)

The following section reviews essential elements from textbook knowledge on neutron spectroscopy. It is based on the following textbooks[29–33] and seminal articles[34–38] that provide an in-depth formulation.

2.2.1 Theoretical background

Neutron scattering

Neutron scattering is a powerful technique for investigating the structure and dynamics of materials at atomic and molecular scales. The scattering kinematics describing the interaction with atomic nuclei, relies on two parameters of neutrons: the momentum $p = m_{\mathrm{n}}v$ (neutron mass: $m_{\mathrm{n}} = 1.657 \times 10^{-27}$ kg, velocity: v) and the non-relativistic kinetic energy $E = m_{\mathrm{n}}v^2/2 = p^2/2m_{\mathrm{n}}$. In the particle-wave duality framework introduced by de Broglie,[39] the momentum p is related to the wavelength λ by

$$p = \frac{h}{\lambda} = \hbar k \tag{2.1}$$

where h is the Planck's constant ($= 6.626 \times 10^{-34}\mathrm{J} \cdot \mathrm{s}$) and $\hbar = h/2\pi$ its reduced form, while $k = 2\pi/\lambda$ is the wave vector. Consequently, the kinetic energy of neutrons can be expressed as:

$$E = \frac{p^2}{2m_{\mathrm{n}}} = \frac{\hbar k^2}{2m_{\mathrm{n}}} \tag{2.2}$$

Thanks to their neutral charge, specific value of the mass, and particle-wave duality, neutrons provide a unique capability to probe materials at atomic scales. They combine high penetration depth with non-destructive measurement properties, making them suitable for experiments in challenging environments, such as cryostats or pressure cells.[32, 33] The scattering kinematics is described by the changes in the neutron's wavevector $\hbar\vec{k}$ and the corresponding kinetic energy, quantified through the momentum $\hbar\vec{q}$ and energy

$\hbar\omega$ transferred to the sample (Fig.2.5). These variations are defined for the neutron's initial (i) and final (f) states during its interaction with the sample:

$$\hbar q = \hbar\vec{k_{\mathrm{i}}} - \hbar\vec{k_{\mathrm{f}}} \tag{2.3}$$

$$\hbar\omega = E_{\mathrm{i}} - E_{\mathrm{f}} = \frac{\hbar^2}{2m_n}(k_{\mathrm{i}}^2 - k_{\mathrm{f}}^2) \tag{2.4}$$

A scattering process is termed *elastic* if $\hbar\omega = 0$, indicating no energy transfer between the neutron and the sample. Conversely, $\hbar\omega \neq 0$ the process is classified as *inelastic*. The accessible length scale (l) in an experiment is determined by the momentum transfer (q). For elastic scattering, the scattering triangle shown in Fig.2.5b is isosceles and Eq.2.3 reduces to:

$$q = \frac{4\pi}{\lambda_{\mathrm{i}}}\sin\frac{\theta}{2} \tag{2.5}$$

When combined with Bragg's law, $\lambda = 2d\sin(\theta/2)$, this yields:

$$l = \frac{4\pi}{q} \tag{2.6}$$

This relationship explains why the momentum transfer q is expressed in units of inverse length (e.g., inverse Angstrom $\mathrm{\AA}^{-1}$). Hence, as a general rule, probing larger structures requires smaller scattering angles (low q), while interatomic distances are investigated at larger angles (high q). For simplicity, $\hbar$ will be omitted in further discussions.

Neutrons are typically delivered in a monochromatic beam, characterized by a constant wavelength and amplitude. The beam can be represented as a plane wave function $\psi(\vec{r})$:

$$\psi_{\mathrm{i}}(\vec{r}) = V^{-1/2}\exp(i\vec{k_{\mathrm{i}}}\cdot\vec{r}) \tag{2.7}$$

where the physical boundary given by the beam volume V is used as the normalized amplitude. The interaction of neutrons with the atomic nuclei of a sample occurs via the *strong nuclear force*, producing, due to its isotropic

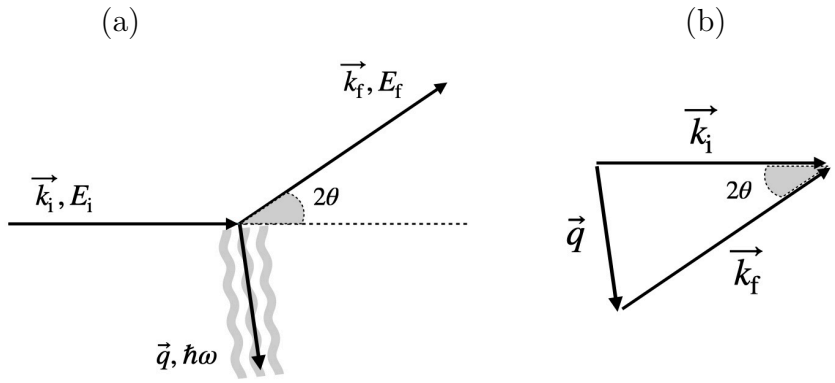

Figure 2.5: (a) Schematic representation of a scattering event in which a neutron with initial wavevector $\vec{k_i}$ and energy E_i transfers momentum $\vec{q}$ and energy $\hbar\omega$ to the sample, exiting with a final wavevector $\vec{k_f}$ and energy E_f.(b) The scattering triangle illustrating the momentum transfer $\vec{q}$. Adapted from Ref.[33]

and short-range nature a spherical wave:

$$\psi_f(\vec{r}) = -\frac{b}{r}\exp(ik \cdot r) \tag{2.8}$$

The amplitude of the scattered wave is modulated by a constant b, known as the *nuclear scattering length*. This constant is an intrinsic property of the nucleus, varying irregularly across the periodic table and among distinct isotopes of the same element due to the non-linear spin coupling between the neutron and the nucleus (Fig. 2.6).[31] This variation in spin coupling explains why the two most abundant isotopes of hydrogen, ^{1}H (protium) and ^{2}H (deuterium), have different scattering lengths: -3.74 fm and 6.68 fm, respectively. Notably, this difference enables the powerful method of isotopic substitution, the exchange of hydrogen isotopes within a sample to enhance or suppress the scattering signal.

These differences arising from the scattering length propagates to the *total scattering cross section* σ_s, which is one of the fundamental quantities in neutron scattering. This is defined as $\sigma_s = N_s/\Phi_0$, where N_s represents the total

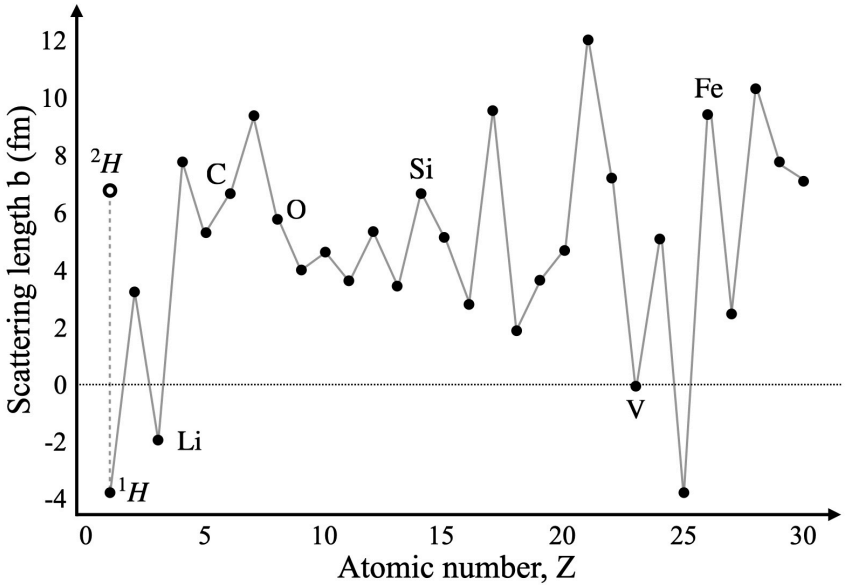

Figure 2.6: Nuclear scattering length, expressed in fm (10^{-15}m) and its non-monotonous dependence on the atomic number Z.

number of neutrons scattered per second, and Φ_0 is the incident neutron flux, i.e. the number of neutrons crossing a unit area per unit time. The total scattering cross section is constrained by the geometry of the system so it is usually better referred to in the general case to the *double differential cross section*, $d^2\sigma/d\Omega d\omega$, that is related to σ_s via integration over the solid angle $d\Omega$ and energy transfer $d\omega$:

$$\sigma_\mathrm{s} = \int d\Omega \int \frac{d^2\sigma}{d\Omega d\omega} d\omega \tag{2.9}$$

The double differential cross section represents the probability for neutrons to be scattered per second into a solid angle $d\Omega$ in a given direction and with an energy change $d\omega$. The total cross section σ_s is related to the scattering length b via:

$$\sigma_s = 4\pi|b|^2 \tag{2.10}$$

and if b as units of length (usually expressed in femtometres (fm): 10^{15} m), σ_s is in barns (b = 10^{-28} m^2).

Table 2.1: Scattering cross sections for selected isotopes, expressed in barns ($10^{-24}\,\mathrm{cm}^2$). Notably, ^{1}H has a much larger incoherent scattering cross section compared to its ^{2}H counterpart. For a complete list, refer to the NIST website: ncnr.nist.gov.

Isotope	σ_{coh}	σ_{inc}
^{1}H	1.76	80.27
^{2}H	5.59	2.05
C	5.559	0
O	4.232	0
Na	11.01	0.50
V	0.018	5.08
Al	1.495	0.008

For a real sample made up of different isotopic species, each with its scattering length b_i and random orientations of nuclear spins, the scattering length is given as an average value of possible configurations $\langle b \rangle$ and a fluctuation around it Δb:

$$b = \langle b \rangle \pm \Delta b \tag{2.11}$$

where $\Delta b = \sqrt{\langle b_i^2 \rangle - \langle b_i \rangle^2}$ is the standard deviation. By combining Eq.2.11 with Eq.2.10 the average scattering cross section $\langle \sigma_{\mathrm{s}} \rangle$ becomes a sum of two components:

$$\langle \sigma_{\mathrm{s}} \rangle = 4\pi \langle b^2 \rangle = 4\pi \langle b \rangle^2 + 4\pi(\Delta b^2) = \sigma_{coh} + \sigma_{inc} \tag{2.12}$$

The coherent cross section (σ_{coh}) results from the constructive interference of scattered neutron waves, providing structural information about the arrangement of atoms. In contrast, the incoherent cross section (σ_{inc}) arises from non-interfering scattered waves and offers no direct structural insights, instead reflecting only the isotopic composition of the sample. Examples of coherent (σ_{coh}) and incoherent (σ_{inc}) cross section for selected isotopes are listed in Tab.2.1. As a result, the double differential cross section can be then

decoupled accordingly into a coherent and incoherent part:

$$\left(\frac{d^2\sigma}{d\Omega d\omega}\right) = \left(\frac{d^2\sigma}{d\Omega d\omega}\right)_{coh} + \left(\frac{d^2\sigma}{d\Omega d\omega}\right)_{inc} \tag{2.13}$$

Dynamic structure factor

The real fingerprint of scattering event is the dynamic structure factor $S(q,\omega)$ related to the double differential cross section via:

$$\frac{d^2\sigma}{d\Omega d\omega} \propto \sigma_{\mathrm{s}} S(q,\omega) = \sigma_{coh} S_{coh}(q,\omega) + \sigma_{inc} S_{inc}(q,\omega) \tag{2.14}$$

Hence the two terms of Eq.2.13 can be written as:

$$\left(\frac{d^2\sigma}{d\Omega d\omega}\right)_{coh} \propto \sum_{\alpha}\sum_{\beta} b_{\alpha,coh} b_{\beta,coh} S_{coh}(q,\omega) \tag{2.15}$$

$$\left(\frac{d^2\sigma}{d\Omega d\omega}\right)_{inc} \propto \sum_{\alpha} b^2_{\alpha,inc} S_{inc}(q,\omega) \tag{2.16}$$

where the sums run over the isotopic species $\{\alpha,\beta\}$ while $S_{inc}(q,\omega)$ and $S_{coh}(q,\omega)$ are called incoherent and coherent dynamic structure factors, respectively. These functions are crucial as they enable to gauge structural and dynamic information about the sample from the raw neutron scattering data collected by the detector. Specifically, $S(q,\omega)$ can be related, through time and space Fourier transforms ($\mathcal{F}$), to the Van Hove correlation functions, which describe the self- and pair-correlations of particle positions (see Eq.1.13 and Eq.1.14 in Chapter 1):[34]

$$S_{coh}(q,\omega) = \mathcal{F}_{\vec{r},t\to q,\omega}\big[G(\vec{r},t)\big] \tag{2.17}$$

$$S_{inc}(q,\omega) = \mathcal{F}_{\vec{r},t\to q,\omega}\big[G_{self}(\vec{r},t)\big] \tag{2.18}$$

with

$$G_{\mathrm{pair}}(\vec{r},t) \sim \langle \vec{r}_i(0)\vec{r}_j(t)\rangle \tag{2.19}$$

$$G_{\mathrm{self}}(\vec{r},t) \sim \langle \vec{r}_i(0)\vec{r}_i(t)\rangle \tag{2.20}$$

Therefore, $S_{inc}(q,\omega)$ and $S_{coh}(q,\omega)$ provide insights into self- and collective correlations, respectively, but in the reciprocal space and energy domain. This representation, as will be shown, facilitates more convenient modeling. As previously mentioned, elastic scattering occurs when the final neutron energy equals the initial energy. However, in practice, this condition depends on the spectrometer's resolution, i.e. the smallest distinguishable energy transfer. If the energy transfer is zero or smaller than the spectrometer's resolution, the scattering appears elastic and $S(q,\omega)$ becomes a narrow peak (Fig.2.7). When the energy transfer is not zero and the neutron induced an excitation in the sample (such as *phonons*), the scattering becomes inelastic giving rise to signals a well separated from the elastic peak. For energy transfers that can be matched by ΔE_{res} resulting from random dynamic processes (such as translational diffusion or rotations) the scattering process is classified as **quasi-elastic**, and it manifests as a broadening of the elastic peak.

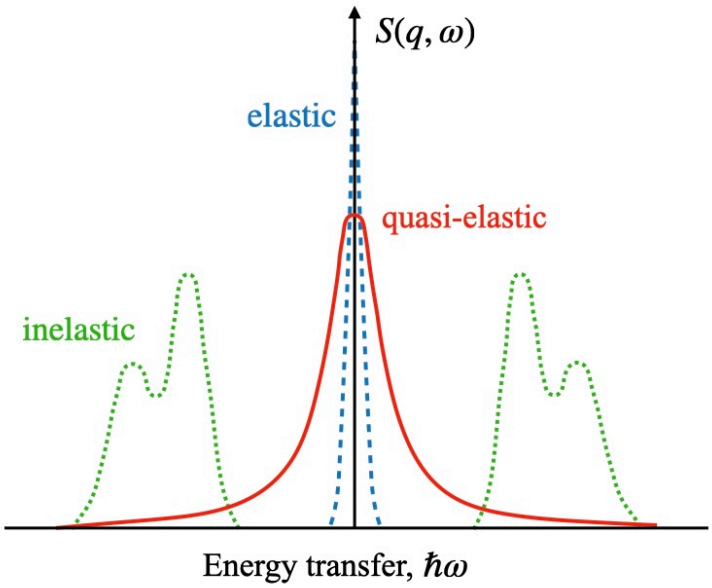

Figure 2.7: Dynamic structure factor and the three different regimes: elastic, quasi-elastic and inelastic. Adapted with permission from Ref.[36] Copyright 2019, Cambridge University Press.

Susceptibility The scattering function $S(q,\omega)$ can be expressed in terms of alternative physical quantities; a common approach is to relate it to the imaginary part of the dynamic susceptibility:

$$\chi''(q,\nu) = \pi \frac{S(q,\nu)}{1+n(\nu)} \tag{2.21}$$

where k_B is the Boltzmann constant and $n(\nu)$ the Bose occupation factor:

$$n(\nu) = \frac{1}{\exp\left(\frac{h\nu}{k_B T}\right) - 1} \tag{2.22}$$

From a theoretical perspective, $\chi''(q,\nu)$, is related to the response function in the framework of the linear response theory.[30, 33] It represents the imaginary part of the complex generalized susceptibility $\chi(q,\nu)$:

$$\chi(q,\nu) = \chi'(q,\nu) + i\chi''(q,\nu) \tag{2.23}$$

and can be interpreted as the loss component of the system's response to an external perturbation, such as neutron scattering. This relation makes $\chi''(q,\nu)$ particularly valuable for comparing neutron scattering data with other loss moduli, such as the mechanical loss modulus $G''(\nu)$ or dielectric loss modulus $\varepsilon''(\nu)$.[40–42] Additionally, susceptibility representation offers the advantage of resolving different dynamic processes as distinct peaks at characteristic frequencies, $\nu_{\max}$, unlike $S(q,\omega)$, where translation, rotations and vibration are convoluted in the same broadening of the elastic peak.[43]

Polarization analysis

In a QENS experiment, the double differential scattering cross section, reads as a linear combination of the respective coherent and incoherent dynamic structure factors (Eq.2.14). The large majority of case studies are based on the approximation $S_{tot}(q,\omega) \simeq S_{inc}(q,\omega)$ owing to the ubiquitous presence of ^1H whose scattering cross section is predominantly incoherent (Table 2.1). The only way to unambiguously solve this approximation and get the two $S(q,\omega)$ separately is by using polarization analysis (PA) option implemented on QENS spectrometers. This mechanism relies on the fact that neutron scattering probabilities depend not only on the isotope but also on the spin state of the neutron.[33] The interaction potential in a neutron scattering event can be expressed as having two components: a spin-independent term, which governs the exchange of energy and momentum with the sample, and a spin-dependent term, which can cause transitions between the neutron's spin states. Since neutrons are spin 1/2 particles, they can exist in two spin eigenstates, parallel ($|\uparrow\rangle$) or antiparallel ($|\downarrow\rangle$) to a chosen quantization axis. In unpolarized experiments, the incident neutron beam has 50% of spin up $|\uparrow\rangle$ and 50% of spin down $|\downarrow\rangle$ neutrons while with PA a supermirror polarizer is implemented to transmit the $|\downarrow\rangle$ state of the neutron beam (Fig.2.8). Subsequently, a precession coil flipper reverses the spins, creating two distinct scattering scenarios: spin-flip events ($|\downarrow\rangle \rightarrow |\uparrow\rangle$) and non-spin-flip events ($|\downarrow\rangle \rightarrow |\downarrow\rangle$). These outcomes are analyzed using a spin filter to resolve the final neutron spin state along a specific axis. The results yield two distinct dynamic structure factors corresponding to spin-flip ($S_{|\downarrow\rangle\rightarrow|\uparrow\rangle}(q,\omega)$) and non-spin-flip ($S_{|\downarrow\rangle\rightarrow|\downarrow\rangle}(q,\omega)$) scattering events. These two functions are related to $S_{\text{inc}}(q,\omega)$ and $S_{\text{coh}}(q,\omega)$ given that in neutron spin incoherent scattering, there is a 66% probability of spin-flip, whereas coherent scattering events involve no spin flip:

$$\begin{cases} S_{|\downarrow\rangle\rightarrow|\downarrow\rangle}(q,\omega) = S_{\text{coh}}(q,\omega) + \frac{1}{3}S_{\text{inc}}(q,\omega) \\ S_{|\downarrow\rangle\rightarrow|\uparrow\rangle}(q,\omega) = \frac{2}{3}S_{\text{inc}}(q,\omega) \end{cases} \tag{2.24}$$

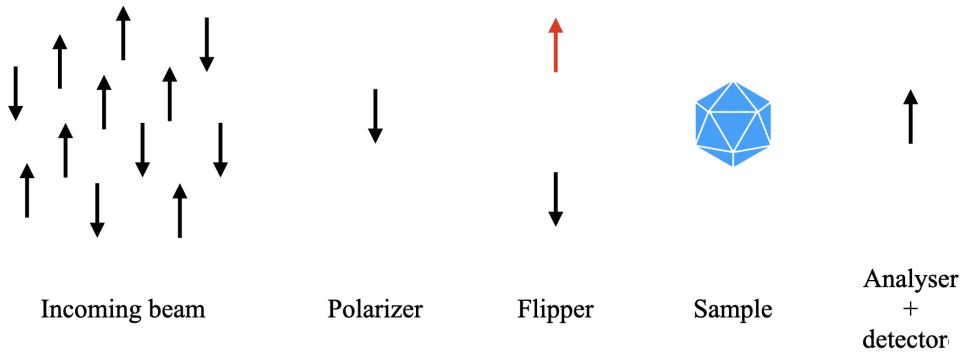

Figure 2.8: Mechanism of polarization analysis.

These are then combined to separately determine $S_{\text{inc}}(q,\omega)$ and $S_{\text{coh}}(q,\omega)$:

$$\begin{cases} S_{\text{coh}}(q,\omega) = S_{|\downarrow\rangle\to|\downarrow\rangle}(q,\omega) - \frac{1}{2}S_{|\downarrow\rangle\to|\uparrow\rangle}(q,\omega) \\ S_{\text{inc}}(q,\omega) = \frac{3}{2}S_{|\downarrow\rangle\to|\uparrow\rangle}(q,\omega) \end{cases} \tag{2.25}$$

Such notable results bear an intrinsic limitation. The separation of the neutron beam in spin-flip and non-spin-flip event effectively cuts the flux, leading to a decrease in counting statistics. As a result, longer measurement times compared to unpolarized instruments are typically required to achieve an acceptable signal-to-noise ratio. The use of polarized QENS is driven by its ability to both extend the scope of accessible dynamics and enhance the accuracy of data interpretation. It uniquely enables the separation of the coherent scattering contribution, which carries information on spatial correlations and collective motions at mesoscopic length scales and picosecond timescales.[43, 44] In hydrogen-rich samples, this signal is typically masked by dominant incoherent scattering, and polarization analysis is essential to extract it reliably.
Equally important is the improved interpretation of incoherent dynamics.

Even small coherent contributions (such as those from protein hydration layers in solution) can distort relaxation parameters, particularly at low and intermediate q, where the assumption of incoherent dominance is often taken for granted. As demonstrated by Sarter et al.,[45] coherent contamination can significantly bias unpolarized QENS results. By resolving the two components, PA-QENS allows a more accurate application of dynamical models and clarifies the conditions under which the incoherent approximation remains valid.

2.2.2 QENS methods

Spectrometers

Neutrons produced at reactor or spallation sources typically have energies on the order of MeV, which must be reduced to the eV or sub-eV range to match the energy scales relevant to atomic and molecular motion. This reduction is achieved using moderators: for example, *cold* neutrons (below 25 meV) are produced using liquid hydrogen at 25 K, while *hot* neutrons (up to 2 eV) are generated with solid graphite at 2400 K. After this initial moderation, the neutrons are delivered to spectrometers via neutron guides, which function similarly to fiber optics. Different types of spectrometers are optimized to target specific spatial and temporal ranges.[46, 47] The key parameter to consider in a spectrometer is its energy resolution, ΔE_{res}, which determines the upper limit of the observable timescale, Δt_{obs}, according to the Heisenberg uncertainty principle:[32]

$$\Delta t_{\text{obs}} \sim \frac{\hbar}{\Delta E_{\text{res}}} \tag{2.26}$$

As a result, instruments with high energy resolution (small ΔE_{res}) are capable of detecting slower motions (large Δt_{obs}), while those with lower energy resolution are better suited for probing faster motions. The energy resolution is determined by measuring the scattering from a strongly incoherent standard material, typically Vanadium (see Table 2.1), whose response is well-approximated by a $\delta(\omega)$, representing the narrowest possible broadening. QENS spectrometers are typically classified into three main types: direct ge-

ometry, inverted geometry, and Neutron Spin Echo (NSE).[32, 48] The primary distinction is that the first two operate in the energy domain to probe energy transfer, while NSE functions in the time domain.

Direct geometry The energy transfer is calculated by directly collecting a range of final ΔE_f energies knowing the incident energy. In practice this is done by counting the arrival time of neutrons, with a defined incident energy E_i (monochromatic beam), relative to a starting time $t = 0$, in a operational mode known as *Time-of-Flight* (ToF) (Fig.2.9). The neutron energy transfer can be calculated by knowing the path lengths L_1 and L_2 as well as the flight times t_1 and t_2 (Fig.2.9).

$$\Delta E = E_i - E_f = \frac{1}{2} m_{\mathrm{n}} \left[\left(\frac{L_1}{t - t_2} \right)^2 - \left(\frac{L_2}{t_2} \right)^2 \right] \tag{2.27}$$

The q range is traditionally spanned by arrays of tubes filled with ^{3}He. Here, the position in the solid angle of the scattered neutrons is detected by looking at the emission in opposite direction of tritium and a proton following absorption by ^{3}He gas:

$$^3_2\mathrm{He} + \mathrm{n} \rightarrow {}^3\mathrm{H} + {}^1\mathrm{H} + 0.764\,\mathrm{MeV} \tag{2.28}$$

On the LET ToF spectrometer at the ISIS Neutron and Muon Source used in this work, the detection system consists of tubes that are 4 m tall and cover a wide scattering angle range (5°–140°).[49] LET uses repetition-rate multiplication (RRM), which takes advantage of the full time frame by simultaneously employing multiple incident energies and analyzing each one independently. A distinctive feature of LET is its ability to simultaneously provide three different energy resolutions in a single measurement, corresponding to distinct incident energies. This capability significantly extends the accessible dynamic range. Additionally, LET includes a polarization analysis option,[50–52] which enables the separation of coherent and incoherent scattering functions, offering valuable insights into both collective and single-particle dynamics. The

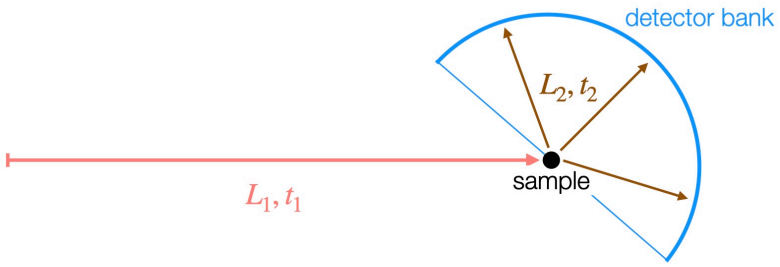

Figure 2.9: Schematic "bird's of eye" view of a direct geometry Time-of-Flight spectrometer. LET spectrometer at ISIS follows this scheme.

primary drawbacks of PA option on LET is the poorer statistic compared to their unpolarized counterparts (because the flux is effectively split); moreover, the energy resolution of LET's PA configuration is relatively low, with ongoing project to complement it with high-resolution instruments featuring PA capabilities.[53]

Inverted geometry Inverted geometry spectrometers operate on the opposite philosophy of direct geometry instruments, by analyzing a fixed final energy E_f and tracing back a range of neutron incident energies ΔE_i (white beam). This final energy discrimination is achieved through an energy analyzer composed of a single crystal. The crystal's lattice spacing, d select a certain λ through Bragg's law:

$$\lambda = 2d\sin\theta \tag{2.29}$$

Neutrons scattered from the sample travel to the analyser array and are scattered back toward the detector bank only if their final wavelength satisfies the Bragg condition. This process is commonly referred to as neutron backscatter-

ing (NBS). The high energy resolution achieved in this setup is not a general feature of NBS per se, but rather a consequence of operating the analyser crystals at scattering angles close to $2\theta \sim 180°$ ($\theta \to 90°$). In this condition, the contribution of angular uncertainty to the wavelength uncertainty becomes negligible, and the resolution is determined almost entirely by the quality of the analyser crystal itself (i.e., the spread in lattice spacing $\Delta d/d$). This can be quantified by propagating uncertainty through Bragg's law, considering θ and d as independent variables:[33]

$$\left(\frac{\Delta\lambda}{\lambda}\right)^2 = \left(\frac{\Delta d}{d}\right)^2 + (\Delta\theta \cot\theta)^2 \tag{2.30}$$

where $\Delta\lambda$ is the spread in wavelength. As $\theta \to 90°$, $\cot\theta \to 0$, and thus the angular term vanishes. This makes the crystal's intrinsic properties the primary determinant of energy resolution, enabling performance that typically surpasses that of common direct geometry instruments.[54] For a full comparison between the different spectrometers used in this project refer to Table2.2. On IRIS and IN16b (Fig.2.10), the two indirect geometry spectrometers used in this project, the crystal analyzers are made of pyrolytic graphite PG(002) and silicon Si(111), respectively. Technically, to avoid intensity losses, IRIS operates under *near*-backscattering conditions, as the analysed beam is scattered at an angle of $2\theta \sim 175°$, slightly below the horizontal plane (exact backscattering).[55–57]

Because of how neutrons are produced at spallation sources, IRIS operates in time-of-flight (TOF) mode, which is the most efficient and practical method for neutron energy analysis. TOF maximizes neutron utilization by capturing the full energy spectrum in a single pulse, avoiding the flux losses typical of mechanical monochromators or choppers. In contrast, IN16B operates at a reactor source, where the same combination of time-of-flight and inverted geometry is achieved using a flexible, high-speed four-disk chopper system with multiple slits. This operational mode called BATS (Backscattering and Time-of-Flight Spectroscopy)[58, 59] allows to combine both NBS and ToF advantages of having high resolution with a wider energy range compared to the standard

IN16b mode (from $\pm 30 \mu eV$ to $\pm 150 \mu eV$). The additional advantage of this hybrid solution at a reactor source is that it offers greater flexibility, allowing repetition rates up to an order of magnitude higher, since the spectrometer is no longer constrained by the source frequency as it is in spallation sources.

Table 2.2: List of QENS spectrometers used in this project with their class, the q-range accessed and the energy resolution ΔE_{res} and energy transfer $\hbar\omega$.$^{(*)}$ the three resolution corresponds to different incident energies ($E_i = 3.84, 1.81$ and 1.05 meV)

name	class	q-range (Å^{-1})	ΔE_{res} (μeV)	$\hbar\omega$ (μeV)
LET (ISIS)	direct	$\sim 0.3 - 2.2$	$\sim 131/45/22^{(*)}$	$\sim \pm 2000$
IRIS (ISIS)	inverted	$\sim 0.42 - 1.85$	~ 17.5	$\sim \pm 500$
BATS (ILL)	inverted	$\sim 0.2 - 1.8$	~ 3.5	$\sim \pm 150$

(a)

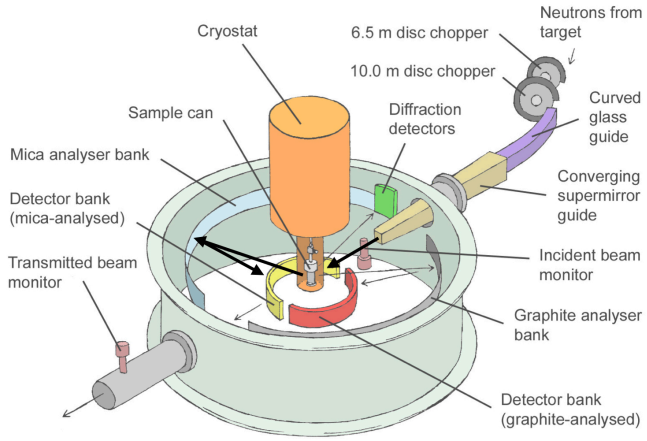

(b)

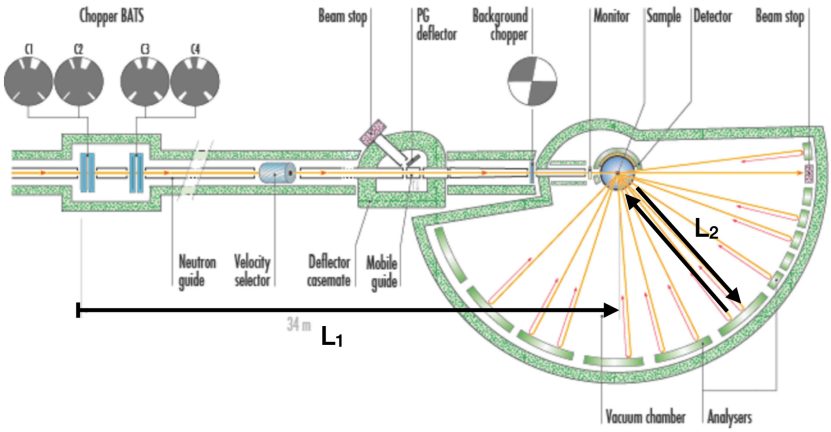

Figure 2.10: Schematic view of (a) IRIS spectrometer at ISIS (Harwell, UK) and (b) IN16b (BATS mode)[58] spectrometer at ILL (Grenoble, France).

Neutron Spin-Echo Neutron Spin-Echo (NSE) spectroscopy, originally developed by Ferenc Mezei (1972),[60, 61] offers the highest energy resolution among techniques for studying quasi-elastic phenomena, without relying on flux-limiting components such as monochromators, energy analyzers, or choppers. Unlike time-of-flight or backscattering spectrometers, which measure scattered neutrons at specific angles and energies, NSE determines energy differences by analyzing changes in the polarization of the neutron beam. This innovative approach provides an energy resolution two orders of magnitude higher—reaching 10^{-3} μeV compared to the 10^{-1} μeV achieved by leading backscattering spectrometers. NSE enables the investigation of slow dynamics on timescales up to 100 ns, within a q-range typically associated with large structures such as polymers and micelles.[62, 63] This capability makes it particularly suited for studying both the dynamics and spatial organization of such systems, which are often complementary to structural studies performed using techniques such as SANS.

The following provides a general overview of the method, leaving a more comprehensive and detailed treatment to specialized literature.[32, 33, 46, 60, 61] At its core, NSE draws inspiration from NMR. However, rather than monitoring the spin of nuclei within a sample, NSE tracks the echo of neutron spins as they interact with the scattering system. A typical NSE spectrometer consists of two branches, each dominated by identical solenoids that generate magnetic fields, with the sample positioned at the junction between them (Fig.2.11). Neutrons entering the first solenoid are velocity-selected (thus in wavelength λ) and polarized along the beam direction with a supermirror polarizer. Before entering the first solenoid, a $\pi/2$ spin flipper rotates the neutron spins to a direction perpendicular to the magnetic field B_1. Inside the first solenoid, the neutron spins undergo Larmor precession, accumulating a total precession angle φ over the path length l:

$$\varphi = \omega\tau = \frac{\gamma_{\mathrm{L}}}{v}\int_0^{L_1} B_1 dl = \frac{\gamma_{\mathrm{L}} m_{\mathrm{n}}\lambda}{h}\int_0^{L_1} B_1 dl \tag{2.31}$$

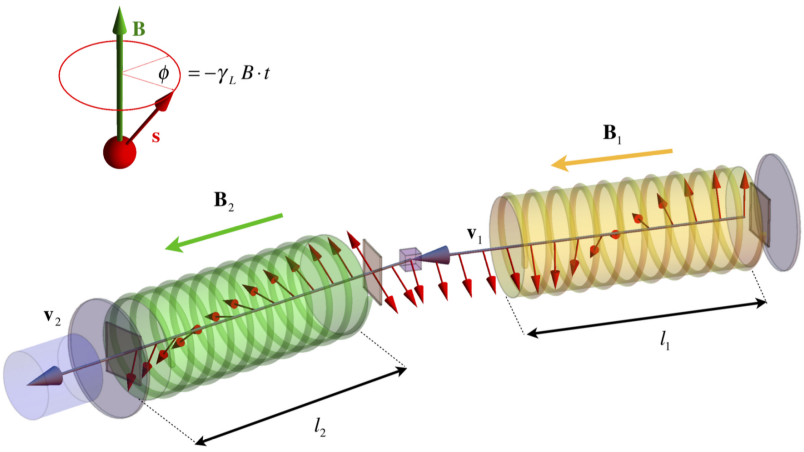

Figure 2.11: Schematic representation of the neutron spin-echo (NSE) principle. Adapted from Ref.[64]

where ω is the Larmor precession frequency, γ_{L} is the neutron gyromagnetic ratio, L_1 is the length of the first solenoid (equal to L_2), v is the neutron velocity, m_{n} is the neutron mass, λ is the neutron wavelength, and $\int B, dl$ accounts for non-uniformities in the magnetic field over the path and τ is the flight time. This precession causes the spins to fan out perpendicular to the beam direction, with faster neutrons experiencing a smaller precession angle and slower neutrons undergoing greater rotations. When neutrons exit the first solenoid, a π spin flipper reverses the sense of precession by 180°, effectively swapping the positions of the fastest and slowest neutrons while preserving their rotational sense. The second solenoid, identical to the first, refocuses the spins such that their polarization is restored. If no interaction occurs between the two solenoids, the polarization will be completely recovered, resulting in the phenomenon known as *echo*. However, when neutrons interact with the sample, quasi-elastic processes can alter their velocities, leading to incomplete recovery of the polarization. By measuring the small differences in polarization, NSE can extract precise quantitative information about the dynamic processes within the sample. The polarization analyzer selects only the spin projections parallel to the axis, expressed as the average of the cosine of the

total Larmor precession angle $\varphi_{\mathrm{T}} = \varphi_1 - \varphi_2$. This precession angle difference is directly linked to the energy transfer $\hbar\omega$ associated with quasi-elastic phenomena and can be expressed as:

$$\varphi_{\mathrm{T}} = \frac{\gamma_{\mathrm{L}} BL}{m_{\mathrm{n}} v^3}\hbar\omega = \frac{\gamma_{\mathrm{L}} m_{\mathrm{n}}^2 BL\lambda^3}{2\pi h^2}\omega = t_{\mathrm{F}}\omega \tag{2.32}$$

Here, the constant t_{F}, recalling Eq.2.31, has units of time (known as *Fourier time*) and depends on the magnetic field strength (i.e. current in the solenoids) and the cube of incident neutron wavelength (λ^3). In practice, during a typical NSE measurement the Fourier time is scanned by varying the solenoid current at a fixed wavelength. If the spin polarization reads as:

$$P_z = \langle\cos(\varphi)\rangle = \int \cos\left(\frac{\gamma_{\mathrm{L}} \int_0^L B dl}{v}\right) dv \tag{2.33}$$

the difference in spin polarization due to quasi-elastic energy transfer will be $P_z = \langle\cos(\omega t_{\mathrm{F}})\rangle$. This value must be averaged over all final neutron energies, which generate a distribution of precession angles. The average is obtained through an energy-weighted integral of the polarization, modulated by the scattering function $S(q,\omega)$:

$$P_z(q, t_{\mathrm{F}}) = \frac{\int S(q,\omega)\cos(\omega t_{\mathrm{F}}) d\omega}{\int S(q,\omega) d\omega} \tag{2.34}$$

where $\int S(q,\omega)d\omega$ is the static structure factor $S(q)$. Notably, the numerator corresponds to the real part of the intermediate scattering function $I(q, t_{\mathrm{F}})$ with the static structure factor $S(q)$ being interpreted as $I(q, t_{\mathrm{F}})$ at $t_{\mathrm{F}} = 0$. Consequently, Eq.2.34 can be rewritten as a normalized intermediate scattering function: $I_{\mathrm{norm}}(q, t_{\mathrm{F}}) = I(q, t_{\mathrm{F}})/I(q, 0)$. This normalization highlights one of the main strength of NSE: despite its complex theoretical foundation, the direct access to the intermediate scattering function in the time domain eliminates the need for normalization via deconvolution required in the energy domain, relying instead on a straightforward division. Importantly, the difference in neutron polarization must reflect only variations in velocity and

not contributions from spin-incoherent scattering. As outlined in Eq.2.24, spin-incoherent scattering has a 66% probability of flipping the neutron spin during scattering. To account for this, the scattering function in Eq.2.34 is adjusted to remove the incoherent component:

$$S_{\mathrm{NSE}}(q,\omega) = S_{coh}(q,\omega) - \frac{1}{3}S_{inc}(q,\omega) \tag{2.35}$$

This adjustment ensures that neutron spin echo primarily captures coherent scattering, which does not flip the neutron spin, while including only a minor contribution from incoherent scattering. Consequently, NSE is particularly well-suited for studying collective dynamics. When studying a polymer or a gel network,[62, 65] similarly to what happen in SANS, the scattering originates from the contrast between solvent and solute (typically protonated polymer in fully deuterated solvent to enhance the signal). As a result, the dynamics of the polymer are indirectly inferred from the "holes" in the dominant coherent scattering signal originating from the solvent. Investigating q values well below the structure factor peak of heavy water ensures sensitivity to the polymer's structure factor. The neutron spin-echo spectrometer used in this project is IN15 at ILL, which provides a maximum Fourier time of 1 μs and covers a q range from 0.01 to 0.42 $\mathrm{\AA}^{-1}$, typical of that achieved by SANS instruments (Fig. 2.12).[66]

Figure 2.12: Overview of the quartz sample holder containing the FmocFF gel, with the IN15 neutron spin-echo spectrometer at ILL visible in the background.

Sample holders The choice of sample size and geometry in neutron scattering experiments involves a critical trade-off between maximizing count rates and minimizing multiple scattering effects. Multiple scattering refers to the phenomenon in which a neutron, after scattering once within the sample, undergoes one or more additional scattering events before reaching the detector. This undermines the ability to precisely determine the energy and momentum transfer of the neutron, as the path length is altered and it becomes impossible to uniquely assign an energy change to a single scattering event. To mitigate these effects, a commonly accepted guideline is to design the sample such that approximately 90% of the incident neutron beam is transmitted through the

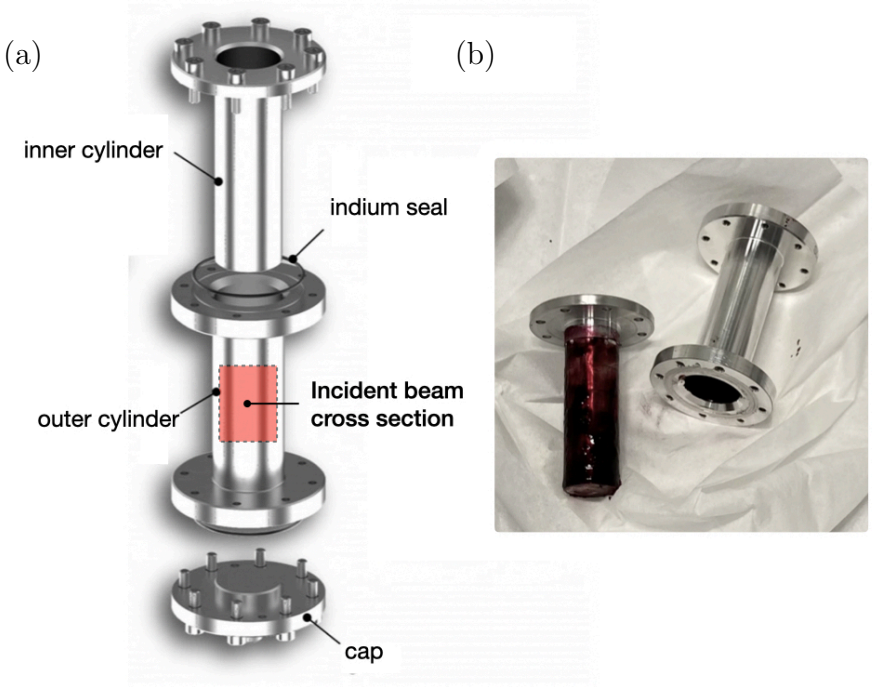

Figure 2.13: (a) Example of standard cylindrical Al sample holder used for time of flight or backscattering experiment. Reproduced from Ref.[32] with permission from the Royal Society of Chemistry. The red square identifies the neutron beam cross section, typically around 3×3 cm^2. (b) Sample holder after a measurement, with traces of F8 gel loaded with Doxorubicin in the inner cylinder.

sample, allowing only ∼10% to be scattered. This ensures that the probability of multiple scattering is sufficiently low while still providing an adequate signal for analysis. This trade-off directly influences the choice of sample path length, which is governed by the Beer–Lambert law:

$$I = I_0 e^{-n(\sigma_s+\sigma_a)t} \tag{2.36}$$

where I is the intensity after attenuation through a sample of thickness t, I_0 is the incident intensity, n is the number density, σ_s and σ_a are the total scattering and absorption cross sections.

Annular sample holders are used because they match the cylindrical geometry of the detector banks, ensuring a uniform path length in all directions. This helps reduce angular dependency and makes multiple scattering more isotropic and evenly distributed. In this project, the sample thickness (annular gap) ranged from 0.1 mm to 0.25 mm. Thinner samples were used for hydrogen-rich systems to reduce multiple scattering, while thicker samples were required for solute diffusion studies in deuterated solvents to increase the count rate. Aluminum (Al) is commonly chosen as a material for sample holders due to its affordability and its transparency to neutrons in the q-range probed by direct and indirect spectrometers, owing to its low coherent, incoherent, and absorption cross-sections. However, aluminum is susceptible to degradation when exposed to corrosive samples or, over time, even to water. In this work, a cylindrical sample holder geometry was utilized, where the sample is uniformly distributed in the space between two concentric cylinders (Fig. 2.13). This design is usually preferred for liquid-like sample as it ensures an isotropic scattering with constant sample thickness, which can be adjusted by modifying the radius of the inner cylinder. In NSE experiments, quartz cells are typically used because they have low incoherent scattering, minimizing background and preserving polarization. Introducing materials with high incoherent cross-sections would worsen the data quality by adding unwanted depolarization. The sample geometry is usually a simple slab, as NSE does not require reproducing a detector solid angle like in time-of-flight instruments.

For the gel samples used in this study, three different loading procedures were employed, tailored to the specific gelation methods of each sample. For FmocFF gel the sample was transferred in its liquid state after addition of GdL by placing the solution at the bottom of the outer cylinder. The inner cylinder was then inserted, spreading the liquid evenly within the interstitial space. For F8 gel and its modified version the procedure was similar to that used for the FmocFF gel. However, since the F8 gel exhibits self-healing properties, it was loaded in its pre-formed gel state. For the bis-urea gel the hot solution was poured into a pre-heated outer cylinder and then compressed with the inner cylinder to ensure uniform distribution during the gelation process.

Data analysis

Data reduction Raw neutron data are recorded as *counts/time* versus detector positions and must be converted into $S(q,\omega)$ (Fig.2.14) through a process known as data reduction.[32, 33] This includes a series of operations that are nowadays encoded in *python*-based scripts within the *Mantid* software[67] tailored to the specific spectrometer, so that the action required by the experimenter in minimal. These operations include incident beam normalization to counting time and flux, corrections for detector efficiency across the solid angle, detector grouping, and energy binning. The latter two steps are particularly important, as they determine the final granularity of q range (defined by the detector coverage and typically spanning $0.2\text{Å}^{-1} \leq q \leq 2\text{Å}^{-1}$) and influence the statistical quality within the energy window. For polarization analysis, an additional correction is applied to account for the time-dependent efficiency of the ^{3}He polarizer, which determines its ability to effectively flip the spin.[52]

In addition to standard steps such as background subtraction, detector efficiency, and instrument resolution corrections, NSE data processing also involves (1) fitting the raw phase-dependent neutron counts at a given Fourier time t_F with a damped cosine function, and (2) calculating the polarization from the amplitude of this fit using the up and down spin counts. Unlike direct or indirect spectrometers, NSE data reduction is less automated and requires careful tuning of fitting parameters, so the detailed processing is typically entirely carried out by the instrument scientist.

Energy domain Incoherent QENS

The primary challenge of this method lies in disentangling the plethora of dynamical processes that contribute to the broadening of the elastic line. The standard method to extract individual contributions involves fitting $S_{\text{inc}}(q,\omega)$, using least-square minimization.[68, 69] The observed peak broadening is typi-

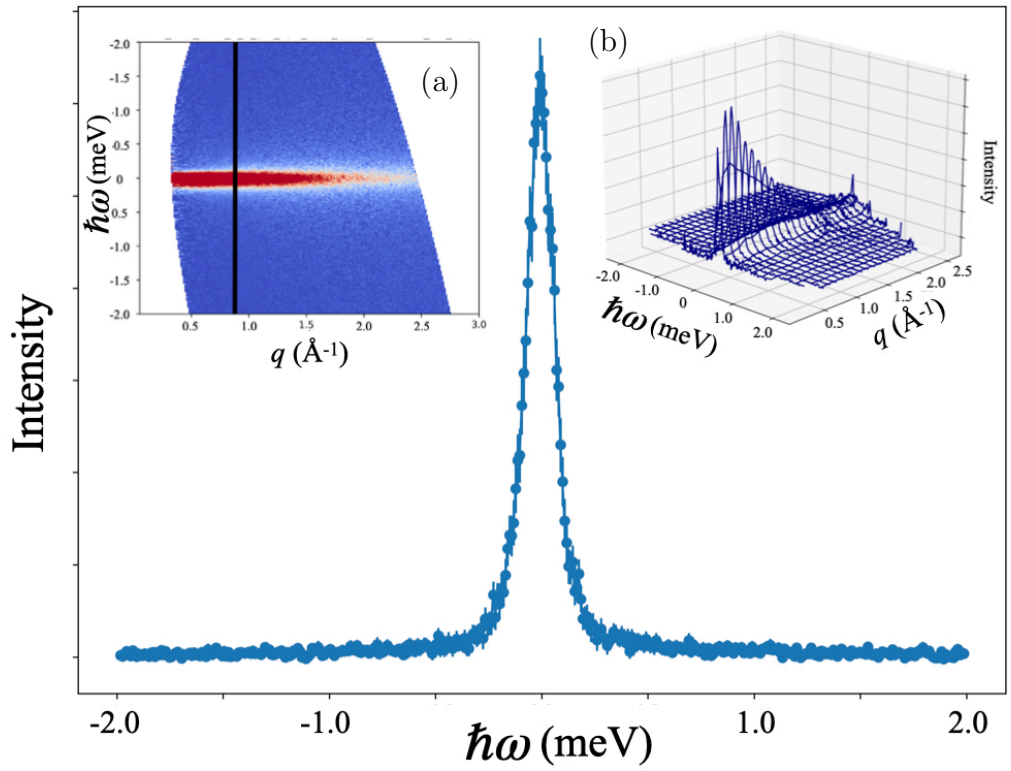

Figure 2.14: Representative QENS spectrum as a function of energy transfer and intensity measured for D_2O/Et-D_6 with 0.3 wt.% bis-urea gelator and 5 wt.% paracetamol, recorded on LET at $T = 290K$ and $E_i = 3.84$ meV. Inset (a) 2D contour map in $q - \hbar\omega$ space, highlighting the specific cut along q used to extract the spectrum shown in the main panel. Inset (b) 3D visualization of the QENS intensity as a function of $q - \hbar\omega$.

cally modeled as a sum of Lorentzian functions, $\mathcal{L}(q, \omega)$, centered at the origin:

$$\mathcal{L}(\gamma(q), \omega) = \frac{1}{\pi} \frac{\gamma(q)}{\omega^2 + \gamma(q)^2} \tag{2.37}$$

where $\gamma(q)$ is the Half Width at Half Maximum (HWHM). Careful consideration must be given when fitting a QENS signal with arbitrary sums of Lorentzians, as each corresponds to distinct physical processes. The optimum number of Lorentzians cannot be determined a priori but depends on the

spectrometer's resolution, the accessible energy window, and sample characteristics, such as the nature of the moving components. In fact, for a sample to produce a measurable QENS signal, its dynamics must lie within the instrument's "sweet spot," defined by its energy resolution and energy window. Motions slower than the resolution limit (e.g., immobile gel networks or sample holders) contribute as elastic signals modeled by $\delta(\omega)$-functions. Conversely, processes faster than the instrument's range appear as a background, typically modeled as $\alpha\omega + \beta$. In the systems studied in this thesis, no more than two distinct dynamical processes (Lorentzians) are considered: one representing slower isotropic translational diffusion (narrower Lorentzian) and another accounting for faster localized motions (broader Lorentzian).[70] Modeling these localized motions is particularly relevant for studies on lateral protein chain dynamics[36] while for small molecules, a single Lorentzian representing center-of-mass motion often suffices.[71] The final model for the incoherent structure factor $S_{\text{inc}}(q, \omega)$ accounting for these contributions, is expressed as:

$$S_{\text{inc}}(q, \omega) = A_0\delta(\omega) + \sum_i A_i \cdot \mathcal{L}_i(\omega, \gamma(q)) + \alpha\omega + \beta \tag{2.38}$$

However, this model assumes an infinite observation time, which is unattainable in practice.[30, 33] Therefore, the instrument resolution, $\mathcal{R}(\omega)$, must be included through a convolution (denoted as $\otimes$) with the fitting functions (i.e. δ and Lorentzian)(Fig.2.15). The resolution function $\mathcal{R}(\omega)$ is obtained by fitting the Vanadium spectrum with a sum of an arbitrarily large number of Gaussian functions $\mathcal{G}(\omega)$:

$$\mathcal{G}(\omega, \sigma, \omega_0) = \frac{1}{\sqrt{2\pi}\sigma} \exp\left[-\frac{(\omega - \omega_0)^2}{2\sigma^2}\right] \tag{2.39}$$

where ω_0 is the peak centre and σ is Full Width at Half Maximum (FWHM) of the bell shape function. The advantage of using $\mathcal{G}(\omega)$ is that the convolution of a Gaussian and a Lorentzian is an analytical function called Voigt function $\mathcal{V}$,

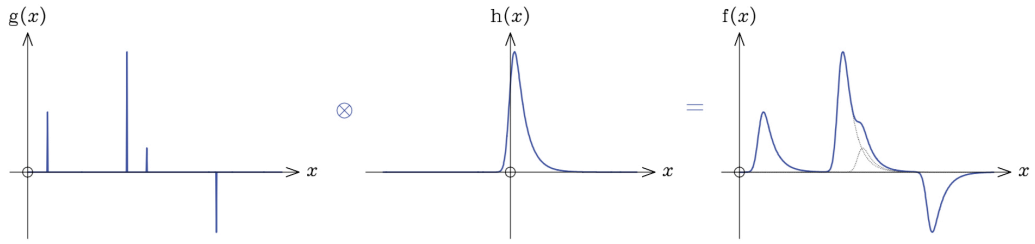

Figure 2.15: Visual example of convolution between a δ-like function g(x) and an asymmetric function h(x). The function f(x)=g(x)$\otimes$h(x) represents a "blurring" of function g(x) by function h(x). Reprinted with permission from Ref.[31] Copyright Oxford University Press.

$$\mathcal{V}(\omega,\sigma,\gamma) = \mathcal{G}(\omega,\sigma) \otimes \mathcal{L}(\omega,\gamma) = \int_{+\infty}^{-\infty} \mathcal{G}(\omega',\sigma)\mathcal{L}(\omega-\omega',\gamma)\, d\omega' \tag{2.40}$$

This convolution combines the Gaussian's broadening effects with the Lorentzian's sharpness, simplifying the fitting process, especially in script-based analyses where the Voigt function is accessible (e.g., via Faddeeva function available in *python*).[69] Importantly, due to the properties of δ-functions, the first term of Eq.2.38 simplifies to:

$$\mathcal{R}(\omega) \otimes \delta(\omega) \simeq \mathcal{R}(\omega) \tag{2.41}$$

The fundamental parameter obtained through fitting is the q-dependent Lorentzian broadening $\gamma(q)$. Its physical significance becomes clear when the Lorentzian $\mathcal{L}(\gamma(q),\omega)$ is anti-Fourier transformed into space and time coordinates. This yields the probability density function $P(r,t|r_0,t_0)$ in an isotropic medium (Eq.1.12) which solves the second Fick's law (Eq.1.2). Recalling the relation between the self-correlation function, $G_{\text{self}}(r,t)$ and the incoherent dynamic structure factor $S_{\text{inc}}(q,\omega)$, $\gamma(q)$ becomes:

$$\gamma_{\text{fick}}(q) = D_{\text{self}} q^2 \tag{2.42}$$

As a result, larger broadening in q of the $\gamma(q)$ corresponds to a larger slope, corresponding to a larger diffusion coefficient D_{self} (Fig.2.16). The diffusion model described by Eq.2.42 is named Fickian as it represents the simplest

case of Brownian motion where a particle undergoes random collisions with its surrounding solvent in a homogeneous medium. However, for q-values probed by QENS that approach interatomic distances, deviations from Fickian diffusion emerge, particularly in complex environments. These deviations from linear q-dependence of $\gamma(q)$ are captured by so-called *jump-diffusion* models. Among the various formulations, the model widely employed in this thesis is that developed by Teixeira et al.[72]

$$\gamma_{\text{jump}}(q) = \frac{D_{\text{self}} q^2}{1 + D_{\text{self}} q^2 \tau_{\text{res}}} \tag{2.43}$$

Here, diffusion proceeds not continuously but via discrete steps or "jumps," required to overcome energy barriers imposed by structural organization, such as hydrogen bonds network.[73, 74] The parameter τ_{res}, is the *residence time* representing the time-interval between successive jumps (Fig.2.16). In this model, the diffusion coefficient D_{self} is obtained from the slope of the curve at low-q while the residence time is related to the asymptotic behavior of the curve at high-q:

$$\gamma_{\text{jump}}(q) \xrightarrow[q \to 0]{} D_{\text{self}} q^2$$
$$\gamma_{\text{jump}}(q) \xrightarrow[q \to +\infty]{} \frac{1}{\tau_{\text{res}}}$$

Thus, the Teixeira jump-diffusion describes a confined diffusion process at atomic scales (high-q) that transitions to an unhindered process at larger scales (low-q). It is worth mentioning that, in some complex systems like zeolites,[37] an asimptotic value for $\gamma(q)$ can be observed even in low-q region. This q-independent $\gamma(q)$ is characteristic of localized motion, with the onset of the plateau marking the spatial scale at which confinement becomes significant.[75, 76]

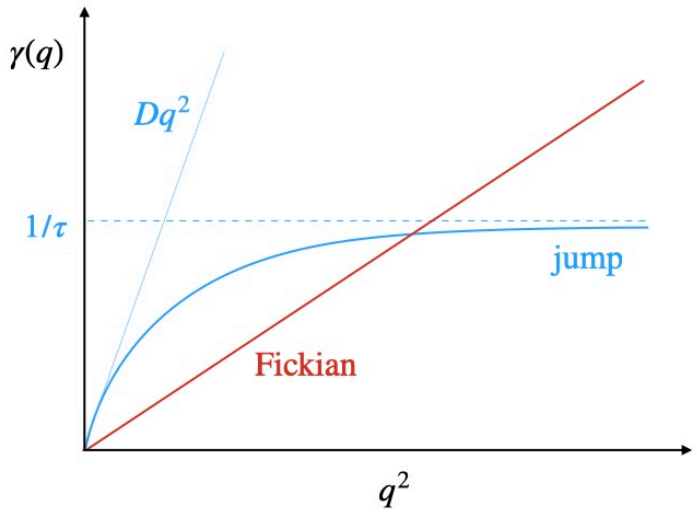

Figure 2.16: Fickian diffusion with linear dependence of HWHM on q^2 (red) and Texeira jump-diffusion (blue) with deviation from linearity at high q. Here the diffusion coefficient D_{self} is taken as the curve's slope at low-q and the curve's asimptote is the reciprocal of the residence time τ_{res}. Adapted with permission from Ref.[36] Copyright 2019, Cambridge University Press.

Coherent QENS

Although the QENS signal inherently carries information about collective dynamics (Eq. 2.14), its analysis is often overlooked in practice, particularly in ToF and NBS. However, coherent contributions can become significant in scenarios where the incoherent component does not strongly dominate, such as when a substantial portion of the sample is composed of deuterated solvents.[32, 43] This interference can affect the incoherent spectrum, with one notable example being the *de Gennes narrowing*.[77] This phenomenon causes the QENS signal to narrow near the peak of the structure factor $S(q)$, which describes the static local arrangement of atoms. De Gennes elucidated this relationship by linking $S(q)$ to the average square of the energy transfer:

$$\overline{(\hbar\omega)^2} \propto \frac{q^2}{S(q)} \tag{2.44}$$

indicating that particles move slower in regions of higher correlation (e.g, for D_2O, this occurs around $q \sim 2\text{Å}^{-1}$, corresponding to the local caging of water molecules at $\sim$3Å).[43] This effect can lead to an underestimation of the peak broadening. The structure factor $S(q)$ is related to the coherent scattering function $S_{\text{coh}}(q,\omega)$ via:

$$S(q) = \int_{-\infty}^{\infty} S_{\text{coh}}(q,\omega)d\omega \tag{2.45}$$

thus, a complete removal of the narrowing effect in the total spectrum requires isolating the coherent contribution (note: this integral is inherently approximate, as the neutron energy exchange is physically bounded and not infinitely available). The limited success of coherent QENS analysis arises from two main challenges: the complexity of separating coherent and incoherent spectra and the lack of robust analytical models due to the many-body nature of the problem.[33] Recent instrumental advancements, such as polarization analysis (PA) implemented on QENS spectrometers like LET, have enabled the acquisition of purely coherent spectra with sub-meV resolution, effectively addressing the first challenge.[50] These developments have promoted a growing

interest in coherent QENS, that can give per sè new insights into liquid collective dynamics[43, 44, 78–80] or can be considered as a non negligible contamination of $S_{\text{inc}}(q,\omega)$ especially for studies of proteins in solution.[45, 81] However, this technological advancement is accompanied by a demand for analytical modeling of coherent QENS. Among the few models available, two key approaches can be identified:

- Vineyard-Skøld model,[82] which consists in expressing the $S_{\text{coh}}(q,\omega)$ as:

$$S_{\text{coh}}(q,\omega) = S_{\text{inc}}\left(\frac{q}{\sqrt{S(q)}},\omega\right)S(q) \tag{2.46}$$

  Heuristically this model assumes that the coherent signal diffusive dynamic is given by a modulation of the incoherent scattering function via the structural correlations given by the structure factor (to be measured in a joint diffraction experiment). The main advantage of this method is the possibility to fit the coherent data with all the models for incoherent QENS described above, as demonstrated by Burankova et al. in their studies on ionic liquids.[78] However, as the authors suggest this interpretation yields a diffusion coefficient which should be collective-like in nature as if it were self-like. In addition, the model's accuracy diminishes for q-values far from the structure factor peak.[79, 83]

- Dynamic Susceptibility-Based Approach: this method, employed by Arbe and Colmenero in their pioneeristic works on collective dynamics at the mesoscale of monoatomic liquid like D_2O[43, 79] and Tetrahydrofuran (THF)[80] consists in converting the $S_{\text{coh}}(q,\omega)$ in form of imaginary part of dynamic susceptibility $\chi''_{\text{coh}}(q,\nu)$ and fitting the model with a sum of Debye-like relaxations:

$$\chi''_{\text{coh}}(q,\nu) = \sum_i A_i(q)\frac{\nu\cdot\nu_i^{\max}(q)}{\nu^2+\nu_i^{\max}(q)^2}. \tag{2.47}$$

  where the relaxation time of the process τ is linked to the peak frequency ν_{max} via $\tau = (2\pi\nu_{max})^{-1}$, and A_i is the amplitude of the function. This

function can be generalized to the Cole-Cole distribution, which accounts for a stretching parameter $\alpha \in [0,1]$:[40–42, 84]

$$\chi''\big(\nu, \nu_{max}, A_0, \alpha\big) = A_0 \frac{\left(\frac{\nu}{\nu_{max}}\right)^{1-\alpha} \cos\frac{\pi\alpha}{2}}{1 + 2\left(\frac{\nu}{\nu_{max}}\right)^{1-\alpha} \sin\frac{\pi\alpha}{2} + \left(\frac{\nu}{\nu_{max}}\right)^{2-2\alpha}} \quad (2.48)$$

Time domain After data reduction, NSE data are in the form of the intermediate scattering function, a correlation function similar to those obtained with techniques like dynamic light scattering or fluorescence correlation spectroscopy. This allows for straightforward fitting of the data by directly visualizing the relaxation times in the time domain, avoiding the complex fitting procedures required by time-of-flight or backscattering methods. The most general function used for fitting is the stretched exponential

$$I(q, t_{\mathrm{F}}) \sim \exp\left[-\left(\frac{t}{\tau}\right)^{\beta}\right] \tag{2.49}$$

which extends the single-exponential decay model by introducing a stretching parameter $\beta \in [0, 1]$ alongside the characteristic relaxation time τ. This expression represents a distribution of multiple relaxation rates that reduces to a single relaxation process for $\beta \sim 1$.

(Note: all the fits above mentioned have been performed using *python 3.5.2* scripts, employing *curve_fit* command from *scipy.optimize*, whilst the plot were made by the *matplotlib* package. The fitting models were stored in a library script and assembled according to the experiment in bespoke scripts.)

2.3 Subcutaneous Injection Site Simulator

The Subcutaneous Injection Site Simulator (SCISSOR) operates as a source-sink system, where a drug formulation initially contained in a deposit chamber (source) flows into a collection chamber (sink) where the concentration over time is measured. The additional features engineered into SCISSOR are specifically designed to replicate, in vitro, the physiological conditions following subcutaneous injection (Fig.2.17).[85–96] Central to SCISSOR's functionality is a specialized cartridge containing an artificial extracellular matrix (ECM) designed to mimic the subcutaneous tissue environment. Hyaluronic acid (HA) forms the primary component of this ECM, chosen for its prevalence in con-

nective, epithelial, and neural tissues, offering superior physiological relevance compared to alternatives like collagen or polyethylene glycol (PEG). This viscous HA-based matrix serves a dual purpose: it provides initial resistance to formulation dynamics, simulating the flow characteristics encountered in vivo, while also enhancing the stability of the formed depot, preventing rapid dispersion.[86] The drug formulation is carefully injected into this cartridge over a period of approximately 20 seconds, ensuring a slow and steady introduction. This ability to inject formulations, rather than having them pre-loaded in a reservoir, is crucial for replicating the physiological stress conditions that can induce aggregation and precipitation of the active pharmaceutical ingredient (API). These phenomena are often associated with suboptimal in vivo release in human subjects, making their accurate simulation in vitro particularly valuable for predicting drug behavior. To reproduce uptake from the injection site, the cartridge features two dialysis membranes on opposite sides, modified with a grid pattern of holes that act as absorption points into blood or lymphatic capillaries. As it has been proved such barrier provides a retention of the HA and regulate the passive transport as a function of molecular

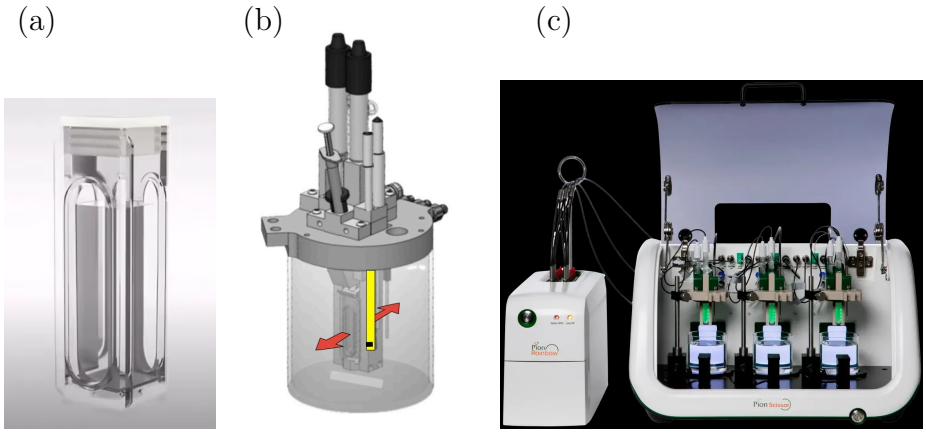

Figure 2.17: SCISSOR layout. (a) Cartridge filled with hyaluronic acid. (b) Cartridge immersed in the buffer chamber, equipped with UV-vis fiber optics (yellow), while red arrows indicate the direction of the drug flow out of the cartridge. Note: the chamber shown has a volume of 300 mL, whereas a 60 mL chamber was used for the measurements. (c) Overview of the multi-chamber setup, enabling parallel measurements and the production of triplicates.

weight.[86] The cartridge is then immersed into the acceptor chamber, typically a beaker containing physiological buffer that mimics the ion composition and pH of the hypodermis, functioning as an "infinite sink" for the released drug. Sink conditions are generally defined as the ability of the dissolution media to dissolve at least three times the amount of drug in the dosage form.[97] The importance of "infinite sink" conditions lies in maintaining a consistent concentration gradient, the primary driving force for drug dissolution and release, thus preventing the dissolution rate from becoming a rate-limiting factor that could mask other release mechanisms. In practice, the volume of the sink medium can vary, typically ranging from 60 to 300 ml, depending on the specific requirements of the study and the properties of the drug being tested. The choice of the buffer, crucial for maintaining physiological conditions, are usually between phosphate and carbonate buffer. Both guarantees the ion composition found in physiological fluids, the maintain the pH at 7.4 and resist to changes, compatible with biological systems. While phosphate buffers are commonly used in drug release studies, carbonate buffers are increasingly preferred due to their greater physiological relevance. Carbonate buffers more closely mimic the bicarbonate buffer system present in human interstitial fluid, which is the primary buffer system in the body. Furthermore, carbonate buffers have shown superior performance in maintaining pH stability over extended periods, making them particularly suitable for long-term drug release studies.[98] The carbonate buffer used in this project primarly consisted of sodium bicarbonate ($NaHCO_3$, 25 mM) as the key buffering agent, supplemented with sodium chloride (NaCl, 110 mM) to maintain physiological osmolarity. Other essential components include calcium chloride dihydrate ($CaCl_2$-$2H_2O$, 1.36 mM), magnesium chloride hexahydrate ($MgCl_2$-$6H_2O$, 0.443 mM), potassium chloride (KCl, 5.36 mM) to mimic the ion composition of interstitial fluid. Sodium azide (NaN_3, 3.08 mM) is included as a preservative. The buffer is prepared by first adding 0.5 M hydrochloric acid to a final concentration of 4.5 mM in Milli-Q water. The salts are then dissolved in this solution, and the volume is adjusted to the final desired amount with additional Milli-Q water. After mixing, the solution is left overnight at room temperature to allow pH

equilibration and the pH is checked and adjusted to 7.40 if necessary (note: the buffer has been prepared by Debra Ashard at AstraZeneca). The advantage of SCISSOR is that it incorporates the two key components (cartridge-chamber) in an all around system that offers precise control over several environmental parameters, crucial for accurately simulating the subcutaneous space. The system maintains a constant temperature of 34°C, while a continuous CO_2 gas flow is employed to maintain pH stability at 7.4. To prevent local saturation and maintain concentration gradients, the buffer is continuously stirred and refreshed using a pump system. This circulation mimics the dynamic nature of interstitial fluid in vivo, ensuring more realistic drug release conditions. The system is equipped with built-in cameras that monitor extracellular matrix changes post-injection and track the evolution of the injected formulation, including gel depot swelling or erosion and aggregation or precipitation of liquid formulations. Additionally, these cameras are utilized to set and monitor the height of the cartridge, which is crucial as it influences hydrostatic pressure within the system, thereby accurately simulating the interstitial pressure found in the hypodermis.[86]

The concentration profile over time is monitored using a UV-vis fiber optic immersed in the buffer, enabling non-invasive, continuous concentration measurement without the need for withdrawing aliquots at fixed intervals. UV-Vis spectroscopy operates on the principle that molecules absorb specific wavelengths of light, causing electrons to transition from their ground state to an excited state.[99, 100] This occurs when a photon with energy matching the difference between two electronic states of a molecule is absorbed. Ultraviolet light spans wavelengths from 100 to 400 nm, while visible light ranges from 400 to 800 nm. The specific wavelengths absorbed depend on the electronic transitions between molecular energy levels. The transitions that occur during absorption can be classified into different types based on the nature of the electronic states involved:

- $\sigma \rightarrow \sigma^*$: promotion of σ electrons (involved in single bond) to the excited state σ^*. This transition usually requires high-energy UV light (shorter wavelengths, generally below 200 nm);

- $n \rightarrow \pi^*$: transition of non-bonding electrons (n) to the excited π^* orbital. This requires less energy (200 - 400 nm);
- $\pi \rightarrow \pi^*$: transition of an electron of bonding π orbital (involved in multiple bonds) to the excited orbital π^*.

This last transition is typically observed in conjugated systems, where the overlap of π orbitals enables electron delocalization across adjacent atoms. This delocalization causes the energy levels to split into multiple closely spaced molecular orbitals, such as π_1, π_2, and their corresponding excited states π_1, π_2. The resulting reduction in the energy gap between bonding and excited states makes the absorption of lower-energy (longer wavelength) light more favorable. This phenomenon is linked to chromophores, specific parts of molecules (aromatic rings, double bonds, carbonyl group etc.) that exhibit strong UV-vis absorption. For instance, in this study Ibuprofen sodium effectively absorbs UV light due to its aromatic structure,[101] while Insulin[102] and Lysozyme[103] due to the presence of aromatic amino acids like tyrosine and tryptophan. The absorbance A(λ) appears as a smooth band rather than a sharp peak because electronic transitions are accompanied by simultaneous changes in rotational and vibrational energy levels. This function can be expressed by the differences between incident I_0 and transmitted light I. According to Beer-Lambert law this quantity is proportional to concentration c of the absorbing substance in solution, path length l in the fibre optic:

$$A(\lambda) = \log\frac{I_0}{I} = l \cdot c \cdot \varepsilon(\lambda) \tag{2.50}$$

where the molar extinction coefficient, $\varepsilon(\lambda)$, is determined by a calibration curve, obtained with the serial addition method. A stock solution of the drug at a known concentration was prepared, and small, measured volumes of this solution were sequentially added to a fixed volume of solvent. After each addition, the UV-vis absorbance response was recorded. The measured absorbance values were then plotted against the corresponding drug concentrations. A linear regression was applied to the resulting data to establish the concentration-response relationship, providing a reliable basis for determining

drug concentrations in subsequent samples.
In this work, the concentration is determined by calculating the area under the curve of the second derivative of the Beer-Lambert Law. The first derivative of the absorption curve yields the slope of $A(\lambda)$ versus λ:

$$\frac{dA(\lambda)}{d\lambda} = l \cdot c \cdot \varepsilon'(\lambda) \tag{2.51}$$

The second derivative, instead, yields the rate of change of the slope

$$\frac{d^2A(\lambda)}{d\lambda^2} = l \cdot c \cdot \varepsilon''(\lambda) \tag{2.52}$$

Baseline scattering from turbidity contributes to only a slow rate of change in the slope, while absorbance from the sample results in faster changes that are captured in the second derivative. This allows for more precise detection of small or closely spaced absorption peaks that are indistinguishable in the raw spectrum, while minimizing the effect of linear scattering baselines.[104–108] However, second derivative spectroscopy significantly reduces the signal-to-noise ratio, decreasing the signal by approximately tenfold and increasing noise by a factor of six. The dissolution data, expressed as the percentage of the released drug, were generated using the AuPro 7 software from Pion. Given the complexity of the system, with multiple release mechanisms and barriers, we opted for a qualitative comparison of the released drug amounts, without fitting the data to a specific model or calculating a diffusion coefficient,[109] to avoid overinterpretation of the results. The major drawback of SCISSOR is its limited ability to replicate in vivo conditions, such as cellular crowding, which significantly impacts the bioavailability of the drug (Fig.2.18).

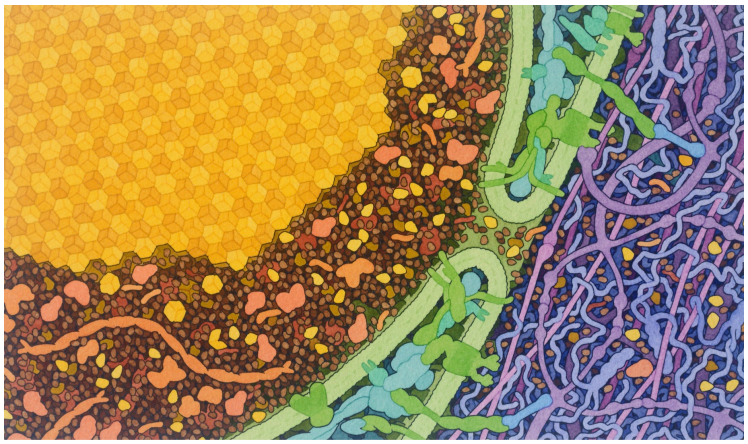

Figure 2.18: The painting highlights the crowding during release: the insulin crystal (yellow), the fused vesicle and cell membranes (green), and the extracellular matrix (browns). Acknowledgment: David S. Goodsell, RCSB Protein Data Bank, and Scripps Research. DOI:10.2210/rcsb$_p$*db*/*goodsell* − *gallery* − 044.

Bibliography

[1] Andrew M Smith, Richard J Williams, Claire Tang, Paolo Coppo, Richard F Collins, Michael L Turner, Alberto Saiani, and Rein V Ulijn. Fmoc-diphenylalanine self assembles to a hydrogel via a novel architecture based on π–π interlocked β-sheets. *Advanced materials*, 20(1):37–41, 2008.

[2] Jaclyn Raeburn, Cristina Mendoza-Cuenca, Beatrice N Cattoz, Marc A Little, Ann E Terry, Andre Zamith Cardoso, Peter C Griffiths, and Dave J Adams. The effect of solvent choice on the gelation and final hydrogel properties of fmoc–diphenylalanine. *Soft Matter*, 11(5):927–935, 2015.

[3] Claire Tang, Andrew M Smith, Richard F Collins, Rein V Ulijn, and Alberto Saiani. Fmoc-diphenylalanine self-assembly mechanism induces apparent p k a shifts. *Langmuir*, 25(16):9447–9453, 2009.

[4] Carlo Diaferia, Elisabetta Rosa, Giancarlo Morelli, and Antonella Accardo. Fmoc-diphenylalanine hydrogels: Optimization of preparation methods and structural insights. *Pharmaceuticals*, 15(9):1048, 2022.

[5] Edgar Fuentes, Kamila Boháčová, Ana M Fuentes-Caparrós, Ralf Schweins, Emily R Draper, Dave J Adams, Silvia Pujals, and Lorenzo Albertazzi. Paint-ing fluorenylmethoxycarbonyl (fmoc)-diphenylalanine hydrogels. *Chemistry–A European Journal*, 26(44):9869–9873, 2020.

[6] Michal Halperin-Sternfeld, Ariel Pokhojaev, Moumita Ghosh, Dana Rachmiel, Raha Kannan, Itzhak Grinberg, Moshe Asher, Moran Aviv,

Peter X Ma, Itzhak Binderman, et al. Immunomodulatory fibrous hyaluronic acid-fmoc-diphenylalanine-based hydrogel induces bone regeneration. *Journal of Clinical Periodontology*, 50(2):200–219, 2023.

[7] Ranjoo Choe and Seok Il Yun. Fmoc-diphenylalanine-based hydrogels as a potential carrier for drug delivery. *e-Polymers*, 20(1):458–468, 2020.

[8] Dave J Adams, Michael F Butler, William J Frith, Mark Kirkland, Leanne Mullen, and Paul Sanderson. A new method for maintaining homogeneity during liquid–hydrogel transitions using low molecular weight hydrogelators. *Soft Matter*, 5(9):1856–1862, 2009.

[9] Assaf Mahler, Meital Reches, Meirav Rechter, Smadar Cohen, and Ehud Gazit. Rigid, self-assembled hydrogel composed of a modified aromatic dipeptide. *Advanced Materials*, 18(11):1365–1370, 2006.

[10] Nikola A Dudukovic and Charles F Zukoski. Mechanical properties of self-assembled fmoc-diphenylalanine molecular gels. *Langmuir*, 30(15):4493–4500, 2014.

[11] Richard J Williams, Andrew M Smith, Richard Collins, Nigel Hodson, Apurba K Das, and Rein V Ulijn. Enzyme-assisted self-assembly under thermodynamic control. *Nature nanotechnology*, 4(1):19–24, 2009.

[12] Emily R Draper and Dave J Adams. Controlling supramolecular gels. *Nature Materials*, 23(1):13–15, 2024.

[13] Mohamed A Elsawy, Jacek K Wychowaniec, Luis A Castillo Diaz, Andrew M Smith, Aline F Miller, and Alberto Saiani. Controlling doxorubicin release from a peptide hydrogel through fine-tuning of drug–peptide fiber interactions. *Biomacromolecules*, 23(6):2624–2634, 2022.

[14] Jacek K Wychowaniec, Andrew M Smith, Cosimo Ligorio, Oleksandr O Mykhaylyk, Aline F Miller, and Alberto Saiani. Role of sheet-edge interactions in β-sheet self-assembling peptide hydrogels. *Biomacromolecules*, 21(6):2285–2297, 2020.

[15] Shuguang Zhang and Michael Altman. Peptide self-assembly in functional polymer science and engineering. *Reactive and Functional Polymers*, 41(1-3):91–102, 1999.

[16] Shuguang Zhang, Davide M Marini, Wonmuk Hwang, and Steve Santoso. Design of nanostructured biological materials through self-assembly of peptides and proteins. *Current opinion in chemical biology*, 6(6):865–871, 2002.

[17] A Saiani, A Mohammed, H Frielinghaus, R Collins, N Hodson, CM Kielty, MJ Sherratt, and AF Miller. Self-assembly and gelation properties of α-helix versus β-sheet forming peptides. *Soft Matter*, 5(1):193–202, 2009.

[18] Mischa Zelzer and Rein V Ulijn. Next-generation peptide nanomaterials: molecular networks, interfaces and supramolecular functionality. *Chemical Society Reviews*, 39(9):3351–3357, 2010.

[19] Jie Gao, Claire Tang, Mohamed A Elsawy, Andrew M Smith, Aline F Miller, and Alberto Saiani. Controlling self-assembling peptide hydrogel properties through network topology. *Biomacromolecules*, 18(3):826–834, 2017.

[20] Jacek K Wychowaniec, Ronak Patel, James Leach, Rachel Mathomes, Vikesh Chhabria, Yogita Patil-Sen, Araida Hidalgo-Bastida, Robert T Forbes, Joseph M Hayes, and Mohamed A Elsawy. Aromatic stacking facilitated self-assembly of ultrashort ionic complementary peptide sequence: β-sheet nanofibers with remarkable gelation and interfacial properties. *Biomacromolecules*, 21(7):2670–2680, 2020.

[21] D Roberts, C Rochas, A Saiani, and AF Miller. Effect of peptide and guest charge on the structural, mechanical and release properties of β-sheet forming peptides. *Langmuir*, 28(46):16196–16206, 2012.

[22] Jieling Li, Ruirui Xing, Shuo Bai, and Xuehai Yan. Recent advances of self-assembling peptide-based hydrogels for biomedical applications. *Soft matter*, 15(8):1704–1715, 2019.

[23] Yuji Yamada, Ananda Chowdhury, Joel P Schneider, and William G Stetler-Stevenson. Macromolecule-network electrostatics controlling delivery of the biotherapeutic cell modulator timp-2. *Biomacromolecules*, 19(4):1285–1293, 2018.

[24] Sotirios Koutsopoulos, Larry D Unsworth, Yusuke Nagai, and Shuguang Zhang. Controlled release of functional proteins through designer self-assembling peptide nanofiber hydrogel scaffold. *Proceedings of the National Academy of Sciences*, 106(12):4623–4628, 2009.

[25] Yusuke Nagai, Larry D Unsworth, Sotirios Koutsopoulos, and Shuguang Zhang. Slow release of molecules in self-assembling peptide nanofiber scaffold. *Journal of controlled release*, 115(1):18–25, 2006.

[26] Gareth O Lloyd, Marc-Oliver M Piepenbrock, Jonathan A Foster, Nigel Clarke, and Jonathan W Steed. Anion tuning of chiral bis (urea) low molecular weight gels. *Soft Matter*, 8(1):204–216, 2012.

[27] Franck S Schoonbeek, Jan H van Esch, Ron Hulst, Richard M Kellogg, and Ben L Feringa. Geminal bis-ureas as gelators for organic solvents: gelation properties and structural studies in solution and in the gel state. *Chemistry–A European Journal*, 6(14):2633–2643, 2000.

[28] Jonathan W Steed. Anion-tuned supramolecular gels: a natural evolution from urea supramolecular chemistry. *Chemical Society Reviews*, 39(10):3686–3699, 2010.

[29] Gordon Leslie Squires. *Introduction to the theory of thermal neutron scattering*. Courier Corporation, 1996.

[30] Marc Bée. *Quasielastic neutron scattering*. Adam Hilger; Bristol (UK), 1988.

[31] Deviderjit Singh Sivia. *Elementary scattering theory: for X-ray and neutron users*. Oxford University Press, 2011.

[32] Mark TF Telling. *A practical guide to quasi-elastic neutron scattering*. Royal Society of Chemistry, 2020.

[33] Andrew T Boothroyd. *Principles of neutron scattering from condensed matter*. Oxford University Press, 2020.

[34] Léon Van Hove. Correlations in space and time and born approximation scattering in systems of interacting particles. *Physical Review*, 95(1):249, 1954.

[35] George H Vineyard. Scattering of slow neutrons by a liquid. *Physical Review*, 110(5):999, 1958.

[36] Marco Grimaldo, Felix Roosen-Runge, Fajun Zhang, Frank Schreiber, and Tilo Seydel. Dynamics of proteins in solution. *Quarterly Reviews of Biophysics*, 52:e7, 2019.

[37] Hervé Jobic and Doros N Theodorou. Quasi-elastic neutron scattering and molecular dynamics simulation as complementary techniques for studying diffusion in zeolites. *Microporous and mesoporous materials*, 102(1-3):21–50, 2007.

[38] Gerald R Kneller. Franck–condon picture of incoherent neutron scattering. *Proceedings of the National Academy of Sciences*, 115(38):9450–9455, 2018.

[39] Louis De Broglie. Waves and quanta. *Nature*, 112(2815):540–540, 1923.

[40] JH Roh, JE Curtis, S Azzam, VN Novikov, I Peral, Z Chowdhuri, RB Gregory, and AP Sokolov. Influence of hydration on the dynamics of lysozyme. *Biophysical journal*, 91(7):2573–2588, 2006.

[41] S Khodadadi, JH Roh, A Kisliuk, E Mamontov, M Tyagi, SA Woodson, RM Briber, and AP Sokolov. Dynamics of biological macromolecules:

not a simple slaving by hydration water. *Biophysical journal*, 98(7):1321–1326, 2010.

[42] Liang Hong, Nikolai Smolin, Benjamin Lindner, Alexei P Sokolov, and Jeremy C Smith. Three classes of motion in the dynamic neutron-scattering susceptibility of a globular protein. *Physical review letters*, 107(14):148102, 2011.

[43] Arantxa Arbe, Gøran J Nilsen, J Ross Stewart, Fernando Alvarez, Victoria García Sakai, and Juan Colmenero. Coherent structural relaxation of water from meso- to intermolecular scales measured using neutron spectroscopy with polarization analysis. *Phys. Rev. Research*, 2(2):022015, 2020.

[44] Riccardo Morbidini, Robert M Edkins, Mark Devonport, Gøran Nilsen, Tilo Seydel, and Katharina Edkins. Molecular structural dynamics in water–ethanol mixtures: Spectroscopy with polarized neutrons simultaneously accessing collective and self-diffusion. *The Journal of Chemical Physics*, 159(22), 2023.

[45] Mona Sarter, J Ross Stewart, Gøran Jan Nilsen, Mark Devonport, and Kirill Nemkovski. Data analysis of dynamics in protein solutions using quasi-elastic neutron scattering important insights from polarized neutrons. *Journal of the American Chemical Society*, 2024.

[46] R Gähler, R Golub, K Habicht, T Keller, and J Felber. Space-time description of neutron spin echo spectrometry. *Physica B: Condensed Matter*, 229(1):1–17, 1996.

[47] J Felber, R Gähler, R Golub, and K Prechtel. Coherence volumes and neutron scattering. *Physica B: Condensed Matter*, 252(1-2):34–43, 1998.

[48] Quentin Berrod, Karine Lagrené, Jacques Ollivier, and Jean-Marc Zanotti. Inelastic and quasi-elastic neutron scattering. application to soft-matter. In *EPJ Web of Conferences*, volume 188, page 05001. EDP Sciences, 2018.

[49] RI Bewley, JW Taylor, and SM Bennington. Let, a cold neutron multi-disk chopper spectrometer at isis. *Nucl. Instrum. Methods A*, 637(1):128–134, 2011.

[50] G J Nilsen, J Košata, M Devonport, P Galsworthy, R I Bewley, D J Voneshen, R Dalgliesh, and J R Stewart. Polarisation analysis on the LET time-of-flight spectrometer. *J. Physics: Conference Series*, 862(1):012019, jun 2017.

[51] J. Košata, G.J. Nilsen, M. Devonport, R.I. Bewley, D.J. Voneshen, P.J. Galsworthy, D. Raspino, and J.R. Stewart. Polarized primary spectrometer on the let instrument at isis. *Physica B: Condensed Matter*, 551:476–479, 2018. The 11th International Conference on Neutron Scattering (ICNS 2017).

[52] G Cassella, J R Stewart, G M Paternò, V García Sakai, M Devonport, P J Galsworthy, R I Bewley, D J Voneshen, D Raspino, and G J Nilsen. Polarization analysis on the let cold neutron spectrometer using a 3he spin-filter: First results. *J. Physics: Conference Series*, 1316(1):012007, oct 2019.

[53] Kirill Nemkovski, Robert Bewley, Victoria García Sakai, Gøran Jan Nilsen, Adrien Perrichon, and Ian Silverwood. Sherpa: A spectrometer with high energy resolution and polarisation analysis. In *EPJ Web of Conferences*, volume 272, page 02004. EDP Sciences, 2022.

[54] Bernhard Frick, Eugene Mamontov, Lambert van Eijck, and Tilo Seydel. Recent backscattering instrument developments at the ill and sns. *Zeitschrift für physikalische Chemie*, 224(1-2):33–60, 2010.

[55] CJ Carlile and Mark A Adams. The design of the iris inelastic neutron spectrometer and improvements to its analysers. *Physica B: Condensed Matter*, 182(4):431–440, 1992.

[56] SI Campbell, MTF Telling, and CJ Carlile. The optimisation of analyser geometry in near-backscattering spectrometers–iris on the isis-pulsed source. *Physica B: Condensed Matter*, 276:206–207, 2000.

[57] MTF Telling, SI Campbell, DD Abbley, DA Cragg, JJP Balchin, and CJ Carlile. Performance of the new pyrolytic graphite analyser bank on the near-backscattering spectrometer iris on the isis pulsed source. *Applied Physics A*, 74:s61–s63, 2002.

[58] Markus Appel, Bernhard Frick, and Andreas Magerl. A flexible high speed pulse chopper system for an inverted neutron time-of-flight option on backscattering spectrometers. *Scientific Reports*, 8(1):13580, 2018.

[59] Markus Appel, Bernhard Frick, and Andreas Magerl. First results with the neutron backscattering and tof spectrometer option bats on in16b. *Physica B: Condensed Matter*, 562:6–8, 2019.

[60] Ferenc Mezei. Neutron spin echo: A new concept in polarized thermal neutron techniques. *Zeitschrift für Physik A Hadrons and nuclei*, 255:146–160, 1972.

[61] Ferenc Mezei. The principles of neutron spin echo. In *Neutron Spin Echo: Proceedings of a Laue-Langevin Institut Workshop Grenoble, October 15–16, 1979*, pages 1–26. Springer, 2005.

[62] Dieter Richter, Michael Monkenbusch, Arantxa Arbe, and Juan Colmenero. Neutron spin echo in polymer systems. *Neutron Spin Echo in Polymer Systems: -/-*, pages 1–221, 2005.

[63] Jason S Gardner, Georg Ehlers, Antonio Faraone, and Victoria García Sakai. High-resolution neutron spectroscopy using backscattering and neutron spin-echo spectrometers in soft and hard condensed matter. *Nature Reviews Physics*, 2(2):103–116, 2020.

[64] Marcus Hennig. *Dynamics of Globular Proteins in Crowded Electrolyte Solutions. Studied by Neutron Scattering*. PhD thesis, Universität Tübingen, 2011.

[65] T Kanaya, N Takahashi, K Nishida, H Seto, M Nagao, and Y Takeba. Dynamic and static fluctuations in polymer gels studied by neutron spin-echo. *Physica B: Condensed Matter*, 385:676–681, 2006.

[66] B Farago, P Falus, I Hoffmann, M Gradzielski, F Thomas, and C Gomez. The in15 upgrade. *Neutron News*, 26(3):15–17, 2015.

[67] Owen Arnold, Jean-Christophe Bilheux, JM Borreguero, Alex Buts, Stuart I Campbell, L Chapon, Mathieu Doucet, N Draper, R Ferraz Leal, MA Gigg, et al. Mantid—data analysis and visualization package for neutron scattering and μ sr experiments. *Nuclear instruments and methods in physics research section a: accelerators, spectrometers, detectors and associated equipment*, 764:156–166, 2014.

[68] Marco Grimaldo, Felix Roosen-Runge, Niina Jalarvo, Michaela Zamponi, Fabio Zanini, Marcus Hennig, Fajun Zhang, Frank Schreiber, and Tilo Seydel. High-resolution neutron spectroscopy on protein solution samples. In *EPJ Web of Conferences*, volume 83, page 02005. EDP Sciences, 2015.

[69] Christian Beck, Kevin Pounot, Ilaria Mosca, Niina H Jalarvo, Felix Roosen-Runge, Frank Schreiber, and Tilo Seydel. Notes on fitting and analysis frameworks for qens spectra of (soft) colloid suspensions. In *EPJ Web of Conferences*, volume 272, page 01004. EDP Sciences, 2022.

[70] Ilaria Mosca, Kévin Pounot, Christian Beck, Louise Colin, Olga Matsarskaia, Christoph Grapentin, Tilo Seydel, and Frank Schreiber. Biophysical determinants for the viscosity of concentrated monoclonal antibody solutions. *Molecular Pharmaceutics*, 20(9):4698–4713, 2023.

[71] Robert M Edkins, Markus Appel, Tilo Seydel, and Katharina Edkins. The modifying effect of supramolecular gel fibres on the diffusion of

paracetamol and ibuprofen sodium on the picosecond timescale. *Physical Chemistry Chemical Physics*, 22(19):10838–10844, 2020.

[72] José Teixeira, M-C Bellissent-Funel, Sow-Hsin Chen, and Albert-José Dianoux. Experimental determination of the nature of diffusive motions of water molecules at low temperatures. *Physical Review A*, 31(3):1913, 1985.

[73] Johan Qvist, Helmut Schober, and Bertil Halle. Structural dynamics of supercooled water from quasielastic neutron scattering and molecular simulations. *The Journal of Chemical Physics*, 134(14), 2011.

[74] Tilo Seydel, Robert M Edkins, and Katharina Edkins. Picosecond self-diffusion in ethanol-water mixtures. *Phys. Chem. Chem. Phys.*, 21(18):9547–9552, 2019.

[75] F Volino and AJ Dianoux. Neutron incoherent scattering law for diffusion in a potential of spherical symmetry: general formalism and application to diffusion inside a sphere. *Molecular Physics*, 41(2):271–279, 1980.

[76] Alexander J O'Malley, M Sarwar, J Armstrong, Charles Richard A Catlow, IP Silverwood, APE York, and I Hitchcock. Comparing ammonia diffusion in nh 3-scr zeolite catalysts: a quasielastic neutron scattering and molecular dynamics simulation study. *Physical Chemistry Chemical Physics*, 20(17):11976–11986, 2018.

[77] P.G. De Gennes. Liquid dynamics and inelastic scattering of neutrons. *Physica*, 25(7):825–839, 1959.

[78] Tatsiana Burankova, Rolf Hempelmann, Andrew Wildes, and Jan P. Embs. Collective ion diffusion and localized single particle dynamics in pyridinium-based ionic liquids. *J. Phys. Chem. B*, 118(49):14452–14460, 2014.

[79] Fernando Alvarez, Arantxa Arbe, and Juan Colmenero. Understanding the coherent dynamic structure factor of liquid water measured by neutron spectroscopy with polarization analysis: a molecular dynamics simulations study. In *EPJ Web of Conf.*, volume 272, page 01011. EDP Sciences, 2022.

[80] Arantxa Arbe, Gøran J Nilsen, Mark Devonport, Bela Farago, Fernando Alvarez, José A Martínez González, and Juan Colmenero. Collective dynamics and self-motions in the van der waals liquid tetrahydrofuran from meso-to inter-molecular scales disentangled by neutron spectroscopy with polarization analysis. *J. Chem. Phys.*, 158(18), 2023.

[81] Agathe Nidriche, Martine Moulin, Philippe Oger, J Ross Stewart, Lucile Mangin-Thro, Wolfgang Schmidt, Gerald Kneller, and Judith Peters. Impact of isotopic exchange on hydrated protein dynamics revealed by polarized neutron scattering. *PRX Life*, 2(1):013005, 2024.

[82] Kurt Sköld. Small energy transfer scattering of cold neutrons from liquid argon. *Phys. Rev. Lett.*, 19(18):1023, 1967.

[83] VN Novikov, Kenneth S Schweizer, and Alexei P Sokolov. Coherent neutron scattering and collective dynamics on mesoscale. *J. Chem. Phys.*, 138(16):164508, 2013.

[84] Kenneth S Cole and Robert H Cole. Dispersion and absorption in dielectrics ii. direct current characteristics. *J. Chem. Phys.*, 10(2):98–105, 1942.

[85] Hanne M Kinnunen and Randall J Mrsny. Improving the outcomes of biopharmaceutical delivery via the subcutaneous route by understanding the chemical, physical and physiological properties of the subcutaneous injection site. *Journal of Controlled Release*, 182:22–32, 2014.

[86] Hanne M Kinnunen, Vikas Sharma, Luis Rodrigo Contreras-Rojas, Yafei Yu, Chlöe Alleman, Alavattam Sreedhara, Stefan Fischer, Leslie Khawli,

Stefan T Yohe, Daniela Bumbaca, et al. A novel in vitro method to model the fate of subcutaneously administered biopharmaceuticals and associated formulation components. *Journal of Controlled Release*, 214:94–102, 2015.

[87] Hanne Kinnunen Bown, Catherine Bonn, Stefan Yohe, Daniela Bumbaca Yadav, Thomas W Patapoff, Ann Daugherty, and Randall J Mrsny. In vitro model for predicting bioavailability of subcutaneously injected monoclonal antibodies. *Journal of Controlled Release*, 273:13–20, 2018.

[88] Michael R Turner and Sathy V Balu-Iyer. Challenges and opportunities for the subcutaneous delivery of therapeutic proteins. *Journal of pharmaceutical sciences*, 107(5):1247–1260, 2018.

[89] Joana AD Sequeira, Ana C Santos, João Serra, Catarina Estevens, Raquel Seiça, Francisco Veiga, and António J Ribeiro. Subcutaneous delivery of biotherapeutics: challenges at the injection site. *Expert Opinion on Drug Delivery*, 16(2):143–151, 2019.

[90] Manuel Sánchez-Félix, Matt Burke, Hunter H Chen, Claire Patterson, and Sachin Mittal. Predicting bioavailability of monoclonal antibodies after subcutaneous administration: open innovation challenge. *Advanced drug delivery reviews*, 167:66–77, 2020.

[91] Sharadvi Thati, Meagan McCallum, Yan Xu, Michelle Zheng, Zhi Chen, Jeff Dai, Duohai Pan, Dilusha Dalpathado, and Neil Mathias. Novel applications of an in vitro injection model system to study bioperformance: case studies with different drug modalities. *Journal of Pharmaceutical Innovation*, 15:268–280, 2020.

[92] Hao Lou, Cory Berkland, and Michael J Hageman. Simulating particle movement inside subcutaneous injection site simulator (scissor) using monte-carlo method. *International Journal of Pharmaceutics*, 605:120824, 2021.

[93] Hao Lou and Michael J Hageman. Development of an in vitro system to emulate an in vivo subcutaneous environment: small molecule drug assessment. *Molecular pharmaceutics*, 19(11):4017–4025, 2022.

[94] Christian Bender, Sabine Eichling, Lutz Franzen, Viktoria Herzog, Ludger M Ickenstein, Dhananjay Jere, Lara Nonis, Gregoire Schwach, Philipp Stoll, Marta Venczel, et al. Evaluation of in vitro tools to predict the in vivo absorption of biopharmaceuticals following subcutaneous administration. *Journal of Pharmaceutical Sciences*, 111(9):2514–2524, 2022.

[95] David Li, Poh Yee Chow, Tzu Ping Lin, Celine Cheow, Zhuoxuan Li, and Matthias G Wacker. Simulate subq: the methods and the media. *Journal of Pharmaceutical Sciences*, 112(6):1492–1508, 2023.

[96] Xavier JH Pepin, Iain Grant, and J Matthew Wood. Subq-sim: A subcutaneous physiologically based biopharmaceutics model. part 1: The injection and system parameters. *Pharmaceutical Research*, 40(9):2195–2214, 2023.

[97] Aristides Dokoumetzidis and Panos Macheras. A century of dissolution research: from noyes and whitney to the biopharmaceutics classification system. *International journal of pharmaceutics*, 321(1-2):1–11, 2006.

[98] Jennifer J Sheng, Daniel P McNamara, and Gordon L Amidon. Toward an in vivo dissolution methodology: a comparison of phosphate and bicarbonate buffers. *Molecular pharmaceutics*, 6(1):29–39, 2009.

[99] Heinz-Helmut Perkampus. *UV-VIS Spectroscopy and its Applications*. Springer Science & Business Media, 2013.

[100] Liudmil Antonov and Daniela Nedeltcheva. Resolution of overlapping uv–vis absorption bands and quantitative analysis. *Chemical Society Reviews*, 29(3):217–227, 2000.

[101] J Choina, H Kosslick, Ch Fischer, G-U Flechsig, L Frunza, and A Schulz. Photocatalytic decomposition of pharmaceutical ibuprofen pollutions in water over titania catalyst. *Applied Catalysis B: Environmental*, 129:589–598, 2013.

[102] Francesca Bugamelli, Maria Augusta Raggi, Isabella Orienti, and Vittorio Zecchi. Controlled insulin release from chitosan microparticles. *Archiv der Pharmazie: An International Journal Pharmaceutical and Medicinal Chemistry*, 331(4):133–138, 1998.

[103] Krishnamoorthy Shanmugaraj, Shanmugam Anandakumar, and Malaichamy Ilanchelian. Probing the binding interaction of thionine with lysozyme: A spectroscopic and molecular docking investigation. *Dyes and Pigments*, 112:210–219, 2015.

[104] Liudmil Antonov and Stefan Stoyanov. Approach for increased information from the second-derivative spectra in uv-vis absorption spectroscopy. *Applied spectroscopy*, 47(10):1712–1715, 1993.

[105] Lei Wang and Mandana Asgharnejad. Second-derivative uv spectrometric determination of simvastatin in its tablet dosage form. *Journal of pharmaceutical and biomedical analysis*, 21(6):1243–1248, 2000.

[106] Chinmay M Jogdeo, Deep S Bhattacharya, Vicky Lin, Parag Kolhe, and Advait Badkar. Assessing physicochemical stability of monoclonal antibodies in a simulated subcutaneous environment. *Journal of Pharmaceutical Sciences*, 2024.

[107] L Rieppo, S Saarakkala, T Närhi, HJ Helminen, JS Jurvelin, and J Rieppo. Application of second derivative spectroscopy for increasing molecular specificity of fourier transform infrared spectroscopic imaging of articular cartilage. *Osteoarthritis and cartilage*, 20(5):451–459, 2012.

[108] Weining Xu, Huibin Yu, Fang Yang, Feng Yang, Dongping Liu, Koutian Lu, Hongjie Gao, and Yonghui Song. Second derivative uv–visible spec-

troscopy characterizing structural components of dissolved and particulate organic matter in an urbanized river. *Environmental Sciences Europe*, 34(1):29, 2022.

[109] Aneta Ostróżka-Cieślik, Sławomir Wilczyński, and Barbara Dolińska. Hydrogel formulations for topical insulin application: Preparation, characterization and in vitro permeation across the strat-m® membrane. *Polymers*, 15(17):3639, 2023.

Blank page

Chapter 3

Comparing Microscopic and Macroscopic Diffusion in Drug Delivery: a Study of Small Drug and Protein Dynamics in a Supramolecular Peptide Hydrogel

Author contribution: The QENS data collected prior to the start of this project include IRIS data provided by Dr. Robert M. Edkins[c] and Prof. Katharina Edkins[f,*], and BATS data on ibuprofen sodium provided by Dr. Javier Carrascosa[a]. Dr. Orsolya Czakkel,[a] and Dr. Tilo Seydel[a], as instrument scientists at IN15 and BATS respectively, supported during beamtimes and data analysis. Dr. Belal I. Hanafy,[d] and Dr. Dhaval R. Kalaria[e] supported the SCISSOR experiments at AstraZeneca. Riccardo Morbidini[a,b] wrote the BATS and IN15 proposals, prepared the gel samples, performed the QENS and SCISSOR experiments and analyzed all the data sets. The project was conceived and supervised by Dr.Dhaval R. Kalaria, Dr. Tilo Seydel and Prof. Katharina Edkins.

[a] Institut Max von Laue - Paul Langevin, 71 Avenue des Martyrs, F-38042 Grenoble, France

[b] Division of Pharmacy and Optometry, University of Manchester, Oxford Road, Manchester M13 9PT, United Kingdom

[c] Department of Pure and Applied Chemistry, University of Strathclyde, 295 Cathedral Street, Glasgow G1 1XL, United Kingdom

[d] Advanced Drug Delivery, Pharmaceutical Sciences, BioPharmaceuticals R&D, AstraZeneca, Cambridge, United Kingdom

[e] Early Product Development and Manufacture, Pharmaceutical Sciences, Macclesfield SK10 2NA, United Kingdom

[f] Strathclyde Institute of Pharmacy and Biomedical Sciences, University of Strathclyde, 161 Cathedral Street, Glasgow G4 0RE, United Kingdom

Abstract

Over recent decades, medicine development has increasingly turned to biologics for their higher efficacy and reduced side effects compared to small molecule drugs. However, the necessity for parenteral administration of these labile compounds poses significant challenges, requiring frequent injections and highlighting the need for sustained release systems to improve patient adherence. Drug delivery vehicles are currently regarded as acting as a diffusion barrier and, particularly supramolecular gels, offer a promising solution due to their tunable properties and biocompatibility. This study focuses on diffusion within a peptide supramolecular hydrogel based on the ultra-short Fmoc–diphenylalanine (FmocFF) moiety, exploring its potential as a drug delivery carrier. By examining dynamics at different timescales, we aim to decouple steric and non-steric effects of the fibre network on solute diffusion. Using Quasi-Elastic Neutron Scattering (QENS), we investigate solvent dynamics, gelator network structure, and the picosecond self-diffusion behavior of various drugs to focus solely on hydrodynamic interactions. In vitro release studies will measure bulk diffusion over 12 hours using the Subcutaneous Injection Site Simulator (SCISSOR), mimicking possible interactions occuring during drug release. Our results demonstrate that from molecular-level to bulk diffusion, hydrodynamic interactions are mitigated and masked by factors such as steric confinement and surface erosion. This work highlights the necessity of bridging short-time to long-time scale bulk diffusion mechanism to tune drug release and ultimately design better drug delivery vehicles.

3.1 Introduction

Over the last decades, the pharmaceutical field has seen an increase in the use of biologics as therapeutic agents, which are generally more effective in treating disease states compared to small molecule drugs and often result in fewer side effects.[1–3] The route of administration for compounds such as proteins or monoclonal antibodies poses a significant challenge. The oral route, which is the best option for patient adherence, is not viable for biologics and biosimilars due to the harsh environment of the stomach and digestive enzymes, which would degrade these compounds before they can be absorbed and exert their therapeutic effect; they currently have to be injected.[4, 5] Parenteral administration, whether intravenous, intramuscular, or subcutaneous, often leads to rapid drug absorption from the injection site. This rapid absorption can result in high peak plasma concentrations ($C_{\max}$), which may cause adverse effects due to the sudden drug's high concentration in the bloodstream.[6] While this rapid onset can be advantageous in many clinical situations, it may also present challenges. For drugs requiring sustained therapeutic levels, the rapid absorption and high $C_{\max}$ may necessitate frequent injections, often on a daily basis, to maintain the desired effect and avoid potential toxicity associated with peak concentrations. This need for frequent administration can, however, negatively impact patient compliance, particularly in cases requiring long-term treatment or self-administration, thereby reducing the overall effectiveness of the therapy.[7] This issues creates a need for sustained drug release systems to reduce injection frequency, improve patient adherence and reduce healthcare costs. One promising approach is the development of gel-based vehicles, due to their enhanced viscosity compared to liquid formulations.[8–11] These materials consist of a large liquid fraction retained by a solid network traditionally based on covalent bonds between polymeric fibres.[12] Recently, there has been growing interest in supramolecular gels, where the fibre entanglement is formed through non-covalent bonds by very small concentration (< 1 wt.%) of low molecular weight gelators (LMWG) that self-assemble upon physical changes in e.g. temperature, pH, or ion concentration.[13] Compared to polymeric gels,

supramolecular gels are more reversible and can be finely tuned through subtle modifications to the initial monomers, such as altering their electrostatic interactions, hydrophobic properties, or other physicochemical characteristics.[14, 15] In this regard, it has been shown that modifying a neutral, phenylalanine (F) based peptide LMWG (FEFKFEFK) by incorporating at both ends charged residues such as lysine (K) (KFEFKFEFKK) can significantly promote greater retention of an anticancer drug.[16] Such tunability, combined with the biocompatible nature of LMWGs and their aqueous solvents, makes these gels highly promising for drug delivery applications.[17] Currently, drug release from gel matrices is often interpreted in terms of the relative size between the drug r_{drug} and the mesh r_{mesh}. For $r_{\text{drug}} \leq r_{\text{mesh}}$ the drug undergoes diffusion-controlled release, while if $r_{\text{drug}} > r_{\text{mesh}}$ the drug can be trapped within the matrix, leading to more complex release mechanisms such as surface erosion or swelling.[11] These studies are typically based on experimental data collected over several hours, which measures the drug's flow from a gel reservoir to a receptor buffer driven by concentration gradient.[18] This approach can be influenced by multiple factors such as pH, temperature, buffer composition and its agitation. Moreover, in equilibrium systems without concentration gradients, drug diffusion is affected by steric confinement (collisions with fibres slowing down the physical random diffusion pathway) and hydrodynamic interactions (resulting from fibre surface chemistry). These complexities make it challenging to develop analytical models for drug release, which are often more descriptive than predictive.[19–21] To address these challenges, we propose to decouple these effects by studying diffusion at the molecular level, focusing primarily on hydrodynamic interactions. While techniques such as Pulse Field Gradient NMR (PFG-NMR) and Fluorescence Correlation Spectroscopy (FCS) have been used to study diffusion in gels, they typically probe molecular displacements, occurring over ms, on the order of hundreds of nm to μm. At these scales, the measured diffusion is significantly influenced by the gel's mesh structure and steric confinement effects. In contrast, our approach aims to examine diffusion at shorter time and length scales, before the diffusing molecules encounter the physical constraints of the gel network.[22–24] Molecu-

lar dynamics (MD) simulations can help quantify hydrodynamic interactions by obtaining individual trajectories, but they require experimental validation to refine force fields.[25] Quasi-Elastic Neutron Scattering (QENS) simultaneously accesses spatial and time correlations associated with diffusive dynamics on the molecular level, focusing on hydrodynamic interactions and minimizing steric confinement effects.[24, 26–28] This method has been employed to resolve subtle differences in drug diffusion in a prototypical bis-urea supramolecular gel, revealing slightly faster diffusion in gels compared to pure solutions for small drugs like ibuprofen sodium and paracetamol.[29] This finding suggests that diffusion at the molecular level is governed by more nuanced parameters than mesh size, which must be understood to design better materials tailored to specific drug release kinetics.

In this study, we report a comprehensive investigation of FmocFF hydrogel as a potential drug delivery carrier.[30–33] The approach involves examining the solvent dynamics, the structure of the gelator network, and the picosecond self-diffusion behaviour of a diverse range of drugs using QENS. The set of drugs includes ibuprofen sodium as an example of a small drug, and two model proteins, insulin and lysozyme. Additionally, in vitro experiments using the Subcutaneous Injection Site Simulator elucidate the drug release kinetics from the gel matrix over 12 hours.[34] This analysis aims to delineate the mechanisms influencing drug diffusion across different time scales and to determine if short-time diffusion probed by QENS correlates with long-term release profiles.

3.2 Material and Methods

3.2.1 Sample preparation

FmocFF (98% purity) was purchased from Bachem. Sodium deuteroxide solution (40 wt.% in D_2O, 99.5 atom% D), glucono-δ-lactone (GdL), ibuprofen sodium (IBU), lysozyme from chicken egg white (LYS), and recombinant human insulin (INS) (both as lyophilized powders) were obtained from Sigma

Aldrich. All chemicals were used without further purification. The FmocFF hydrogel formation was triggered by a pH change, achieved through a carefully controlled process.[30] Initially, 5 mg of FmocFF gelator (0.5 wt.%) was dissolved in 1 ml aqueous NaOH solution at pH around 10.4; this high pH needed for the deprotonation of the C-terminal carboxylic acid of FmocFF, was achieved with one mole equivalent of NaOH (0.1M). Once the FmocFF was added, the solution has been through cycles of vortexing and sonication to ensure complete dissolution of the solid gelator. Following dissolution, 6.4 mg of GdL was introduced to the solution. GdL was chosen for its ability to gradually lower the pH over an 18-hour period, unlike faster-acting acids such as HCl. This gradual pH reduction not only minimizes solvent mixing effects but also guarantees a more uniform gel formation, thereby enhancing reproducibility.[35] After the addition of GdL, the drug compounds dissolved in H_2O were introduced to the solution to achieve a final concentration of 5 wt.% for ibuprofen sodium and 2.4 wt.% for insulin and lysozyme. The lower concentration for the two proteins is due to a balance between ensuring a

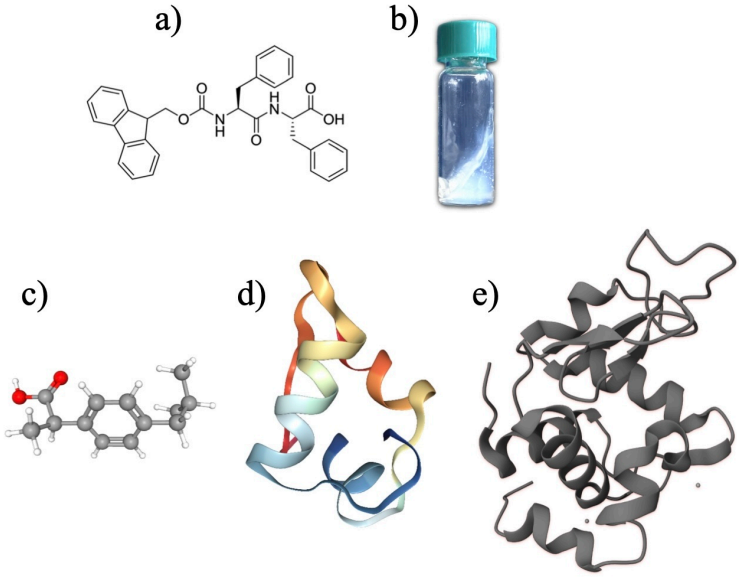

Figure 3.1: (a) Molecular structure of FmocFF; (b) vial inversion test of the FmocFF 0.5 wt.% gel in water after setting for 18 hours; (c) molecular structure of ibuprofen; tertiary structure of (d) insulin and (e) lysozyme.

sufficient signal for QENS measurement and maintaining gel stability. Subsequently, while still in solution, the sample was transferred to a double-walled cylindrical aluminium can for neutron experiments, and into the syringe for SCISSOR experiment. To confirm successful gel formation, a control aliquot was subjected to the vial inversion test (Fig.3.1b). The use of deuterated solvent (D_2O and NaOD) was necessary for QENS experiments to emphasize the signal from the drug against the background. For comprehensive data analysis, each drug was measured both in gel and pure solution, along with pure deuterated backgrounds (unloaded gel and solution), all prepared following the same procedure also without the gelator to guarantee an accurate comparison.

3.2.2 Quasi-elastic neutron scattering (QENS)

Time-of-Flight and Backscattering spectroscopy

QENS probes diffusive random motions such as translations and rotations involving energy exchanges between neutrons and sample typically below 2 meV.[36] The main observable in QENS is the dynamic structure factor $S(q, \omega)$, a function of momentum $\hbar q$ and energy $\hbar\omega$ transfer that carries information about the time-dependent ensemble-average particle positions. This function appears as a spectral line broadening around the zero energy exchange $\hbar\omega = 0$ peak, and it can be modelled with a Lorentzian function:

$$\mathcal{L}_\gamma(q) = \frac{\gamma(q)}{\pi} \frac{1}{\gamma(q)^2 + \omega^2} \tag{3.1}$$

where the $\gamma(q)$ is the q-dependent linewidth (half-width at half-maximum, HWHM) and relates to the self-diffusion coefficient via $\gamma(q) \propto D_{\text{self}} q^2$. However, QENS in a drug-loaded gel system can arise from a superposition of the contribution from the drug, the solvent and the network. Different energy resolutions and energy ranges covered by QENS spectrometers enable discrimination between the distinct sources of scattering across various energies $\hbar\omega$. In fact, the energy resolution sets the slowest motion that can be probed by the instrument while the energy window yields the fastest accessible dynamics

via the relation $t \propto (2\pi\hbar\omega)^{-1}$. The momentum transfer, on the other hand, provides the length scales accessible via $L = 2\pi/q$, thus making it possible to decouple the solvent and gelator dynamics by probing relatively larger and smaller q, respectively.

Solvent dynamics in the FmocFF gel has been measured with the Time-of-Flight indirect geometry spectrometer IRIS at the ISIS facility, Rutherford Appleton Laboratory (Didcot, UK). The instrument operates with an energy resolution of 17.5 μeV FWHM, covering a range of -300 μeV $\leq \hbar\omega \leq$ +1200 μeV and 0.3 Å^{-1} $\leq q \leq$ 1.8 Å^{-1}. These parameters correspond to displacements on timescales of 0.5-30 ps and lengths of 3.5-21 Å. The main contribution to the QENS spectrum arises from the incoherent cross section of mobile ^{1}H, with the hydrogen atoms in the gel network contributing only to the elastic line.

Drug diffusion in the FmocFF gel was measured at the hybrid Backscattering and Time-of-Flight (BATS) option on the IN16b spectrometer at the Institut Laue-Langevin (ILL, Grenoble, France). This instrument accesses the same length scale as IRIS but with a much narrower energy range (-150 μeV $\leq \hbar\omega \leq$ +150 μeV) and a smaller energy resolution (3.5 μeV) FWHM thus enabling study of dynamics on the order of 1-200 ps. At this dynamic scale, the diffusion of the center of mass of small drugs is observed, along with the combined translational and rotational diffusion of proteins, while the solvent and the gelator network move too quickly and too slowly, respectively, to be examined. Additionally, by using a fully deuterated solvent, the drug signal is enhanced from the solvent background exploiting the different incoherent scattering cross sections of ^{1}H and ^{2}H isotopes. In both experiments, samples were placed inside double-walled cylindrical aluminum cans with a 0.3 mm gap. These were sealed using indium wire and then inserted into a standard cryo-furnace to ensure temperature control during the 4.5 h long data acquisition. The data were firstly reduced using standard routines in Mantid,[37] and subsequently analysed with *python* scripts.

For data analysis, the models for the $S(q,\omega)$ have to be convoluted with the energy resolution $\mathcal{R}$. This operation is implemented by measuring the scat-

tering of the vanadium and analytically represented by fitting with a sum of Gaussian functions, one in the case of BATS and multiple in the case of IRIS (Fig. S1). The analysis of solvent diffusion in FmocFF gel, measured on IRIS, consisted of a sum of two Lorentzian functions $\mathcal{L}_{\gamma}(q)$ convoluted with the fit of vanadium sample. The first, narrow q-dependent Lorentzian represents solvent molecule translations, while the second, included for the broad energy range of IRIS, accounts for faster processes such as rotations:

$$\begin{aligned} S_{\mathrm{H_2O}}(q,\omega) = \quad & a(q)\mathcal{L}_{\gamma_{\mathrm{trans}}}(q) + b(q)\mathcal{L}_{\gamma_{\mathrm{rot}}}(q) \\ & + c(q)\delta_1(\omega) \end{aligned} \tag{3.2}$$

For BATS data, an additional scattering contribution from the empty cryofurnace was fitted with a polynomial and subtracted from the spectra to avoid the noise from direct subtraction and error propagation. The modeling of the drug diffusion in the FmocFF gel followed a two-step procedure: first the deuterated solvent background was described with only one Lorentzian, due to the narrow energy range of BATS, a Dirac function $\delta(\omega)$ representing the elastic contribution of the gel network and the empty Al can, and a sloped apparent background $\alpha\omega + \beta$ accounting for faster motions:

$$S_{\mathrm{D_2O}}(q,\omega) = a(q)\mathcal{L}_{\gamma_{\mathrm{solvent}}}(q) + b(q)\delta_1(\omega) + \alpha\omega + \beta \tag{3.3}$$

Subsequently, the free fit parameters $a(q)$, $\gamma_{\mathrm{solvent}}$, $b(q)$, α and β obtained through a q-independent analysis, were fixed and passed to the fit of the drug loads:

$$\begin{aligned} S_{\mathrm{drug}}(q,\omega) = \quad & \left[c(q)\mathcal{L}_{\gamma_{\mathrm{glob}}}(q) + (1-c(q))\,\mathcal{L}_{\gamma_{\mathrm{int}}}(q)\right] \\ & + d(q)\delta_2(\omega) + (1-\varphi)\cdot S_{\mathrm{D_2O}}(q,\omega) \end{aligned} \tag{3.4}$$

Here two additional Lorentzian functions account for the global centre-of-mass diffusion $\mathcal{L}_{\gamma_{\mathrm{glob}}}(q)$ and the faster localized motions $\mathcal{L}_{\gamma_{\mathrm{int}}}(q)$, an additional Dirac function accounting for the elastic scattering of immobile drug molecules and a calculated scaling factor φ to account for the volume fraction occupied by

the drug:[38]

$$\varphi = \frac{\theta m_{\text{drug}}}{V_{\text{solv}} + \theta m_{\text{drug}}} \tag{3.5}$$

where θ is the drug specific volume ($\theta_{\text{INS/LYS}} = 0.74$ ml/g and $\theta_{\text{IBU}} = 0.97$ ml/g), m is the mass of the drug dissolved ($m_{\text{proteins}} = 24$ mg and $m_{\text{IBU}} = 50$ mg), for a $V_{\text{solvent}} = 1$ ml leads to a $\varphi \sim 1.7\%$ for the proteins and $\varphi \sim 4.6\%$ for ibuprofen sodium. Finally, to determine quantitatively the diffusion coefficient D from line broadening, a model is imposed on q^2. In the case of a continuous free diffusion the dependence is linear, with the diffusion coefficient D being the slope

$$\gamma(q) = Dq^2 \tag{3.6}$$

For more complex systems, this relation can be generalized to a jump-diffusion mechanism:[39]

$$\gamma(q) = \frac{Dq^2}{1 + \tau Dq^2} \tag{3.7}$$

At the small q limit, the above equation reduces to eq.3.6 while at higher q values, corresponding to the first coordination shell, the linewidth $\gamma(q)$ tends to an asymptotic value $1/\tau$. The term τ, known as *residence time* characterizes a hindered diffusion process at the molecular level. According to this model instead of continuous movement, molecules undergo a series of discrete jumps with static waiting periods.

The above diffusion coefficient should be more correctly named "apparent" since it has a dependence on rotations and translations $D = D(q, D_t, D_r)$. This relation can be made explicit with a concept from colloid physics for short-time self diffusion,[40–42] by solving the equation:

$$\sum_{l=0}^{\infty} B_l(q) \frac{D_r l(l+1) + (D_t - D)q^2}{[D_r l(l+1) + (D_t + D)q^2]^2} = 0 \tag{3.8}$$

where D_t and D_r are the translational and rotational diffusion, respectively, while

$$B_l(q) = (2l+1) \int \rho_H(r) j_l^2(qr) dr \tag{3.9}$$

contains the lth-order spherical Bessel function of first kind and $\rho_H(r)$ the hydrogen density at radius r.

Neutron Spin-Echo

Neutron Spin-Echo (NSE) measurements were carried out on the IN15 spectrometer at ILL to study the geleator network dynamics. Here, the observable is the normalized intermediate scattering function $I(q,t)/I(q,0)$, related to $S(q,\omega)$ via Fourier transform in the time domain. This function represents an autocorrelation, similar to dynamic light scattering (DLS) or FCS, decaying from 1 at zero lag time to 0 at longer times. IN15 can probe time scales of 0.5 - 500 ns with a q range of 0.025 $\text{Å}^{-1} \leq q \leq 0.088$ Å^{-1}, corresponding to the length scale of 70-250 Å. Multiple diffusive phenomena can be modeled by analyzing the number of slopes in the decay, corresponding to multiple Lorentzians in the energy domain. The sample of the gel set in deuterated solvent was placed in a 2 ml quartz cuvette and measured for 12 h to maximize the signal to noise ratio. The data have been fitted with a single exponential decay with only two free parameters,

$$\frac{I(q,t)}{I(q,0)} = A(q) \cdot \exp\left(-\Gamma(q) \cdot t\right) \tag{3.10}$$

the amplitude $A(q)$ and the q-dependent relaxation rate $\Gamma(q)$.

3.2.3 Subcutaneous Injection Site Simulator (SCISSOR)

The drug release measurements have been performed on a Pion N3 Subcutaneous Injection Site Simulator (SCISSOR), a device engineered to emulate, in vitro, the drug release kinetics observed in vivo following subcutaneous injection.[34, 43–48] Fundamentally, the apparatus operates on a source/sink principle, i.e. measuring the concentration driven mass flow from a central cartridge (source) to an external buffer (sink). The cartridge contained hyaluronic acid (HA) - based extracellular matrix (ECM), while a 60 ml beaker was filled with carbonate-based buffer to reproduce the physiological conditions emulat-

ing the ion composition and pH of the hypodermis (pH$\sim$ 7.4) and emulate the sink conditions of the body. A volume of 0.5 mL of the drug formulation was slowly injected (over approximately 20 s) into the cartridge with a 1 ml hypodermic syringe with a 16 mm 23 G needle. The injection is followed by an equilibration time $t < 1$ h to let the whole system stabilize to subcutaneous temperature T = 34 °C and pH 7.4. The temperature of the system is kept constant at 34 °C and the pH between cartridge and buffer is kept constant by a continuous CO_2 gas flow and controlled with calibrated pH electrodes. To avoid artifacts in mass transfer due to saturation of the concentration in the buffer, the system continuously stirs and refreshes the buffer using a pump system. Extracellular matrix changes post-injection were monitored using the built-in cameras. Each formulation was measured in triplicates.
The concentration profile over time is recorded using a UV-vis fibre optic immersed in the buffer, allowing for concentration determination without the need to withdraw aliquots at specific time intervals. After obtaining a calibration curve for the specific drug (Fig. S10), the system operates fully automated, inferring on the concentration by calculating the area under the curve of the second derivative of the Beer-Lambert Law;[49–51]

$$\frac{d^2A(\lambda)}{d\lambda^2} = l \cdot c \cdot \epsilon''(\lambda) \tag{3.11}$$

where $A(\lambda)$ is the absorption at wavelength lambda, l is the sample thickness, c is the concentration and $\epsilon''(\lambda)$ is the second derivative of the molar extinction coefficient ϵ. The second derivative allows for more precise identification of small and closely situated absorption peaks, which are not distinguishable in the original spectrum, and eliminates linear baselines from scattering (Fig. S11). The dissolution data, expressed as the percentage of the released drug, are then plotted using the integrated software AuPro 7 from Pion.

3.3 Results and Discussion

3.3.1 Water diffusion in FmocFF gel

We started with modelling the pure solvent to compare to the bis-urea gel[24] and to generate a baseline for solute diffusion. The model eq.3.2 correctly describes the QENS data for H_2O:NaOH + GdL diffusion in FmocFF gel that requires an additional broad Lorentzian function (Fig. S2) due to a long asymmetric tail in the energy gain axis.[52] The result shows that the FmocFF fibre network does not affect pure solvent dynamics, consistent with earlier results on a different gel system.[53] As shown in Fig. S3, $\gamma(q)$ for H_2O in bulk solvent and in FmocFF gel superimpose over the entire q range and for all probed temperatures (275 K, 285 K, 295 K, 305 K). As expected for hydrogen bonded liquids the linewidth trend deviates from linearity and was therefore modeled with jump diffusion in q^2 according to eq.5.2. Values for the diffusion coefficient D obtained from the fit are identical as their differences are within one standard deviation (σ, Table 4.1). This result, along with others on hydrogen-bonded and organic solvent dynamics in supramolecular gels,[24, 27] does not allow generalization of the solvent behavior. In these prior studies, toluene diffusion was unaffected,[27] while water diffusion was slowed in a supramolecular gel based on an α-D-mannopyranoside derivative,[27] while another study showed an increased diffusion for water-ethanol mixture in the presence of a bis-urea gel.[24] In the latter, the main hypothesis for the faster diffusion of water/ethanol mixture is that the hydrophobicity of the fibres disrupts the hydrogen bond network of the solvent, thus locally reducing the viscosity. Our results in the FmocFF gel reflect its unique structure, distinct from the bis-urea gel. At pH 3.6-3.9, the FmocFF gel forms a network of entangled nanocylindrical fibres (3 nm diameter) arranged in anti-parallel β-sheets with π-stacked fluorenyl groups.[30] This arrangement likely influences solvent-gel interactions more significantly than gelator concentration alone would do. The gel's translucence for visible light, even at 0.5 wt.% FmocFF, indicates that the fibres or aggregates are significantly smaller than visible light wavelengths,[54, 55] suggesting

Table 3.1: Fit results for diffusion coefficients (D) and residence times (τ) for bulk solution and FmocFF gel, measured on IRIS and fitted using a jump diffusion model (Eq. 5.2).

sample	T [K]	D [10^{-9}m^2/s]	τ [ps]
solution	275	1.50 ± 0.03	2.4 ± 0.2
FmocFF gel		1.54 ± 0.03	2.7 ± 0.1
solution	285	1.94 ± 0.03	1.6 ± 0.2
FmocFF gel		1.98 ± 0.04	1.8 ± 0.2
solution	295	2.46 ± 0.06	1.2 ± 0.2
FmocFF gel		2.55 ± 0.04	1.5 ± 0.2
solution	305	3.01 ± 0.10	0.9 ± 0.1
FmocFF gel		3.13 ± 0.10	1.2 ± 0.2

a high surface area exposed to the liquid. This structural characteristic may promote specific interaction sites between solvent and gel network, in contrast to the bis-urea system, where an increase in gelator concentration from 0.3 wt.% to 0.5 wt.% leads to larger crystalline areas, reducing the available fiber surface area and diminishing the effects of hydrophobic moieties on solvent diffusion.[24] Notably, the solvent phase within the pores of the gel network is not substantially different from its gel-free counterpart, despite the macroscopic differences in bulk viscosity between the FmocFF gel and the pure solution. This finding suggests a baseline for drug diffusion studies, indicating that any observed drug diffusion is not driven by fast solvent dynamics. Instead, other factors, such as interactions with the gel matrix or the drug's own properties, must be considered.

3.3.2 Picosecond drug diffusion in FmocFF gel

We used QENS to investigate the hydrodynamic effect of the gel fibre surface on diffusion of three model drugs: ibuprofen sodium, insulin and lysozyme. Ibuprofen sodium allows comparison with previous studies on a different gel system,[29] while insulin and lysozyme, differing in size and complexity, enable examination of molecular dimension effects on diffusion.

Firstly, the QENS spectra of ibuprofen sodium, summed over q have been inspected, allowing comparison of the spectra at maximum statistics, but at the expense of information carried by momentum transfer. As a result, only a qualitative comparison between drug diffusion in solution and gel can be made showing a slightly wider signal for the solution sample. To quantitatively assess this difference, a fit based on eq.3.4 was imposed using one Lorentzian function,

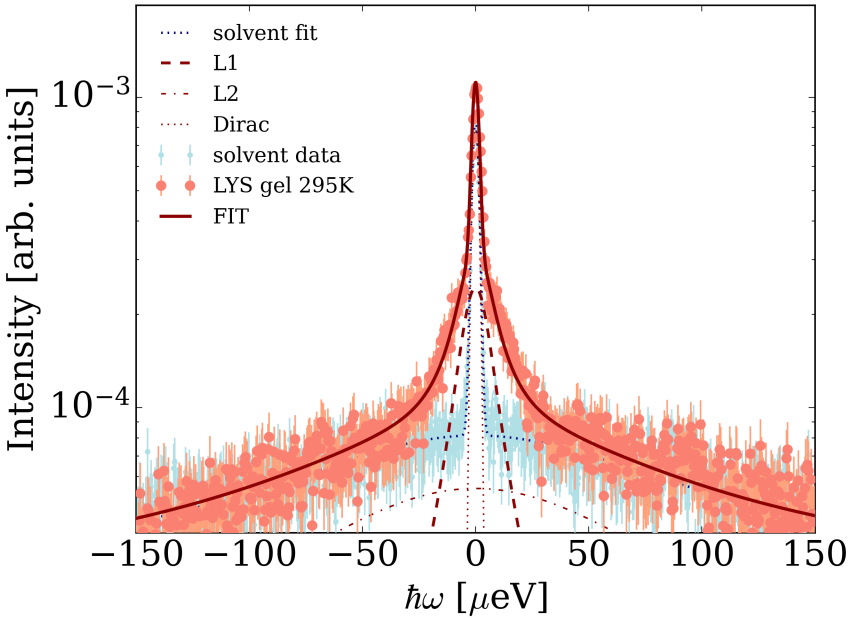

Figure 3.2: Example BATS spectrum of 2.5 wt.% lysozyme (full circle symbols) in FmocFF gel (0.5 wt.%) (light point symbols), at $T = 295\,\mathrm{K}$ and $q = 1.3\,\mathrm{Å}^{-1}$, and corresponding pure deuterated solvent. Full line represents the fit of eq.3.4 consisting of the combined solvent and container contribution (dotted lines), global protein diffusion (narrow thick dashed line) and internal protein diffusion (dash-dotted line) convoluted with the spectrometer resolution.

in addition to that of the solvent, to describe the drug dynamics (Fig. S4). A jump diffusion model was applied to the linewidth $\gamma_{\text{drug}}(q)$ attributed to the drug molecule diffusion (Fig.3.3 and Fig. S5) as previously done for ibuprofen diffusion in a different supramolecular gel.[29] The result indicates that diffusion of ibuprofen sodium is substantially slower in FmocFF gel compared to the pure solution, as indicated by the model-free approach. This finding contrasts with previous observations in a bis-urea gel where ibuprofen sodium was found to diffuse ∼10% faster than in the pure solution;[29] in FmocFF gel, instead, it diffuses ∼40% slower, highlighting that the drug diffusion is highly system-specific. This observation could be attributed to an enhanced drug-gelator interaction especially considering the higher FmocFF gel concentration (0.5 wt.%) compared to the bis-urea gel (0.3 wt.%), the different surface chemistry and the different viscosity of the solvent. However, this hypothesis cannot be fully explained by QENS alone, as it provides the ensemble representation over what occurs within the gel, averaging diffusion of different drug populations such as molecules in the bulk, in close proximity to the fibre and those attached to the fibre. The trend of slower drug diffusion in FmocFF gel compared to pure solution persists when increasing the solute size from small molecules to proteins. In this case, modeling the $S(q, \omega)$ requires an additional component to account for fast dynamic processes associated with internal fluctuations of the protein's backbone and side chains, which contribute to the signal. Thus, for proteins the final fit of eq.3.4 comprises a contribution arising from the solvent plus a sum of two Lorentzian functions: a narrow one whose q-dependence encodes the global diffusion coefficient, and a second broader one accounting for faster relaxations from the internal dynamics (dash-dotted line in Fig.3.2, Fig. S6 (insulin) and Fig. S7 (lysozyme)). This internal diffusion is usually found to be approximated by jump diffusion[39, 56] but is beyond the scope of the current work on BATS. The q-dependence of the $\gamma(q)$ in Fig.3.3(b-c) proves that the dynamics is not localized and it is a diffusion process. This follows a Fickian diffusion (eq.3.6) different from the jump diffusion found for ibuprofen sodium (Fig. S8). This finding is expected for centre-of-mass diffusion of large diffusing solutes like proteins that are not hindered by the surrounding

hydrogen bond network, in contrast to small molecules that experience more hindrance from this network, resulting in a diffusion process characterized by

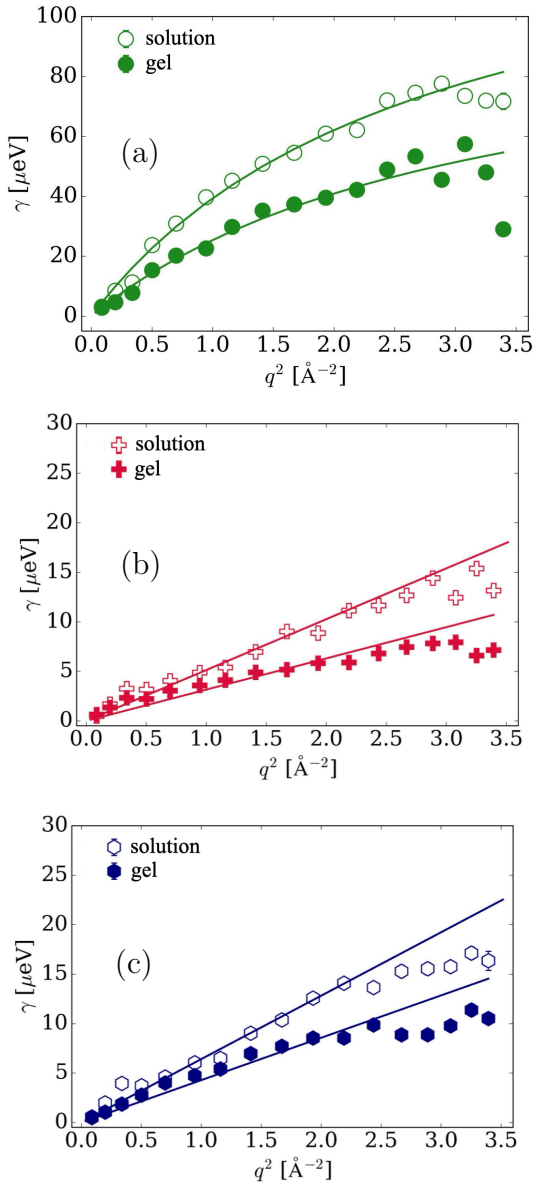

Figure 3.3: Summary of the fitted narrow Lorentzian linewidths $\gamma_{\text{glob}}(q)$ corresponding to the apparent centre of mass diffusion at $T = 295K$ of (a) ibuprofen sodium fitted with a jump-diffusion (eq.5.2); (b) insulin and (c) lysozyme fitted with Fickian model (eq.3.6).

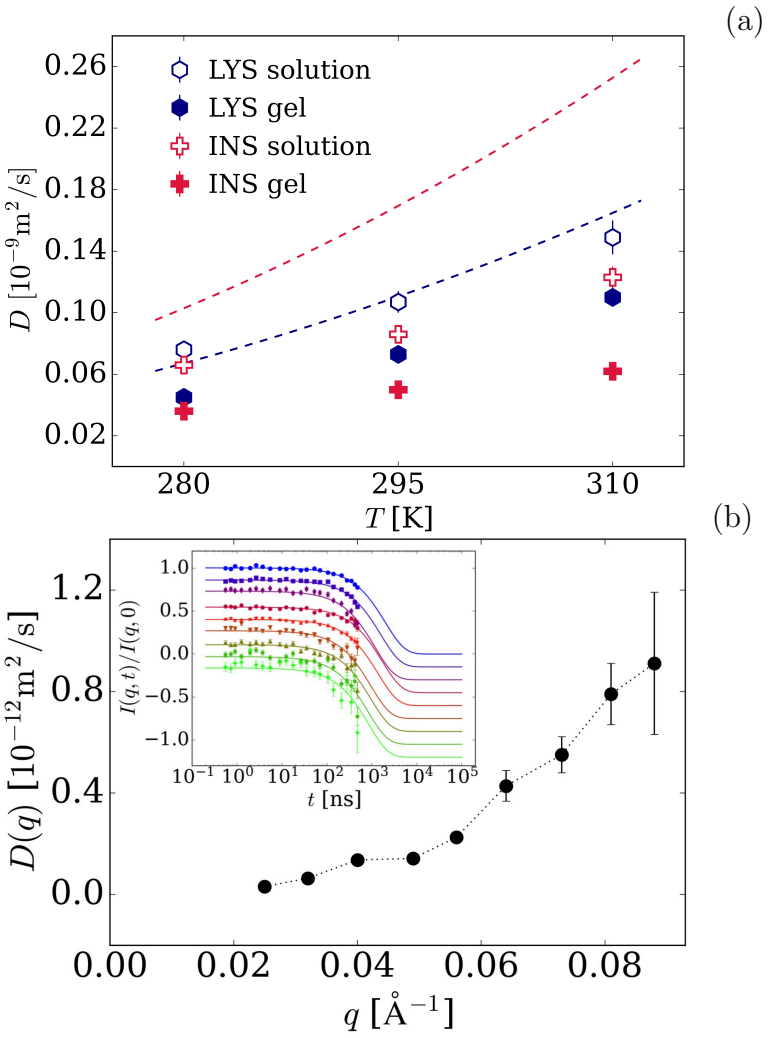

Figure 3.4: (a) Apparent diffusion coefficient (i.e., translation and rotation combined) of 25 mg/ml insulin and lysozyme in 0.5 wt.% FmocFF gel (full symbols) and in pure solution (empty symbols), respectively. Dashed lines: Predicted apparent diffusion, assuming Stokes-Einstein diffusion of spheres and the literature hydrodynamic radius for monomeric insulin and lysozyme, accounting for the temperature dependent viscosity $\eta(T)$ of D_2O.[57] (b) Collective diffusion function $D(q) = 1/\Gamma(q)$ plotted as a function of q for FmocFF gel network. Inset: normalized intermediate scattering function $I(\mathrm{q}, t)/I(\mathrm{q}, 0)$ of FmocFF gel in recorded on IN15 at $T = 290\,\mathrm{K}$ (curves are offset in y-axis for visibility). Solid curves are the result of fit with Eq.3.10 (Fig. S9).

jumps between sites.[29, 52] Fig.3.4a compares the short-time diffusion coefficients of insulin and lysozyme in solvent and gel environments, highlighting differences in aggregation behavior and interactions with the FmocFF matrix. The short-time self-diffusion measurements of the drugs in pure solvent show that insulin diffuses more slowly than lysozyme, even though it has a smaller hydrodynamic radius (Fig.3.4a). According to the Stokes–Einstein relation:

$$D_{\mathrm{t}} = \frac{k_B T}{6\pi\eta(T) R_{\mathrm{h}}} \tag{3.12}$$

where $\eta(T)$ is the temperature-dependent viscosity and R_{h} is the hydrodynamic radius (insulin: 1.5 nm,[58] lysozyme: 2 nm[59–61]), a smaller protein should diffuse faster. However, the measured diffusion coefficient for insulin is significantly lower than that predicted by eq.3.12 for a monomeric sphere (dashed lines in Fig.3.4a). This discrepancy clearly indicates that insulin forms larger aggregates in solution. This finding aligns with a reported TEM observation of insulin aggregation at pH 3 into spherical agglomerates of 100-500 nm already at a concentration of 0.125 mg/ml.[62] The higher concentration of the present study together with the pH change which gradually crosses the isoelectric point of insulin (pH $\sim$ 5.8) may promote such aggregation.

Lysozyme on the other hand does not show any aggregation in solution with values for the diffusion coefficient D only slightly above the monomer region, with a more pronounced effect at lower T (Fig.3.4a). This small excess can be explained by the higher complexity of the dynamics associated to proteins with respect to small molecules.[56]

On the ps/ns timescale, protein translations couple with rotations, while resolving small drug rotations requires higher q. Therefore, the protein diffusion coefficient extracted from QENS spectra should be more accurately be named "apparent" to account for the combination of translational D_t and rotational D_r diffusion coefficients $D = D(q, D_t, D_r)$. Hence, the small excess for the lysozyme expected translational diffusion coefficients can be attributed to the contribution of rotational diffusion. The impact of the latter can be quantified with the formalism of eq.3.8 by using the program HYDROPRO,[60]

and that has been accounted for in the calculation of the dashed lines in figure 3.4a. Neutron backscattering spectroscopy provides access to short-time self-diffusion, offering an unambiguous measure of lysozyme's hydrodynamic size in solution. After accounting for rotational contributions, the translational diffusion coefficient (D_t) of lysozyme aligns to the monomer region Fig.3.4a. These findings complement and extend previous Neutron Spin Echo studies at similar concentrations,[63, 64] reinforcing the argument for the absence of significant lysozyme aggregation at these low concentrations.

When loaded in the FmocFF gel, both insulin and lysozyme exhibit slowed short-time diffusion. Assuming insulin is in cluster form, the slowdown follows a size-dependent rule: lysozyme is on average 30% slower in the gel compared to the solvent, while insulin is on average 40% slower. This difference can be explained by the drug size approaching the mesh size of the gel or by enhanced protein aggregation within the gel.[54] It is also important to stress that the proteins stay in solution and they do not precipitate since the diffusion coefficients do not drop to zero but follow a Stokes-Einstein temperature dependence. If the size effect can explain the different sieving effects of the gel for insulin and lysozyme, the comparison between ibuprofen sodium ($r_h \sim 0.7$ nm)[65] and lysozyme ($r_h \sim 2$ nm) presents a more complex scenario. One possible explanation is that ibuprofen sodium has a higher tendency to interact with the fibres compared to lysozyme. The strong interaction of ibuprofen sodium with the fibres has been supported by evidence showing its affinity to bind to the N-terminal residues and fibril edges of A$\beta_{1\text{-}40}$ and A$\beta_{1\text{-}42}$ amyloid polypeptides.[66] Given that diphenylalanine (FF) is one of the crucial aggregative motifs in Alzheimer's β-amyloid polypeptides,[67] its affinity for ibuprofen sodium could explain the significant slowing down of this drug in the FmocFF gel.

3.3.3 FmocFF fibre network dynamics

Both the previous[29] and the current QENS studies on drug diffusion in gels have relied on the assumption that the gel scaffold contributes only to the

elastic response, essentially behaving as a solid. However, at the temporal and spatial resolution probed by QENS, the network and fibres within the gel may influence drug dynamics beyond a merely static hindrance. In fact, as it has been recently indicated, tracer molecules in polymer matrices may adhere to the fibres and follow their dynamics.[68] This effect is particularly relevant in supramolecular gels, where non-covalent bonds make the structure potentially more flexible than polymer gels with covalent bonds. Furthermore, such effect might be even more relevant when moving from small molecular drugs to larger solutes like proteins, whose dynamics is significantly slower. To unambiguously determine whether gelator dynamics contributes to drug diffusion we performed NSE on unloaded FmocFF gel. The q range probed by IN15 covers the same probed by Small Angle Neutron Scattering (0.25-0.88 nm^{-1} corresponding to lengths of 7-25 nm via $l = 2\pi/q$), which can be used to probe both primary fibres and some features of the network, without introducing artifacts due to drying or freezing the sample, as would be necessary for electron microscopy.[69–71] The normalized intermediate scattering function $I(q,t)$ shows the beginning of a decay above 100 ns over the observed q range (Fig. S9). This behavior suggests the presence of relatively rigid fibres whose dynamics are nearly frozen on the timescale probed by the NSE spectrometer. To quantitatively assess the relaxation time of the process, the scattering signal is fitted with a single exponential decay (Fig.3.4b (inset) and Fig. S9). The fit based on two free parameters reproduces the trend of the experimental data. The pre-factor $A(q)$ is approximately ~ 1 while the relaxation rate $\Gamma(q)$ in eq.3.10 can be associated with a characteristic q-dependent diffusion coefficient, denoted collective diffusion function $D(q) = \Gamma(q)q^2$ (Fig.3.4b). At the length scale where we probe drug diffusion, the hydrogel fibres' movement is negligible, being three orders of magnitude slower than drug movement. Consequently, fibre dynamics do not significantly influence our observations of drug behavior. We speculate that the low values of D at low q might be associated with de Gennes narrowing approaching the gel mesh size.[72] Hence, the hypothesis of an elastic contribution arising from the fibres holds true over the investigated q range and on the ps/ns time scale probed with QENS.[73]

3.3.4 In vitro drug release

We conducted SCISSOR experiments to provide a macroscopic counterpart to the short-time diffusion studied with QENS and to understand drug behavior over longer time scales relevant to practical drug release applications. However, before interpreting SCISSOR data it is crucial to understand the sequence of events leading to the final release profiles. The injection process exposes the formulation to multiple stresses, including shear forces, localized heating, and pressure changes as it passes through the needle. This step is then followed by the interaction of the formulation with ECM, which increases viscosity and reduces the release rate.[43] Subsequently, the formulation diffuses within the cartridge and through the cartridge membrane to the buffer driven by concentration gradient. A qualitative analysis of injection into the cartridge reveals significant differences among the formulation of the three drugs, even in their pure solution formulations (Fig.3.5). A notable effect observed is the decrease in injection chamber clarity, attributed to a pH drop following the addition of formulations at pH between 3.6 and 3.9 (Fig. S12). The two studied proteins exhibit different behaviors post-injection due to their distinct isoelectric points (pI). Lysozyme (pI 10.7) shows no visible precipitation, whereas insulin (pI 5.4) undergoes significant aggregation as the pH crosses its pI, before recovering as pH re-equilibrates to 7.4, a previously observed phenomenon.[34, 74] A decrease in the injection cartridge clarity is also observed for ibuprofen sodium, even though the formulation remains above its pK_a of 4.9, keeping the drug in the ionized form and thus limiting its precipitation. Hence, the decrease in clarity can be attributed to the higher concentration of the drug compared to proteins or specific drug-HA interactions. We started from the pure solution formulations to have a reference for the respective gel. The release curves correlate with injection chamber images, with lysozyme rapidly released into the buffer (with 30% released within the first 30 minutes) while ibuprofen sodium takes about 4 hours to achieve the same released amount (Fig.3.5). The study primarily focuses on the first 12 hours, as it has been observed that after this period the degradation and leakage of HA may affect the measurements.[46] The

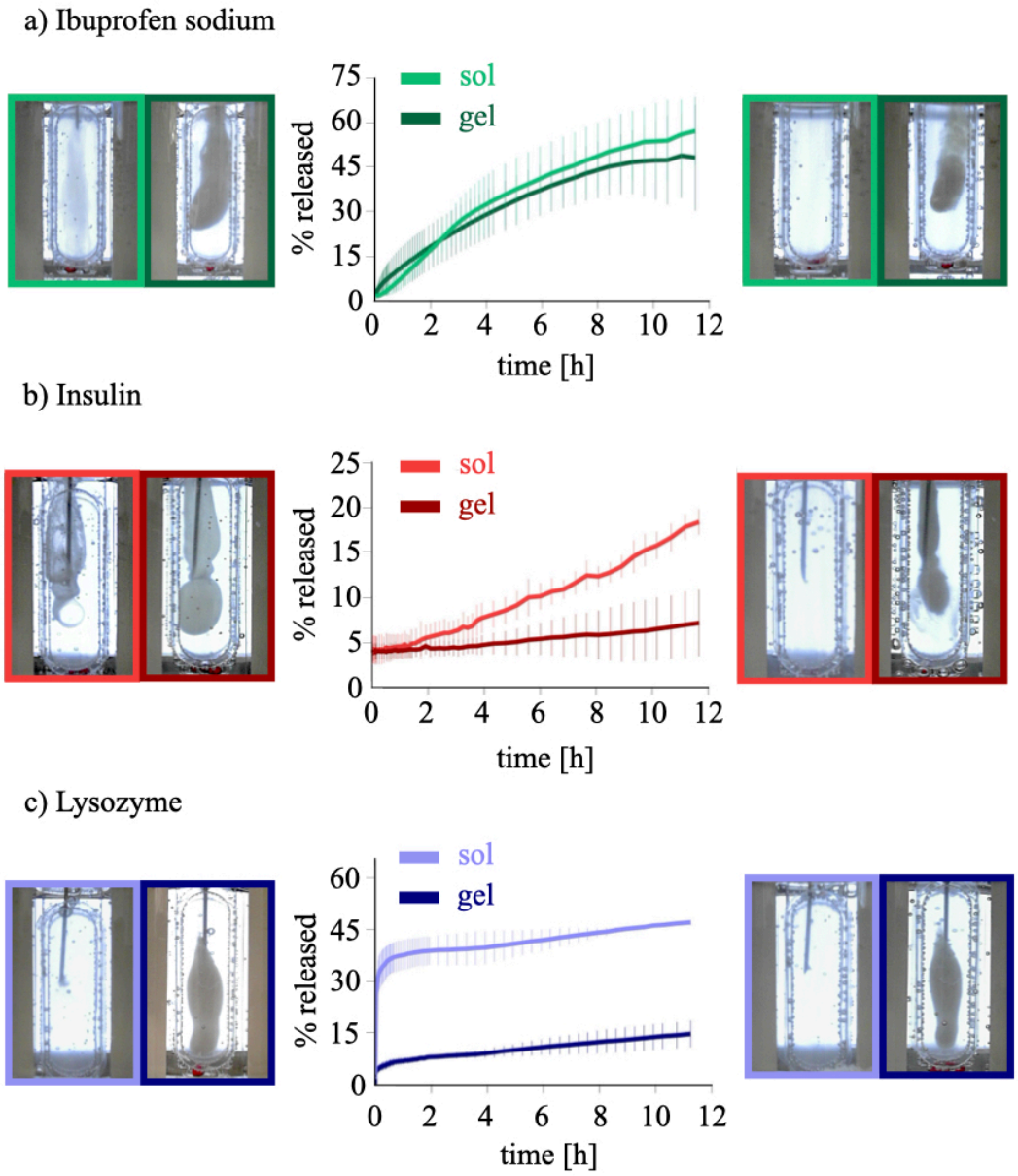

Figure 3.5: Release curves obtained from SCISSOR experiment for (a) ibuprofen sodium, (b) insulin and (c) lysozyme. The data represent mean ± standard deviation from 3 repetitions (except for the lysozyme in gel which is here reported in 2 repetition for clarity. The third repetition is reported in Fig. S13). Images of the inner cartridge at the injection (left column) and after 24 h (right column) for both solution and gel formulation.

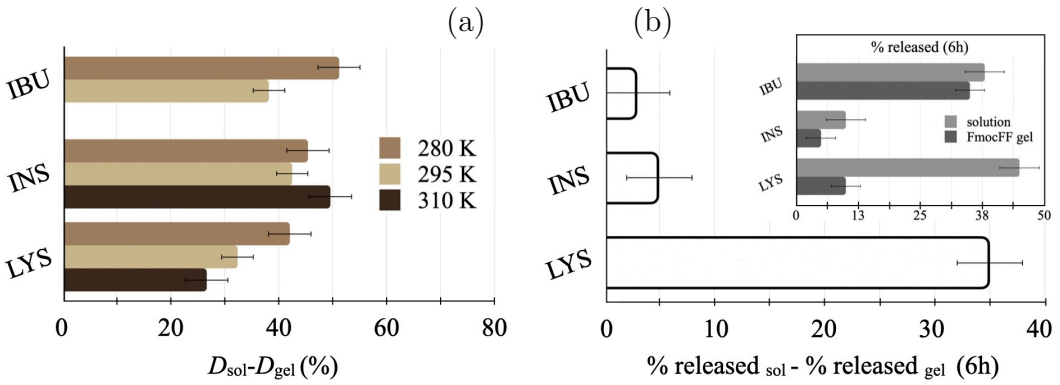

Figure 3.6: (a) Percentage difference $(D_{sol} - D_{gel}) \cdot 100/D_{sol}$ of ibuprofen sodium, insulin and lysozyme diffusion coefficients between solution and FmocFF gel. (b) Difference of drug released from solution and FmocFF gel at T = 34 °C after 6 h on SCISSOR. Inset: cumulative amount of drug released after 6 h from pure solution and FmocFF gel.

three drugs exhibit distinct release kinetics, with ibuprofen sodium showing a steady release rate and lysozyme having a biphasic release process (rapid <1 h followed by slower release). This diversity between ibuprofen sodium and lysozyme correlates with visible loss of clarity observed for the small drug in the injection compartment. In contrast, insulin shows significant retention in the cartridge, with only 10% gradually released after 6 hours, likely due to a lag time as a result of dissolution of the precipitated formulation as the pH returns to 7.4.[34]

Taking advantage of FmocFF gel's thixotropic properties,[31, 75] we set the gels directly in syringes, where they could be injected as a temporary sol under stress, before reforming into a gel at the injection site. The gel depot formed in the injection cartridge introduces an additional barrier to the release compared to liquid formulations. Upon immersion in HA, a pH gradient establishes between the hydrogel and its surrounding, leading to an ion diffusion to equilibrate the system pH.[76] During this process, the gel depot undergoes structural modifications, like surface erosion, as shown in Fig.3.5. The two-step release process (FmocFF gel to HA, then HA to buffer) affects the three drugs differently (Fig.3.5). Ibuprofen sodium shows no significant difference between gel

and liquid formulations: this aligns with the hypothesis that small drugs with a hydrodynamic radius smaller than the mesh size of the gel are released from a gel via a simple diffusion-controlled mechanism. In contrast, the two proteins exhibit distinct behaviors within the first 12 hours: insulin remains mostly within the FmocFF gel, likely due to large cluster size and the increased viscosity of the medium, while lysozyme shows rapid initial release, likely driven by molecule migration from the gel surface followed by slower diffusion-controlled release. Among the three drugs, lysozyme displays the most promising sustained release profile, significantly delaying the time to achieve 15% drug release compared to liquid formulations by approximately 12 hours (Fig.3.5 and Fig.3.6b). While the interplay of multiple effects (diffusion, surface erosion and potential swelling) presents challenges for quantitative analysis, our SCISSOR experiments provide valuable insights into the long-term drug release behavior of FmocFF hydrogel. The results indicate that the hydrogel provides sustained release for larger drugs, while smaller drugs show no significant difference in release compared to the solution. Importantly, these findings highlight the critical role of timescale in drug release studies as QENS revealed significant differences in molecular mobility for ibuprofen sodium at ps timescales, which are not detectable in the 12 hour release profiles of SCISSOR (Fig.3.6).

3.4 Conclusion

This study provides crucial insights into the diffusion behaviour of drug molecules, of different molecular sizes, in FmocFF hydrogel across various timescales. Our multi-scale approach, using neutron scattering and bulk release methods, demonstrates that the FmocFF gel in aqueous solvent consistently slows down the release of the diverse set of drugs examined: ibuprofen sodium, insulin, and lysozyme. At the picosecond timescale, QENS data show an average 40% decrease, from bulk solution to gel, in the self-diffusion of drug molecules. This difference disappears in 12-hour bulk release studies probed by SCISSOR, except for lysozyme, whose release remains sustained even at longer timescales. Insulin shows no direct correlation between short and long-time diffusion, with

significant slowing at the molecular level but less pronounced retardation after 12 hours. Notably, QENS results for insulin in pure solution reveal strong aggregation, deviating from the theoretical diffusion expected for monomers. The case of ibuprofen sodium highlights two crucial insights of our investigation. First, short-time self-diffusion is system-specific; while in another gel system, ibuprofen diffusion was faster than in pure solution, FmocFF hydrogel slows it down, indicating specific drug-gel interactions. Second, the slowing effect at short timescales is comparable to that of larger drug compounds but diminishes at longer timescales, demonstrating the limitations of relying solely on the Stokes-Einstein equation or simple drug size/mesh size ratios to describe self-diffusion in complex liquids such as gels. These results reveal the limits of QENS and SCISSOR when taken individually but highlight the advantages of their combined use. QENS provides unambiguous access to hydrodynamic interactions without considering the steric confinement of the gel network. Moreover neutron scattering reveals that drug diffusion is neither governed by the aqueous solvent entrapped in the network (IRIS data) nor by the gelator dynamics (NSE data). SCISSOR, while unable to resolve individual factors affecting diffusion, provides insights more directly applicable to pharmaceutical drug delivery by incorporating physical boundaries and macroscopic effects not captured in molecular-level QENS measurements (such as membrane permeation and solution mixing effects). This work underscores the importance of observation timescales in identifying factors affecting diffusion in gels, distinguishing between steric and non-steric influences. It also paves the way for integrating the observation timescale with complementary techniques like FCS and PFG-NMR. This approach can help the community optimize formulations to match specific drug-gel combinations, rationalizing the design of release kinetics to achieve a control across multiple timescales. Future directions include expanding the range of drug molecules and hydrogel compositions to establish broader structure-function relationships.[31] The ultra-short peptide sequence of FmocFF can serve as a reference platform due to its ability to gel with various solvents, leading to macroscopically different features.[77]This multi-scale procedure could ultimately lead to a unified theoretical framework bridging

short-time and long-time diffusion behavior in hydrogels, facilitating ab initio modeling and shifting drug release studies from a descriptive to a more predictive approach.

3.5 Supporting information

Spectrometer resolution functions

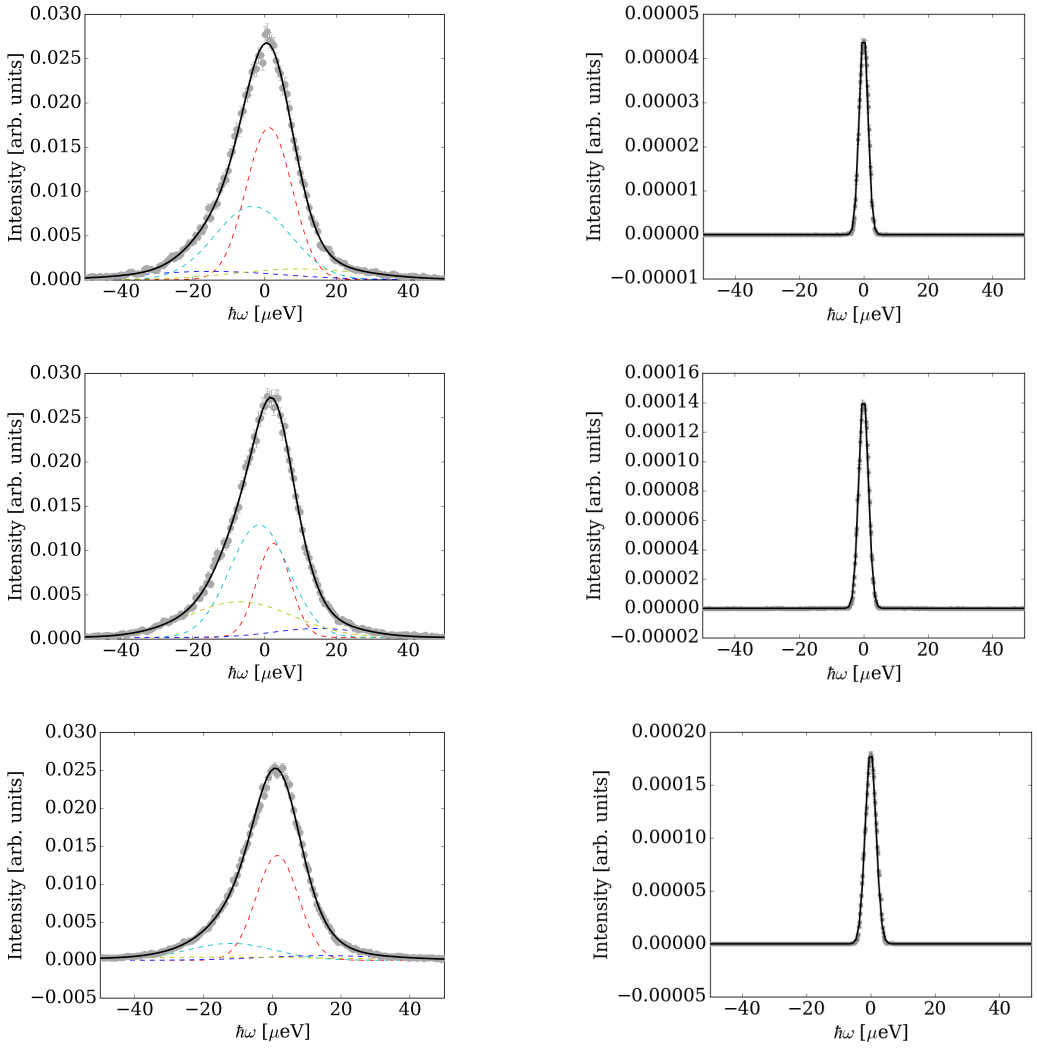

Figure S1: Fit of the energy resolution measured with vanadium on IRIS (left column) and IN16B in BATS mode (right column) at $q = 0.6$ Å^{-1} (top row), $q = 1.3$ Å^{-1} (middle row), $q = 1.7$ Å^{-1} (bottom row). Fit with a sum of four and one Gaussian functions for IRIS and IN16B, respectively.

Example IRIS spectra

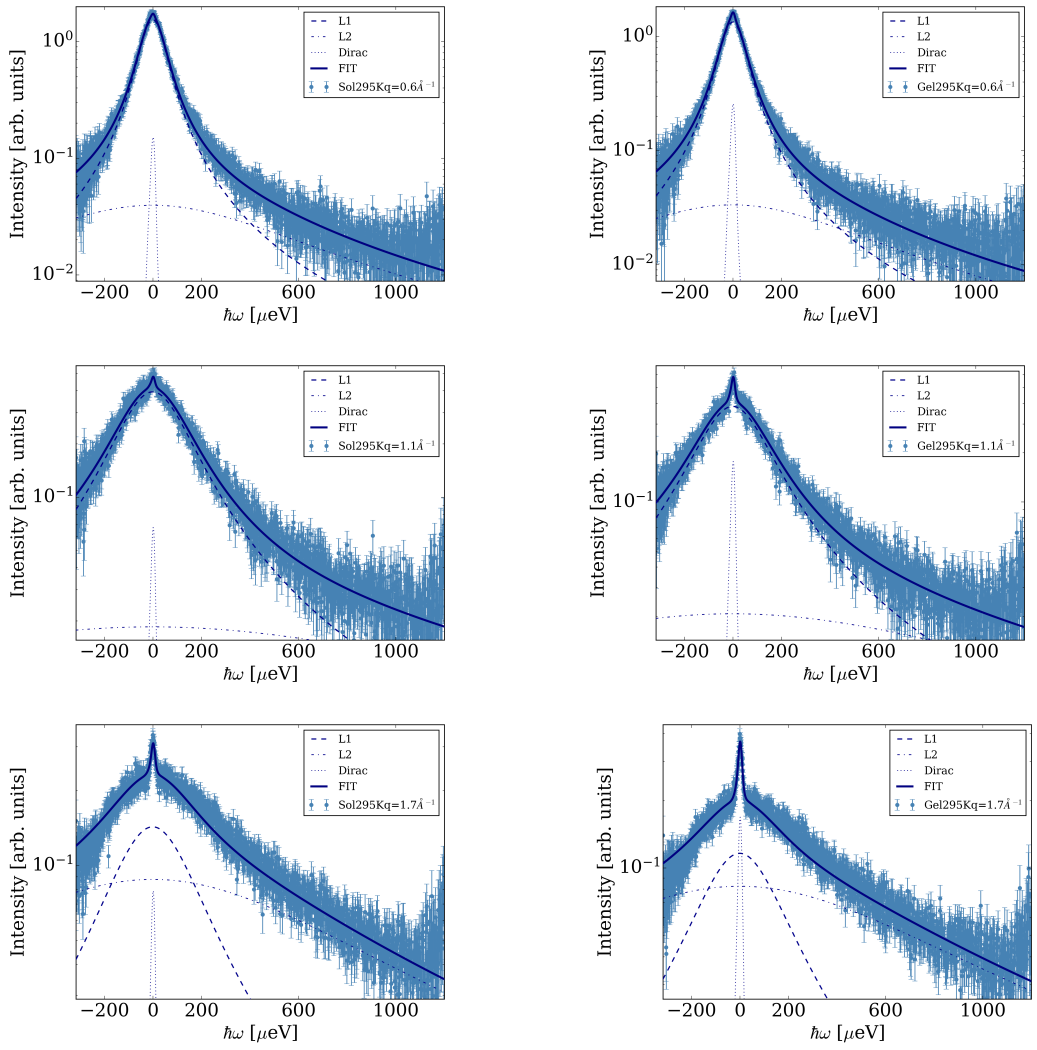

Figure S2: Example IRIS spectra of pure solution (left column) and FmocFF gel (0.5 wt.%) $q = 0.6\,\text{Å}^{-1}$ (top row), at $q = 1.2\,\text{Å}^{-1}$ (middle row) and at $q = 1.7\,\text{Å}^{-1}$ (bottom row) at $T = 295\,\text{K}$.

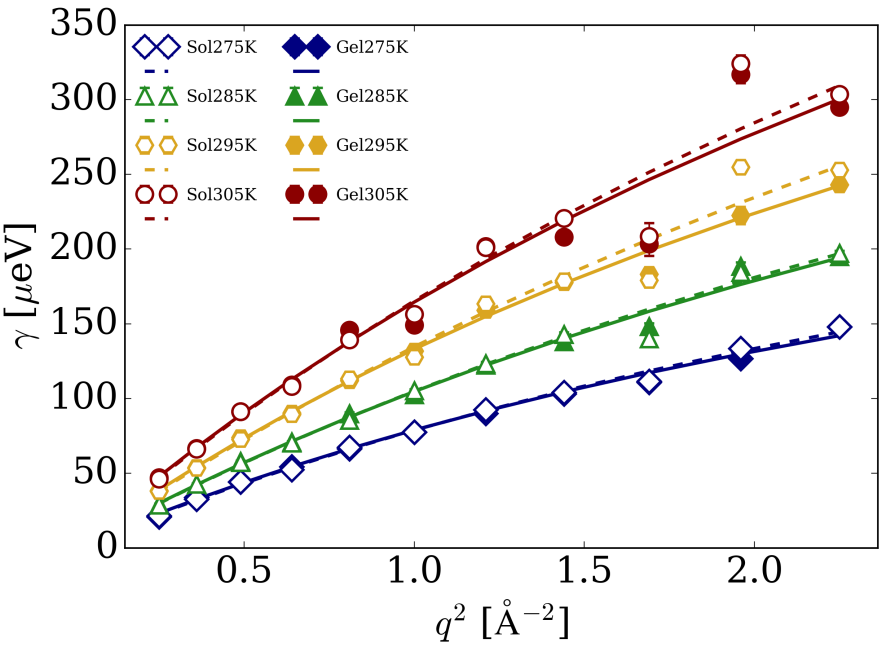

Figure S3: Lorentzian linewidth γ assigned to the solvent in the pure solution (empty symbols) and in the gel (full symbols). Fits of a jump diffusion process (dotted line: solution, continuous line: gel)

Example BATS spectra

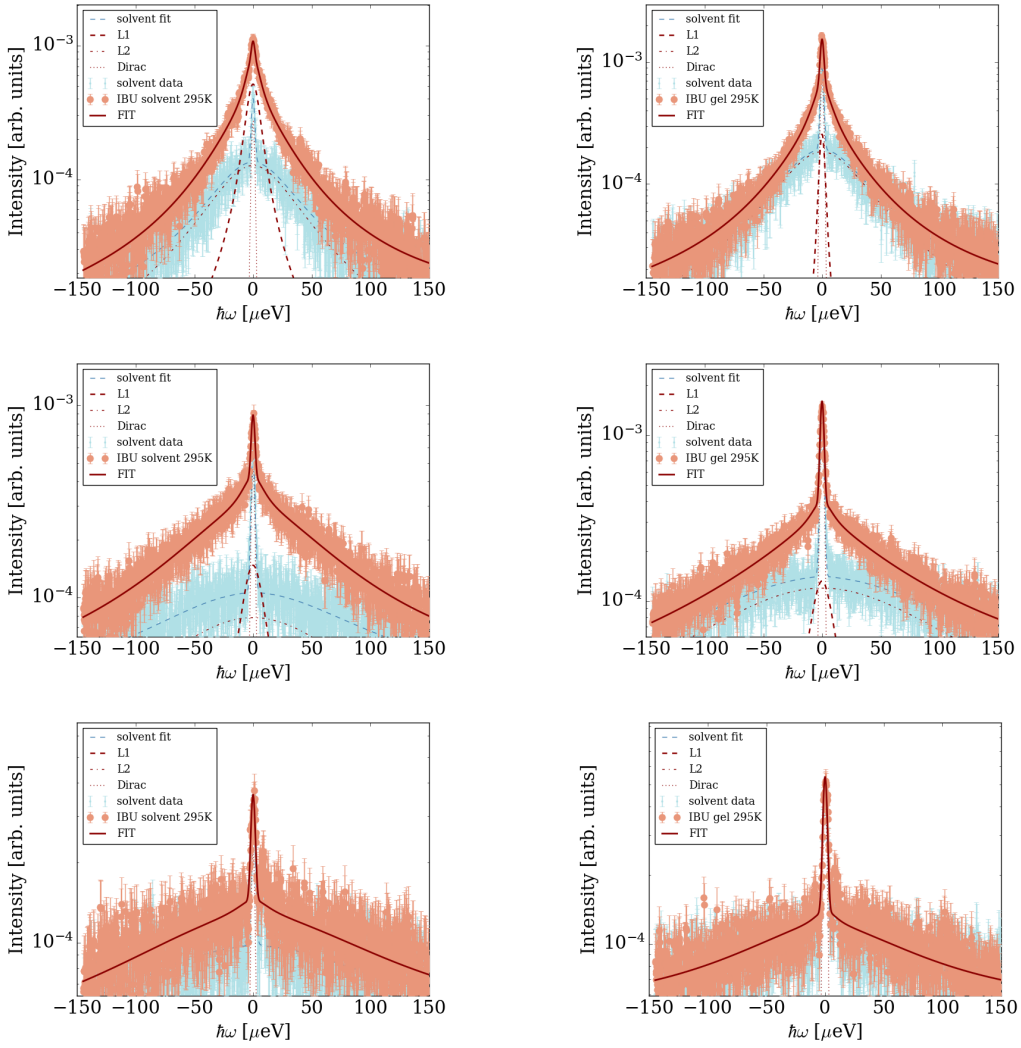

Figure S4: Example BATS spectrum of 5 wt.% IBU (full orange circle symbols) in pure solution (left column) and in 0.5 wt.% FmocFF gel (right column) at $q = 0.6\,\text{Å}^{-1}$ (top row), at $q = 1.2\,\text{Å}^{-1}$ (middle row) and at $q = 1.7\,\text{Å}^{-1}$ (bottom row) at $T = 295\,\text{K}$ and corresponding unloaded background (blue circle). Full line represents the fit of consisting of the combined solvent and container contribution (dotted lines), global diffusion (narrow thick dashed line) convoluted with the spectrometer resolution.

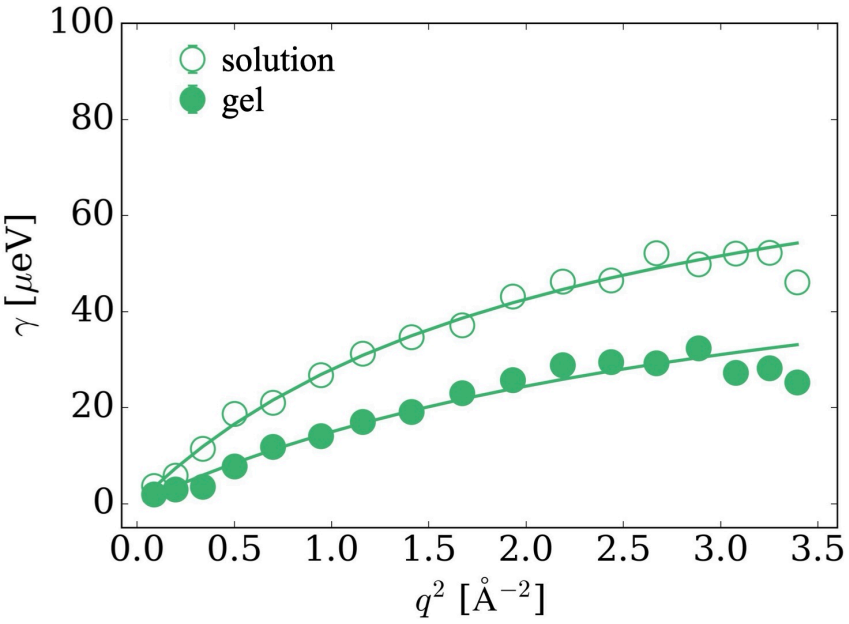

Figure S5: Summary of the fitted narrow Lorentzian linewidths $\gamma(q)$ corresponding to the apparent centre of mass diffusion fitted with a jump-diffusion model of IBU at T = 280 K. Drug in pure solution (empty symbols) and in FmocFF gel (full symbols). (Associated data recorded on BATS)

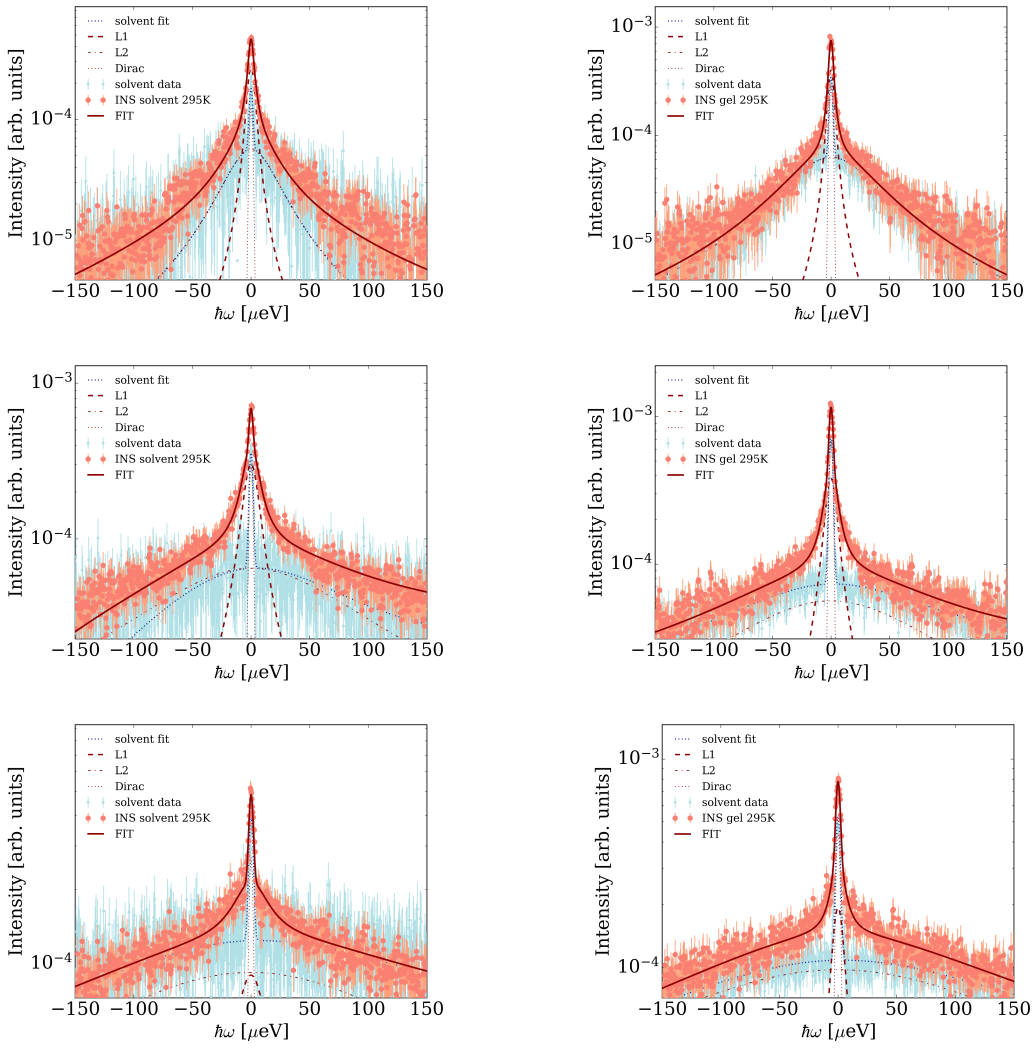

Figure S6: Example BATS spectrum of 2.5 wt.% INS (full orange circle symbols) in pure solution (left column) and in 0.5 wt.% FmocFF gel (right column) at $q = 0.6\,\text{Å}^{-1}$ (top row), at $q = 1.2\,\text{Å}^{-1}$ (middle row) and at $q = 1.7\,\text{Å}^{-1}$ (bottom row) at $T = 295\,\text{K}$ and corresponding unloaded background (blue circle). Full line represents the fit of consisting of the combined solvent and container contribution (dotted lines), global protein diffusion (narrow thick dashed line) and internal protein diffusion (dash-dotted line) convoluted with the spectrometer resolution.

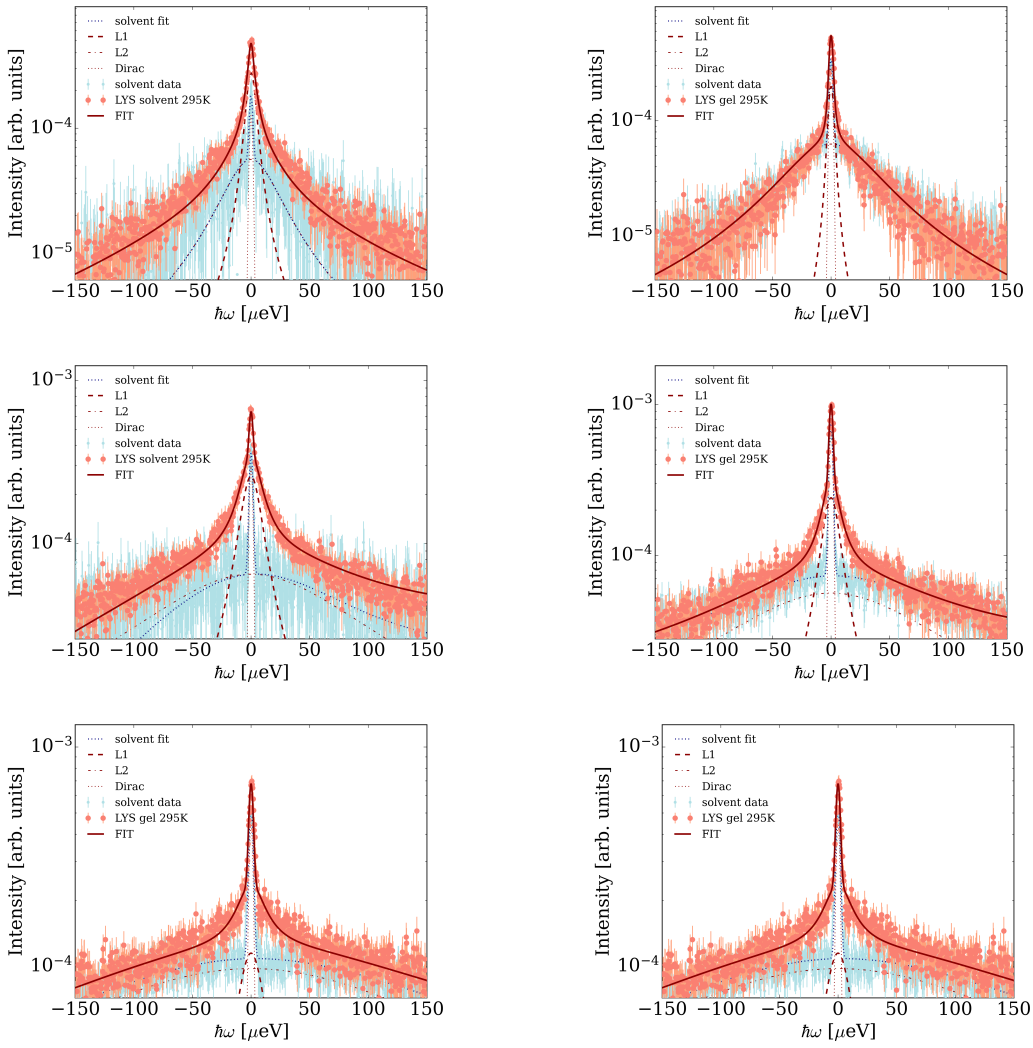

Figure S7: Example BATS spectrum of 2.5 wt.% LYS (full orange circle symbols) in pure solution (left column) and in 0.5 wt.% FmocFF gel (right column) at $q = 0.6\,\text{Å}^{-1}$ (top row), at $q = 1.2\,\text{Å}^{-1}$ (middle row) and at $q = 1.7\,\text{Å}^{-1}$ (bottom row) at $T = 295\,\text{K}$ and corresponding unloaded background (blue circle). Full line represents the fit of consisting of the combined solvent and container contribution (dotted lines), global protein diffusion (narrow thick dashed line) and internal protein diffusion (dash-dotted line) convoluted with the spectrometer resolution.

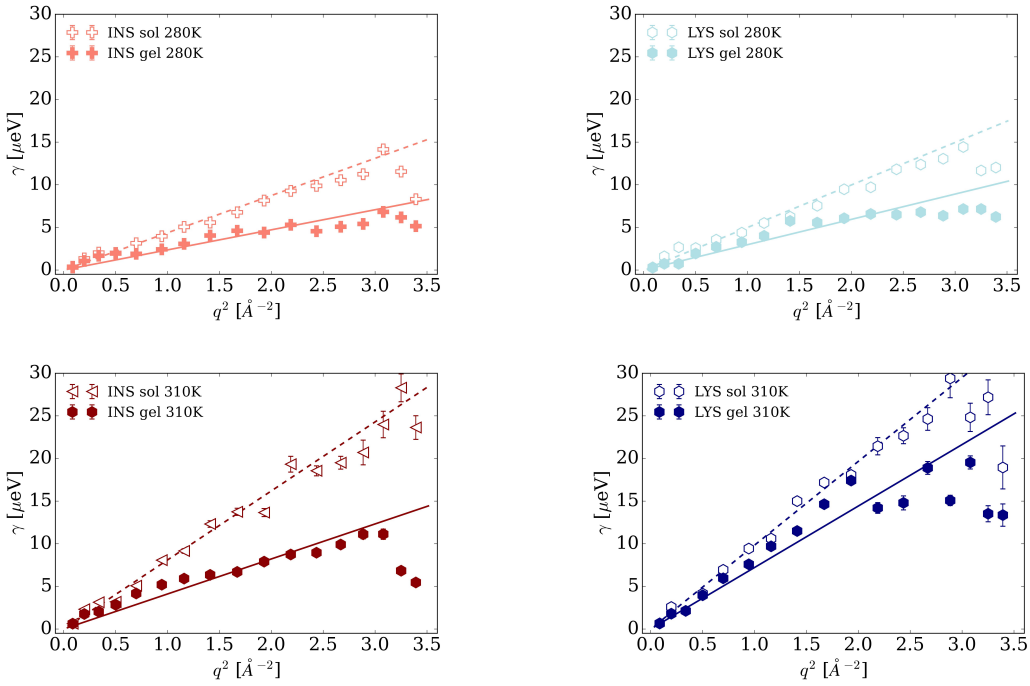

Figure S8: Summary of the fitted narrow Lorentzian linewidths $\gamma(q)$ corresponding to the apparent centre of mass diffusion fitted with a Fickian model of INS (left column) and LYS (right column) at $T = 280K$ (top) and $T = 310K$ (bottom). Drug in pure solution (empty symbols) and in FmocFF gel (full symbols). (Associated data recorded on IN16b in BATS mode)

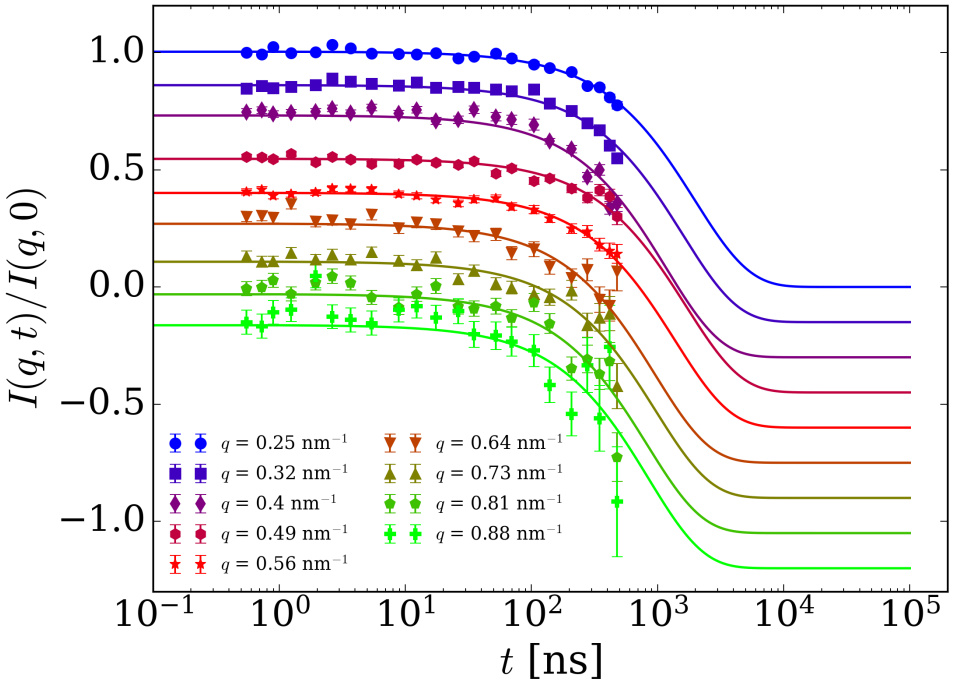

Figure S9: Normalized intermediate scattering function $I(\mathrm{q},t)/I(\mathrm{q},0)$ of FmocFF gel in recorded on IN15 at 290 K (curves are offset in y-axis for visibility). Solid curves are the result of fit with eq.10.

SCISSOR results

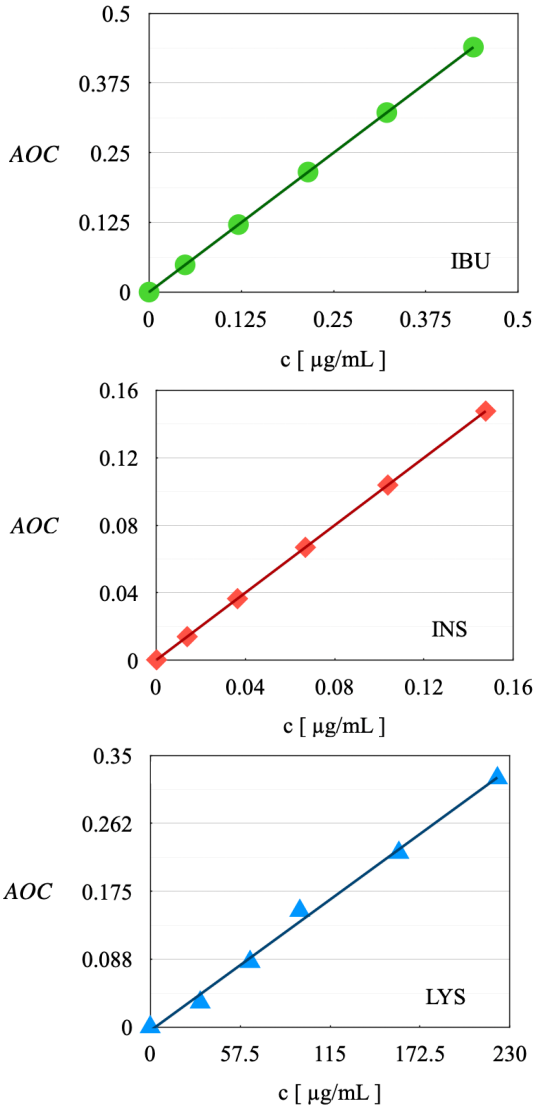

Figure S10: Calibration curves obtained via linear regression of the concentration values obtained via serial addition method and taking the area under the curve (AUC) of the second derivative of the UV-vis absorption spectra for (circles) ibuprofen sodium (R^2 = 0.998), (triangles) lysozyme (R^2 = 0.995) and (squares) insulin (R^2 = 0.998).

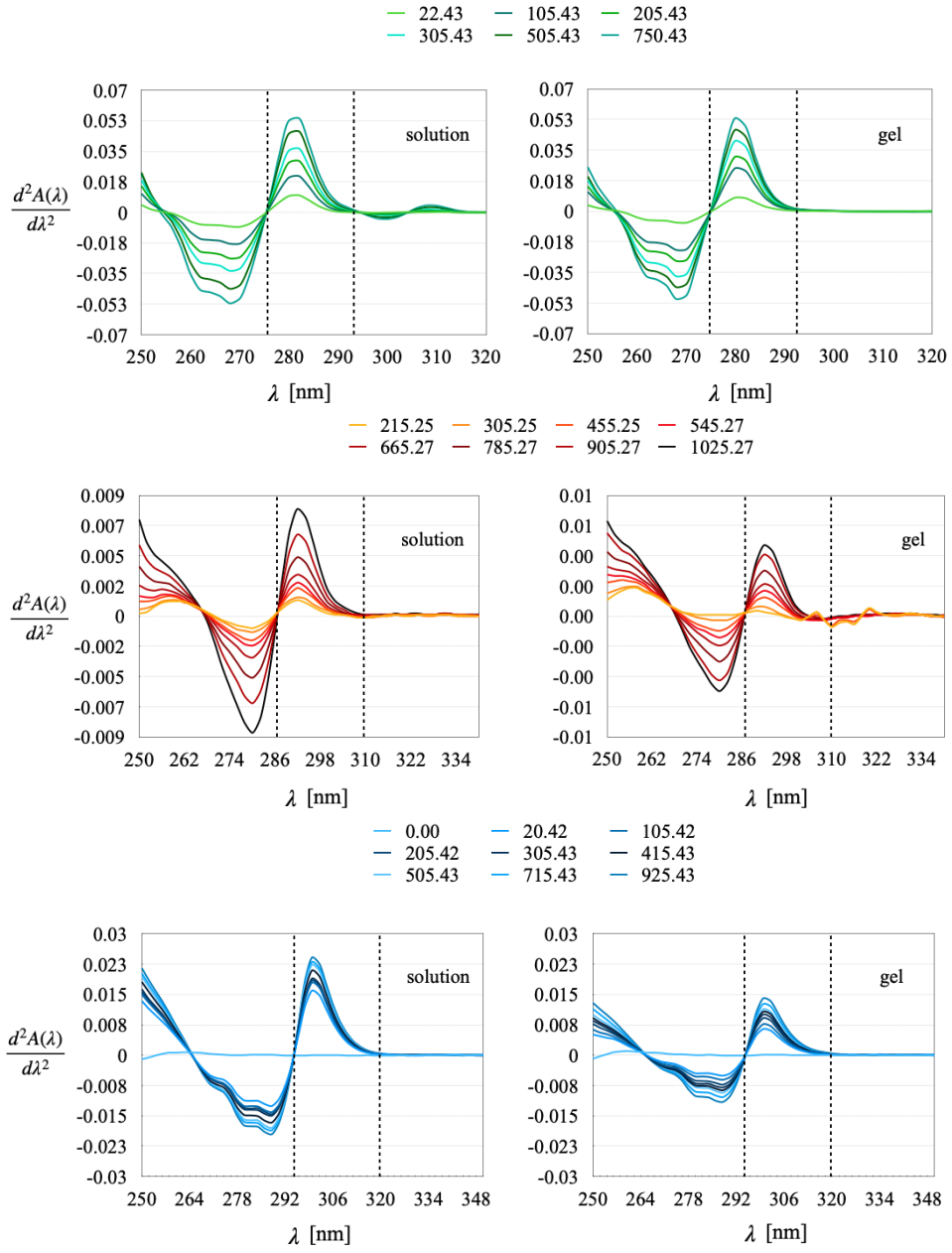

Figure S11: Second derivative of UV absorption spectra of the SCISSOR release data for ibuprofen sodium (top row), insulin (middle row), and lysozyme (bottom row) in pure solution (left column) and FmocFF gel (right column) at T = 34 °C. Dashed lines indicate the spectral region used for concentration calculations. Legend shows sampling time points in minutes

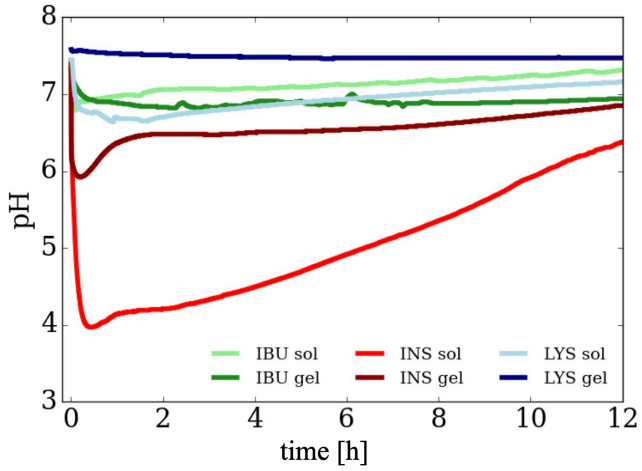

Figure S12: Time evolution of pH in the SCISSOR injection chamber from the injection (t = 0) to 12 h.

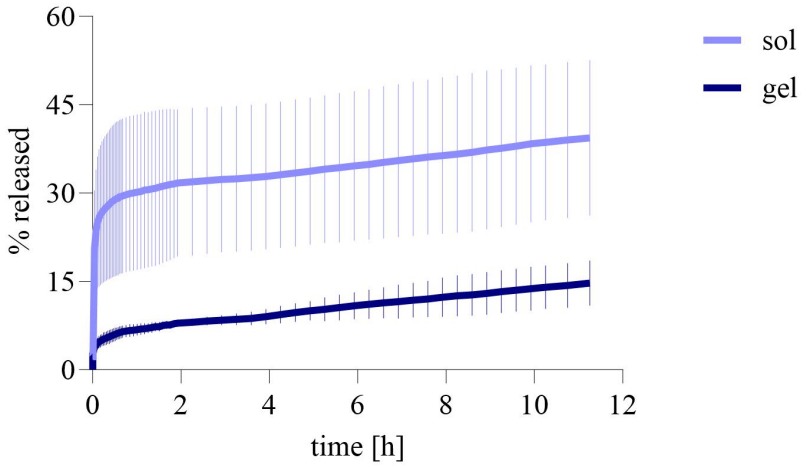

Figure S13: Release curve obtained from SCISSOR experiment for lysozyme after 12h. The data represent mean ± standard deviation from 3 repetitions.

Data Availability Statement

The neutron data are permanently curated by the ISIS facility and can be accessed by the experiment number RB1830530, https://doi.org/10.5286/ISIS.E.RB1820530 and by ILL via the DOI: https://doi.org/10.5291/ILL-DATA.9-11-1951-
https://doi.org/10.5291/ILL-DATA.9-13-1044 (BATS)
https://doi.org/10.5291/ILL-DATA.9-13-1042 (IN15).

Bibliography

[1] Michael J Espiritu, Abby C Collier, and Jon-Paul Bingham. A 21st-century approach to age-old problems: the ascension of biologics in clinical therapeutics. *Drug discovery today*, 19(8):1109–1113, 2014.

[2] DL Scott. Biologics-based therapy for the treatment of rheumatoid arthritis. *Clinical Pharmacology & Therapeutics*, 91(1):30–43, 2012.

[3] Michael S Kinch. An overview of fda-approved biologics medicines. *Drug discovery today*, 20(4):393–398, 2015.

[4] Xin Xu and Yulia Vugmeyster. Challenges and opportunities in absorption, distribution, metabolism, and excretion studies of therapeutic biologics. *The AAPS journal*, 14:781–791, 2012.

[5] Nataša Škalko-Basnet. Biologics: the role of delivery systems in improved therapy. *Biologics: Targets and Therapy*, pages 107–114, 2014.

[6] Yuchen Sun, Yue Cheng, and Daniel L Hertz. Using maximum plasma concentration (cmax) to personalize taxane treatment and reduce toxicity. *Cancer Chemotherapy and Pharmacology*, pages 1–15, 2024.

[7] Tsvetelina H Baryakova, Brett H Pogostin, Robert Langer, and Kevin J McHugh. Overcoming barriers to patient adherence: the case for developing innovative drug delivery systems. *Nature Reviews Drug Discovery*, 22(5):387–409, 2023.

[8] Yong Qiu and Kinam Park. Environment-sensitive hydrogels for drug delivery. *Advanced drug delivery reviews*, 53(3):321–339, 2001.

[9] Todd R Hoare and Daniel S Kohane. Hydrogels in drug delivery: Progress and challenges. *polymer*, 49(8):1993–2007, 2008.

[10] Ferdinand Brandl, Fritz Kastner, Ruth M Gschwind, Torsten Blunk, Jörg Teßmar, and Achim Göpferich. Hydrogel-based drug delivery systems: Comparison of drug diffusivity and release kinetics. *Journal of Controlled Release*, 142(2):221–228, 2010.

[11] Jianyu Li and David J Mooney. Designing hydrogels for controlled drug delivery. *Nature Reviews Materials*, 1(12):1–17, 2016.

[12] Mehrdad Hamidi, Amir Azadi, and Pedram Rafiei. Hydrogel nanoparticles in drug delivery. *Advanced drug delivery reviews*, 60(15):1638–1649, 2008.

[13] Kathryn J Skilling, Francesca Citossi, Tracey D Bradshaw, Marianne Ashford, Barrie Kellam, and Maria Marlow. Insights into low molecular mass organic gelators: a focus on drug delivery and tissue engineering applications. *Soft Matter*, 10(2):237–256, 2014.

[14] Jonathan W Steed. Anion-tuned supramolecular gels: a natural evolution from urea supramolecular chemistry. *Chemical Society Reviews*, 39(10):3686–3699, 2010.

[15] Jacek K Wychowaniec, Andrew M Smith, Cosimo Ligorio, Oleksandr O Mykhaylyk, Aline F Miller, and Alberto Saiani. Role of sheet-edge interactions in β-sheet self-assembling peptide hydrogels. *Biomacromolecules*, 21(6):2285–2297, 2020.

[16] Mohamed A Elsawy, Jacek K Wychowaniec, Luis A Castillo Dí'az, Andrew M Smith, Aline F Miller, and Alberto Saiani. Controlling doxorubicin release from a peptide hydrogel through fine-tuning of drug–peptide fiber interactions. *Biomacromolecules*, 23(6):2624–2634, 2022.

[17] Sandrine Tanga, Marique Aucamp, and Poornima Ramburrun. Injectable thermoresponsive hydrogels for cancer therapy: challenges and prospects. *Gels*, 9(5):418, 2023.

[18] Margaux Vigata, Christoph Meinert, Dietmar W Hutmacher, and Nathalie Bock. Hydrogels as drug delivery systems: A review of current characterization and evaluation techniques. *Pharmaceutics*, 12(12):1188, 2020.

[19] Brian Amsden. Solute diffusion within hydrogels. mechanisms and models. *Macromolecules*, 31(23):8382–8395, 1998.

[20] Brian Amsden. Solute diffusion in hydrogels.: an examination of the retardation effect. *Polymer Gels and Networks*, 6(1):13–43, 1998.

[21] Filipp V Lavrentev, Vladimir V Shilovskikh, Varvara S Alabusheva, Veronika Yu Yurova, Anna A Nikitina, Sviatlana A Ulasevich, and Ekaterina V Skorb. Diffusion-limited processes in hydrogels with chosen applications from drug delivery to electronic components. *Molecules*, 28(15):5931, 2023.

[22] Matthew Wallace, Dave J Adams, and Jonathan A Iggo. Analysis of the mesh size in a supramolecular hydrogel by pfg-nmr spectroscopy. *Soft Matter*, 9(22):5483–5491, 2013.

[23] Nicolas Fatin-Rouge, Konstantin Starchev, and Jacques Buffle. Size effects on diffusion processes within agarose gels. *Biophysical Journal*, 86(5):2710–2719, 2004.

[24] Tilo Seydel, Robert M Edkins, Christopher D Jones, Jonathan A Foster, Robert Bewley, Juan A Aguilar, and Katharina Edkins. Increased rate of solvent diffusion in a prototypical supramolecular gel measured on the picosecond timescale. *Chemical Communications*, 54(49):6340–6343, 2018.

[25] Hyun Woo Cho, Haein Kim, Bong June Sung, and Jun Soo Kim. Tracer diffusion in tightly-meshed homogeneous polymer networks: A brownian dynamics simulation study. *Polymers*, 12(9):2067, 2020.

[26] Marc Bée. Localized and long-range diffusion in condensed matter: state of the art of qens studies and future prospects. *Chemical Physics*, 292(2-3):121–141, 2003.

[27] Sylvie Spagnoli, Isabelle Morfin, Miguel A Gonzalez, Pierre Carcabal, and Marie Plazanet. Solvent contribution to the stability of a physical gel characterized by quasi-elastic neutron scattering. *Langmuir*, 31(8):2554–2560, 2015.

[28] MPM Marques, ALM Batista De Carvalho, V Garcia Sakai, L Hatter, and LAE Batista De Carvalho. Intracellular water–an overlooked drug target? cisplatin impact in cancer cells probed by neutrons. *Physical Chemistry Chemical Physics*, 19(4):2702–2713, 2017.

[29] Robert M Edkins, Markus Appel, Tilo Seydel, and Katharina Edkins. The modifying effect of supramolecular gel fibres on the diffusion of paracetamol and ibuprofen sodium on the picosecond timescale. *Physical Chemistry Chemical Physics*, 22(19):10838–10844, 2020.

[30] Andrew M Smith, Richard J Williams, Claire Tang, Paolo Coppo, Richard F Collins, Michael L Turner, Alberto Saiani, and Rein V Ulijn. Fmoc-diphenylalanine self assembles to a hydrogel via a novel architecture based on π–π interlocked β-sheets. *Advanced materials*, 20(1):37–41, 2008.

[31] Ranjoo Choe and Seok Il Yun. Fmoc-diphenylalanine-based hydrogels as a potential carrier for drug delivery. *e-Polymers*, 20(1):458–468, 2020.

[32] Haniyeh Najafi, Samira Sadat Abolmaali, Reza Heidari, Hadi Valizadeh, Mahboobeh Jafari, Ali Mohammad Tamaddon, and Negar Azarpira. Nitric oxide releasing nanofibrous fmoc-dipeptide hydrogels for amelioration

of renal ischemia/reperfusion injury. *Journal of Controlled Release*, 337:1–13, 2021.

[33] Carlo Diaferia, Elisabetta Rosa, Giancarlo Morelli, and Antonella Accardo. Fmoc-diphenylalanine hydrogels: Optimization of preparation methods and structural insights. *Pharmaceuticals*, 15(9):1048, 2022.

[34] Hanne M Kinnunen, Vikas Sharma, Luis Rodrigo Contreras-Rojas, Yafei Yu, Chlöe Alleman, Alavattam Sreedhara, Stefan Fischer, Leslie Khawli, Stefan T Yohe, Daniela Bumbaca, et al. A novel in vitro method to model the fate of subcutaneously administered biopharmaceuticals and associated formulation components. *Journal of Controlled Release*, 214:94–102, 2015.

[35] Dave J Adams, Michael F Butler, William J Frith, Mark Kirkland, Leanne Mullen, and Paul Sanderson. A new method for maintaining homogeneity during liquid–hydrogel transitions using low molecular weight hydrogelators. *Soft Matter*, 5(9):1856–1862, 2009.

[36] George H Vineyard. Scattering of slow neutrons by a liquid. *Physical Review*, 110(5):999, 1958.

[37] Owen Arnold, Jean-Christophe Bilheux, JM Borreguero, Alex Buts, Stuart I Campbell, L Chapon, Mathieu Doucet, N Draper, R Ferraz Leal, MA Gigg, et al. Mantid—data analysis and visualization package for neutron scattering and μ sr experiments. *Nuclear instruments and methods in physics research section a: accelerators, spectrometers, detectors and associated equipment*, 764:156–166, 2014.

[38] Marco Grimaldo, Hender Lopez, Christian Beck, Felix Roosen-Runge, Martine Moulin, Juliette M Devos, Valerie Laux, Michael Hartlein, Stefano Da Vela, Ralf Schweins, et al. Protein short-time diffusion in a naturally crowded environment. *The journal of physical chemistry letters*, 10(8):1709–1715, 2019.

[39] José Teixeira, M-C Bellissent-Funel, Sow-Hsin Chen, and Albert-José Dianoux. Experimental determination of the nature of diffusive motions of water molecules at low temperatures. *Physical Review A*, 31(3):1913, 1985.

[40] Marco Grimaldo, Felix Roosen-Runge, Niina Jalarvo, Michaela Zamponi, Fabio Zanini, Marcus Hennig, Fajun Zhang, Frank Schreiber, and Tilo Seydel. High-resolution neutron spectroscopy on protein solution samples. In *EPJ Web of Conferences*, volume 83, page 02005. EDP Sciences, 2015.

[41] Adolfo J Banchio and Gerhard Nägele. Short-time transport properties in dense suspensions: From neutral to charge-stabilized colloidal spheres. *The Journal of chemical physics*, 128(10), 2008.

[42] Michal K Braun, Marco Grimaldo, Felix Roosen-Runge, Ingo Hoffmann, Orsolya Czakkel, Michael Sztucki, Fajun Zhang, Frank Schreiber, and Tilo Seydel. Crowding-controlled cluster size in concentrated aqueous protein solutions: structure, self-and collective diffusion. *The journal of Physical Chemistry Letters*, 8(12):2590–2596, 2017.

[43] Hanne M Kinnunen and Randall J Mrsny. Improving the outcomes of biopharmaceutical delivery via the subcutaneous route by understanding the chemical, physical and physiological properties of the subcutaneous injection site. *Journal of Controlled Release*, 182:22–32, 2014.

[44] Hanne Kinnunen Bown, Catherine Bonn, Stefan Yohe, Daniela Bumbaca Yadav, Thomas W Patapoff, Ann Daugherty, and Randall J Mrsny. In vitro model for predicting bioavailability of subcutaneously injected monoclonal antibodies. *Journal of Controlled Release*, 273:13–20, 2018.

[45] Joana AD Sequeira, Ana C Santos, João Serra, Catarina Estevens, Raquel Seiça, Francisco Veiga, and António J Ribeiro. Subcutaneous delivery of biotherapeutics: challenges at the injection site. *Expert Opinion on Drug Delivery*, 16(2):143–151, 2019.

[46] Sharadvi Thati, Meagan McCallum, Yan Xu, Michelle Zheng, Zhi Chen, Jeff Dai, Duohai Pan, Dilusha Dalpathado, and Neil Mathias. Novel applications of an in vitro injection model system to study bioperformance: case studies with different drug modalities. *Journal of Pharmaceutical Innovation*, 15:268–280, 2020.

[47] Hao Lou, Cory Berkland, and Michael J Hageman. Simulating particle movement inside subcutaneous injection site simulator (scissor) using monte-carlo method. *International Journal of Pharmaceutics*, 605:120824, 2021.

[48] David Li, Poh Yee Chow, Tzu Ping Lin, Celine Cheow, Zhuoxuan Li, and Matthias G Wacker. Simulate subq: the methods and the media. *Journal of Pharmaceutical Sciences*, 112(6):1492–1508, 2023.

[49] Liudmil Antonov and Stefan Stoyanov. Approach for increased information from the second-derivative spectra in uv-vis absorption spectroscopy. *Applied Spectroscopy*, 47(10):1712–1715, 1993.

[50] Lei Wang and Mandana Asgharnejad. Second-derivative uv spectrometric determination of simvastatin in its tablet dosage form. *Journal of pharmaceutical and biomedical analysis*, 21(6):1243–1248, 2000.

[51] Chinmay M Jogdeo, Deep S Bhattacharya, Vicky Lin, Parag Kolhe, and Advait Badkar. Assessing physicochemical stability of monoclonal antibodies in a simulated subcutaneous environment. *Journal of Pharmaceutical Sciences*, 2024.

[52] Johan Qvist, Helmut Schober, and Bertil Halle. Structural dynamics of supercooled water from quasielastic neutron scattering and molecular simulations. *The Journal of Chemical Physics*, 134(14), 2011.

[53] Tilo Seydel, Lutz Wiegart, Fanni Juranyi, Bernd Struth, and Helmut Schober. Unaffected microscopic dynamics of macroscopically arrested water in dilute clay gels. *Physical Review E—Statistical, Nonlinear, and Soft Matter Physics*, 78(6):061403, 2008.

[54] Edgar Fuentes, Kamila Boháčová, Ana M Fuentes-Caparrós, Ralf Schweins, Emily R Draper, Dave J Adams, Silvia Pujals, and Lorenzo Albertazzi. Paint-ing fluorenylmethoxycarbonyl (fmoc)-diphenylalanine hydrogels. *Chemistry–A European Journal*, 26(44):9869–9873, 2020.

[55] Baolu Shi, Long Xie, Bin Ma, Zhiliang Zhou, Baosheng Xu, and Lijie Qu. Preparation and properties of highly transparent sio2 aerogels for thermal insulation. *Gels*, 8(11):744, 2022.

[56] Marco Grimaldo, Felix Roosen-Runge, Fajun Zhang, Frank Schreiber, and Tilo Seydel. Dynamics of proteins in solution. *Quarterly Reviews of Biophysics*, 52:e7, 2019.

[57] CH Cho, J Urquidi, S Singh, and G Wilse Robinson. Thermal offset viscosities of liquid h2o, d2o, and t2o. *The Journal of Physical Chemistry B*, 103(11):1991–1994, 1999.

[58] Sabrine S Jensen, Henrik Jensen, Claus Cornett, Eva H Møller, and Jesper Østergaard. Insulin diffusion and self-association characterized by real-time uv imaging and taylor dispersion analysis. *Journal of pharmaceutical and biomedical analysis*, 92:203–210, 2014.

[59] Stefania Perticaroli, Georg Ehlers, Christopher B Stanley, Eugene Mamontov, Hugh O'Neill, Qiu Zhang, Xiaolin Cheng, Dean AA Myles, John Katsaras, and Jonathan D Nickels. Description of hydration water in protein (green fluorescent protein) solution. *Journal of the American Chemical Society*, 139(3):1098–1105, 2017.

[60] Alvaro Ortega, D Amorós, and J García De La Torre. Prediction of hydrodynamic and other solution properties of rigid proteins from atomic- and residue-level models. *Biophysical Journal*, 101(4):892–898, 2011.

[61] Anna Stradner, Frédéric Cardinaux, and Peter Schurtenberger. A small-angle scattering study on equilibrium clusters in lysozyme solutions. *The Journal of Physical Chemistry B*, 110(42):21222–21231, 2006.

[62] Megren HA Fagihi, Chanaka Premathilaka, Tiina O'Neill, Massimiliano Garré, and Sourav Bhattacharjee. An investigation into the acidity-induced insulin agglomeration: Implications for drug delivery and translation. *ACS Omega*, 8(28):25279–25287, 2023.

[63] Lionel Porcar, Peter Falus, Wei-Ren Chen, Antonio Faraone, Emiliano Fratini, Kunlun Hong, Piero Baglioni, and Yun Liu. Formation of the dynamic clusters in concentrated lysozyme protein solutions. *The Journal of Physical Chemistry Letters*, 1(1):126–129, 2010.

[64] Anna Stradner, Helen Sedgwick, Frédéric Cardinaux, Wilson CK Poon, Stefan U Egelhaaf, and Peter Schurtenberger. Equilibrium cluster formation in concentrated protein solutions and colloids. *Nature*, 432(7016):492–495, 2004.

[65] Marija Bešter-Rogač. Nonsteroidal anti-inflammatory drugs ion mobility: A conductometric study of salicylate, naproxen, diclofenac and ibuprofen dilute aqueous solutions. *Acta Chimica Slovenica*, 56(1), 2009.

[66] E Prabhu Raman, Takako Takeda, and Dmitri K Klimov. Molecular dynamics simulations of ibuprofen binding to aβ peptides. *Biophysical Journal*, 97(7):2070–2079, 2009.

[67] Meital Reches and Ehud Gazit. Casting metal nanowires within discrete self-assembled peptide nanotubes. *Science*, 300(5619):625–627, 2003.

[68] Sebastian Milster, Fabian Koch, Christoph Widder, Tanja Schilling, and Joachim Dzubiella. Tracer dynamics in polymer networks: generalized langevin description. *arXiv preprint arXiv:2402.10148*, 2024.

[69] Jean-Baptiste Guilbaud and Alberto Saiani. Using small angle scattering (sas) to structurally characterise peptide and protein self-assembled materials. *Chemical Society Reviews*, 40(3):1200–1210, 2011.

[70] Laura LE Mears, Emily R Draper, Ana M Castilla, Hao Su, Zhuola, Bart Dietrich, Michael C Nolan, Gregory N Smith, James Doutch, Sarah

Rogers, et al. Drying affects the fiber network in low molecular weight hydrogels. *Biomacromolecules*, 18(11):3531–3540, 2017.

[71] Emily R Draper and Dave J Adams. How should multicomponent supramolecular gels be characterised? *Chemical Society Reviews*, 47(10):3395–3405, 2018.

[72] P _ G De Gennes. Liquid dynamics and inelastic scattering of neutrons. *Physica*, 25(7-12):825–839, 1959.

[73] Jorge Ramirez, Thomas J Dursch, and Bradley D Olsen. A molecular explanation for anomalous diffusion in supramolecular polymer networks. *Macromolecules*, 51(7):2517–2525, 2018.

[74] Anirban Das, Mosami Shah, and Ishu Saraogi. Molecular aspects of insulin aggregation and various therapeutic interventions. *ACS bio & med Chem Au*, 2(3):205–221, 2022.

[75] Zahra Janipour, Haniyeh Najafi, Samira Sadat Abolmaali, Reza Heidari, Negar Azarpira, Emine Dilek Özyılmaz, and Ali Mohammad Tamaddon. Simvastatin-releasing nanofibrous peptide hydrogels for accelerated healing of diabetic wounds. *ACS Applied Bio Materials*, 6(11):4620–4628, 2023.

[76] Muhammad Rizwan, Rosiyah Yahya, Aziz Hassan, Muhammad Yar, Ahmad Danial Azzahari, Vidhya Selvanathan, Faridah Sonsudin, and Cheyma Naceur Abouloula. ph sensitive hydrogels in drug delivery: Brief history, properties, swelling, and release mechanism, material selection and applications. *Polymers*, 9(4):137, 2017.

[77] Jaclyn Raeburn, Cristina Mendoza-Cuenca, Beatrice N Cattoz, Marc A Little, Ann E Terry, Andre Zamith Cardoso, Peter C Griffiths, and Dave J Adams. The effect of solvent choice on the gelation and final hydrogel properties of fmoc–diphenylalanine. *Soft Matter*, 11(5):927–935, 2015.

Blank page

Chapter 4

Electrostatic Tuning of Doxorubicin Diffusion: Molecular-Level Insights into Long-Term Drug Release in Supramolecular Peptide Hydrogel

Author contribution: Riccardo Morbidini [a,b] wrote the proposal, performed the QENS experiment and analyze the data, with assistance from Dr. Mona Sarter,[c] Prof. Katharina Edkins[d,*] and Tilo Seydel[a]. The gel samples were prepared by Nastaran Zoghi,[e] under the supervision of Prof. Alberto Saiani[b]. The experiment was conceived by Riccardo Morbidini under the supervision of Prof. Katharina Edkins.

[a] Institut Max von Laue - Paul Langevin, 71 Avenue des Martyrs, F-38042 Grenoble, France. [b] Division of Pharmacy and Optometry, University of Manchester, Oxford Road, Manchester M13 9PT, United Kingdom.

[c] ISIS Neutron and Muon Source, Rutherford Appleton Laboratory, Didcot, OX11 0QX, United Kingdom.

[d,*] Strathclyde Institute of Pharmacy and Biomedical Sciences, University of Strathclyde, 161 Cathedral Street, Glasgow G4 0RE, United Kingdom.

[e] Department of Materials and Manchester Institute of Biotechnology, School of Natural Sciences, Faculty of Science and Engineering, The University of Manchester, Oxford Road, M13 9PL, United Kingdom

Abstract

Small molecule drugs, despite the spread of more complex therapeutics, remain essential in modern medicine. The oncologic drug Doxorubicin (DOX) serves as a model compound to study the challenges faced by small molecules, with its clinical use limited by toxicity and suboptimal pharmacokinetics, highlighting the need for improved delivery methods. Peptide-based supramolecular hydrogels offer promising solutions due to their biocompatibility, ease of tunability, and ability to control drug release. This study employs quasi-elastic neutron scattering (QENS) to investigate how electrostatic modifications of β-sheet-forming peptides influence DOX sub-nanosecond self-diffusion within supramolecular hydrogels. Our findings reveal that non-covalent interactions, particularly cation–π, significantly slow DOX diffusion, correlating with pre-existing long-term drug release studies on the same system. The results highlight the complexity of drug-fiber interactions at molecular level and emphasize the potential of this specific class peptide-based hydrogels as a reference drug delivery vehicle to study tunable transport across different timescale.

4.1 Introduction

Despite the rise of new therapeutics like proteins, antibodies, nucleic acids, and living cells,[1] small molecule drugs (<900 daltons) remain crucial in modern medicine due to their ease of synthesis, stability, ability to cross biological barriers, and suitability for oral administration.[2] However, challenges such as poor solubility or short half-life due to absorption hinder their delivery and efficacy. Doxorubicin (DOX), a widely used chemotherapeutic, exemplifies the success and drawbacks of small molecule drugs.[3, 4] Despite its effectiveness against various cancers, its clinical impact is constrained by severe off-target toxicity and suboptimal pharmacokinetics, underscoring the need for improved delivery methods.[4]Conventionally, drug delivery strategies focus on three different approaches: modifying the drug, altering the microenvironment or designing delivery vehicles.[5] Although DOX modification strategies, such as the PEGylated liposomal formulation Doxil®, have enhanced pharmacokinetics and reduced toxicity,[6] persistent challenges in achieving precision targeting and minimizing systemic side effects have stimulated interest in alternative delivery vehicles.[7]

In this regard, hydrogels stand out as highly versatile materials with properties that make them ideal for drug delivery applications.[8, 9] Their entangled polymer networks enable effective drug encapsulation while maintaining excellent biocompatibility due to their high water content (> 99%). Moreover, their mechanical properties, swelling behavior, and degradation rates can be precisely tailored to match the requirements of specific tissues and drug release profiles.[10] Injectable hydrogels form localized depots at the injection site, enabling controlled drug release while minimizing off-target toxicity and leakage, which together reduce dosing frequency and enhance patient adherence.[11, 12]Notably, many hydrogels are stimuli-responsive, allowing targeted drug release in response to environmental changes such as pH or temperature, further enhancing their therapeutic potential.[13, 14] The subclass of supramolecular gels, based on the non-covalent physically-triggered self-assembly of low-molecular-weight gelators (LMWG) at small concentrations (< 1 wt.%), of-

fers distinct advantages in terms of tunability and adaptability.[15–17] Unlike polymer-based gels, their properties can be easily adjusted through simple molecular modifications, providing a versatile platform for finely tuning drug release while ensuring biodegradability and low toxicity.[18] Among supramolecular gels, peptide-based systems stand out for their inherent biodegradability, minimal toxicity, and the ease of tailoring their properties through precise molecular design.[19]

One notable example is the development of a series of peptide hydrogels using amphipathic short peptides (8 to 12 amino acids) with alternating hydrophilic and hydrophobic residues. These peptides self-assemble into antiparallel β-sheet-rich fibers, with hydrophobic cores buried between the β-sheet layers, resulting in stable, shear-thinning and injectable hydrogels.[20–22] Importantly, subtle electrostatic modifications of the LMWGs in this family of hydrogels have been shown to favour DOX retention, establishing a direct relation between macroscopic drug release and a range of molecular interactions between the drug and the hydrogel network, including hydrophobic, electrostatic, and cation-π or π-π stacking.[23]

However, establishing a direct correlation between molecular-level hydrodynamic interactions and macroscopic drug release observations is neither straightforward nor unambiguous.[24] Common drug dissolution methods probe drug dynamics over several hours, capturing a superposition of steric and non-steric drug-fiber interactions, as well as gel swelling and erosion.[8, 10] Quasi-elastic neutron scattering (QENS) stands out among techniques for probing drug diffusion at the molecular level.[25–27] By capturing motions on picosecond to nanosecond timescales, QENS decouples long-timescale effects like steric confinement and gel erosion, which dominate during long-term drug release, isolating hydrodynamic interactions effective over molecular-scale displacements. This approach unambiguously reveals the influence of subtle changes in local environments, such as hydrophobic fiber-induced alterations, on the diffusion of small molecule drugs.[28] This study aims to investigate the molecular-level dynamics of DOX in peptide hydrogels using QENS, focusing on how electrostatic modifications of the self-assembling peptides influence sub-nanoscale

diffusion, thereby linking these minute effects to the macroscopic drug release behavior previously observed.[23]

4.2 Materials and methods

Sample preparation

Peptide powders were purchased from LifeTein® LLC (US) as HCl salts with over 95% purity and stored at -20°C. Doxorubicin hydrochloride (DOX, purity ∼95%) was obtained from Fluorochem (UK), while all other solvents and reagents were purchased from Sigma-Aldrich. Following the previously outlined method,[22, 23] peptide hydrogels (both unloaded and DOX-loaded) were prepared by dissolving peptide powder and/or DOX in deuterium oxide (D_2O) (used instead of H_2O to minimize hydrogen signal interference in QENS). The pH was then adjusted to 5–5.7 through incremental additions of 50 mM NaOD (replacing NaOH). After each NaOD addition, samples were vortexed, and gentle centrifugation was used to remove any trapped air bubbles. Final concentrations were set at 14 mM for the peptide and 5 wt.% for DOX (86 mM instead of 240 μM) and samples were then stored overnight at 4 °C before use. The higher amount of drug loaded is due to the requested signal for QENS for small drugs.[28] The peptide sequences used are FEFKFEFK (F8), FKFEFKFK (FK), and KFEFKFEFKK (KF8K) (F: phenylalanine; E: glutamic acid; K: lysine): FK and KF8K sequences carry charge +2 while F8 carries a neutral charge in the studied pH range.

Quasi-Elastic Neutron Scattering (QENS)

QENS is utilized to examine random movements, including translation and rotation, which involve energy exchanges between neutrons and the sample, generally below 2 meV.[29] The primary quantity analyzed in QENS is the dynamic structure factor $S(q, \omega)$, which depends on the transfer of momentum $\hbar q$ and energy $\hbar\omega$, providing details about the time-dependent average positions of particles in the ensemble. This function is observed as a broadening

of the spectral feature centered at zero energy exchange ($\hbar\omega = 0$), known as the elastic peak, and is typically described by a Lorentzian function:

$$\mathcal{L}_\gamma(q) = \frac{1}{\pi}\frac{\gamma(q)}{\gamma(q)^2 + \omega^2} \tag{4.1}$$

where $\gamma(q)$ is the linewidth that depends on q (half-width at half-maximum, HWHM) and is connected to the self-diffusion coefficient via $\gamma(q) \propto D_{\text{self}}q^2$. Doxorubicin diffusion has been measured with the Time-of-Flight indirect geometry spectrometer IRIS at the ISIS facility, Rutherford Appleton Laboratory (Didcot, UK), using the PG002 analyser reflection to yield an energy resolution (FWHM) at the elastic line of 17.5 μeV and -500 μeV $\leq \hbar\omega \leq$ +500 μeV and 0.4 Å$^{-1} \leq q \leq$ 1.5 Å^{-1} corresponding to displacements in the time scale of 0.5-30 ps and lengths of 4-16 Å. The main contribution to the QENS spectrum arises from the large incoherent cross section of mobile ^{1}H, with the isotopes in the solid gel network contributing only to the elastic line.[28, 30] Furthermore, employing a fully deuterated solvent enhances the drug signal relative to the solvent background by taking advantage of the distinct incoherent scattering cross-sections of the ^{1}H and ^{2}H isotopes. Samples were placed inside double-walled cylindrical aluminum cans with a 0.25 mm gap. These were sealed using indium wire and then inserted into a top loading closed cycle refrigerator to ensure temperature control during 4.5 h long data acquisition. The data were firstly reduced using standard routines in Mantid,[31] and subsequently analysed with *python* scripts.[32] Before conducting a quantitative analysis of the diffusion coefficients, a model-free qualitative inspection of the spectra was performed by summing over q to improve statistical quality. This comparison highlights a clear distinction between the drug signal and the solvent background in the DOX-loaded versus DOX-unloaded gels (Fig.4.1). Significant differences are observed between the spectra of the drug in solution and in the gel states, while only minor variations are evident across different gel sequences (Fig.S1). To accurately analyze the QENS spectra, it is essential to account for the intrinsic spectral shape of the instrument, by making a convolution between the energy resolution and the sample spectra. In QENS, the model

scattering function $S(q,\omega)$ typically comprises Lorentzian and elastic contributions. Convolution with a Gaussian resolution function yields Voigt profiles, which can be analytically computed using the Faddeeva function. Taking advantage of this, we fit the energy resolution function $\mathcal{R}$ with a sum of Gaussian functions, enabling an efficient analytical convolution $\mathcal{R} \otimes S(q,\omega)$ and avoiding numerical convolution with potentially noisy measured resolution data. To obtain the energy resolution function $\mathcal{R}$, we measured the purely incoherent scattering of a vanadium standard in the same geometry as the samples, effectively representing the instrument's response. The vanadium spectrum was then fitted with a dominant central Gaussian peak centered at zero energy transfer, accounting for the majority of the resolution function and five additional, smaller Gaussian components to model the asymmetric tails and fine structure of the resolution (Fig.4.2 and Fig.S2).[32] The modeling of DOX diffu-

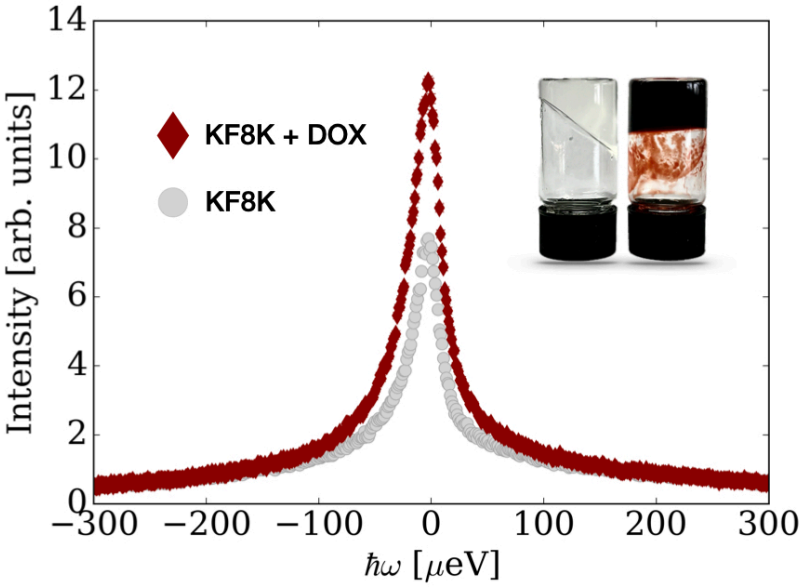

Figure 4.1: Model-free comparison of QENS spectra summed over q DOX-loaded and unloaded KF8K gel. Inset: picture of inverted vials of (left) DOX-unloaded and (right) DOX-loaded KF8K hydrogel.

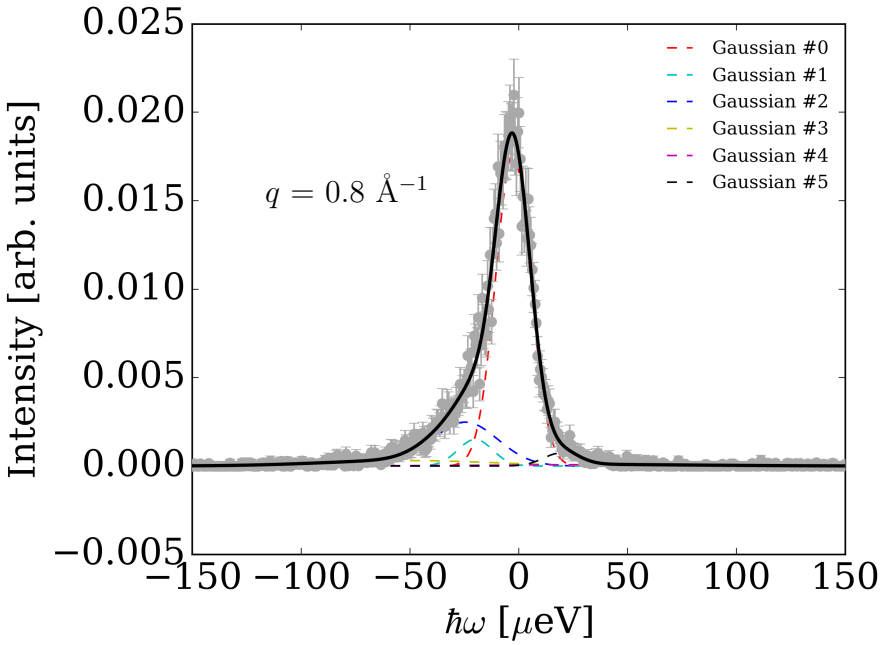

Figure 4.2: Energy resolution obtained from the fit, consisting of a sum of six Gaussian functions, of Vanadium spectrum measured on IRIS.

sion is preceeded by the fit of the deuterated unloaded solution and unloaded gel including one Lorentzian, a Dirac function $\delta(\omega)$ representing the elastic contribution of the gel network and the empty Al can, and a q-dependent sloped background $\alpha(q)\omega + \beta(q)$ for faster motions:

$$S_{\mathrm{D_2O}}(q,\omega) = a(q)\mathcal{L}_{\gamma_{\mathrm{solvent}}}(q) + b(q)\delta(\omega) + \alpha(q)\omega + \beta(q) \tag{4.2}$$

For the drug-loaded samples, we employed a model where the free fit parameters $a(q)$, $\gamma_{\mathrm{solvent}}$, $b(q)$, $\alpha(q)$, and $\beta(q)$ obtained from q-independent analysis of the solvent were fixed:

$$S_{\mathrm{drug}}(q,\omega) = c(q)\mathcal{L}_{\gamma_{\mathrm{drug}}}(q) + (1-\varphi)\cdot S_{\mathrm{D_2O}}(q,\omega) \tag{4.3}$$

Here, $\mathcal{L}_{\gamma_{\text{drug}}}(q)$ represents the Lorentzian function for the center-of-mass diffusion of DOX, and φ is the volume fraction occupied by DOX (set to $\varphi \sim 4.6\%$ in accordance with previous QENS studies on small drugs).[28]

4.3 Results and discussion

In the complex system studied in this work, the QENS signal may arise from the dynamics of the solvent, gel network, and drug molecules. These contributions can be distinguished by taking advantage of dynamical separation and selective deuteration. Our primary focus is on DOX, whose diffusion lies between the fast dynamics of water molecules and the slow fluctuations of the peptide network. The HWHM resulting from the fit of the solvent background (i.e., the unloaded solution and gel) according to eq. 4.2 (Fig. S3-S4) shows no discernible differences between the solution and all gel sequences across the observed q range and probed temperatures (Fig. S5c,d). Hence, any differences in DOX diffusion cannot be primarily attributed to changes in the dynamic behavior of the respective background.[28] The most notable variations arise from the Dirac intensity $b(q)$, which represents the elastic contributions of the solid gel network and follow, as expected the trend: sol $<$ F8 $<$ FK $<$ KF8K (Fig. S5(e)-(f)). The fitting results for the solvent were subsequently incorporated into the model for DOX (eq.4.3), which involved a single Lorentzian function to minimize the number of fitting parameters (Fig. S3-S4), ensuring stability across the investigated q range. To determine the diffusion coefficient (D) a jump-diffusion model was applied to the q-dependent line broadening, $\gamma_{\text{drug}}(q)$, derived from the spectral fits:

$$\gamma_{\text{drug}}(q) = \frac{Dq^2}{1 + \tau Dq^2} \tag{4.4}$$

This model describes a diffusion process that transitions from continuous Brownian motion at small q ($\gamma(q) \sim Dq^2$) to an asymptotic plateau at higher q ($\gamma(q) \sim \tau^{-1}$), reflecting motion that occurs through discrete "jumps" separated by a characteristic residence time τ, rather than as a continuous trajec-

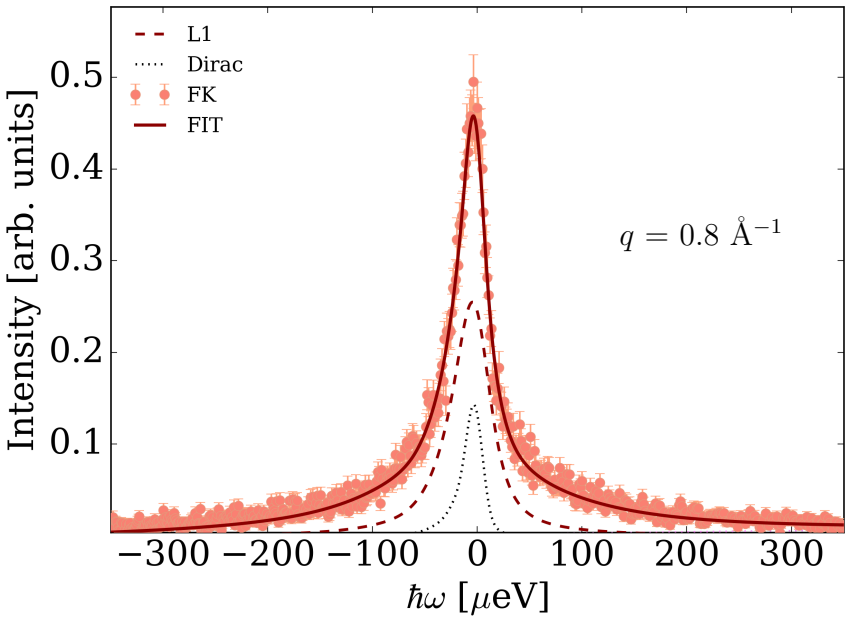

Figure 4.3: Example IRIS spectrum of 86 mM DOX in FK gel (14 mM), at $T = 310$ K and $q = 0.8$ Å^{-1}. Full line represents the fit of eq.4.3 consisting of the combined solvent and container contribution (dotted lines), drug diffusion (narrow thick dashed line) convoluted with the spectrometer resolution.

tory. The jump-diffusion framework has been successfully applied to solvent molecules and small drugs,[28, 33] though it is less effective for larger molecules like proteins.[34] Although DOX is larger than other studied drugs like ibuprofen sodium or paracetamol, it still falls within the category of small molecule drugs and its $\gamma(q)$ values in pure solution at 280 K, 295 K, and 310 K demonstrates this jump-like behavior, with temperature-dependent linewidth broadening (Fig. S6a). The first finding of this study is the significant retardation effect of the gels on DOX diffusion compared to the solvent alone. This retardation is observed at all temperatures, with a reduction in diffusion of approximately $\sim$ 70% (Fig. 4.4 and Table 4.1). The nonzero linewidth at low-q (Fig. 4.4) likely arises from the limited q range rather than macroscopic confinement effects caused by the gel fibers. This would appear as a plateau in the linewidths below $q \sim 2\pi/L_{\text{conf}}$, as shown in other confined media like zeolites.[35] According to Volino–Dianoux model of confined diffusion,[36] given

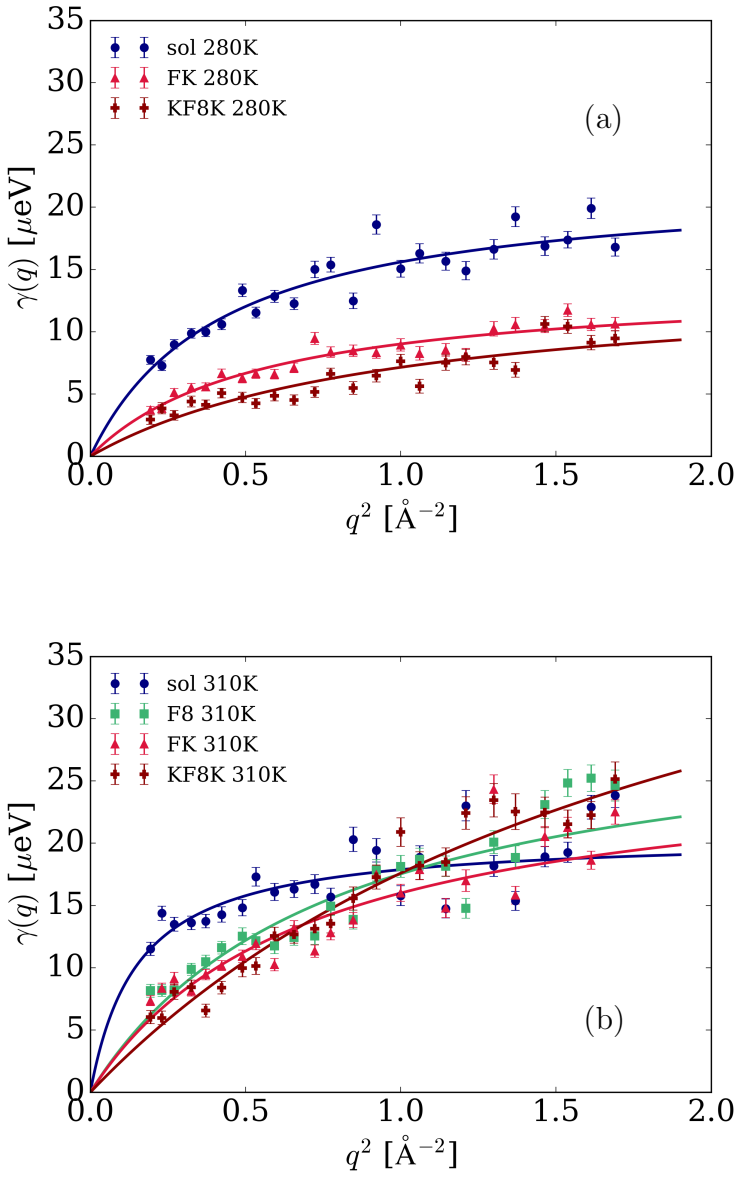

Figure 4.4: Summary of the Lorentzian linewidths $\gamma_{\text{drug}}(q)$ corresponding to the centre of mass diffusion at (a) $T = 280K$ and (b) $T = 310K$ of DOX fitted with a jump-diffusion model (Eq.4.4). F8, FK, and KF8K linewidths are shown separately in Fig.S8 for the ease of visualization.

the typical mesh size of this hydrogel family (20 – 40 nm)[23] confined motions would only become apparent at $q < 10^{-2}$ Å^{-1}, which is an order of magnitude smaller than the q range accessed in this study. Before discussing the results, it is important to recall the underlying assumption of this model: that the drug signal primarily consists of incoherent scattering, while the deuterated solvent background predominantly contributes coherent scattering. Recent neutron polarization analysis studies on proteins in solution have shown that non-negligible coherent contamination in the solute spectrum can lead to overestimation of peak broadening.[37] According to this study, this assumption strictly holds true where the incoherent signal dominates over the coherent, over a q-range that can be identified with neutron diffraction or by comparing the integrated spectral intensities of the drug and buffer. As shown in Fig.S7, the spectral intensities the DOX-loaded sample overlap at ~ 1.1Å^{-1} with those of unloaded deuterated backgrounds that become dominant above ~ 1.3Å^{-1}. This indicates that above ~ 1.3Å^{-1}, significant coherent contamination, likely originating from the hydration shell of the drug,[37] occurs and must be excluded to ensure the analysis primarily reflects incoherent contributions. Fig. S6 provides a complete analysis of the spectrum above this cutoff, with noisier Lorentzian linewidths that may reflect the coherent contamination. The measurement of DOX in pure solution provides a crucial and novel reference as it allows to account for the general effects of this family of peptide hydrogels, including F8, which was used as the reference in the previous study,[23] where its retardation effect was overlooked. Examining the molecular structure of the gel shown in Fig. 4.1a, the F8 gel offers one primary interaction site via hydrophobic or π-π stacking between the aromatic rings of DOX and the phenyl ring at the fiber edges. Alternatively, a cation-π interaction between DOX and lysine residues on the fiber surface could also occur.[23] However, this latter interaction was not considered significant on the UV-vis time scale, likely due to its transient nature and the proximity of oppositely charged glutamic acid residues, whose carboxyl groups may weaken the interaction. Cation-π interactions are highly dependent on the specific cation, the π-system involved, and the surrounding environment.[38] With QENS, which probes subtle hydro-

Table 4.1: Jump diffusion coefficients (D), obtained from eq. 4.4), for DOX diffusion in pure solution and F8, FK, KF8K gel

sample	**T [K]**	**D [10^{-9}m^2/s]**
solution	280	0.80 ± 0.06
FK gel		0.39 ± 0.03
KF8K gel		0.22 ± 0.03
solution	295	1.34 ± 0.02
KF8K gel		0.24 ± 0.02
solution	310	2.05 ± 0.37
F8 gel		0.61 ± 0.06
FK gel		0.59 ± 0.06
KF8K gel		0.40 ± 0.02

dynamic changes and ensemble-average diffusion on a timescale where such transient interactions might occur, it is plausible that this technique captures the breaking and reformation of these interactions at the fiber surface. This observation regarding the fiber surface effect on the neutral gel sequence F8 establishes a crucial baseline for the other studied gel sequences, FK and KF8K. While these sequences have electrostatic modifications at the fiber edges, they share the same surface chemistry as the neutral F8 gel.

A key breakthrough enabled by IRIS's energy resolution is the detection of subtle differences in DOX diffusion among the gel sequences, with a progressive slowdown observed from the neutral F8 to the lysine-rich, positively charged FK and KF8K sequences (Fig.4.4). This trend mirrors the order of slowing in

drug release studies, highlighting a clear correlation between short-timescale diffusion probed by QENS and long-timescale release behavior. However, before addressing the implications and correlations across time scales, it is important to first highlight the intrinsic differences between these two types of diffusion. The QENS-derived coefficient represents the self-diffusion of individual particles (H atoms of DOX, in this case), reflecting the ensemble-averaged dynamics at the molecular level. This self-diffusion is the thermodynamically-driven Brownian motion and exists even with homogeneous particle distribution. In contrast, the long-time diffusion coefficient represents bulk diffusion, determined by the concentration gradient between a drug reservoir and a receptor buffer, and is obtained by fitting the time-dependent drug concentration profile. Although the bulk diffusion coefficient approaches the short-time diffusion coefficient at high momentum transfer q (corresponding to very short length scales), the two parameters describe fundamentally different mechanisms and environments governing the drug dynamics. To correlate the diffusion coefficients obtained by QENS and UV-vis, we reference the coefficients derived from fitting the Higuchi equation, using the first burst release data.[23] This choice is based on the fact that the second release phase (after 17 hours) is likely influenced by imperfect sink conditions and receptor buffer saturation, which can slow the release. The two diffusion coefficients differ by two orders of magnitude (D_{UV} $\sim$$10^{-7}\mathrm{m}^2/\mathrm{s}$ and D_{QENS} $\sim$ $10^{-9}\mathrm{m}^2/\mathrm{s}$) and thus they are normalized for comparison in the scatter plot (Fig.4.5). Despite the limited sample size of three gel sequences, a positive correlation suggests that the impact of gel modification extends across two orders of magnitude. This indicates that the specific drug-gel interactions influencing short-time diffusion also affect long-time diffusion, even before steric confinement from the gel matrix becomes significant. The differential slowing down of bulk diffusion from FK and KF8K sequences has been attributed to differences in their chemistry.[23] The observed differences between FK and KF8K gels arise from variations in the fiber edge structure, which dictate the strength of cation-π interactions, the dominant force over electrostatic repulsion. In FK, the presence of a single lysine per edge leaves sections of the hydrophobic core exposed, enabling

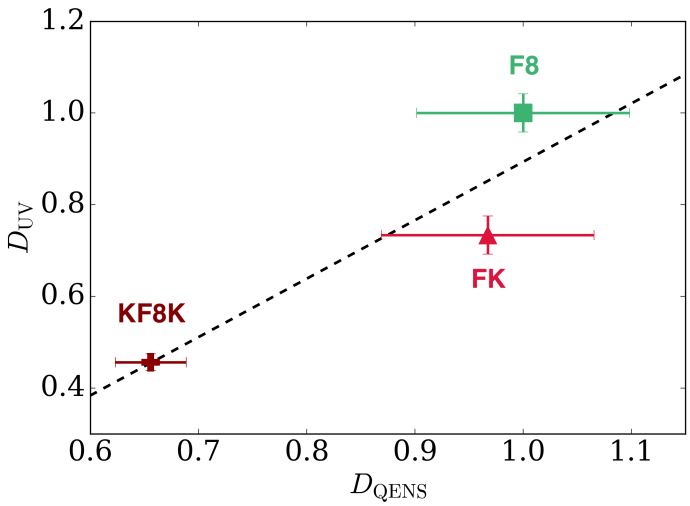

Figure 4.5: Correlation between the self-diffusion coefficient measured with QENS (D_{QENS} [10^{-9}m^2/s]) and bulk diffusion coefficient from Ref.[23] (D_{UV} [10^{-7}m^2/s]) of DOX in F8, FK and KF8K hydrogels at $T = 310K$, normalized to their respective maximum values. The scatter plot shows the experimental data with error bars representing the uncertainty in both measurements. The dashed red line represents the trend observed in the data.

additional hydrophobic interactions with DOX and weakening the strength of the cation-π interaction. In contrast, KF8K's two lysines per edge provide a different configuration: one lysine shields the hydrophobic core while the other aligns to the those decorating the surface. This difference in edge architecture significantly increases drug retention in KF8K compared to FK, although they share they same charge (Fig.4.1b). Specifically, KF8K retains 70% of DOX after 72 hours, whereas FK continuously allows drug release over the same period. Such hypothesis is supported by experimental conditions, particularly the low DOX-to-peptide molar ratio (240 μM DOX to 14 mM peptide), which enables precise control over the binding capacity. As a result, KF8K achieves a final bound DOX concentration of 170 μM.

Unlike drug release studies, where the strong UV absorbance of DOX enables measurements at low concentrations, QENS experiments operate under significantly different conditions. The technique requires a high concentration of

hydrogen-rich scatterers to distinguish the drug signal from the deuterated background. Consequently, the DOX concentration in QENS experiments is increased to 86 mM, compared to 240 μM in UV-vis studies. This substantial difference means that QENS provides orthogonal insights. Under these conditions, where all available cation-π interaction sites are likely saturated, QENS measurements are expected to capture the ensemble-averaged behavior of multiple DOX populations within the gel network.[39, 40] One population likely consists of bulk-like DOX molecules moving through the gel pores without direct interactions with the fibers, primarily influenced by hydrodynamic interactions. Another population may reside near the fiber surfaces, involved in transient cation-π interactions with lysine residues. However, these interactions could be weakened by the competing effect of neighboring carboxylic acid groups.[23] This population is likely common across all three gel sequences investigated in this work and therefore does not account for the differential slowing down observed. A third population may include DOX molecules directly interacting with fiber edges, exhibiting strong interactions in the KF8K and weaker interactions in FK and F8. However, this population likely has a minimal impact on the average diffusion coefficient measured by QENS. With bound DOX accounting for only $\sim 0.2\%$ of the total concentration, even assuming all fiber edges are exposed rather than hidden within larger bundles, these interactions are difficult to be detected with this technique. Hence, while the hypothesis of multiple DOX populations sheds light on the range of non-covalent interactions with the gel fibers, it may not fully account for the QENS results, particularly given the high DOX concentration used in these experiments. In fact, at the elevated DOX concentration in our QENS experiments, it is plausible that aggregation could occur, introducing a new factor that may dramatically alter the system's behavior. DOX aggregation has already been observed in previous studies in solution using transmission electron microscopy, dynamic light scattering and MD simulations,[41, 42] and favored by the presence of amphiphilic β-sheet forming peptide.[43] These studies show that this amphiphilic molecule forms dimers even at very low concentrations (73μM at pH 7.4) and at concentrations around 1 mM, aggregates of approx-

imately 40 molecules are present, with sizes approximately three times that of the monomer ($\sim$ 1.2 nm). The different fibre edge compositions and their effect on aggregation might explain the different observed diffusion coefficient. The varying fiber edge compositions in our gel systems likely influence DOX aggregation, which may help explain the observed differences in diffusion coefficients. Gels can create localized regions where DOX binds with varying strength, primarily through hydrophobic interactions and π-π stacking. For example, the KF8K gel, with more stable binding sites, could promote aggregate formation and increase cluster size, while the FK and F8 gels, with less stable interactions, would support weaker binding and fewer aggregates. Given that pH significantly influences DOX aggregation behavior,[41] it is important to assess whether the observed differences in diffusion coefficients and aggregation across gel sequences arise from varying protonation states of DOX, due to pH differences (5.0-5.7). This can be evaluated with the Henderson-Hasselbalch equation:

$$\mathrm{pH} = \mathrm{p}K_\mathrm{a} + \log_{10}\left(\frac{[\mathrm{A}^-]}{[\mathrm{HA}]}\right) \tag{4.5}$$

where $\mathrm{p}K_\mathrm{a}$ is the acid dissociation constant of DOX ($\mathrm{pK_a} \sim 8.2$ for the primary amine group, ~ 9.5 for the hydroxyl group), $[\mathrm{A}^-]$ is the concentration of the deprotonated form, and [HA] is the concentration of the protonated form. Our calculations reveal that the difference in DOX protonation between pH 5.0 and 5.7 is minimal, with 99.94% of molecules protonated at pH 5.0 and 99.68% at pH 5.7 for the primary amine group. Such small variation (0.26%) suggests that pH-induced changes in DOX protonation are unlikely to significantly influence its aggregation state or contribute substantially to the observed differences in diffusion coefficients across gel sequences. Consequently, the observed diffusion behaviors are driven by variations in gel fiber composition and their interactions with DOX aggregates, rather than pH-induced effects on DOX protonation, providing a more comprehensive explanation than the multiple population model alone. Another hyphotesis is that the differential slowing down of DOX diffusion is due to the altered solvent environment around the molecule. In previous studies, faster diffusion of solvent and drug in gels was

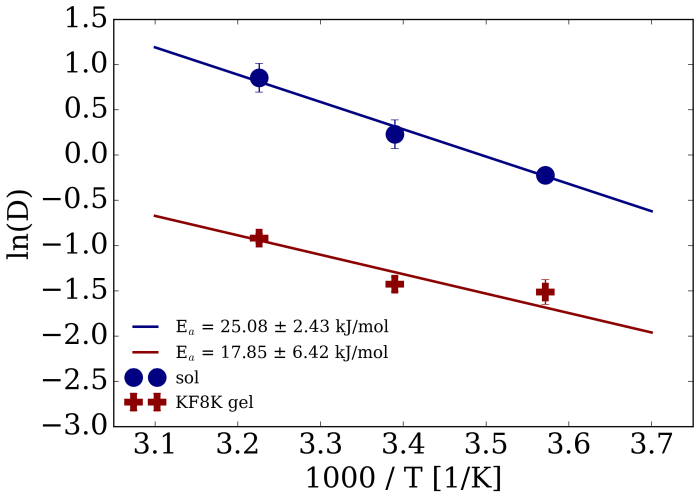

Figure 4.6: Arrhenius plot showing the temperature dependence of the jump-diffusion coefficients obtained via eq.4.4 for DOX in solution (circles) and DOX in KF8K gel (cross). Data reported in $\ln(D)$ vs $1000/T$ to simplify the visualization of the fit (lines) according to eq.4.6. In this representation the slope represents the Arrhenius activation energy E_a while the intercept is the pre-exponential factor A.

linked to the disruption of the solvent network caused by the hydrophobic nature of bis-urea supramolecular gels.[28, 33] In contrast, the gels used here, with their hydrophilic surfaces, may have the opposite effect, structuring water near the fibers and increasing local viscosity.[44] Additionally, the charged nature of the DOX molecule itself could further influence the structure of the surrounding solvent. This combined effect may account for the observed differences in diffusion, with the KF8K gel, having two lysine moieties per fiber edge, enhancing hydrophilicity and water structuring, while FK and F8 gels exhibit a less pronounced effect. To further support this hypothesis, the temperature dependence of DOX diffusion can be described using an Arrhenius-type relationship, where the observed changes in diffusion can be linked to the increase in local viscosity around the gel fibers. This relationship is expressed by the

equation:

$$D = A \exp\left(-\frac{E_a}{RT}\right) \tag{4.6}$$

where D is the measured diffusion coefficient, A is the Arrhenius pre-exponential factor, E_a is the Arrhenius activation energy, R the gas constant and T the temperature. From Fig.4.6, it is clear that both environments exhibit comparable activation energies for diffusion within the confidence bounds, as indicated by the nearly parallel slopes of the Arrhenius plots. In the case of solution, the activation energy can be attributed to the hindrance from the hydrogen-bond network, while for DOX in KF8K gel, the energy barrier reflects the combined effects of various non-covalent interactions, such as cation-π interactions and hydrogen bonds. These interactions, sharing similar non-covalent nature, contribute similarly to the overall barrier. However, despite the comparable activation energies, the two systems differ significantly in their pre-exponential factors $\ln(A)$, as shown by the different intercepts on the Arrhenius plot. The pre-exponential factor, often interpreted as a frequency factor, represents the likelihood of diffusion and its lower value in the KF8K gel might indicate that diffusion in this environment is less likely to occur than in solution. This can be viewed as a consequence of the gel structuring due to gel network, which potentially restricts the availability of free pathways for diffusion, thereby reducing the diffusion rate.[45]

4.4 Conclusions

This study provides critical insights into the role of subtle electrostatic modifications in β-sheet-forming peptide gelator to control molecular-level diffusion of DOX within hydrogels. QENS demonstrates that this class of hydrogels, including the neutral peptide sequence, effectively slows the dynamics of DOX even at very short time scales. Notably, QENS diffusion coefficients reveal a strong correlation with long-term drug release studies, with a slowing down of diffusion proportional to the number and position of terminal lysines at the

fiber edges (F8 FK KF8K), reflecting the strength of cation–π interactions that contribute to DOX retention.

While the higher DOX loading required for QENS experiments alters the stoichiometry of end-lysine/DOX interactions crucial in prior studies,[23] it provides orthogonal insights. At the high DOX concentration used here (86 mM), cation–π binding sites are likely saturated. As a result, QENS highlights the average slowing of diffusion as an outcome of multiple non-covalent interactions and mechanisms. These could include the existence of multiple populations of DOX molecules experiencing distinct forces (bulk-like dynamics, π–π stacking, hydrophobic and cation–π interactions), an increase in local viscosity due to solvent structuring by hydrophilic gel fibers, or DOX aggregation driven by local increase in concentration at stronger binding sites. The high loading of DOX, coupled with the stabilization of aggregates via peptide modification, presents a potential strategy to address the challenges associated with hydrogels for small oncologic drugs. Such drugs, often smaller than the hydrogel mesh size, can rapidly leak and cause off-target toxicity. The localized DOX-loaded depots, which can swell or degrade in response to the acidic pH characteristic of tumor environments,[46] offer a promising avenue for controlled drug release.[7, 13, 46, 47]

Our findings highlight the importance of adopting a multi-scale approach to study drug dynamics in complex materials such as hydrogels. By probing molecular-level dynamics at the shortest accessible time scales, our study complements existing research at the opposite end of the temporal spectrum, offering a more comprehensive description of how drug-fibre interactions evolve and influence drug release. Across time scales, the factors governing drug transport evolve, transitioning from non-steric to steric interactions, gel erosion or swelling, and shifts in diffusion mechanisms from Brownian motion to concentration gradient-driven processes. To fully capture this complexity, involving methods that probe intermediate time scales will be essential for bridging the gap between short-term dynamics and long-term drug release. This approach could boost traditional drug delivery studies, which typically focus on specific drug-hydrogel systems at a single time scale, by shifting from a phenomenolog-

ical description[48] to the systematic development of models that predict drug release based on molecular-level drug-fiber interactions. The class of peptides, examined here, represents an ideal toolbox for further investigation. By exploiting the functional diversity of the 20 natural amino acids, this peptide library enables systematic exploration of correlations between short- and long-time-scale drug dynamics. This approach can initially focus on further exploring the behavior of DOX as a reference model and later extend to other small-molecule therapeutics.

4.5 Supporting information

Model-free QENS spectra

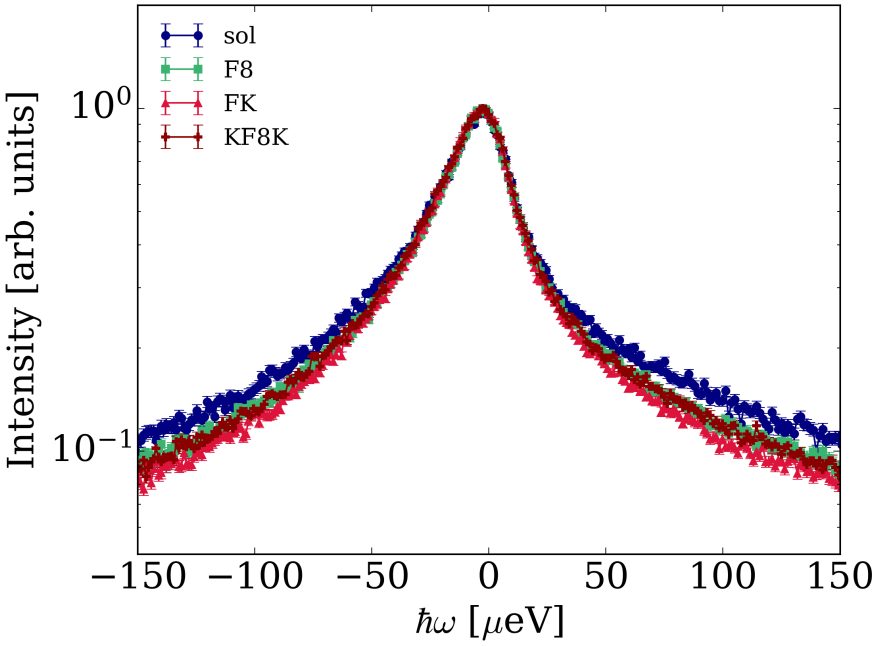

Figure S1: QENS spectra of DOX in solution, F8, FK and KF8K gels at $T = 310K$, normalized to peak maximum and summed over q. (Plot in lin-log)

Spectrometer resolution functions

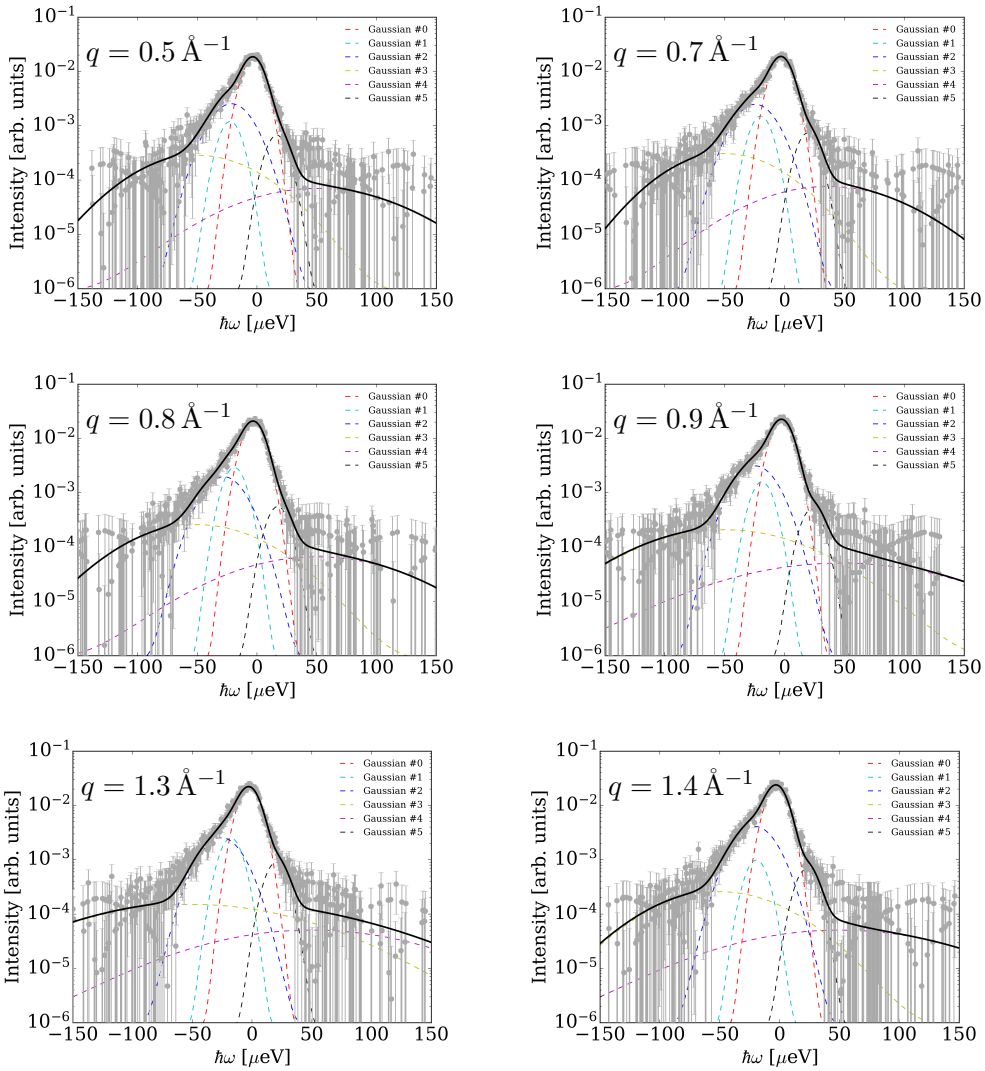

Figure S2: Fit of the energy resolution, measured with vanadium on IRIS, consisting in a sum of six Voigt functions. Plot shown in lin-log scale for a better visualization of the different Gaussian functions.

Fit: DOX in solution

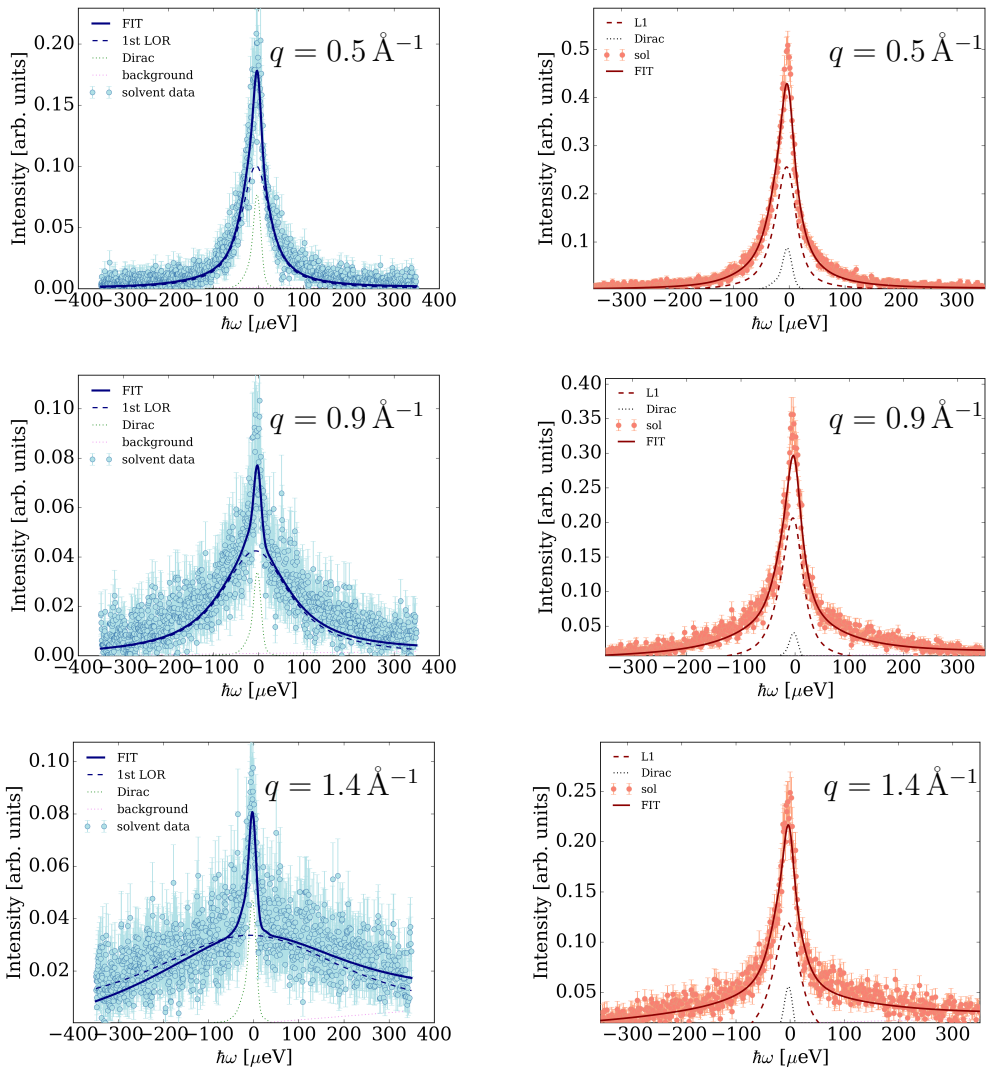

Figure S3: Example IRIS spectra of (right column) DOX in pure solution and (left column) respective background at $T = 310\,\text{K}$. The solid lines represent the fits according to eq.3 and eq.2, respectively.

Fit: DOX in KF8K gel

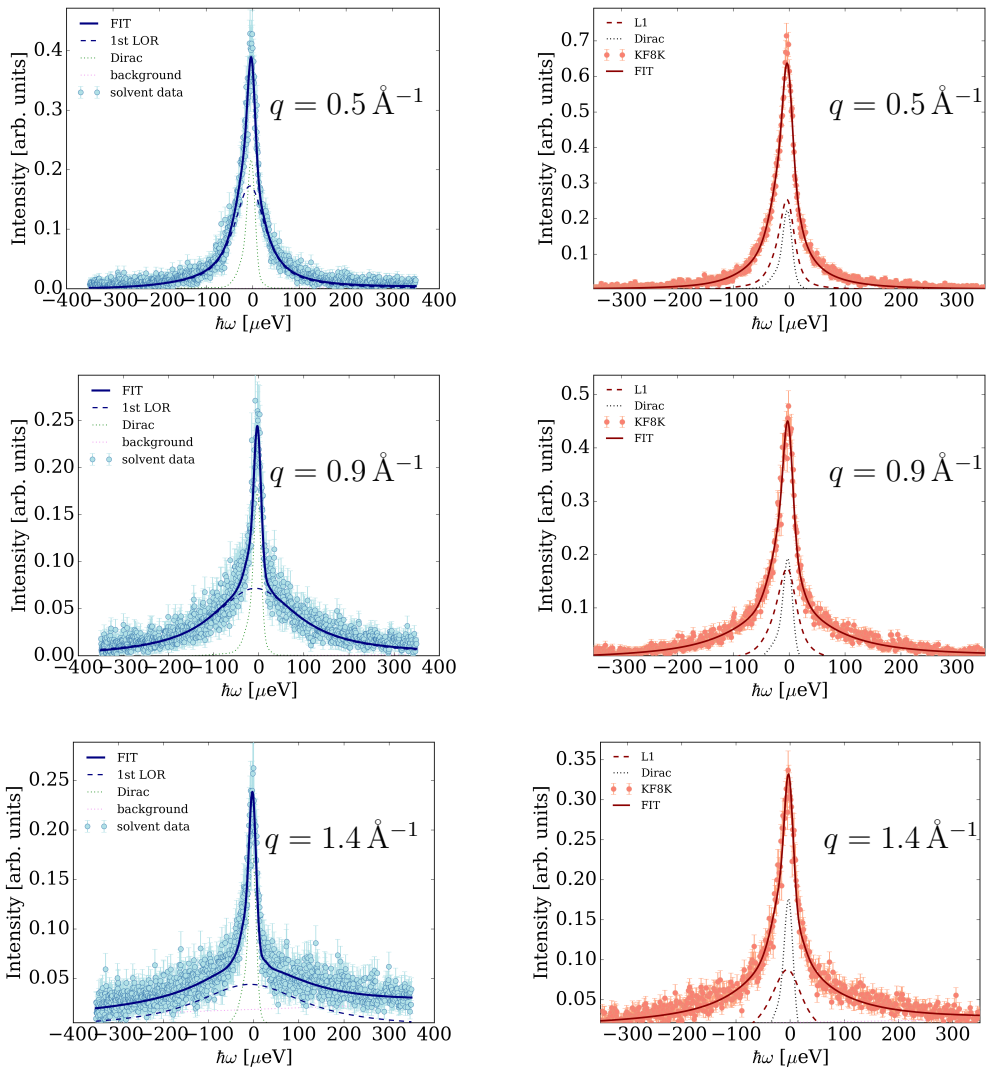

Figure S4: Example IRIS spectra of (right column) DOX in KF8K gel and (left column) respective background at $T = 310\,\text{K}$. The solid lines represent the fits according to eq.3 and eq.2, respectively.

Solvent fit parameters

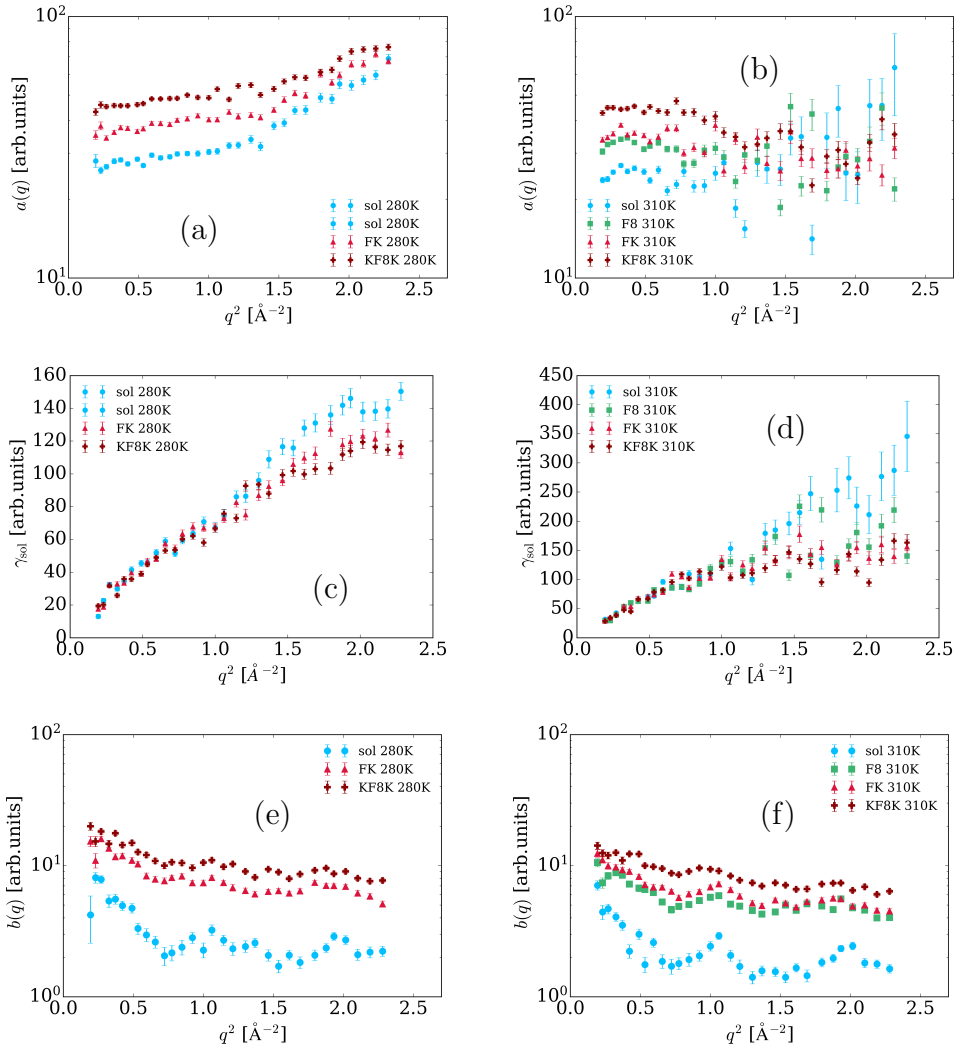

Figure S5: Fit parameters of deuterated background according to eq.2: (a)-(b) Lorentzian intensity $a(q)$;(c)-(d) Lorentzian $\gamma_{\text{sol}}(q)$;(e)-(f) Dirac intensity $b(q)$ at $T = 280K$ (left column) and $T = 310K$ (right column).

DOX fit parameters: $\gamma(q)$

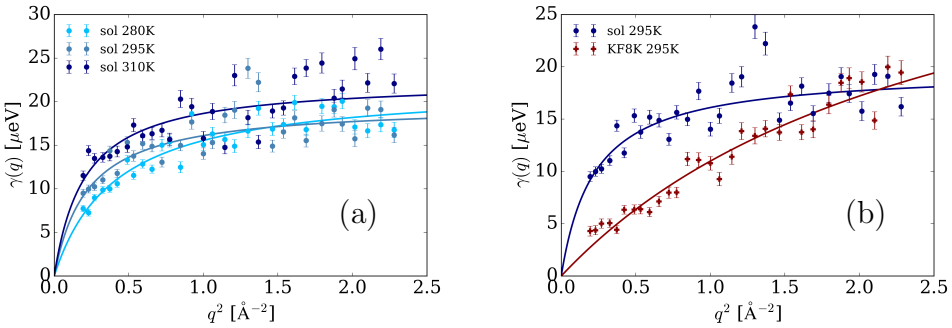

Figure S6: Summary of the Lorentzian linewidths $\gamma_{\text{drug}}(q)$ corresponding to the centre-of-mass diffusion of (a) DOX in pure solution as a function of temperature and (b) DOX in solution and KF8K gel at $T = 295$ K, fitted with a jump-diffusion model (Eq.4.4).

Integrated spectral intensity

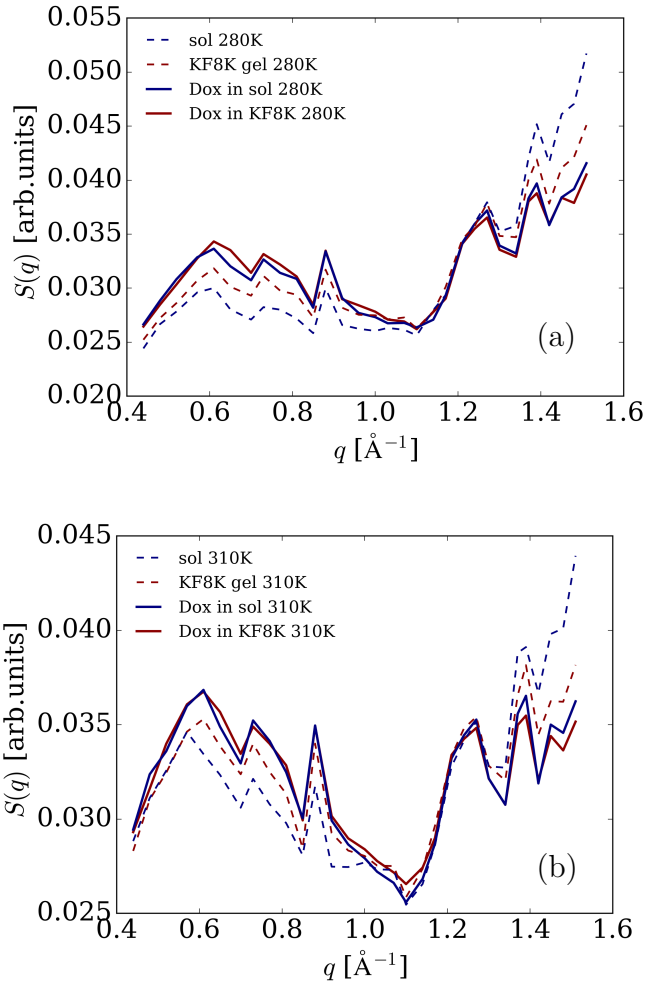

Figure S7: Integrated $S(q, \omega)$ intensity in the range -350 μeV $\leq \hbar\omega \leq$ +350 μeV at (a) $T = 280K$ and (b) $T = 310K$.

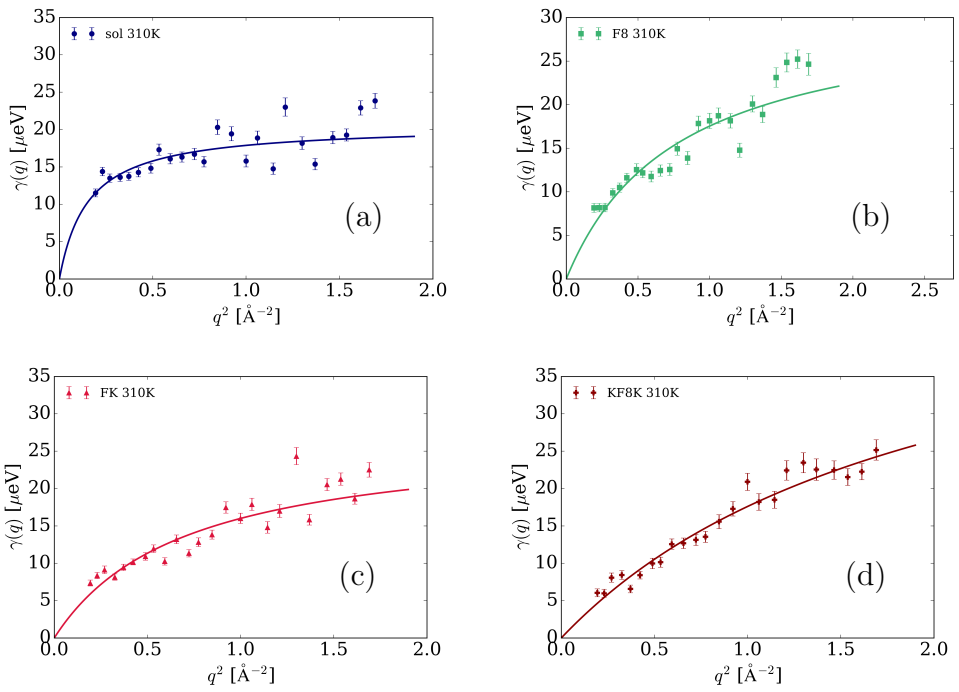

Figure S8: Summary of the Lorentzian linewidths $\gamma_{\text{drug}}(q)$ corresponding to the centre-of-mass diffusion of DOX at $T = 310K$ in (a) pure solution,(b) F8,(c) FK and (d) KF8K gel, fitted with a jump-diffusion model (Eq.4.4).

Data accessibility

The neutron data are permanently curated by the ISIS facility and accessible via the experiment number RB2310608, `https://doi.org/10.5286/ISIS.E.RB2310608-1`

Bibliography

[1] Aaron C Anselmo, Yatin Gokarn, and Samir Mitragotri. Non-invasive delivery strategies for biologics. *Nature Reviews Drug Discovery*, 18(1):19–40, 2019.

[2] Lei Zhong, Yueshan Li, Liang Xiong, Wenjing Wang, Ming Wu, Ting Yuan, Wei Yang, Chenyu Tian, Zhuang Miao, Tianqi Wang, et al. Small molecules in targeted cancer therapy: advances, challenges, and future perspectives. *Signal transduction and targeted therapy*, 6(1):1–48, 2021.

[3] Oktay Tacar, Pornsak Sriamornsak, and Crispin R Dass. Doxorubicin: an update on anticancer molecular action, toxicity and novel drug delivery systems. *Journal of pharmacy and pharmacology*, 65(2):157–170, 2013.

[4] NA Zhao, Martin C Woodle, and A James Mixson. Advances in delivery systems for doxorubicin. *Journal of nanomedicine & nanotechnology*, 9(5), 2018.

[5] Ava M Vargason, Aaron C Anselmo, and Samir Mitragotri. The evolution of commercial drug delivery technologies. *Nature biomedical engineering*, 5(9):951–967, 2021.

[6] Kenan Aloss and Peter Hamar. Recent preclinical and clinical progress in liposomal doxorubicin. *Pharmaceutics*, 15(3):893, 2023.

[7] Chunbao Zang, Yu Tian, Yujing Tang, Min Tang, Dingyi Yang, Fangfang Chen, Mohammadreza Ghaffarlou, Yanyang Tu, Milad Ashrafizadeh, and

Yan Li. Hydrogel-based platforms for site-specific doxorubicin release in cancer therapy. *Journal of Translational Medicine*, 22(1):879, 2024.

[8] Jianyu Li and David J Mooney. Designing hydrogels for controlled drug delivery. *Nature Reviews Materials*, 1(12):1–17, 2016.

[9] Trideva K Sastri, Vishal N Gupta, Souvik Chakraborty, Sharadha Madhusudhan, Hitesh Kumar, Pallavi Chand, Vikas Jain, Balamuralidhara Veeranna, and Devegowda V Gowda. Novel gels: an emerging approach for delivering of therapeutic molecules and recent trends. *Gels*, 8(5):316, 2022.

[10] Margaux Vigata, Christoph Meinert, Dietmar W Hutmacher, and Nathalie Bock. Hydrogels as drug delivery systems: A review of current characterization and evaluation techniques. *Pharmaceutics*, 12(12):1188, 2020.

[11] Sandrine Tanga, Marique Aucamp, and Poornima Ramburrun. Injectable thermoresponsive hydrogels for cancer therapy: challenges and prospects. *Gels*, 9(5):418, 2023.

[12] Qiang Zhang, Yu Zhang, Hui Chen, Lei-Na Sun, Bin Zhang, Dong-Sheng Yue, Chang-Li Wang, and Zhen-Fa Zhang. Injectable hydrogel with doxorubicin-loaded zif-8 nanoparticles for tumor postoperative treatments and wound repair. *Scientific Reports*, 14(1):9983, 2024.

[13] Mahrokh Dadsetan, Zen Liu, Matthias Pumberger, Catalina Vallejo Giraldo, Terry Ruesink, Lichun Lu, and Michael J Yaszemski. A stimuli-responsive hydrogel for doxorubicin delivery. *Biomaterials*, 31(31):8051–8062, 2010.

[14] Néstor A Pérez-Chávez, Victor Nosthas Aguiar, Juan A Allegretto, Alberto G Albesa, Juan M Giussi, and Gabriel S Longo. Triggering doxorubicin release from responsive hydrogel films by polyamine uptake. *Soft Matter*, 16(32):7492–7502, 2020.

[15] Kathryn J Skilling, Francesca Citossi, Tracey D Bradshaw, Marianne Ashford, Barrie Kellam, and Maria Marlow. Insights into low molecular mass organic gelators: a focus on drug delivery and tissue engineering applications. *Soft matter*, 10(2):237–256, 2014.

[16] JYC Lim, Q Lin, K Xue, and XJ Loh. Recent advances in supramolecular hydrogels for biomedical applications. *Materials Today Advances*, 3:100021, 2019.

[17] Danielle M Raymond, Brittany L Abraham, Takumi Fujita, Matthew J Watrous, Ethan S Toriki, Takahiro Takano, and Bradley L Nilsson. Low-molecular-weight supramolecular hydrogels for sustained and localized in vivo drug delivery. *ACS applied bio materials*, 2(5):2116–2124, 2019.

[18] Rienk Eelkema and Andrij Pich. Pros and cons: supramolecular or macromolecular: what is best for functional hydrogels with advanced properties? *Advanced Materials*, 32(20):1906012, 2020.

[19] Carlos BP Oliveira, Valéria Gomes, Paula MT Ferreira, José A Martins, and Peter J Jervis. Peptide-based supramolecular hydrogels as drug delivery agents: recent advances. *Gels*, 8(11):706, 2022.

[20] Shuguang Zhang, Davide M Marini, Wonmuk Hwang, and Steve Santoso. Design of nanostructured biological materials through self-assembly of peptides and proteins. *Current opinion in chemical biology*, 6(6):865–871, 2002.

[21] D Roberts, C Rochas, A Saiani, and AF Miller. Effect of peptide and guest charge on the structural, mechanical and release properties of β-sheet forming peptides. *Langmuir*, 28(46):16196–16206, 2012.

[22] Jacek K Wychowaniec, Andrew M Smith, Cosimo Ligorio, Oleksandr O Mykhaylyk, Aline F Miller, and Alberto Saiani. Role of sheet-edge interactions in β-sheet self-assembling peptide hydrogels. *Biomacromolecules*, 21(6):2285–2297, 2020.

[23] Mohamed A Elsawy, Jacek K Wychowaniec, Luis A Castillo Dí'az, Andrew M Smith, Aline F Miller, and Alberto Saiani. Controlling doxorubicin release from a peptide hydrogel through fine-tuning of drug–peptide fiber interactions. *Biomacromolecules*, 23(6):2624–2634, 2022.

[24] Aristides Dokoumetzidis and Panos Macheras. A century of dissolution research: from noyes and whitney to the biopharmaceutics classification system. *International journal of pharmaceutics*, 321(1-2):1–11, 2006.

[25] Marc Bée. Localized and long-range diffusion in condensed matter: state of the art of qens studies and future prospects. *Chemical Physics*, 292(2-3):121–141, 2003.

[26] Sylvie Spagnoli, Isabelle Morfin, Miguel A Gonzalez, Pierre Carcabal, and Marie Plazanet. Solvent contribution to the stability of a physical gel characterized by quasi-elastic neutron scattering. *Langmuir*, 31(8):2554–2560, 2015.

[27] MPM Marques, ALM Batista De Carvalho, V Garcia Sakai, L Hatter, and LAE Batista De Carvalho. Intracellular water–an overlooked drug target? cisplatin impact in cancer cells probed by neutrons. *Physical Chemistry Chemical Physics*, 19(4):2702–2713, 2017.

[28] Robert M Edkins, Markus Appel, Tilo Seydel, and Katharina Edkins. The modifying effect of supramolecular gel fibres on the diffusion of paracetamol and ibuprofen sodium on the picosecond timescale. *Physical Chemistry Chemical Physics*, 22(19):10838–10844, 2020.

[29] George H Vineyard. Scattering of slow neutrons by a liquid. *Physical Review*, 110(5):999, 1958.

[30] Gaio Paradossi, Francesca Cavalieri, Ester Chiessi, and Mark TF Telling. Supercooled water in pva matrixes: I. an incoherent quasi-elastic neutron scattering (qens) study. *The Journal of Physical Chemistry B*, 107(33):8363–8371, 2003.

[31] Owen Arnold, Jean-Christophe Bilheux, JM Borreguero, Alex Buts, Stuart I Campbell, L Chapon, Mathieu Doucet, N Draper, R Ferraz Leal, MA Gigg, et al. Mantid—data analysis and visualization package for neutron scattering and μ sr experiments. *Nuclear instruments and methods in physics research section a: accelerators, spectrometers, detectors and associated equipment*, 764:156–166, 2014.

[32] Christian Beck, Kevin Pounot, Ilaria Mosca, Niina H Jalarvo, Felix Roosen-Runge, Frank Schreiber, and Tilo Seydel. Notes on fitting and analysis frameworks for qens spectra of (soft) colloid suspensions. In *EPJ Web of Conferences*, volume 272, page 01004. EDP Sciences, 2022.

[33] Tilo Seydel, Robert M Edkins, Christopher D Jones, Jonathan A Foster, Robert Bewley, Juan A Aguilar, and Katharina Edkins. Increased rate of solvent diffusion in a prototypical supramolecular gel measured on the picosecond timescale. *Chemical Communications*, 54(49):6340–6343, 2018.

[34] Marco Grimaldo, Felix Roosen-Runge, Fajun Zhang, Frank Schreiber, and Tilo Seydel. Dynamics of proteins in solution. *Quarterly Reviews of Biophysics*, 52:e7, 2019.

[35] Alexander J O'Malley, M Sarwar, J Armstrong, Charles Richard A Catlow, IP Silverwood, APE York, and I Hitchcock. Comparing ammonia diffusion in nh 3-scr zeolite catalysts: a quasielastic neutron scattering and molecular dynamics simulation study. *Physical Chemistry Chemical Physics*, 20(17):11976–11986, 2018.

[36] F Volino and AJ Dianoux. Neutron incoherent scattering law for diffusion in a potential of spherical symmetry: general formalism and application to diffusion inside a sphere. *Molecular Physics*, 41(2):271–279, 1980.

[37] Mona Sarter, J Ross Stewart, Gøran Jan Nilsen, Mark Devonport, and Kirill Nemkovski. Data analysis of dynamics in protein solutions using

quasi-elastic neutron scattering important insights from polarized neutrons. *Journal of the American Chemical Society*, 2024.

[38] Dennis A Dougherty. The cation- π interaction. *Accounts of chemical research*, 46(4):885–893, 2013.

[39] Bing Li, Miryam Criado-Gonzalez, Alexandre Adam, Joëlle Bizeau, Christophe Mélart, Alain Carvalho, Sylvie Bégin, Dominique Bégin, Loïc Jierry, and Damien Mertz. Peptide hydrogels assembled from enzyme-adsorbed mesoporous silica nanostructures for thermoresponsive doxorubicin release. *ACS Applied Nano Materials*, 5(1):120–125, 2022.

[40] Anna Jagusiak, Katarzyna Chlopas, Grzegorz Zemanek, Pawel Wolski, and Tomasz Panczyk. Controlled release of doxorubicin from the drug delivery formulation composed of single-walled carbon nanotubes and congo red: A molecular dynamics study and dynamic light scattering analysis. *Pharmaceutics*, 12(7):622, 2020.

[41] Zoltán Fülöp, Ruxandra Gref, and Thorsteinn Loftsson. A permeation method for detection of self-aggregation of doxorubicin in aqueous environment. *International journal of Pharmaceutics*, 454(1):559–561, 2013.

[42] Sadaf Shirazi-Fard, Amin Reza Zolghadr, and Axel Klein. How does aggregation of doxorubicin molecules affect its solvation and membrane penetration? *New Journal of Chemistry*, 47(48):22063–22077, 2023.

[43] Shlomo Zarzhitsky and Hanna Rapaport. The interactions between doxorubicin and amphiphilic and acidic β-sheet peptides towards drug delivery hydrogels. *Journal of colloid and interface science*, 360(2):525–531, 2011.

[44] Manuel R Uhlig, Simone Benaglia, Ravindra Thakkar, Jeffrey Comer, and Ricardo Garcia. Atomically resolved interfacial water structures on crystalline hydrophilic and hydrophobic surfaces. *Nanoscale*, 13(10):5275–5283, 2021.

[45] Sergey Vyazovkin. Determining preexponential factor in model-free kinetic methods: how and why? *Molecules*, 26(11):3077, 2021.

[46] Ebbe Boedtkjer and Stine F Pedersen. The acidic tumor microenvironment as a driver of cancer. *Annual review of physiology*, 82(1):103–126, 2020.

[47] Jie Zhu, Rui Gao, Zhongshi Wang, Zhiming Cheng, Zhonghua Xu, Zaiyang Liu, Yiqun Wu, Min Wang, and Yuan Zhang. Sustained and targeted delivery of self-assembled doxorubicin nonapeptides using ph-responsive hydrogels for osteosarcoma chemotherapy. *Pharmaceutics*, 15(2):668, 2023.

[48] Brian Amsden. Solute diffusion within hydrogels. mechanisms and models. *Macromolecules*, 31(23):8382–8395, 1998.

Blank page

Chapter 5

Molecular structural dynamics in water–ethanol mixtures: Spectroscopy with polarized neutrons simultaneously accessing collective and self-diffusion

Author contribution: The neutron experiment were performed, prior to the beginning of the PhD project by Dr. Robert M. Edkins[c] and Prof. Katharina Edkins [e,*] with assistance from Mark Devonport[d] and Dr.Gøran Nilsen[d]. Riccardo Morbidini [a,b] performed the data analysis under the supervision of Dr. Tilo Seydel[a,*] and Dr.Gøran Nilsen. The project was conceived and supervised by Dr. Tilo Seydel and Prof. Katharina Edkins.

[a] Institut Max von Laue - Paul Langevin, 71 Avenue des Martyrs, F-38042 Grenoble, France.

[b] Division of Pharmacy and Optometry, University of Manchester, Oxford Road, Manchester M13 9PT, United Kingdom.

[c] WestCHEM Department of Pure and Applied Chemistry, University of Strathclyde, 295 Cathedral Street, Glasgow G1 1XL, United Kingdom.

[d] ISIS Neutron and Muon Source, Rutherford Appleton Laboratory, Didcot, OX11 0QX, United Kingdom.

[e] Strathclyde Institute of Pharmacy and Biomedical Sciences, University of Strathclyde, 161 Cathedral Street, Glasgow G4 0RE, United Kingdom

Abstract

Binary mixtures of water with lower alcohols display non-linear phase behaviour upon mixing which are attributed to potential cluster formation at molecular level. Unravelling such elusive structures requires the investigation of hydrogen-bonding sub-nanosecond dynamics. We employ high-resolution neutron time-of-flight spectroscopy with polarization analysis in combination with selective deuteration to study the concentration-dependent structural dynamics, in the water rich part of the phase diagram of water-ethanol mixtures. This method enables the simultaneous access to atomic correlations in space and time, and allows us to separate spatially incoherent scattering probing self-diffusion of the ethanol fraction from the coherent scattering probing collective diffusion of the water network as a whole. Our observations indicate an enhanced rigidity of the hydrogen bond network at mesoscopic lengthscale compared to the intra-molecular scale as the ethanol fraction increases, which is consistent with the hypothesis of clusters.

5.1 Introduction

Due to their role in food and pharmaceutical industry, as well as for biological and chemical research, water[1] and its binary mixtures with monohydroxy alcohols[2] have been the subject of sustained focus. Water and lower alcohols, such as methanol, ethanol and 1-propanol,[3] display intriguing properties e.g. negative excess entropy,[4] non-ideal phase behaviour upon mixing, and non-monotonous dependencies of volume, refractive index and viscosity on the mixing ratio.[5, 6] These macroscopic properties relate to the molecular complexity of the water hydrogen-bond network perturbed by the amphiphilic nature of alcohol molecules.[7, 8] The microheterogeneity at the molecular level is commonly interpreted in terms of local clusters,[9–12] whose topology and temperature, pressure and concentration dependence has been systematically examined through structural methods such as X-ray and neutron diffraction,[13–16] nuclear magnetic resonance spectroscopy (NMR)[17] or simulations.[12, 18] However, the structural description is not accompanied by a comprehensive dynamic profile,[19] due to the difficulty of tracking the elusive nature of H-bonded associates, whose lifetimes are typically on the order of picoseconds or less.[20] Pulsed-field gradient NMR spectroscopy (PFG-NMR) allows the measurement of the molecular self-diffusion[17] despite averaging over the cluster fluctuations, which are $\sim 10^9$ times faster than the NMR time resolution (millisecond). MD simulations match the desired observation scale for self diffusion of the individual species although the choice of the intermolecular force fields need experimental support.[21–25] Along with the self-diffusion of individual species, studying the dynamics of the H-bonded network as a collective ensemble is equally important. Dielectric spectroscopy (DS) has been widely used to identify collective dipole relaxation of water-ethanol mixtures.[26–31] Here, a low-frequency mode (corresponding to a timescale of $\sim$10 ps) has been attributed to the cooperative dynamics of the whole network which becomes less flexible with increasing ethanol ratio.[32, 33] However, these observations do not contain direct information on the spatial correlations. Neutron spectroscopy simultaneously accesses spatial and time correlations at the molecular level by measuring momentum

transfer $\hbar q$ and energy transfer $\hbar\omega$ and provides an ideal probe complementing NMR, MD simulations and DS.

Quasi-elastic neutron scattering (QENS) has been successfully employed to study the single-particle self-dynamics in pure water[34, 35] and in water-ethanol mixtures,[36] focusing on the ensemble-average response of hydrogen atoms that dominate the incoherent scattering. In contrast, measurements of collective motions have been limited to the ns timescale[37] with their impact on the ps timescale often minimized by limiting the coherent scattering length in the samples. Polarization analysis (PA)[38, 39] is the only way to unambiguously separate the coherent and incoherent QENS signals and it has already been applied to H-bonded liquids[40–42] building on theoretical concepts of collective density fluctuation in liquids on the mesoscale ($0.4\,\text{Å}^{-1} \leq q \leq 1.9\,\text{Å}^{-1}$).[43] The recent progress of polarization analysis on cold neutron spectrometers with sub-meV resolution allowed the heterogeneous coherent structural relaxation of water (D_2O) to be unravelled.[44, 45] Building on this result, we combine selective deuteration and PA to simultaneously measure self-diffusion of individual species in water-ethanol mixtures while analysing collective density fluctuations as a function of alcohol concentration.

5.2 Material and Methods

We performed neutron spectroscopy with polarization analysis on the cold neutron time-of-flight spectrometer LET at the ISIS facility, Rutherford Appleton Laboratory, Didcot, UK.[39, 46] The multi-chopper system of this direct geometry instrument provides three different sequential incident energies E_i of 3.84, 1.81 and 1.05 meV in a single measurement associated with three distinct energy resolutions, respectively $\Delta E \approx 131\mu$eV (3.4%E_i), $\Delta E \approx 45\mu$eV (2.5%E_i) and $\Delta E \approx 22\mu$eV (2.1%E_i) FWHM (example plots in the SI). We obtain separate QENS spectra for the coherent $S_{\text{coh}}(q,\omega)$ and incoherent $S_{\text{inc}}(q,\omega)$ scattering functions. We used specific deuteration, mixing deuterium oxide (D_2O) and ethanol-OD (C_2H_5OD) to distinguish water and ethanol at different ethanol mole fractions (0.0, 0.02, 0.05, 0.08, 0.12, 0.16, 0.20, 0.25, 0.30) near the max-

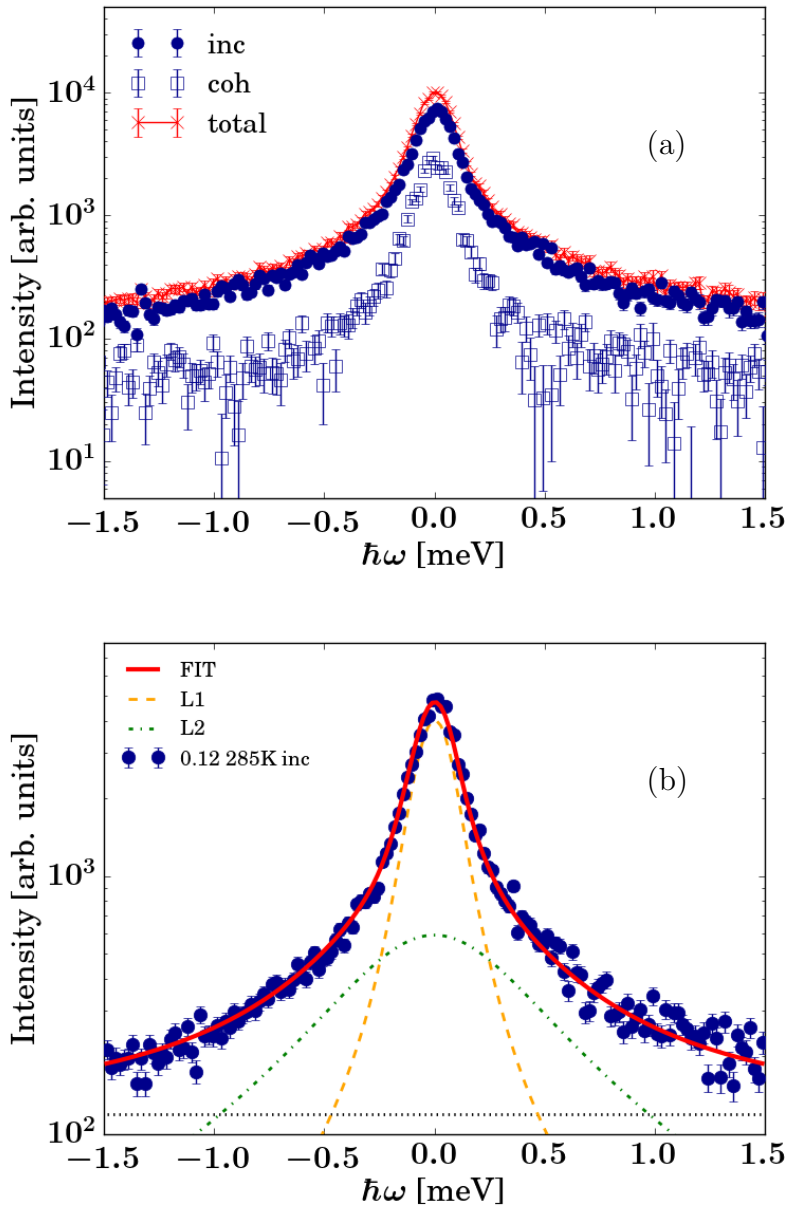

Figure 5.1: (a) Comparison of the coherent (open squares), incoherent (full circles) and total (red) scattering functions measured on LET on D_2O/C_2H_5OD at 0.12 ethanol mole fraction, T=285 K at q=1.6 Å^{-1}. (b) Example incoherent scattering function at q=1.4 Å^{-1} recorded on LET at E_i=3.84 meV. Fit (red solid line) according to eq.5.1 consisting of a sum of two Lorentzians (dashed and dash-dotted line) and an almost negligible flat apparent background (dotted line).

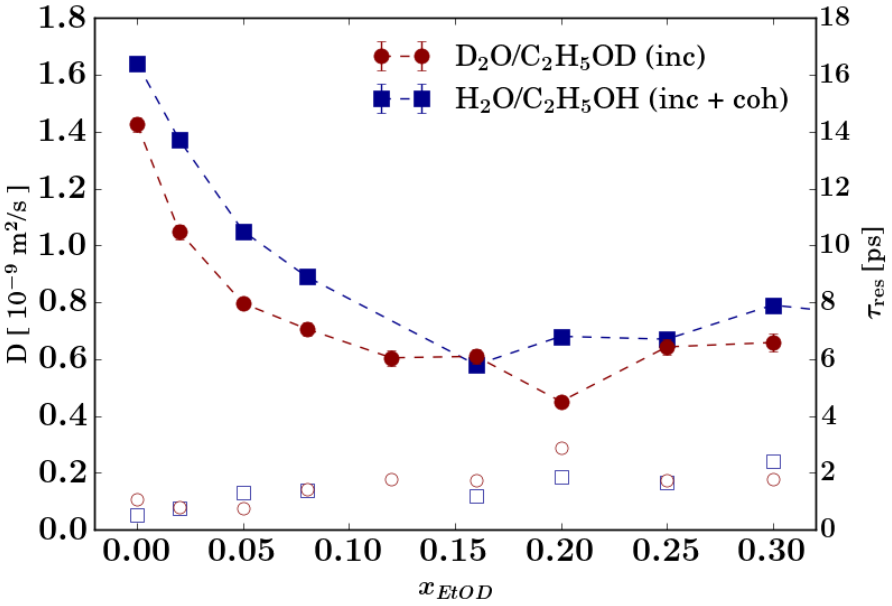

Figure 5.2: Diffusion coefficients D (full red circles) and residence times τ_{res} (open red circles) of D_2O/C_2H_5OD mixtures as a function of ethanol mole fraction x_{EtOD} at T=285 K and E_i=3.84 meV retrieved by imposing a jump diffusion model eq.5.2 on the HWHM vs q^2 of the fitted $S_{\text{inc}}(q,\omega)$. Hydrogen-rich mixtures H_2O/C_2H_5OH previously studied on LET without polarization analysis is reported for comparison (full blue squares D, open blue squares τ_{res}).[36] The error bars denote the 1σ confidence bounds from the diagonal elements of the covariance matrix of the fits, which are smaller than symbols for most data.

imum of macroscopic viscosity. Therefore, $S_{\mathrm{coh}}(q,\omega)$ will represent D_2O dynamics, while the five non-exchangeable hydrogens of C_2H_5OD give the higher incoherent scattering cross section and dominate $S_{\mathrm{inc}}(q,\omega)$. In addition, a mixture of D_2O and ethanol C_2D_5OD was measured to account for the effect of selective deuteration on the coherent structural relaxation of the hydrogen bond (HB) network.

5.3 Results and Discussions

Examples of coherent and incoherent QENS spectra are depicted in Fig. 5.1(a) displaying the comparison of the collected coherent, incoherent and calculated total scattering. While for pure D_2O the coherent term is dominant over the incoherent especially at q near the peak of the structure factor $S(q)$,[44] already at low alcohol concentration the coherent term is masked throughout the whole q range by the incoherent response arising from the non-exchangeable hydrogens of ethanol (see Fig. 5.1(a) and Fig.S1). Thus, only polarization analysis allows $S_{\mathrm{coh}}(q,\omega)$ to be accessed and at the same time to circumvent the De Gennes narrowing[47] which may affect the $S_{\mathrm{inc}}(q,\omega)$ when not separated from the $S_{\mathrm{coh}}(q,\omega)$. It has been shown how this leads to an underestimation of the self diffusion coefficient when there is no clear separation between coherent and incoherent spectra.[40]

Firstly we focused on the self-diffusion by fitting the reduced incoherent spectra with $S_{\mathrm{inc}}(q,\omega) \otimes \mathcal{R}(q,\omega)$ wherein the spectrometer resolution function $\mathcal{R}(q,\omega)$ is obtained by fitting a vanadium sample (Fig. S2) for each q independently and $S_{\mathrm{inc}}(q,\omega)$ is described by well established model for H_2O,[35]

$$S_{\mathrm{inc}}(q,\omega) = a_1(q)\frac{1}{\pi}\frac{\gamma_1(q)}{\gamma_1(q)^2+\omega^2} + a_2(q)\frac{1}{\pi}\frac{\gamma_2(q)}{\gamma_2(q)^2+\omega^2} + b(q), \tag{5.1}$$

consisting of a sum of two Lorentzian functions with amplitudes $a_i(q)$ and half width at half maximum (HWHM) $\gamma_i(q)$ accounting for slow translational process (i=1) and fast motions (i=2) with a small flat background $b(q)$ arising from instrument, sample, and sample environment contributions (Fig.5.1

and Fig. S3). Subsequently, the fit of the resulting HWHM for the narrower Lorentzian $\gamma_1(q)$ with the jump diffusion model,[34]

$$\gamma_1(q) = \frac{D_s q^2}{1 + \tau_{\text{res}} D_s q^2} \tag{5.2}$$

(see Figs. S4, S5, S6) yields the self-diffusion coefficients D_s and residence times τ_{res} displayed as a function of ethanol mole fraction x_{EtOD} in Fig. 5.2. Herein values found on H_2O/C_2H_5OH mixtures in the absence of polarization analysis are reported for comparison.[36] We find D_s for pure H_2O and D_2O consistent with previously published values.[34, 44, 48] The overall trend of D_s for the partially deuterated mixture shows a minimum near 0.2 mole fraction ethanol corresponding to the maximum of the macroscopic viscosity and aligns with the results for the ensemble average self diffusion of fully protiated mixtures.[36] Compared to those results, the larger decrease of the D_s found in the present work is in good agreement with PFG-NMR results,[17] where it is attributed to the H-bonded caging effect of water molecules around the alkyl group of ethanol. It is remarkable that PA with selective deuteration allows to observe a similar trend for the self-diffusion of the ethyl group protons to that observed by NMR but with a higher time resolution (from *ms* to *ps*). We further analyze the coherent neutron scattering data in terms of the imaginary part of the dynamic susceptibility $\chi''(q,\nu) = \pi S(q,\nu)[1+n(\nu)]^{-1}$, where ν is the frequency and $n(\nu)$ the Bose occupation number given by $n(\nu) = (e^{h\nu/k_B T} - 1)^{-1}$, allowing us to analyse the data in a model-free manner in the absence of analytical models describing the broadening of the coherent dynamic structure factor, especially at the mesoscale (cf. Figs. S7, S8 and S9).[40, 42–44, 49, 50] Moreover, the conversion to dynamic susceptibility enhances the dynamic components of the spectrum displaying them as separated peaks. In the case of D_2O, $\chi''_{\text{coh}}(q,\nu)$ displays two main dynamic features: a structural relaxation in the low frequency region ($\nu < 10^2$ GHz) associated with non-vibrational motion and a higher frequency process linked to vibrations.[44, 51] Increasing the fraction of ethanol C_2H_5OD in D_2O, the first clear effect of perturbation of the pure water system brought on by ethanol is the appearance of the a peak in the low

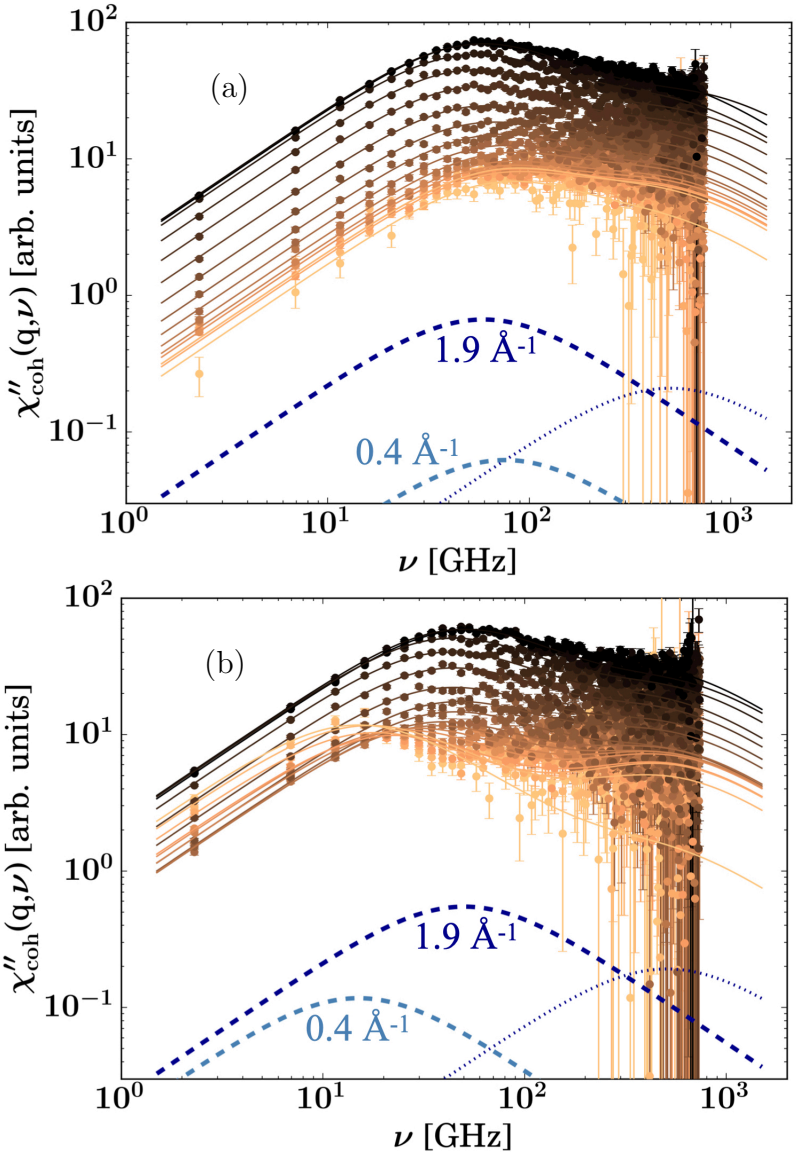

Figure 5.3: Imaginary part of the dynamical susceptibility for the coherent spectrum of D_2O (a) and C_2H_5OD in D_2O at 0.02 ethanol mole fraction (b). Spectra recorded at 285K with E_i=3.84 meV in the range (orange) $0.4\,\text{Å}^{-1} \leq q \leq 1.9\,\text{Å}^{-1}$ (black). The ethanol rich sample shows a q-dependent peak at $\nu \sim 10\,\text{GHz}$ while for pure D_2O the maximum is almost q-independent. The solid lines stand for the fit according to eq.6.2 consisting of the main Debye process (dashed lines, scaled by a factor 100 for visibility) depicted at smallest (lightblue) and highest (darkblue) q, and of the second Debye process (dotted lines, scaled by a factor 0.6 for visibility). Error bars hidden beneath markers.

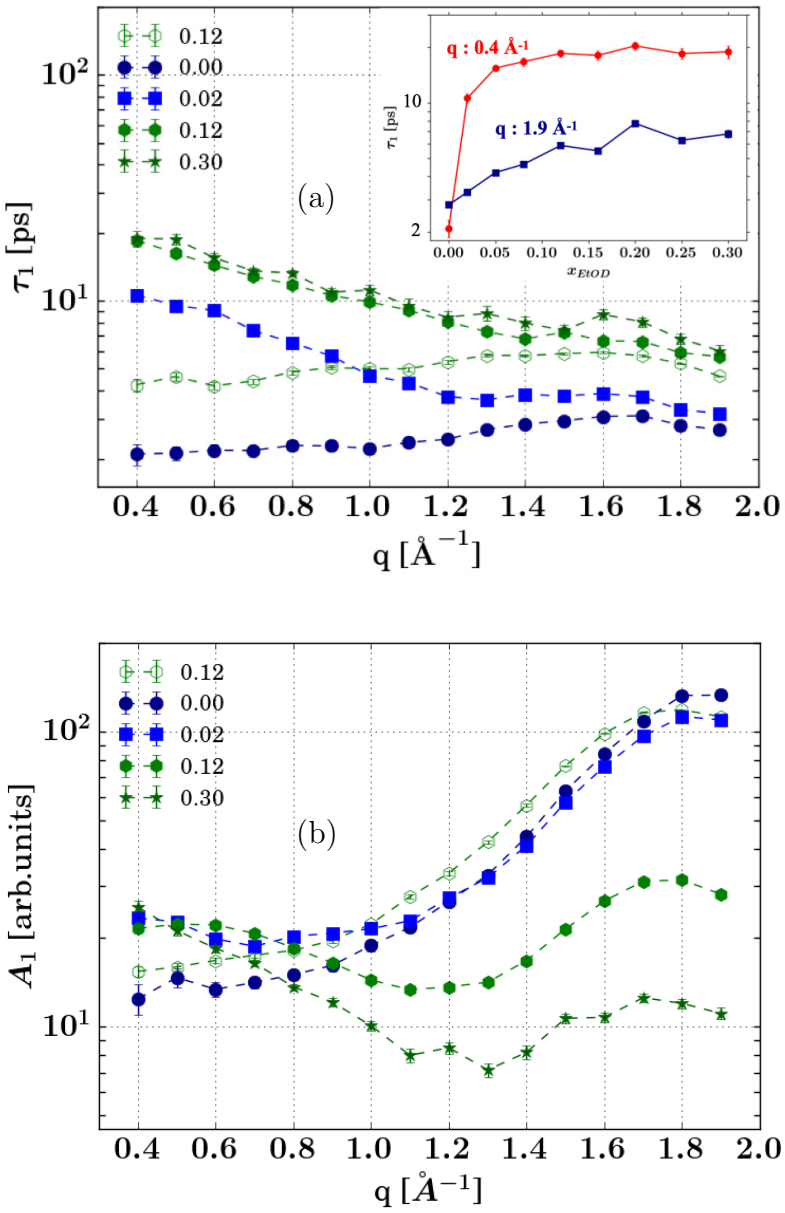

Figure 5.4: (a) Relaxation times $\tau_1(q)$ and (b) amplitude $A_1(q)$ of the main relaxation process of $\chi''_{\rm coh}(q,\nu)$ as a function of ethanol mole fraction at T=285 K and for E_1=3.84 meV (*solid symbols*: C_2H_5OD in D_2O). Values obtained from the fit through eq.6.2 and τ_1 retrieved from the peak position $\nu_i^{\rm max} = (2\pi\tau_1)^{-1}$. *Open symbols*: C_2D_5OD in D_2O, 0.12 ethanol mole fraction and T=290 K. *Inset*: τ_1 vs ethanol mole fraction at q=0.4 Å^{-1} (red) and q=1.9 Å^{-1} (blue). A_1 is obtained from the spectra solely normalized to the incident beam intensity. Error bars hidden beneath markers.

frequency region ($\nu \approx 10\,\mathrm{GHz}$, Fig. 5.3). To quantitatively model $\chi''_{\mathrm{coh}}(q,\nu)$ we use a linear combination of Debye-like relaxations,

$$\chi''_{\mathrm{coh}}\big(q,\nu\big) = \sum_i A_i(q) \frac{\nu \cdot \nu_i^{\max}(q)}{\nu^2 + \nu_i^{\max}(q)^2}. \tag{5.3}$$

i.e. Lorentzians in susceptibility with peak position $\nu_i^{\max}$ and amplitudes $A_i(q)$ with index i, corresponding to exponential decays in the time domain with the relaxation time $\tau_i(q) = \big(2\pi\nu_i^{\max}(q)\big)^{-1}$. In this picture we find two processes, as for pure D_2O: a main slow relaxation at low frequencies, also referred to as "α-relaxation", and a second mode in the THz region (Fig. 5.3). The resulting $\tau_1(q)$, associated with the peak position of the main relaxation process, is depicted in Fig. 5.4 for the coherent part. Different models have been tested, with a variable number of generalized Debye processes (*i.e.* Cole-Cole or Cole-Davidson relaxations) but the presented model with a sum of two Lorentzians provides the best match without over-fitting the experimental data. For pure D_2O, we observe a q-independent relaxation $1\,\mathrm{ps} \leq \tau_1 \leq 3\,\mathrm{ps}$ up to 1.2 $\mathrm{\AA}^{-1}$ followed by a maximum at ~ 1.7 $\mathrm{\AA}^{-1}$ associated with the D_2O nearest neighbour distance. This result shows a good agreement with the recent work on pure D_2O by Arbe *et al.* who interpret the q-independent τ as consequence of the combination of terms making up the $S_{\mathrm{coh}}(q,\omega)$.[44] This comprises three main components,

$$S_{\mathrm{coh}}(q,\omega) = \sum_{\alpha,\beta} b^{\alpha}_{\mathrm{coh}} b^{\beta}_{\mathrm{coh}} S_{\alpha\beta}(q,\omega) \tag{5.4}$$

$$S_{\alpha\beta}(q,\omega) = S^{\mathrm{self}}_{\alpha\alpha}(q,\omega) + S^{\mathrm{dist}}_{\alpha\alpha}(q,\omega) + S^{\alpha\neq\beta}_{\alpha\beta}(q,\omega) \tag{5.5}$$

where $S_{\alpha\beta}(q,\omega)$ are the partial dynamic structure factors of all pairs of atomic species α and β (H, D, O and C for water-ethanol mixture) weighted by their coherent scattering lengths $b^{\alpha}_{\mathrm{coh}}$ and b^{β}_{coh}; $S^{\mathrm{self}}_{\alpha\alpha}$ and $S^{\mathrm{dist}}_{\alpha\alpha}$ refers to the same and distinct particles of the same species α, respectively. With the help of MD, Arbe *et al.* interpreted the q-independent $\tau \leq 1\,\mathrm{\AA}^{-1}$ as a consequence of the cancelling out of $S^{\mathrm{dist}}_{\alpha\alpha}$ and $S^{\mathrm{self}}_{\alpha\alpha}$.[45] In our work, we find that in the range

between 0.02 and 0.3 ethanol mole fraction the relaxation times increase by up to one order of magnitude to $8\,\mathrm{ps} \leq \tau_1 \leq 20\,\mathrm{ps}$ (Fig. 5.4). This finding aligns to what has been shown for the same system by dielectric spectroscopy (DS) in the microwave region: the analysis of the dielectric loss for water-ethanol mixtures in terms of Debye relaxations reveals that τ_1, associated with the structural reorganization of the HB network, [26, 33] linearly increases with ethanol mole fraction. According to the "wait-and-switch" model, [26, 33] the fluctuation of the hydrogen bond donors and acceptors between water and the -OH group are hindered by the reduction of available hydrogen bonding sites with increasing ethanol fraction. Our model fit for $\chi''_{\mathrm{coh}}(q,\nu)$ confirms this dynamical observation while adding structural information encoded in q. Two distinct regions can be distinguished in figure 5.4 also at lower incident energies (Fig. S10): for $0.4\,\mathrm{Å}^{-1} \leq q \leq 1.2\,\mathrm{Å}^{-1}$ $\chi''_{\mathrm{coh}}(q,\nu)$ has a marked q dependence while the slope observed for pure water in $1.2\,\mathrm{Å}^{-1} \leq q \leq 1.9\,\mathrm{Å}^{-1}$ flattens. The overall increase in the relaxation time is more pronounced in the low q region and is not linearly related to mole fraction. Looking at τ_1 as a function of ethanol mole fraction for two q values it is clear how two different functional forms describe the relaxation time for meso- to intra-molecular scale (Fig.5.4a (inset)). We note that the susceptibility representation can lead to instabilities in the total spectral area calculation for some samples due to noise in the high frequency region (cf. Fig. S11). Importantly, the observed time scales may be influenced by limitations imposed by the spectrometer energy resolution (cf. Fig. S12) and be reflecting maxima of distributions of times, as possibly expected for clusters with a distribution of lifetimes. We note that the resolution has not explicitly been accounted for in χ''_{coh} but is nearly independent of q for a given incident energy (Fig.S2).

Interestingly, the observed steeper increase of $\tau_1(x_{EtOD})$ at low q (inset of Fig.4(a), $q = 0.4\,\mathrm{Å}^{-1}$) corresponds to length scales that can be associated with the angular reorientations of the molecular dipoles probed by DS in terms of an "effective q".[52] Thus, at this low q, the dipole reorientations seen by DS can be connected with collective density fluctuations seen by coherent QENS, as previously reported for pure water.[52] These density fluctuations may be asso-

ciated with short-lived concentration fluctuations due to transient mesoscale inhomogeneities[53] seen, e.g., by simulations,[54] small-angle scattering,[55] and indirectly inferred by thermodynamic analysis.[56] The distinct q-dependence of $\chi''_{\rm inc}(q,\nu)$ illustrates the key information from polarization analysis to access collective motions. Here, the relaxation time $\tau_1^{\rm inc}$ displays a strong q-dependence over the entire q range consistent with the underlying diffusive process with a self-diffusion coefficient given by $D_{\rm s} \sim (\tau_1^{\rm inc} q^2)^{-1}$ (Fig. S13). While $\tau_1^{\rm inc}$ and $\tau_1^{\rm coh}$ for D_2O are one order of magnitude apart in the low q region(Fig. 5.4(a), Fig. S13),[44] self- and collective relaxations for the binary mixture attain the same time window already at small ethanol fraction. Therefore the q-dependence of $\tau_1^{\rm coh}$ implies a diffusive process that is collective in nature as it arises from the pair-correlation function embodied in the coherent part of the spectrum in $\chi''_{\rm coh}(q,\nu)$. As such, the "wait-and-switch" between different hydrogen-bonding sites is driven by approaching molecules at the ps time scale and neutron data with PA can directly probe these motions. In contrast to the increase in τ_1, we observe a divergent trend for the per-deuteration (Fig.5.4 open symbols): the relaxation profile D_2O/C_2D_5OD is closer to that of pure D_2O than to its partially deuterated D_2O/C_2H_5OD counterpart at the same ethanol mole fraction. This effect of deuteration might be linked to the interplay between the terms that make up the $S_{\rm coh}(q,\omega)$ (eq.5.5). It is likely that in the fully deuterated mixture the self and distinct terms cancel out similarly to the case of water,[44] while for D_2O/C_2H_5OD they do not. This cancellation leads to the absence of the prepeak, expected in the mesoscale, in S(q) which is obtained by integration over the final energy,

$$S(q) = \int_{-\infty}^{\infty} S_{\rm coh}(q,\omega) d\omega \tag{5.6}$$

(Fig. S14). The prepeak usually appears as a shoulder on the low-q side of the S(q) maximum and, although its origin is still debated, in case of other lower alcohols is thought to be related to H-bonded molecular associates at distances longer than the first coordination shell.[13, 57] There is an increasing consensus regarding the significance of deuteration in observing the prepeak.[38] It has

been shown that the prepeak in the coherent structure factor of methanol is only visible in CH_3OD and not in CD_3OD, [38, 41, 42] consistent with MD simulations. This observation agrees with the picture of the cancellation of the different partial factors for H and D depending on the q range. The connection between structure and dynamics embodied in τ_1 is clearly depicted in the plots of the amplitude $A_1(q)$, *i.e.* the second free fit parameter of eq.6.2, for $\chi''_{\mathrm{inc}}(q,\nu)$ (Fig. S13) and $\chi''_{\mathrm{coh}}(q,\nu)$ (Fig. 5.4b). Due to the normalization of the spectra to the incident beam intensity, $A_1(q)$ (Fig. 4b) reports the different coherent scattering intensities depending on mixing ratio, which in terms of average over q are similar across the range explored (cf. figure S15). While for the incoherent spectra $A_1(q)$ is constant in q with only a non monotonous dependence on the ethanol mole fraction (see Fig. S13), the amplitude of the main coherent relaxation process has an additional q-dependence (Fig.5.4b). In particular for D_2O, $A_1(q)$ matches the $S(q)$ shape[44] with a gradual drop for $q \geq 1.1$ Å^{-1} and conversely an increase for $q \leq 1.1$ Å^{-1} upon ethanol addition. Even for $A_1(q)$ the fully deuterated mixture (open symbols) better aligns to the case of pure D_2O than to its partially deuterated counterpart. These findings for $A_1(q)$ are consistent with the picture of $S_{\mathrm{coh}}(q,\omega)$ being $S_{\mathrm{inc}}(q,\omega)$ modulated by the structure factor $S(q)$.

5.4 Conclusions

In conclusion, employing the newly established sub-meV resolution polarization analysis and partial deuteration, we simultaneously measure: (i) self-diffusion of ethanol in the water matrix circumventing de Gennes narrowing; (ii) collective density fluctuations of the hydrogen bond network in the picosecond regime on a q range from the meso- to intra-molecular scale. Compared to pure water, we observe a slower collective relaxation time upon increasing ethanol fraction with a steeper decrease in the mesoscale (0.4-1.2 Å^{-1}) where the prepeak for lower alcohols has been observed. Coherent QENS reveals that the addition of small amounts of ethanol renders the hydrogen bond network significantly more rigid compared to pure water, consistent with long

lived H-bonded cluster-like mesostructures. By studying a binary molecular mixture, this work fills a gap around the H-bonded fluids in the ps and mesoscale, that were previously only investigated as mono-molecular systems by high-resolution polarized QENS,[44, 58] and provides a non-MD dependent experimental basis suggesting the existence of clusters in water-ethanol mixtures.

5.5 Supporting information

Polarization analysis

In a quasi elastic scattering experiment, both collective and self motions contribute to the broadening of the elastic peak (figure S1), and the double differential scattering cross section, *i.e.* the probability that a neutron is scattered by a nucleus into a solid angle element $\partial\Omega$ and with a change in energy $\partial\hbar\omega$, thus reads as linear combination of the coherent $S^{\mathrm{coh}}(q,\omega)$ and incoherent $S^{\mathrm{inc}}(q,\omega)$ dynamic structure factors

$$\frac{\partial^2\sigma}{\partial\Omega\partial\hbar\omega} \propto \sum_{\alpha,\beta} \bar{b_\alpha}\bar{b_\beta} S^{\mathrm{coh}}_{\alpha\beta}(q,\omega) + \sum_{\alpha} \Delta\bar{b}^2_\alpha S^{\mathrm{inc}}_\alpha(q,\omega) \tag{5.7}$$

where the sums run over the atomic species α,β (H, D, O and C for water-ethanol mixtures) weighted by their scattering lengths $b_{\alpha,\beta}$. $S^{\mathrm{coh}}(q,\omega)$ and $S^{\mathrm{inc}}(q,\omega)$ are related via time and real space Fourier transform to the Van Hove correlation functions $G_{\alpha\beta}(r,t)$ and $G^{\mathrm{self}}_\alpha(r,t)$ describing the correlations between the position of distinct nuclei at different times and of the same nucleus at different times, respectively. For the majority of studied systems $\frac{\partial^2\sigma}{\partial\Omega\partial\hbar\omega}$ $\simeq S^{\mathrm{inc}}(q,\omega)$ due to the ubiquitous presence of hydrogen atoms whose scattering is predominantly incoherent. However, this approximation shows limits for poorly incoherent scattering samples or for those systems in which the solvent contribute is masked by deuteration. In this cases both coherent and incoherent terms coexist making data interpretation more complex. The only way to decouple the two contributions from eqn.(5.7) is by polarization analysis (PA),

a method that relies on the principles that the neutron scattering probability is not only isotope but also spin-dependent and that for incoherent scattering the neutron spin has a 66% probability to flip while for coherent scattering no spin flip happens. In an unpolarized experiment the incident neutron beam has 50% of spin up $|\uparrow\rangle$ and 50% of spin down $|\downarrow\rangle$ neutrons while with PA a supermirror polarizer is implemented to transmit the $|\downarrow\rangle$ state of the neutron beam. In order to exploit the link between spin-flip $|\downarrow\rangle \rightarrow |\uparrow\rangle$/non-spin-flip $|\downarrow\rangle \rightarrow |\downarrow\rangle$ and incoherent $S^{\mathrm{inc}}(q,\omega)$/coherent $S^{\mathrm{coh}}(q,\omega)$ dynamic structure factors, spin are reversed using a precession coil flipper and the spin polarization of the scattered neutron beam is analyzed.[59, 60] On LET this last step is made with a ^{3}He spin filter with a typical initial polarization of 63% and lifetime of 48 hours. The cell was replaced every $\sim$ 24 hours. The polarization corrections were performed using the correction scheme described in Ref.[61] The combined flipper and polarizer efficiencies for the three incident energies E_i = 3.84, 1.81, 1.05 meV were 90%, 91%, and 91%, respectively.

The result of this process are two distinct dynamic structure factors related to spin-flip $S_{|\downarrow\rangle\rightarrow|\uparrow\rangle}(q,\omega)$ and non-spin-flip $S_{|\downarrow\rangle\rightarrow|\downarrow\rangle}(q,\omega)$ events which are then combined to obtain the separation between $S_{\mathrm{inc}}(q,\omega)$ and $S_{\mathrm{coh}}(q,\omega)$ as follows:

$$\begin{cases} S_{|\downarrow\rangle\rightarrow|\uparrow\rangle}(q,\omega) = S_{\mathrm{coh}}(q,\omega) + \frac{1}{3}S_{\mathrm{inc}}(q,\omega) \\ S_{|\downarrow\rangle\rightarrow|\downarrow\rangle}(q,\omega) = \frac{2}{3}S_{\mathrm{inc}}(q,\omega) \end{cases} \quad \begin{cases} S_{\mathrm{coh}}(q,\omega) = S_{|\downarrow\rangle\rightarrow|\downarrow\rangle}(q,\omega) - \frac{1}{2}S_{|\downarrow\rangle\rightarrow|\uparrow\rangle}(q,\omega) \\ S_{\mathrm{inc}}(q,\omega) = \frac{3}{2}S_{|\downarrow\rangle\rightarrow|\uparrow\rangle}(q,\omega) \end{cases} \tag{5.8}$$

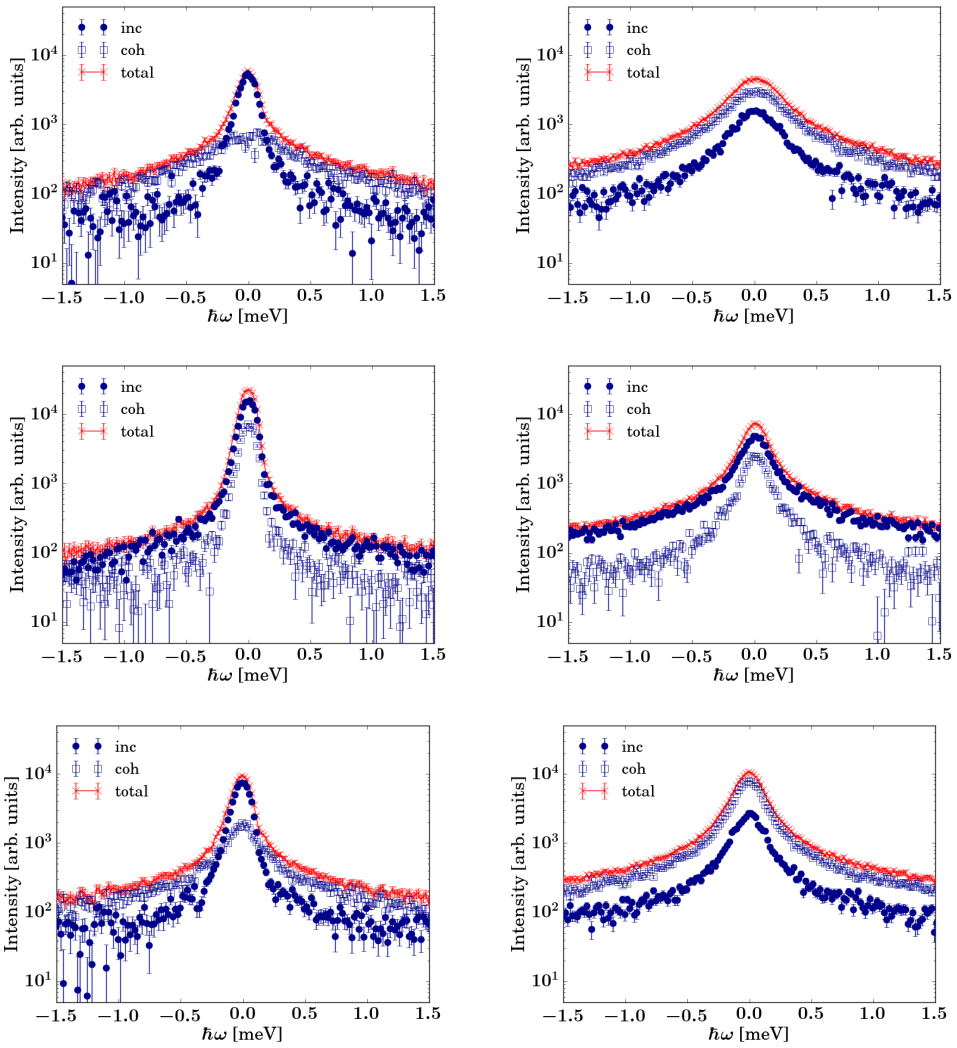

Figure S1: Comparison of the coherent (empty squares), incoherent (dark full circles) and total (red crosses) scattering functions measured on LET at $q = 1.0$ Å^{-1} (left column) and $q = 1.9$ Å^{-1} (right column). In the case of pure D_2O (top row) the coherent spectrum becomes dominant at higher q, corresponding to $S(q)$. At lower q, the incoherent spectrum is dominant and, thus, polarization analysis becomes crucial to obtain collective-like dynamic information. When mixed with C_2H_5OD (0.12 ethanol mole fraction, middle row) there is no q value where the coherent signal is dominant so polarization is even more crucial to account for collective motion even at the intramolecular scale. The fully deuterated mixture D_2O/C_2D_5OD (0.12 ethanol mole fraction, bottom row), on the other hand, shows a similar behaviour to that of pure D_2O.

Instrument resolution

Instrument resolution has been accounted for by fitting the vanadium incoherent spectrum with a sum of up to five Gaussian functions (depending on q and incident energy), due to the asymmetric shape of the instrument response (Fig. S2).

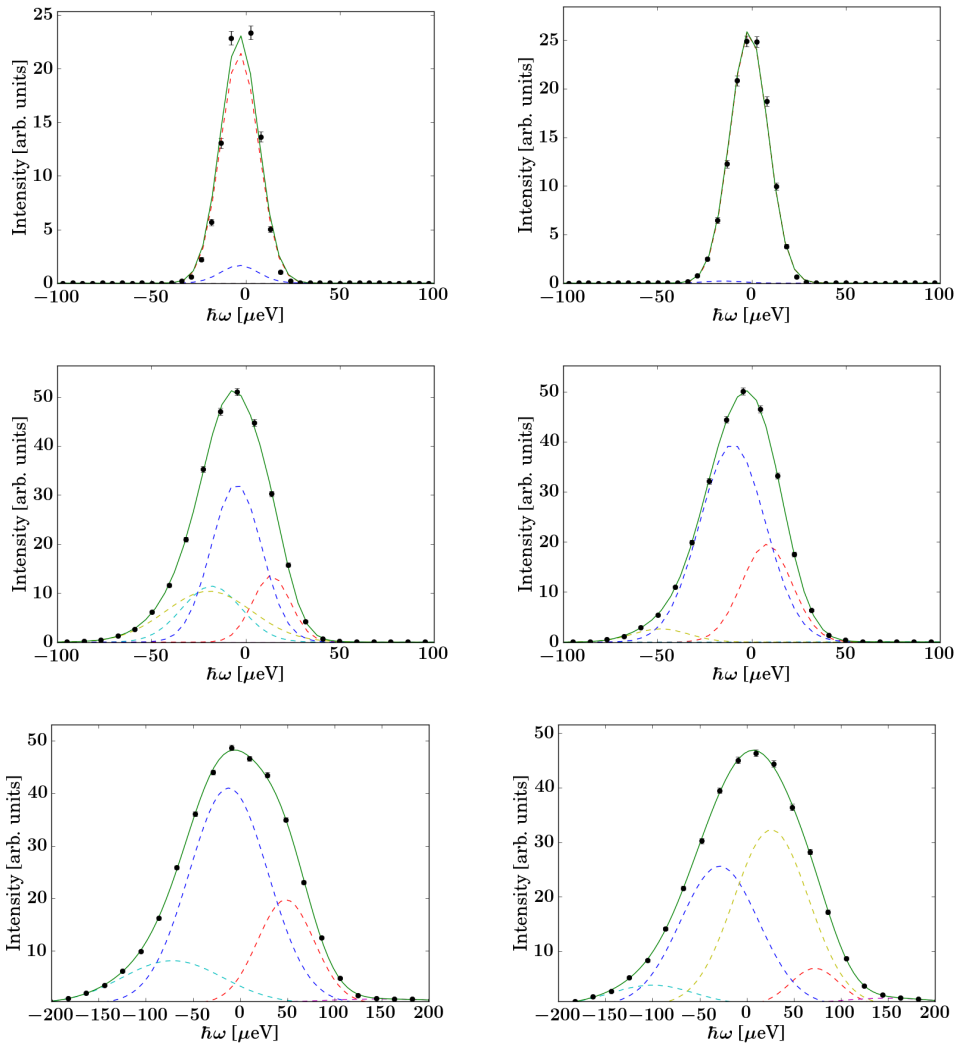

Figure S2: Energy resolution data of LET (symbols), measured on Vanadium foil at $T = 285$K, and fits of a sum (solid lines) of up to 5 Gaussian functions (dashed lines), at $q = 0.7$ Å^{-1} (left column) and $q = 1.1$ Å^{-1} (right column). The three different incident energies $E_i = 1.05$ meV (first row), 1.81 meV (second row) and 3.84 meV (third row) provide three distinctly different widths which each weakly depend on q.

Self-diffusion in the partially deuterated mixture

To favour convergence of the fit to physically meaningful values, the second Lorentzian has been constrained to be broader than the first Lorentzian, in agreement with a convolution of these two motions, as done in previous work.[35] This constraint prevented cross-talking (i.e. inversion) between the two Lorentzian functions during the iterative least squares minimization. The essential fit parameters and goodness-of-fit χ^2 are summarized in the figures S4 and S5 for different mixing ratios. Other models have been tested as well, including a Dirac contribution to account for immobile fractions and un-subtracted empty cell signal, but the finally chosen model presented was the most aligned with the experimental data.

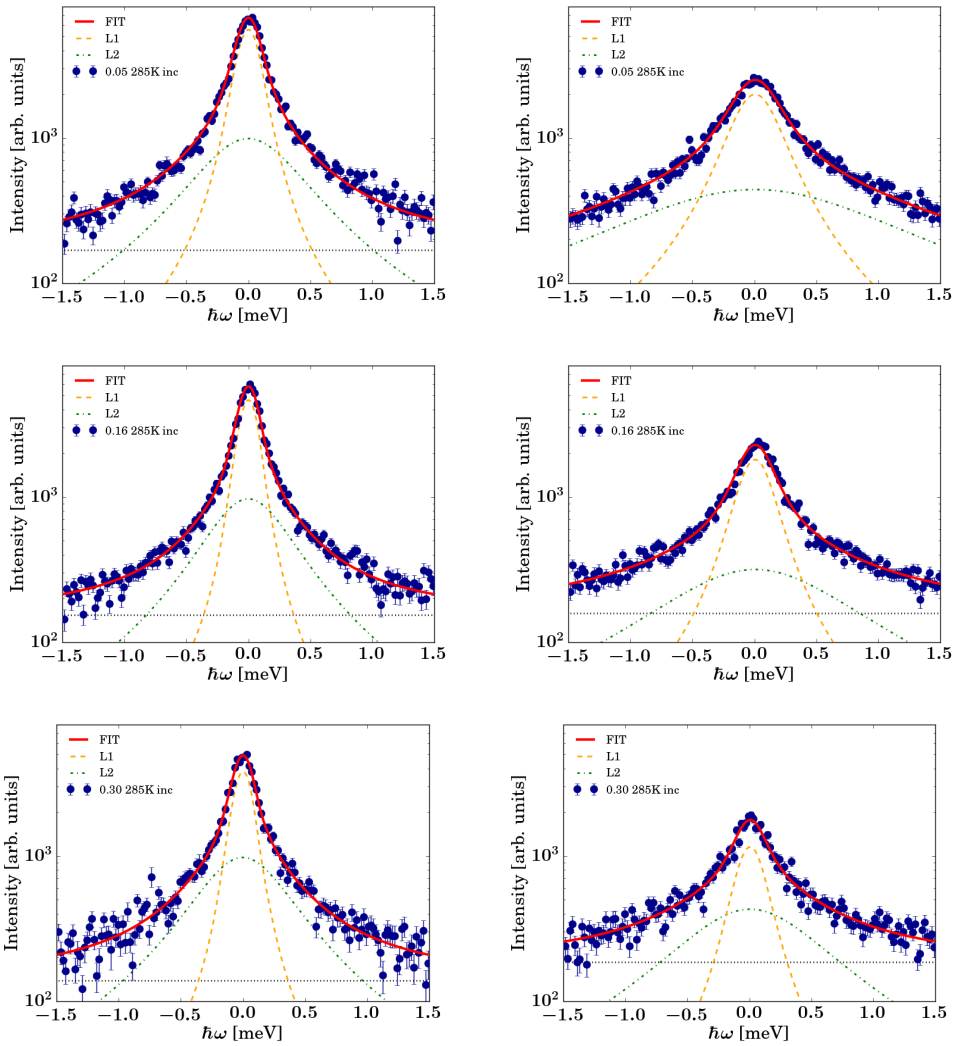

Figure S3: Example incoherent scattering function at q=1.3 Å^{-1} (left column) and q=2.1 Å^{-1} (right column) recorded on LET at E_i=3.84 meV at T=285K. Fit (red solid line) according to eqn. 1 of the main text consisting of a sum of two Lorentzians (dashed and dash-dotted line) and an almost negligible flat apparent background (dotted line). Top row: 0.05 ethanol mole fraction, middle row: 0.16 ethanol mole fraction, bottom row, 0.3 ethanol mole fraction.

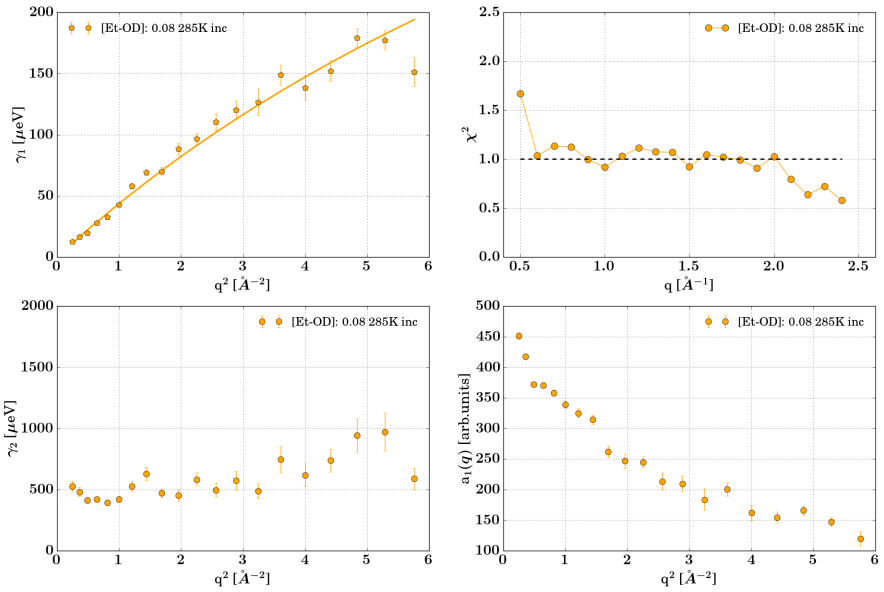

Figure S4: Plot of the fit parameters according to eqn. 1 of the main text for D_2O/C_2H_5OD at 0.08 ethanol mole fraction, at T=285K and E_i=3.84meV. Top left: Lorentzian width $\gamma_1(q)$ associated with the center of mass translation of the molecule. The solid line stands for the fit of the jump diffusion model. Bottom left: Lorentzian width of the second faster process $\gamma_2(q)$ that can be attributed to localized motions with no marked q-dependence. Top right: reduced χ^2 for the fit. Bottom right: Intensity of the first Lorentzian $a_1(q)$.

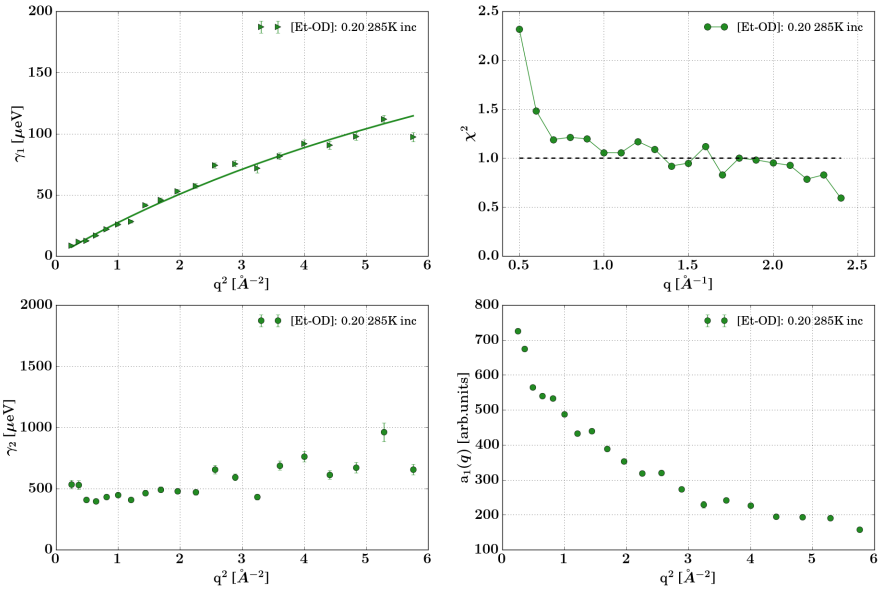

Figure S5: Plot of the fit parameters according to eqn. 1 of the main text for D_2O/C_2H_5OD at 0.2 ethanol mole fraction, at T=285K and E_i=3.84meV. Top left: Lorentzian width $\gamma_1(q)$ associated with the center of mass translation of the molecule. The solid line stands for the fit of the jump diffusion model. Bottom left: Lorentzian width of the second faster process $\gamma_2(q)$ that can be attributed to localized motions with no marked q-dependence. Top right: reduced χ^2 for the fit. Bottom right: Intensity of the first Lorentzian $a_1(q)$.

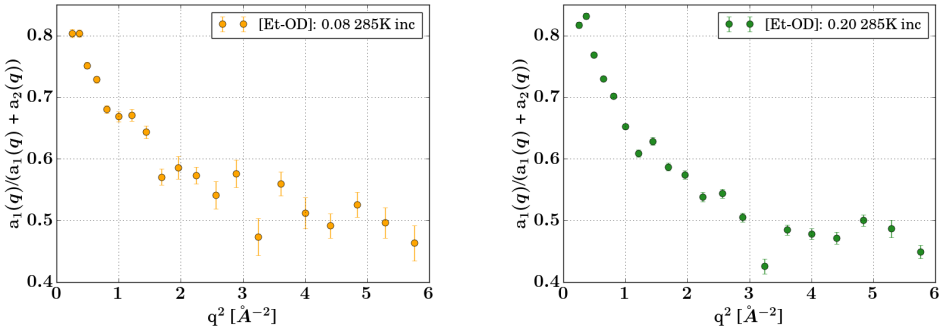

Figure S6: Fractional intensity of the first Lorentzian $a_1(q)/(a_1(q)+a_2(q))$ for 0.08 (left) and 0.2 (right) ethanol mole fraction.

Collective diffusion in the partially deuterated mixture

We also tested the same approach employed for the incoherent spectra on coherent spectra, i.e., imposing a sum of two Lorentzians convoluted with the spectrometer resolution (see Figure S7-S8 below). However, the lack of a theoretical model to interpret the quasi-elastic signal of the coherent part of the spectrum prevents us from interpreting the underlying collective dynamics.
One heuristic approach is to relate collective to single particle motion via renormalization by the static structure factor $S(q)$ as proposed by Sköld:[62]

$$\frac{S_{coh}(q,\omega)}{S(q)} \approx S_{inc}\left(\frac{q}{\sqrt{S(q)}},\omega\right) \tag{5.9}$$

We did not follow this approach for two main reasons:
(1) It fails to predict the correct q-dependence of $S(q,\omega)$ at q lower than the peak of the structure factor.[43] This would affect our observations which are more pronounced in the mesoscale.
(2) The interpretation of the resulting apparent collective diffusion function $D_c(q)$ would be subject to the same lack of theory.
In contrast, the susceptibility picture provides these advantages:
- In this representation, well separated peaks allow to distinguish distinct processes.
- The results can be directly compared with dielectric spectroscopy.
- Due to the novelty of our data, we benefit from relying on an established approach for data analysis, permitting to compare with the work on pure D_2O.
- The effect of the instrument resolution at ambient temperature does not pose a substantial problem since the dynamics is sufficiently fast. It would be a limit for systems with slower dynamics, such as in the supercooled regime.

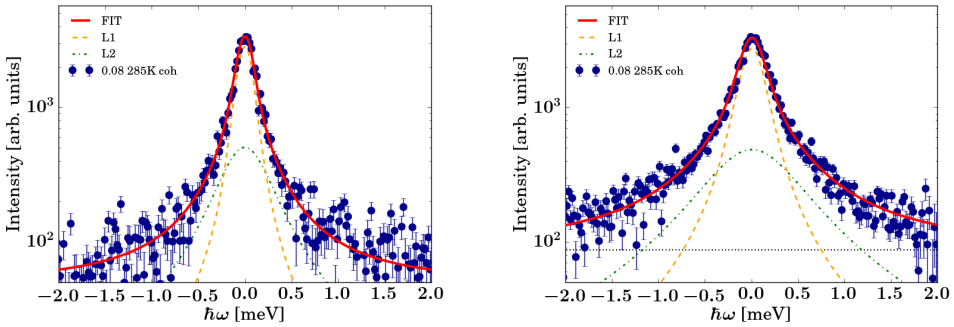

Figure S7: Example coherent scattering function at q=1.3 Å^{-1} (left column) and q=2.1 Å^{-1} (right column) recorded on LET at E_i=3.84 meV, T=285K and 0.08 ethanol mole fraction. Fit (red solid line) according to eqn. 1 of the main text consisting of a sum of two Lorentzians (dashed and dash-dotted line) and an almost negligible flat apparent background (dotted line).

Coherent susceptibility

The conversion to susceptibility $\chi''_{\mathrm{coh}}(q,\omega)$ and the model used to fit $\chi''_{\mathrm{coh}}(q,\omega)$ is inspired by previous neutron work on polarized neutrons[44]

$$\chi(q,\nu) \simeq \frac{1}{1+i\omega\tau} \tag{5.10}$$

with the imaginary part given by

$$\chi''(q,\nu) \simeq \frac{\omega\tau}{1+\omega^2\tau^2}. \tag{5.11}$$

The more general case of this symmetric and not stretched Lorentzian-like function is called Havriliak-Negami relaxation, where the asymmetry and broadness are accounted for, through the two terms α and β,

$$\chi(q,\nu) \simeq \frac{1}{(1+(i\omega\tau)^\alpha)^\beta}. \tag{5.12}$$

For $\beta = 1$ the Havriliak-Negami reduces to the Cole-Cole equation,

$$\chi''(q,\nu) \simeq \frac{(\omega\tau)^{1-\alpha} cos(\alpha\pi/2)}{1+2(\omega\tau)^{1-\alpha}\sin(\alpha\pi/2)+(\omega\tau)^{2(1-\alpha)}}, \tag{5.13}$$

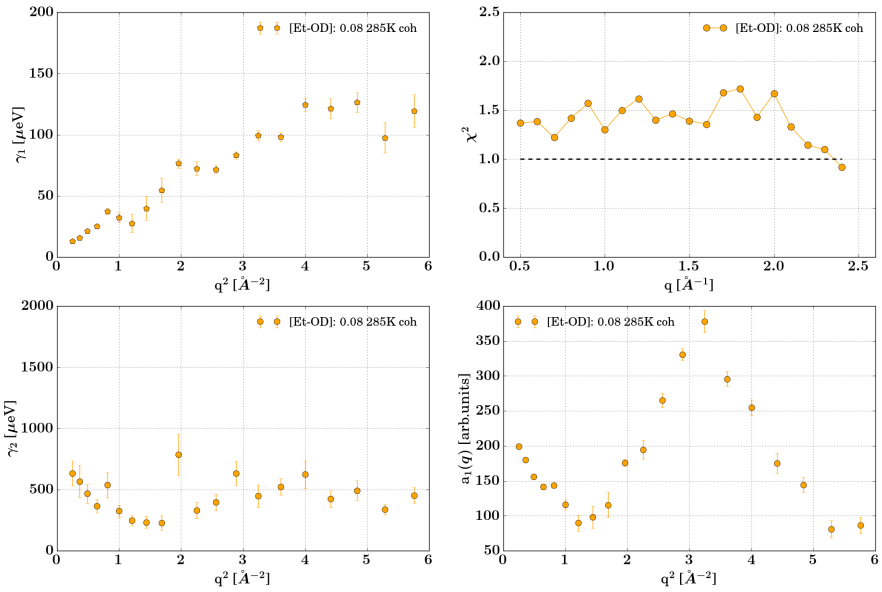

Figure S8: Plot of the fit parameters according to eqn. 1 of the main text for D_2O/C_2H_5OD at 0.08 ethanol mole fraction, at T=285K and E_i=3.84meV. Top left: Lorentzian width $\gamma_1(q)$. Bottom left: Lorentzian width of the second faster process $\gamma_2(q)$ that can be attributed to localized motions with no marked q-dependence. Top right: reduced χ^2 for the fit. Bottom right: Intensity of the first Lorentzian $a_1(q)$.

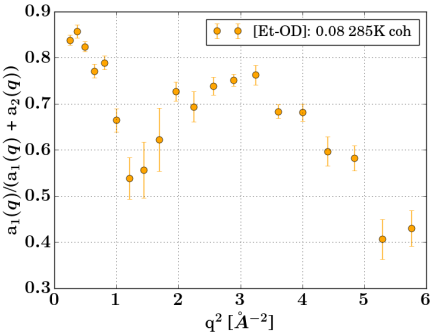

Figure S9: Fractional intensity of the first Lorentzian $a_1(q)/(a_1(q)+a_2(q))$ for the experimental parameters as in the preceding figure S8.

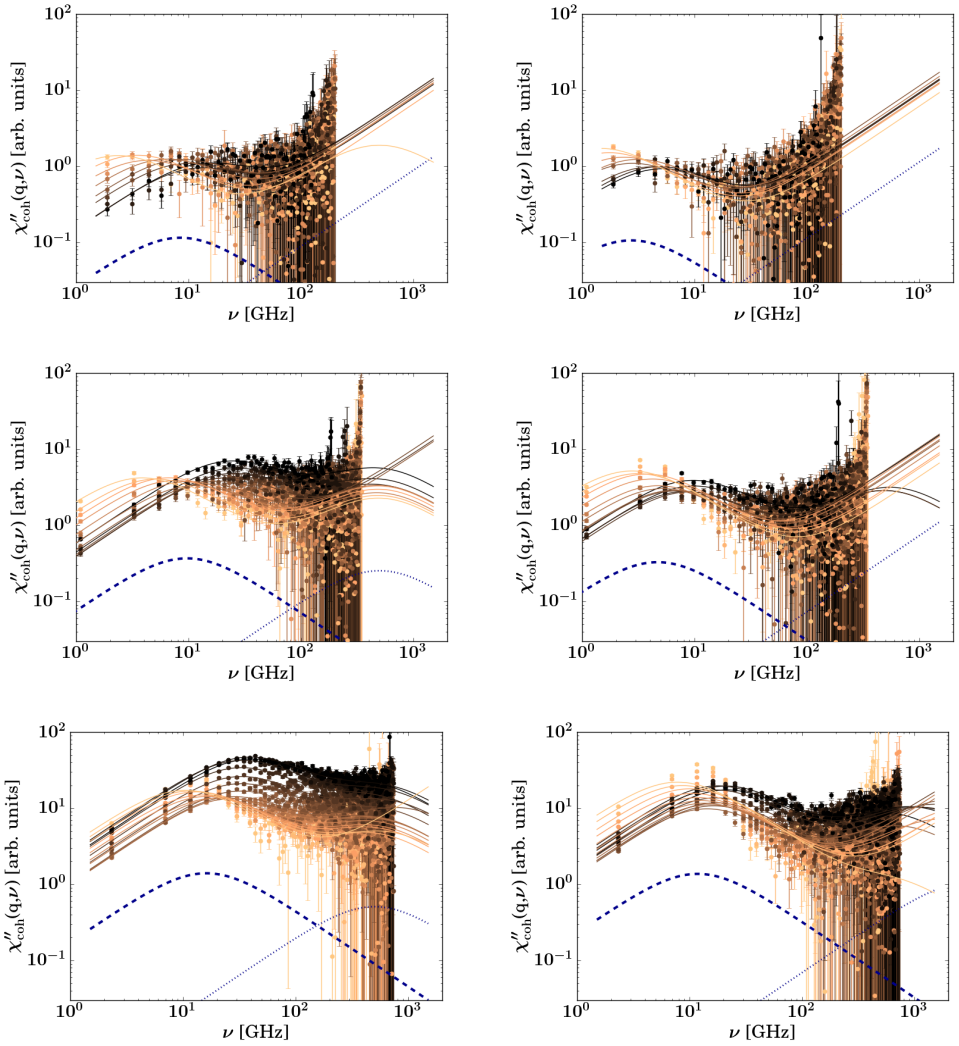

Figure S10: Imaginary part of the dynamical susceptibility for the coherent spectrum of D_2O/C_2H_5OD at 0.05 ethanol mole fraction (left column) and at 0.20 ethanol mole fraction (right column). The solid lines stand for the fit according to eqn. 3 of the main text with blue dashed and dotted lines depicting the main and the second Debye process (scaled by a factor 0.6 for visibility) respectively. Top row: E_i=1.05 meV in the range (orange) $0.4\,\text{Å}^{-1} \leq q \leq 1.1\,\text{Å}^{-1}$ (black); middle row: E_i=1.81 meV in the range (orange) $0.4\,\text{Å}^{-1} \leq q \leq 1.5\,\text{Å}^{-1}$ (black); bottom row: E_i=3.84 meV in the range (orange) $0.4\,\text{Å}^{-1} \leq q \leq 1.9\,\text{Å}^{-1}$ (black).

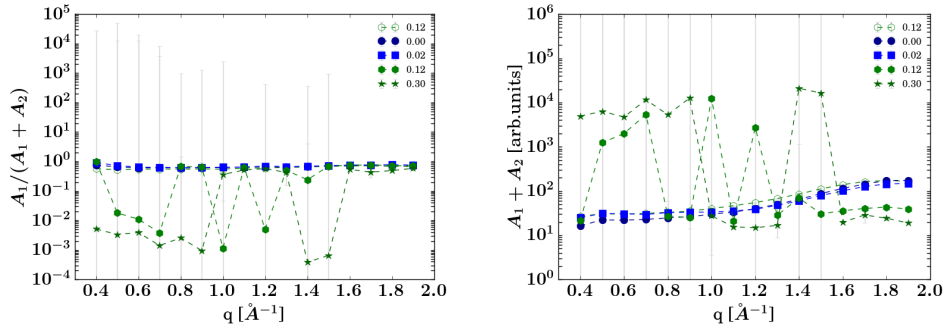

Figure S11: Left: Fractional amplitude $A_1(q)/(A_1(q)+A_2(q))$ of the main relaxation process of $\chi''(q,\nu)$ as a function of ethanol mole fraction at T=285K and for E_i=3.84 meV. Right: Total amplitude $A_1(q)+A_2(q)$. (Cf. eqn. 3 of the main text.) Due to the poorer statistics when approaching the THz regime the parameters of the second process A_2 and τ_2, representing the vibrational relaxation, display broad confidence bounds (grey), especially at low q.

and for $\alpha = 1$ to the Cole-Davidson relaxation,

$$\chi''(q,\nu) \simeq (1+(\omega\tau)^2)^{-\beta/2}\sin(\beta\arctan(\omega\tau)). \tag{5.14}$$

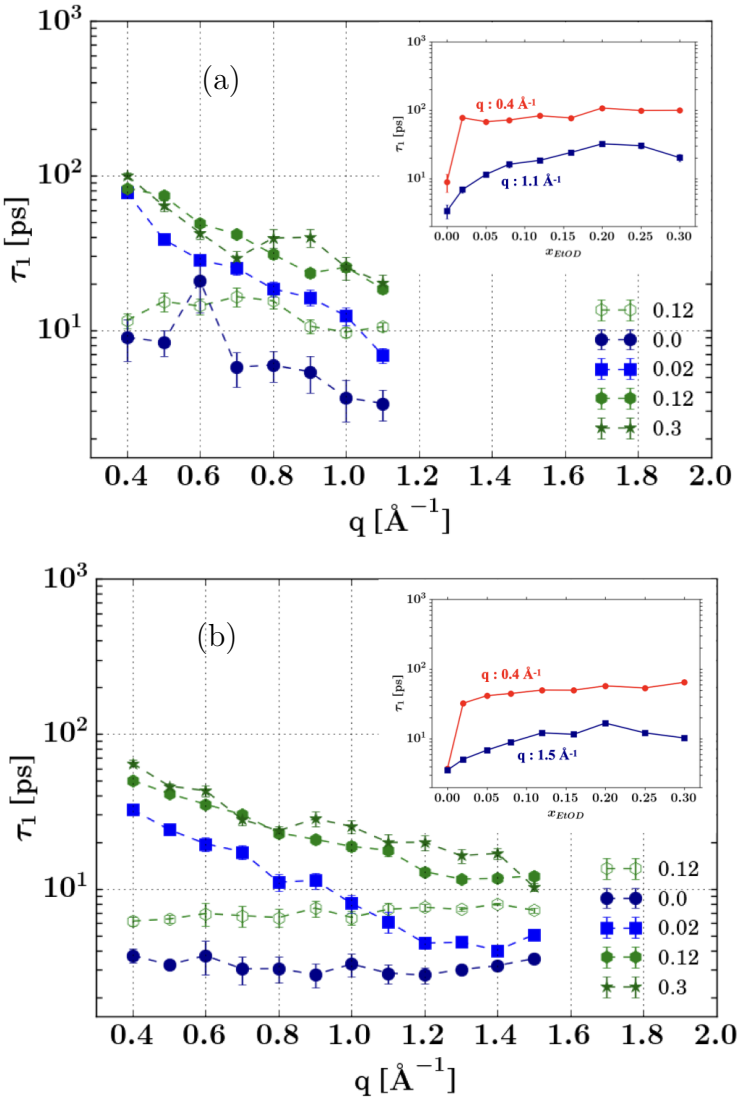

Figure S12: Relaxation times $\tau_1(q)$ (symbols) of the main relaxation process of $\chi''_{\mathrm{coh}}(q,\nu)$ as a function of q (main parts, ethanol mole fractions specified in the legends) and as a function of ethanol mole fraction for two distinct q values (insets, q values specified next to the lines), respectively, at T=285K and for E_i=1.05meV (a) and E_i=1.81meV (b). The lines are guides to the eye. Error bars hidden beneath markers.

Incoherent susceptibility

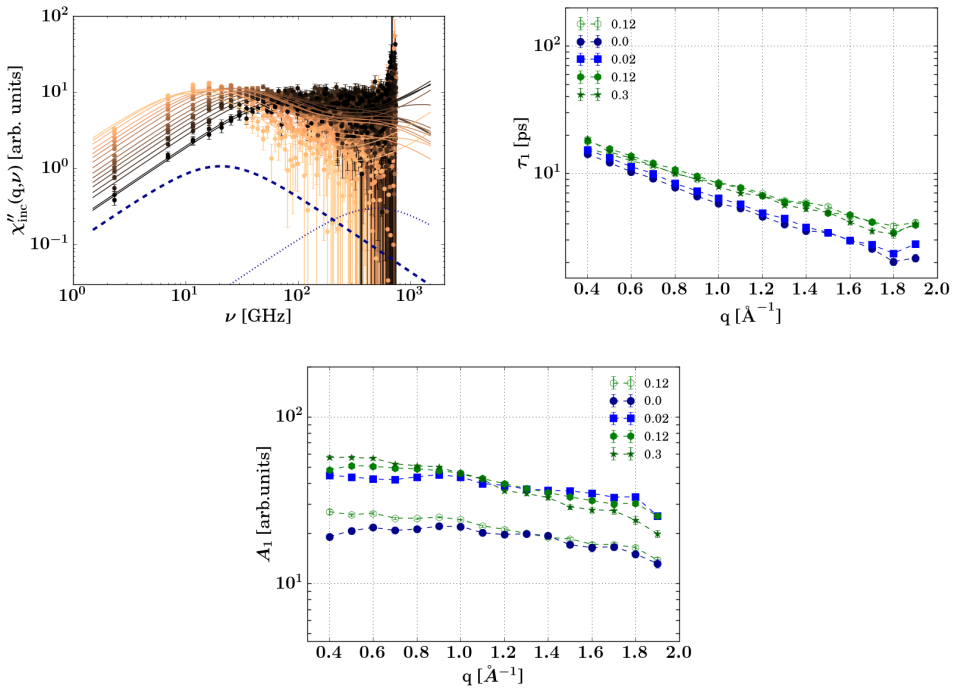

Figure S13: Top left: Imaginary part of the dynamical susceptibility for the incoherent spectrum of D_2O recorded at T=285K with E_i=3.84meV in the range $0.4\,\text{Å}^{-1} \leq q \leq 1.9\,\text{Å}^{-1}$. Top right: Relaxation times $\tau_1(q)$ and amplitude $A_1(q)$ (bottom) of the main relaxation process of $\chi''_{\text{inc}}(q,\nu)$ as a function of ethanol mole fraction at T=285K and for E_i=3.84meV. Values obtained from the peak position of $\nu_i^{\max} = (2\pi\tau_1)^{-1}$. Error bars hidden beneath markers.

Apparent static structure factors

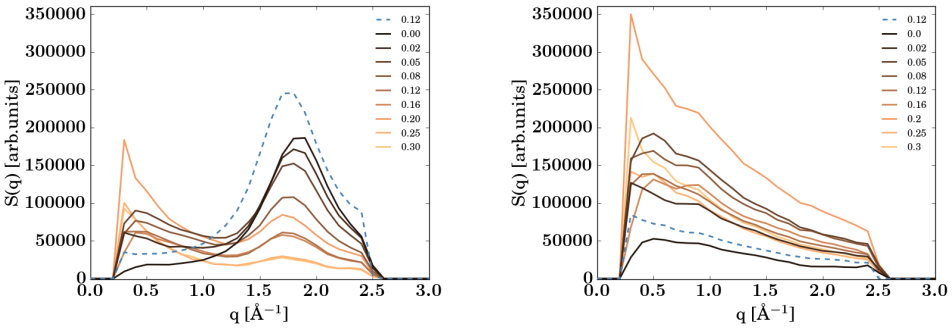

Figure S14: Apparent static structure factor depending on the ethanol-D_2O mixing ratio (cf. legend) obtained by integrating the coherent part (left) and incoherent part (right) of the LET dynamic scattering function $S(q, \omega)$ in the range $-260\mu eV \leq \hbar\omega \leq 260\mu eV$, which corresponds to approximately twice the spectrometer resolution line width at this incident energy (E_i = 3.84 meV, cf. figure S2). The dashed blue lines report the per-deuterated spectrum measured on the mixture of D_2O and C_2D_5OD. The intensities of $S(q)$ are proportional to the measured intensities normalized to the incident beam intensities. The left and right plots are drawn on the same scale to render the coherent and incoherent intensities comparable across the plots. The change in absolute intensity depending on the mixing ratio mainly arises from the changing total coherent cross section. In the coherent part (left) we identify a local maximum which might be associated with the pre-peak near 0.4 Å^{-1} and the liquid structure peak near 1.6 Å^{-1}. We note that these observations can depend on dynamical and instrumental effects. Nevertheless, a corresponding observation, i.e., the presence of a pre-peak in the partially deuterated mixture and its absence in the per-deuterated mixture has been reported for methanol solutions based on CD_3OD and CH_3OD, respectively (cf. main article for a discussion).

Cross sections

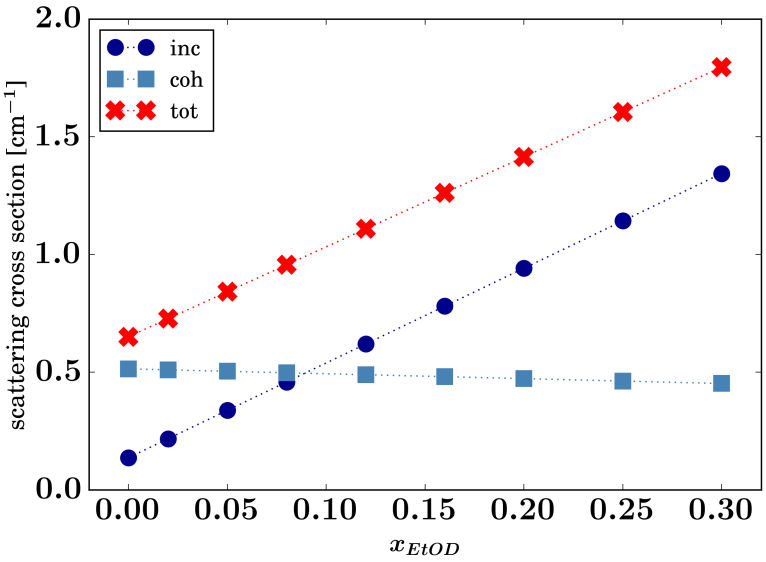

Figure S15: Scattering cross sections as a function of ethanol mole fraction, calculated from eq.5.15 with NIST values for isotopes cross sections (b=10^{-24}cm^2).

Thanks to the high degree of polarization and the long measurement time, both coherent and incoherent scattering signals are sufficient across all mixing ratios (see Fig. S1). Indeed, due to selective deuteration and polarization analysis we can differently weigh different species within the different samples. In this regard, in Fig.S15 we report the total scattering cross section Σ^i for the incoherent, coherent and sum obtained by

$$\Sigma^i = n_{D_2O}\sigma^i_{D_2O} + n_{EtOD}\sigma^i_{EtOD} = \frac{N_A\rho_{D_2O}(1-x_{EtOD})}{M_{D_2O}}\sigma^i_{D_2O} + \frac{N_A\rho_{EtOD}x_{EtOD}}{M_{EtOD}}\sigma^i_{EtOD} \tag{5.15}$$

with the number density n expressed in term of the Avogadro number N_A, the density ρ, molecular weight M, ethanol mole fraction x_{EtOD}, and $i \in \{\text{inc}, \text{coh}, \text{tot}\}$. As shown in this figure, the incoherent cross section increases with increasing ethanol ratio, and it exceeds the coherent one near 8% ethanol

contents. Between the extremes of the mixing ratios (100% water and 100 % Ethanol, respectively) the incoherent signal rapidly shifts from being due to D_2O to be dominated by ethanol.

Data accessibility

The neutron data are permanently curated by the ISIS facility and accessible via `https://doi.org/10.5286/ISIS.E.RB1920548` and `https://doi.org/10.5286/ISIS.E.RB2210240`.

Bibliography

[1] Philip Ball. Water as an active constituent in cell biology. *Chem. Rev.*, 108(1):74–108, 2008.

[2] F. Franks and DJG Ives. The structural properties of alcohol–water mixtures. *Q. Rev. Chem. Soc.*, 20(1):1–44, 1966.

[3] Georg H Großmann and Klaus H Ebert. Formation of clusters in 1-propanol/water-mixtures. *Berich. Bunsen. Gesell.*, 85(11):1026–1029, 1981.

[4] Alan. K. Soper, Lorna Dougan, Jason Crain, and John. L. Finney. Excess entropy in alcohol water solutions: A simple clustering explanation. *J. Phys. Chem. B*, 110(8):3472–3476, 2006.

[5] Elena Gòmez Begoña Gonzàlez, Noelia Calvar and Angeles Dominguez. Density, dynamic viscosity, and derived properties of binary mixtures of methanol or ethanol with water, ethyl acetate, and methyl acetate at t=(293.15, 298.15, and 303.15)k. *J. Chem. Thermodynamics*, 39(12):1578–1588, 2007.

[6] Jose V Herráez and R Belda. Refractive indices, densities and excess molar volumes of monoalcohols water. *J. Solution Chem.*, 35:1315–1328, 2006.

[7] J-H Guo, Yi Luo, Andreas Augustsson, Stepan Kashtanov, J-E Rubensson, David K Shuh, Hans Ågren, and Joseph Nordgren. Molecular structure of alcohol-water mixtures. *Phys. Rev. Lett.*, 91(15):157401, 2003.

[8] Sergei Yu Noskov, Guillaume Lamoureux, and Benoît Roux. Molecular dynamics study of hydration in ethanol- water mixtures using a polarizable force field. *J. Phys. Chem. B*, 109(14):6705–6713, 2005.

[9] Martina Požar, Bernarda Lovrinčević, Larisa Zoranić, Tomislav Primorać, Franjo Sokolić, and Aurélien Perera. Micro-heterogeneity versus clustering in binary mixtures of ethanol with water or alkanes. *Phys. Chem. Chem. Phys.*, 18(34):23971–23979, 2016.

[10] S Dixit, Jason Crain, WCK Poon, John L Finney, and Alan K Soper. Molecular segregation observed in a concentrated alcohol-water solution. *Nature (London)*, 416(6883):829–832, 2002.

[11] Akihiro Wakisaka and Kazuo Matsuura. Microheterogeneity of ethanol–water binary mixtures observed at the cluster level. *J. Mol. Liquids*, 129(1):25–32, 2006.

[12] Orsolya Gereben and László Pusztai. Cluster formation and percolation in ethanol-water mixtures. *Chem. Phys.*, 496:1–8, 2017.

[13] Samuel Lenton, Natasha H Rhys, James J Towey, Alan K Soper, and Lorna Dougan. Temperature-dependent segregation in alcohol-water binary mixtures is driven by water clustering. *J. Phys. Chem. B*, 122(32):7884–7894, 2018.

[14] Ildikó Pethes, László Pusztai, Koji Ohara, Shinji Kohara, Jacques Darpentigny, and László Temleitner. Temperature-dependent structure of methanol-water mixtures on cooling: X-ray and neutron diffraction and molecular dynamics simulations. *J. Mol. Liquids*, 314:113664, 2020.

[15] L Dougan, SP Bates, R Hargreaves, JP Fox, J Crain, JL Finney, V Reat, and AK Soper. Methanol-water solutions: A bi-percolating liquid mixture. *J. Chem. Phys.*, 121(13):6456–6462, 2004.

[16] Toshiyuki Takamuku, Kensuke Saisho, Shuntarou Nozawa, and Toshio Yamaguchi. X-ray diffraction studies on methanol–water, ethanol–water,

and 2-propanol–water mixtures at low temperatures. *J. Mol. Liquids*, 119(1-3):133–146, 2005.

[17] William S. Price, Hiroyuki Ide, and Yoji Arata. Solution dynamics in aqueous monohydric alcohol systems. *J. Phys. Chem. A*, 107:4784–4789, 2003.

[18] Szilvia Pothoczki, László Pusztai, and Imre Bakó. Temperature dependent dynamics in water-ethanol liquid mixtures. *J. Mol. Liquids*, 271:571–579, 2018.

[19] Bernarda Lovrinčević, Ivo Jukić, and Martina Požar. An overview on the dynamics in aqueous mixtures of lower alcohols. In Katsura Nishiyama, Tsuyoshi Yamaguchi, Toshiyuki Takamuku, and Norio Yoshida, editors, *Molecular Basics of Liquids and Liquid-Based Materials*, pages 169–193. Springer Nature Singapore, 2021.

[20] Jukić, I., Požar, M., Lovrinčević, B. et al. Lifetime distribution of clusters in binary mixtures involving hydrogen bonding liquids. *Sci. Rep. (UK)*, 12, 2022.

[21] Abdalla Obeidat and Hind Abu-Ghazleh. The validity of the potential model in predicting the structural, dynamical, thermodynamic properties of the unary and binary mixture of water-alcohol: Methanol-water case. *AIP Advances*, 8(6):065203, 2018.

[22] Abdalla Obeidat, Rakan Al-Salman, and Hind Abu-Ghazleh. The validity of the potential model in predicting the structural, dynamical, thermodynamic properties of the unary and binary mixture of water-alcohol: Ethanol-water case. *AIP Advances*, 8:075321, 07 2018.

[23] Encarnación García Pérez, Diego González-Salgado, and Enrique Lomba. Molecular dynamics simulations of aqueous solutions of short chain alcohols. excess properties and the temperature of maximum density. *Fluid Phase Equilibria*, 528:112840, 2021.

[24] Imre Bakó, Tünde Megyes, Szabolcs Bálint, Tamás Grósz, and Viorel Chihaia. Water–methanol mixtures: Topology of hydrogen bonded network. *Phys. Chem. Chem. Phys.*, 10(32):5004–5011, 2008.

[25] Erik JW Wensink, Alex C Hoffmann, Paul J van Maaren, and David van der Spoel. Dynamic properties of water/alcohol mixtures studied by computer simulation. *J. Chem. Phys.*, 119(14):7308–7317, 2003.

[26] Roland Bohmer, Catalin P. Gainaru, and Ranko Richert. Structure and dynamics of monohydroxy alcohols—milestones towards their microscopic understanding, 100 years after debye. *Physics Reports*, 545:125–195, 2014.

[27] P Wieth and M Vogel. Dynamical and structural properties of monohydroxy alcohols exhibiting a debye process. *J. Chem. Phys.*, 140(14):144507, 2014.

[28] Takaaki Sato and Richard Buchner. Dielectric relaxation processes in ethanol/water mixtures. *J. Phys. Chem. A*, 108(23):5007–5015, 2004.

[29] C. Gainaru, R. Meier, S. Schildmann, C. Lederle, W. Hiller, E. A. Rössler, and R. Böhmer. Nuclear-magnetic-resonance measurements reveal the origin of the debye process in monohydroxy alcohols. *Phys. Rev. Lett.*, 105:258303, Dec 2010.

[30] Ruoyu Li, Carmine D'Agostino, James McGregor, Michael D. Mantle, J. Axel Zeitler, and Lynn F. Gladden. Mesoscopic structuring and dynamics of alcohol/water solutions probed by terahertz time-domain spectroscopy and pulsed field gradient nuclear magnetic resonance. *J. Phys. Chem. B*, 118(34):10156–10166, 2014.

[31] Per Sillrén, Aleksandar Matic, Maths Karlsson, Michael Koza, Marco Maccarini, Peter Fouquet, M Götz, Thomas Bauer, Rudolf Gulich, Peter Lunkenheimer, Alois Loidl, J Mattsson, Catalin Gainaru, Eugen Vynokur, S Schildmann, Stefan Bauer, and R Böhmer. Liquid 1-propanol studied by neutron scattering, near-infrared, and dielectric spectroscopy. *J. Chem. Phys.*, 140:124501, 03 2014.

[32] U. Kaatze, R. Behrends, and R. Pottel. Hydrogen network fluctuations and dielectric spectrometry of liquids. *J. Non-Crystalline Solids*, 305(1):19–28, 2002.

[33] Javier Cardona, Martin B. Sweatman, and Leo Lue. Molecular dynamics investigation of the influence of the hydrogen bond networks in ethanol/water mixtures on dielectric spectra. *J. Phys. Chem. B*, 122(4):1505–1515, 2018.

[34] José Teixeira, M-C Bellissent-Funel, Sow-Hsin Chen, and Albert-José Dianoux. Experimental determination of the nature of diffusive motions of water molecules at low temperatures. *Phys. Rev. A*, 31(3):1913, 1985.

[35] Johan Qvist, Helmut Schober, and Bertil Halle. Structural dynamics of supercooled water from quasielastic neutron scattering and molecular simulations. *J. Chem. Phys.*, 134(14):144508, 2011.

[36] Tilo Seydel, Robert M Edkins, and Katharina Edkins. Picosecond self-diffusion in ethanol-water mixtures. *Phys. Chem. Chem. Phys.*, 21(18):9547–9552, 2019.

[37] Peng Luo, Yanqin Zhai, Peter Falus, Victoria García Sakai, Monika Hartl, Maiko Kofu, Kenji Nakajima, and Antonio Faraone. Q-dependent collective relaxation dynamics of glass-forming liquid ca0. 4k0. 6 (no3) 1.4 investigated by wide-angle neutron spin-echo. *Nature Communications*, 13(1):2092, 2022.

[38] Wangchun Chen, Shannon Watson, Yiming Qiu, Jose A. Rodriguez-Rivera, and Antonio Faraone. Wide-angle polarization analysis on the multi-axis crystal spectrometer for the study of collective and single particle dynamics of methanol at its prepeak. *Physica B: Condensed Matter*, 564:166–171, 2019.

[39] GJ Nilsen, J Košata, M Devonport, P Galsworthy, RI Bewley, DJ Voneshen, R Dalgliesh, and JR Stewart. Polarisation analysis on the

let time-of-flight spectrometer. *Journal of Physics: Conference Series*, 862(1):012019, 2017.

[40] Tatsiana Burankova, Rolf Hempelmann, Andrew Wildes, and Jan P. Embs. Collective ion diffusion and localized single particle dynamics in pyridinium-based ionic liquids. *J. Phys. Chem. B*, 118(49):14452–14460, 2014.

[41] C. E. Bertrand, J. L. Self, J. R. D. Copley, and A. Faraone. Dynamic signature of molecular association in methanol. *J. Chem. Phys.*, 145(1):014502, 2016.

[42] C. E. Bertrand, J. L. Self, J. R. D. Copley, and A. Faraone. Nanoscopic length scale dependence of hydrogen bonded molecular associates' dynamics in methanol. *J. Chem. Phys.*, 146(19):194501, 2017.

[43] VN Novikov, Kenneth S Schweizer, and Alexei P Sokolov. Coherent neutron scattering and collective dynamics on mesoscale. *J. Chem. Phys.*, 138(16):164508, 2013.

[44] Arantxa Arbe, Gøran J Nilsen, J Ross Stewart, Fernando Alvarez, Victoria García Sakai, and Juan Colmenero. Coherent structural relaxation of water from meso- to intermolecular scales measured using neutron spectroscopy with polarization analysis. *Phys. Rev. Research*, 2(2):022015, 2020.

[45] Fernando Alvarez, Arantxa Arbe, and Juan Colmenero. Understanding the coherent dynamic structure factor of liquid water measured by neutron spectroscopy with polarization analysis: a molecular dynamics simulations study. In *EPJ Web of Conf.*, volume 272, page 01011. EDP Sciences, 2022.

[46] RI Bewley, JW Taylor, and SM Bennington. Let, a cold neutron multidisk chopper spectrometer at isis. *Nucl. Instrum. Methods A*, 637(1):128–134, 2011.

[47] P.G. De Gennes. Liquid dynamics and inelastic scattering of neutrons. *Physica*, 25(7):825–839, 1959.

[48] R. Mills. Self-diffusion in normal and heavy water in the range 1-45.deg. *J. Phys. Chem.*, 77(5):685–688, 1973.

[49] Antonio Faraone, Kunlun Hong, Larry R. Kneller, Michael Ohl, and John R. D. Copley. Coherent dynamics of meta-toluidine investigated by quasielastic neutron scattering. *J. Chem. Phys.*, 136(10):104502, 2012.

[50] Kurt Sköld. Small energy transfer scattering of cold neutrons from liquid argon. *Phys. Rev. Lett.*, 19:1023–1025, Oct 1967.

[51] A. Arbe, P. Malo de Molina, F. Alvarez, B. Frick, and J. Colmenero. Dielectric susceptibility of liquid water: Microscopic insights from coherent and incoherent neutron scattering. *Phys. Rev. Lett.*, 117:185501, Oct 2016.

[52] Arantxa Arbe and Juan Colmenero. Relaxation processes in liquids and glass-forming systems: What can we learn by comparing neutron scattering and dielectric spectroscopy results? In Friedrich Kremer and Alois Loidl, editors, *The Scaling of Relaxation Processes*, pages 247–277. Springer International Publishing, Cham, 2018.

[53] Deepa Subramanian, Christopher T Boughter, Jeffery B Klauda, Boualem Hammouda, and Mikhail A Anisimov. Mesoscale inhomogeneities in aqueous solutions of small amphiphilic molecules. *Faraday Discussions*, 167:217–238, 2013.

[54] Rikhia Ghosh and Biman Bagchi. Temperature dependence of static and dynamic heterogeneities in a water–ethanol binary mixture and a study of enhanced, short-lived fluctuations at low concentrations. *J. Phys. Chem. B*, 120(49):12568–12583, 2016.

[55] Keiko Nishikawa and Takao Iijima. Small-angle x-ray scattering study of fluctuations in ethanol and water mixtures. *J. Phys. Chem.*, 97(41):10824–10828, 1993.

[56] K Takaizumi and T Wakabayashi. The freezing process in methanol-, ethanol-, and propanol-water systems as revealed by differential scanning calorimetry. *J. Solution Chemistry*, 26:927–939, 1997.

[57] Aziz Ghoufi. Molecular origin of the prepeak in the structure factor of alcohols. *J. Phys. Chem. B*, 124(50):11501–11509, 2020.

[58] Arantxa Arbe, Gøran J Nilsen, Mark Devonport, Bela Farago, Fernando Alvarez, José A Martínez González, and Juan Colmenero. Collective dynamics and self-motions in the van der waals liquid tetrahydrofuran from meso-to inter-molecular scales disentangled by neutron spectroscopy with polarization analysis. *J. Chem. Phys.*, 158(18), 2023.

[59] G J Nilsen, J Košata, M Devonport, P Galsworthy, R I Bewley, D J Voneshen, R Dalgliesh, and J R Stewart. Polarisation analysis on the LET time-of-flight spectrometer. *J. Physics: Conference Series*, 862(1):012019, jun 2017.

[60] J. Košata, G.J. Nilsen, M. Devonport, R.I. Bewley, D.J. Voneshen, P.J. Galsworthy, D. Raspino, and J.R. Stewart. Polarized primary spectrometer on the let instrument at isis. *Physica B: Condensed Matter*, 551:476–479, 2018. The 11th International Conference on Neutron Scattering (ICNS 2017).

[61] G Cassella, J R Stewart, G M Paternò, V García Sakai, M Devonport, P J Galsworthy, R I Bewley, D J Voneshen, D Raspino, and G J Nilsen. Polarization analysis on the let cold neutron spectrometer using a 3he spin-filter: First results. *J. Physics: Conference Series*, 1316(1):012007, oct 2019.

[62] Kurt Sköld. Small energy transfer scattering of cold neutrons from liquid argon. *Phys. Rev. Lett.*, 19(18):1023, 1967.

Blank page

Chapter 6

Perturbation of Water-Ethanol Solvent Structural Relaxation by a Bis-Urea Supramolecular Gel and Paracetamol

Author contribution: Riccardo Morbidini[a,b] wrote the neutron proposal and performed the experiment, including sample preparation, with assistance from Dr. Robert M. Edkins,[c] Prof. Katharina Edkins,[e,*] Dr.Tilo Seydel,[a,*] Kirill Nemkovski[d] and Dr.Gøran Nilsen[d]. Riccardo Morbidini performed the data analysis under the supervision of Dr. Tilo Seydel and Dr.Gøran Nilsen. The project was conceived and supervised by Dr. Tilo Seydel and Prof. Katharina Edkins.

[a] Institut Max von Laue - Paul Langevin, 71 Avenue des Martyrs, F-38042 Grenoble, France.

[b] Division of Pharmacy and Optometry, University of Manchester, Oxford Road, Manchester M13 9PT, United Kingdom.

[c] WestCHEM Department of Pure and Applied Chemistry, University of Strathclyde, 295 Cathedral Street, Glasgow G1 1XL, United Kingdom.

[d] ISIS Neutron and Muon Source, Rutherford Appleton Laboratory, Didcot, OX11 0QX, United Kingdom.

[e] Strathclyde Institute of Pharmacy and Biomedical Sciences, University of Strathclyde, 161 Cathedral Street, Glasgow G4 0RE, United Kingdom

Abstract

Understanding structural dynamics on the picosecond/nanometer scale in complex fluids is crucial for advancing various fields, from material chemistry to drug delivery. We employ polarized quasi-elastic neutron spectroscopy to investigate the perturbation to the hydrogen-bond network of water-ethanol mixtures induced by a supramolecular gel network and by paracetamol (PCM) molecules. Interestingly, while the supramolecular gelator significantly alters the macroscopic behavior of the solvent at concentrations of 0.3 and 0.5 wt.%, it does not affect the hydrogen bond network at the microscopic level. In contrast, the addition of PCM at 5 wt.%, which does not change the macroscopic properties, modifies the structural dynamics of water-ethanol mixtures at length scales commensurate with and below the PCM-PCM correlation length in the mixture. This study reveals the intricate interplay between solute, solvent, and gel interactions, demonstrating a lack of direct correlation between macroscopic and microscopic properties in such complex systems.

6.1 Introduction

Understanding the dynamics of solute-solvent interactions is crucial for elucidating the fundamental principles governing various physical and chemical processes within solutions.[1] The current state of research often overlooks the significant perturbations that occur in the solvent structure when a solute or a polymer is dissolved, assuming that the resulting solution retains the same structural characteristics as the pure solvent. This assumption neglects the intricate interplay between solute and solvent molecules, which can profoundly affect the macroscopic properties of the solution.[2] The limitations of this approach become particularly evident when considering complex systems such as gels. These are a unique class of materials that exhibit solid-like behavior at the macroscopic level despite being composed of generally more than 99% liquid, a property arising from the entrapment of fluid within an entangled network of polymeric fibers.[3] A notable sub-class of gels, known as supramolecular gels, forms when low molecular weight gelator (LMWG) monomers self-assemble non-covalently in response to an external physical stimulus.[4] Thus, with the two-step solvent perturbation induced by monomer dissolution and fiber formation, the assumption that bulk and trapped solvent share the same structural characteristics may be too simplistic. Overcoming this assumption could potentially explain the dynamic behaviour within these systems which has been shown to be influenced by solvent-network interaction.[5–7] As an example, water-ethanol dynamics show a small but significant increase when incorporated into prototypical supramolecular gels composed of bis-urea LMWG.[8] The complexity of solvent perturbation increases with the introduction of additional solutes, such as drug molecules, a factor particularly relevant in pharmaceutical applications where supramolecular gels are studied as platforms for achieving sustained release in injectable formulations.[9, 10] Notably, it has been observed that drug dynamics are faster in bis-urea gels than in the respective bulk solutions.[11] These studies have primarily relied on quasi-elastic neutron scattering (QENS), a spectroscopic method that simultaneously probes self-diffusion at ps - ns time scales and Å - nm length scales.[12]

While this technique allows for the distinction of solute dynamics from the surrounding deuterated solvent, it fails to capture the changes in solvent molecule dynamics induced by the solute. To address these limitations, we have coupled QENS with polarization analysis, a technique implemented on only a few spectrometers world-wide,[13, 14] to distinguish single-molecule dynamics of dissolved solutes while simultaneously providing information about the molecular structural dynamics of the solvent.[15, 16] Our initial investigations using this method revealed increased rigidity in the hydrogen bond network of bulk D_2O upon addition of ethanol at the mesoscopic length scale (0.2 $Å^{-1} \leq q \leq$ 0.7 $Å^{-1}$),[17] often associated to the cluster region of water and its mixture with alcohol. In the present work, we apply this approach to study the perturbations introduced by a model small drug (paracetamol, PCM), a bis-urea gel, and a combination of the two on water-ethanol structural dynamics. This investigation aims to provide a more comprehensive description of the complex interplay between solutes, gels, and solvent structure in these systems.

6.2 Materials and methods

Sample preparation

PCM and all solvents were obtained from Sigma Aldrich and used as received without additional purification, while the bis-urea gelator was synthesized according to the published method.[18] The sample preparation involved dissolving 0.3 or 0.5 wt.% of the gelator to the water:ethanol mixture of 7:3 *v/v* and to ensure consistency, both gel and respective solution samples were prepared using the same cycle of heating and cooling. The process began by heating the samples in a sealed vial up to 70 °C to fully dissolve the gelator. The resulting clear solutions were transferred, while still hot, into double-walled cylindrical aluminum cans and sealed with indium wires. The samples were then allowed to cool and set into gel form for a minimum of 30 minutes. For drug-loaded samples 5 wt.% of PCM were dissolved prior to the heating and cooling cycle. To achieve comparable statistics, different gap sizes were used for the

sample holders: 1 mm for fully deuterated samples and 0.06 mm for those containing protiated PCM. Neutron scattering measurements were conducted with each spectrum taking approximately 6 hours at 290 K. The samples analyzed included: the perdeuterated solvent mixture (D_2O:C_2D_5OD), a 0.3 wt.% gel in the deuterated solvent mixture and a 5 wt.% protiated PCM in both the deuterated solvent mixture and the 0.3 wt.% gel. To gain further insight into how the gel affects solvent structural relaxation, measurements were conducted on partially deuterated solvents consisting of 7:3 *v/v* D_2O:C_2H_5OD at two different gelator concentrations (0.3 wt.% an 0.5 wt.%). This approach also facilitates comparison with results from the pure solvent mixture.[17]

Quasi-Elastic Neutron Scattering

QENS with polarization analysis was performed at the cold neutron time-of-flight spectrometer LET at the ISIS facility, Rutherford Appleton Laboratory, Didcot, UK.[13, 14] The LET spectrometer is best adapted to the fast picosecond diffusion of the solvent molecules, whereas the slower drug molecule diffusion itself is not optimally resolved. In standard unpolarized QENS experiments, both nuclear spin-coherent and spin-incoherent spectra are measured together, with the protiated drug molecule's contribution masking the coherent signal from the fully deuterated solvent (Fig.S1). However, by employing LET with polarization analysis, we can separately record these spectra, effectively removing much of the incoherent signal from the protiated drug molecules. This option allows us to isolate and analyze the spin-coherent scattering spectra, thereby gauging the perturbations of the drug and gelator to the deuterated solvent molecules, which are the main contributors to coherent scattering. As shown in Fig.6.1, when studying the structural relaxation of the solvent in the presence of a gel network and drug molecules, deuteration alone is not sufficient to separate the contributions of the individual components. Notably, the coherent signal becomes the dominant part only at q values around the De Gennes narrowing of water (Fig.6.1b),[19] while at lower q the incoherent signal prevails (Fig.6.1a). Therefore, without polarization analysis and relying

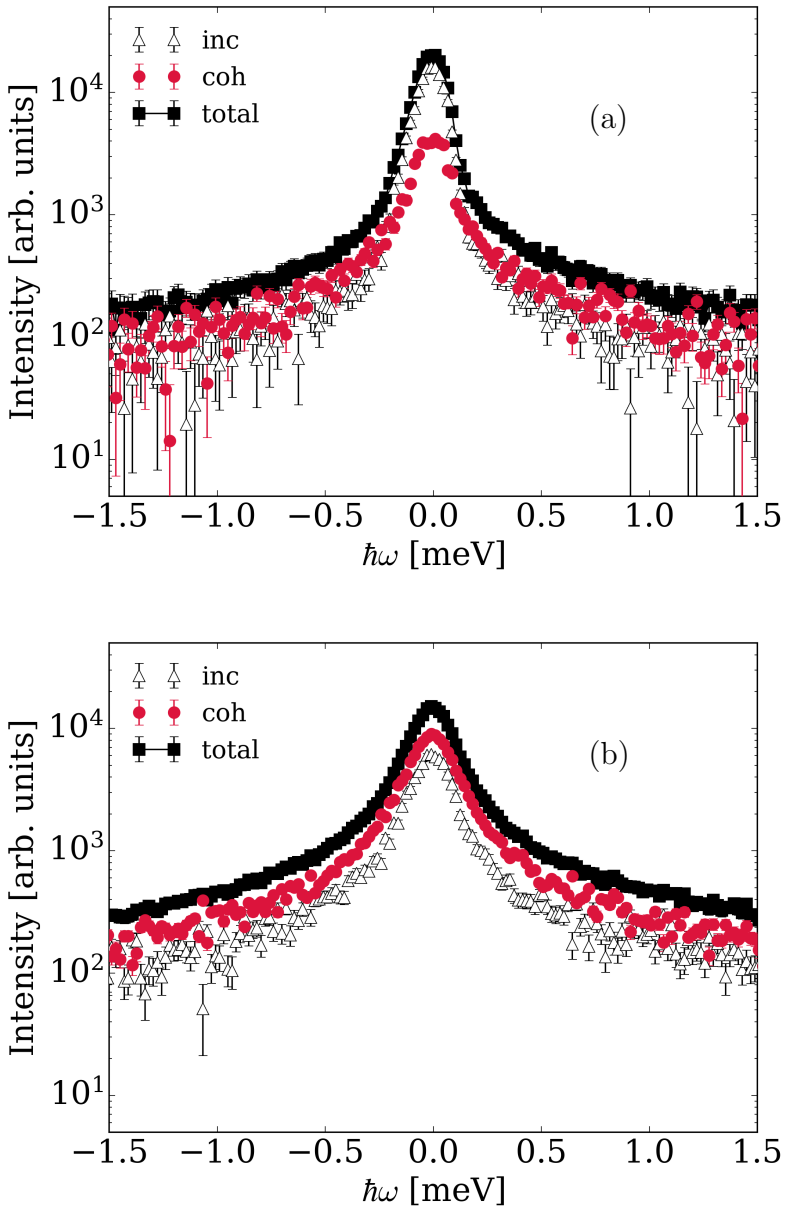

Figure 6.1: Comparison of the coherent (circles), incoherent (triangles) and total (squares) scattering function for a sample with 0.3 wt.% bis-urea gel in a 7:3 *v/v* D_2O:Ethanol-D_6 solvent, containing 5 wt.% paracetamol. Spectra measured on LET at $T = 290$ K, incident energy $E = 3.84$ meV at (a) $q = 1.0\,\text{Å}^{-1}$ and (b) $q = 1.9\,\text{Å}^{-1}$. Error bars hidden beneath markers.

solely on selective deuteration the study of the solvent structural relaxation would limit to a narrow q-range. We transform the coherent part of the QENS spectra $S_{\mathrm{coh}}(q,\nu)$ to the coordinates of dynamic susceptibility

$$\chi''_{\mathrm{coh}}(q,\nu) = \pi S_{\mathrm{coh}}(q,\nu)\,[1+n(\nu)]^{-1}, \tag{6.1}$$

where ν is the frequency and $n(\nu)$ the Bose occupation number given by $n(\nu) = (e^{h\nu/k_BT}-1)^{-1}$. In these coordinates, the spectra can be analyzed without relying on specific analytical models, as such models are currently unavailable for describing the broadening of the coherent dynamic structure factor, especially at mesoscopic length scales and in the presence of small molecules.[15, 20–24] As established previously,[15, 17] we model this coherent part of the signal by a linear combination of Debye relaxations

$$\chi''_{\mathrm{coh}}\big(q,\nu\big) = \sum_i A_i(q)\frac{\nu\cdot\nu_i^{\max}(q)}{\nu^2+\nu_i^{\max}(q)^2}. \tag{6.2}$$

Equation 6.2 is synonymous with a sum of Lorentzian functions expressed in coordinates of susceptibility with the peak position ν_i^{max} and amplitudes $A_i(q)$ with the summation index i, corresponding to exponential decays in the time domain with the relaxation time

$$\tau_i(q) = \left(2\pi\nu_i^{max}(q)\right)^{-1}. \tag{6.3}$$

6.3 Results and discussions

We first perturbed the partially deuterated solvent mixture previously studied[17] by adding two different concentrations of bis-urea gel. The coherent QENS spectra, expressed as the imaginary part of the dynamic susceptibility $\chi''(q,\nu)$, show no significant difference following the formation of the gel network (Fig.S3). At an ethanol mole fraction of 0.12, where the gel sets, the peak position reflected in $\tau_1(q)$ (eq.6.3, Fig.6.3a), of the susceptibility exhibits a trend consistent with that of the pure solution counterpart. Specifically, a

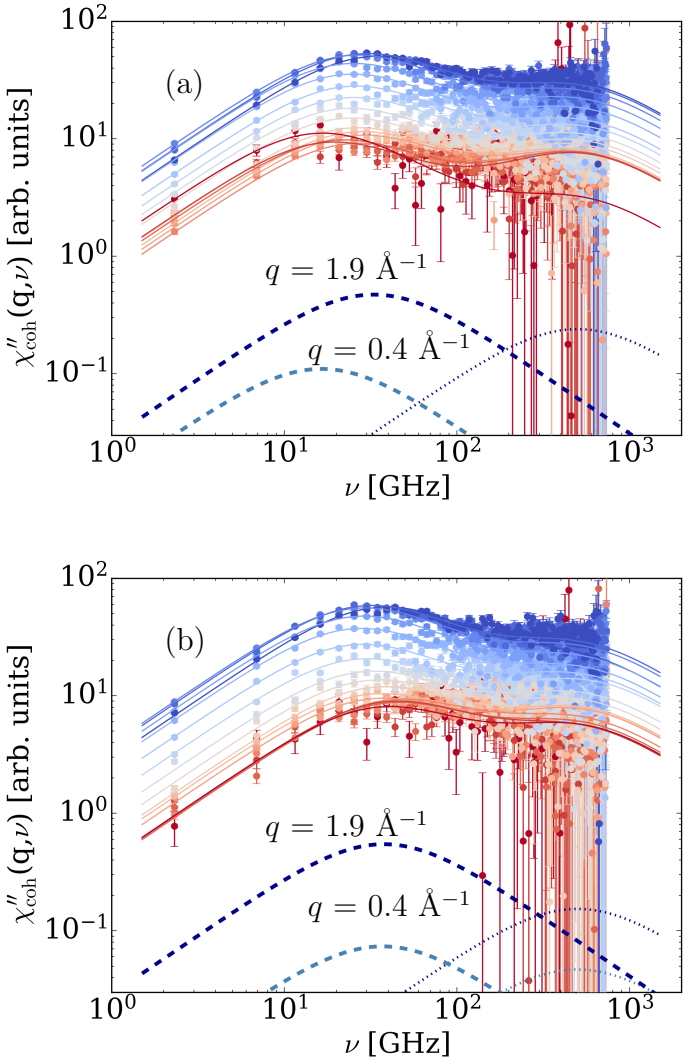

Figure 6.2: Coherent part of the QENS spectra (symbols) in form of the imaginary part of the dynamic susceptibility calculated from eq.6.1 and fits with the Debye model eq.6.2 (lines), recorded on 7:3 *v/v* D_2O:C_2D_5OD with 5 wt.% paracetamol (a) and on a 0.3 wt.% bis-urea gel (b), at $T = 290\,K$. The color encodes data for q from $0.3\,Å^{-1}$ (red) to $1.9\,Å^{-1}$ (blue). The fit according to eq.6.2, consisting of the main Debye process associated to structural relaxation (dashed lines, scaled by a factor 100 for visibility) depicted at the smallest (light blue) and highest (dark blue) q and of the second Debye process linked to vibrational contributes (dotted lines, scaled by a factor 0.6 for visibility).

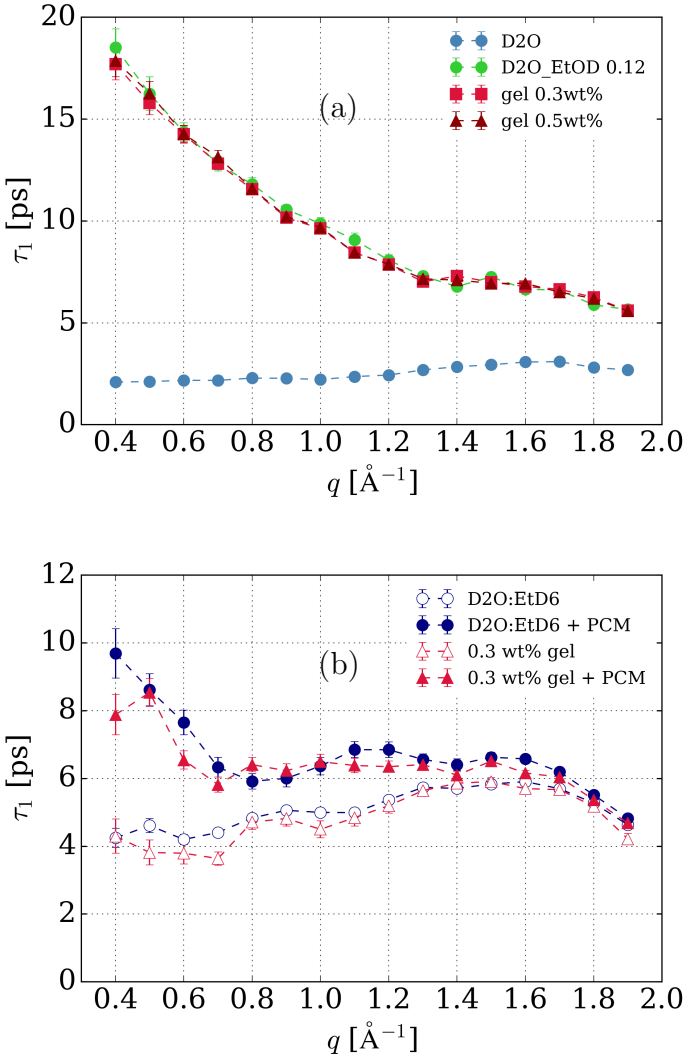

Figure 6.3: Relaxation times $\tau_1(q)$ (eq.6.3) of the main relaxation process of $\chi''_{\mathrm{coh}}(q,\nu)$ at $T = 290\,\mathrm{K}$ and incident energy $E_i = 3.84$ meV. $\tau_1(q)$ was determined by fitting eq.6.2 and identifying the peak position $\nu_i^{\max} = (2\pi\tau_1)^{-1}$ (Fig.6.2). (a) Comparison of the results for pure D_2O and for the partially deuterated D_2O : C_2H_5OD 7:3 v/v solvent mixture, corresponding to 0.12 ethanol mole fraction, at $T = 290\,\mathrm{K}$, for pure solvent, 0.3 and 0.5 wt.% gel. The results for pure D_2O from the previous paper are reported as a reference.[17] (b) Comparison of the results in the presence (full symbols) and absence (open symbols) of Paracetamol, for the pure fully deuterated water-ethanol solvent mixture and for the 0.3 wt.% bis-urea gel based on the same solvent, respectively. The lines are guides to the eye. Error bars hidden beneath markers.

strong shift towards higher frequencies is observed in the low-q region, reflecting a q-dependent relaxation process at the mesoscopic scale. As previously noted,[17] this effect corresponds to an increase in the relaxation time τ_1 in the water-ethanol mixture compared to pure D_2O. This effect is independent from whether or not the gel is present. Thus, while the solvent mixture presents a more rigid structure after ethanol addition, this rigidity is not further enhanced by the presence of the gel, regardless of whether the gelator concentration is 0.3 or 0.5 wt.% (Fig.6.3a). Based on this reference for the pure unloaded solvent, we subsequently observed the perturbation to the system due to the introduction of paracetamol. The susceptibility representation for the perdeuterated solvent, shown in Fig.6.2, indicates that the main relaxation process displays a nearly q-independent peak position, with a slight shift towards lower frequencies occurring above $q = 1.2\,\text{Å}^{-1}$. This trend aligns with previous observations made on D_2O, which have been explained as a consequence of the combination of terms contributing to the coherent dynamic structure factor in the low-q region.[16] The susceptibility $\chi''(q,\nu)$, as shown in Fig.6.2 (symbols) alongside the associated fits from eq.6.2 (lines), reveals a shift in the apparent main peak position towards lower frequencies upon the addition of PCM to the solvent. The observed increase in the relaxation time τ_1 below $q = 1.4$ Å^{-1} largely exceeds 3σ confidence bounds for both paracetamol-loaded solution and gel, while the respective unloaded samples show overlapping results. The results on the relaxation times are closely related to the structural organization of the hydrogen bond network. This relationship is expressed via the apparent static structure factor $S(q)$, obtained by integrating the coherent spectra over ω within approximately twice the energy resolution full width at half maximum (FWHM):

$$S(q) = \int_{-\infty}^{+\infty} S_{\text{coh}}(q,\omega)d\omega \tag{6.4}$$

Such quantity provides information about the spatial correlations between particles in the system, reflecting molecular organization at various length scales. In our previous work on D_2O-ethanol mixtures, we observed significant changes in the structure factor as ethanol concentration increased: a pre-peak appeared

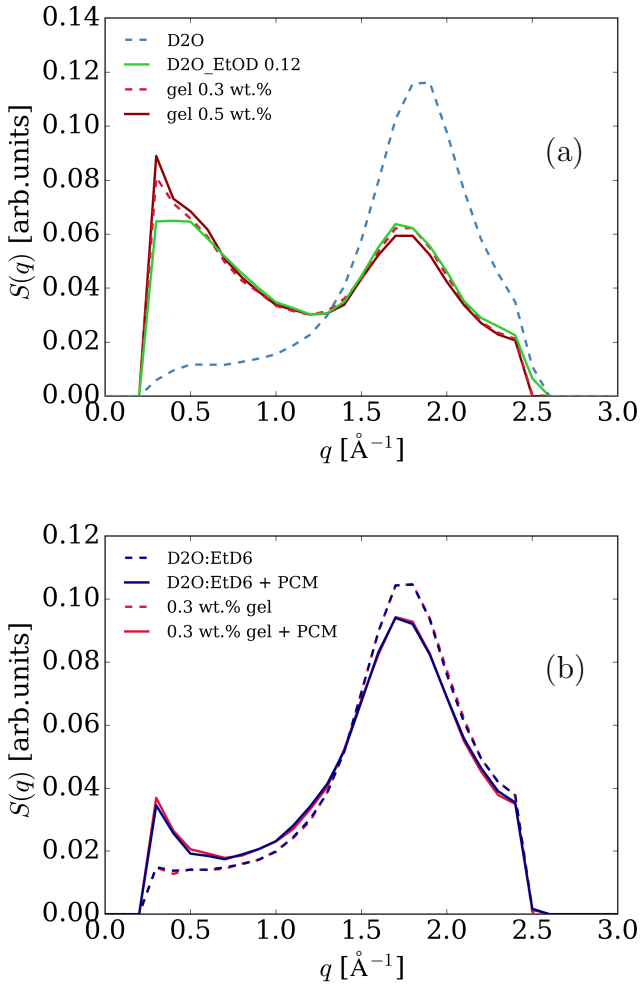

Figure 6.4: Apparent static structure factor obtained by integrating the coherent part of the LET dynamic scattering function $S(q,\omega)$ in the range -260 μeV $\leq \hbar\omega \leq$ +260 μeV, which corresponds to approximately twice the spectrometer resolution line width at this incident energy (E_i = 3.84 meV). The intensities of $S(q)$ are proportional to the measured intensities normalized to the incident beam intensities. (a) The dashed blue lines report the pure D_2O while the solid lines represent the spectrum of D_2O/ C_2D_5OH mixture at 0.12 ethanol mole fraction in pure solution (green) and at two bis-urea gel concentrations 0.3 wt.% (red) and 0.5 wt.% (dark red). The results from for D_2O-C_2D_5OD 0.12, previously published,[17] were rescaled to identical total signal to be comparable. (b) Results from the integration of D_2O/C_2D_5OD without (blue) and with (red) 0.3 wt.% bis-urea gel in the presence (full lines) and absence (dashed lines) of 5 wt.% paracetamol.

at $q \leq 1.2$ Å^{-1}, indicating the formation of mesoscopic transient structures, and the decrease in intensity of the main peak near 1.9 Å^{-1}, corresponding to D_2O nearest-neighbor correlation length.[17] The introduction of either 0.3 or 0.5 wt.% bis-urea gel does not further alter this structural reorganization (Fig.6.4a), corroborating our earlier findings on the stability of the hydrogen bond network in these mixtures. The $S(q)$ for the gel samples overlaps with that of the bulk water-ethanol mixture in both the pre-peak and main peak regions, aligning with the results of the relaxation times. Notably, these observations of unaffected structural reorganization and relaxation times persist in the fully deuterated solution, confirming that the gel's minimal impact is not an effect of partial deuteration (Fig.6.3b and Fig.6.4b). Hence, the addition of ethanol alters the microscopic solvent structure more significantly than the introduction of bis-urea molecules, despite the substantial macroscopic changes associated with gel formation. Dissolved paracetamol molecules, in contrast, induce substantial modifications to the solvent microscopic structure. As shown in Fig.6.4b, the $S(q)$ changes upon addition of paracetamol, both in bulk solution and in bis-urea gel, with a small decrease in the main correlation peak at around 1.9 Å^{-1} together with an equally small increase in the pre-peak region which we attribute to the disruption of the water structure by the paracetamol molecules. Such a transition suggests that paracetamol induces a restructuring of the solvent network, weakening short-range correlations while promoting the formation of larger-scale structural features. This observation of long-range structural changes is particularly noteworthy given that paracetamol is a neutral molecule. Typically, for uncharged solutes, one would expect perturbation effects to diminish rapidly beyond the first coordination shell.[1, 25] The persistence of paracetamol influence at mesoscopic scales thus suggests a more complex solute-solvent interaction than previously anticipated. Interestingly, paracetamol exerts a more pronounced influence on the solvent molecular structure than the gelator does, despite the gelator's more significant macroscopic effect. This counterintuitive trend can be explained by considering the surface available for molecular interactions: the higher concentration of dissolved paracetamol molecules results in numerous

solute-solvent interactions throughout the solution. In contrast, the gelator, present in minute amounts, has limited contact with the solvent. Consequently, paracetamol forms a greater number of hydrogen bonds with the liquid, leading to more extensive restructuring of the solvent network at the molecular level. This finding is consistent with studies showing how small amphiphilic molecules can induce mesoscale ordering in aqueous solutions, altering the hydrogen bond network over long-range correlation distances.[26]

6.4 Conclusions

In conclusion, this study provides significant insights into the structural dynamics of fully deuterated water-ethanol mixtures perturbed by a bis-urea supramolecular gel network and paracetamol. The polarization analysis, implemented on the spectrometer LET, allows us to decouple the coherent signal from the solvent and the incoherent signal arising from the protiated solutes, providing unprecedented perspective into these complex systems. We find that for the solvent no difference is observed in the structural relaxation resulting from the addition of up to 0.5 wt.% gelator, while the self-diffusion, detected previously with standard QENS at higher energy resolution than LET by the dominant scattering from the hydrogen protons on the paracetamol drug molecules, revealed slightly faster dynamics of these drug molecules within the bis-urea gel.[8] Surprisingly, with the present polarized QENS study we observe a solvent structuring upon solute addition of 5 wt.% paracetamol that substantially increases liquid structural relaxation times at the mesoscopic length scale. This result constitutes an important complement for the previous observation of faster solute self-diffusion within a gel network compared to the pure liquid structure,[11] highlighting the complexity of solute-solvent interactions and indicating that the resulting solution differs from the original solvent. This research lays a foundation for analyzing coherent dynamics in solvents containing drugs or other compounds, with applications extending to different alcohols and concentrations of gels or drugs, potentially utilizing future higher-resolution polarized neutron spectrometers to further investigate

structural relaxations of slower processes.[27]

6.5 Supporting information

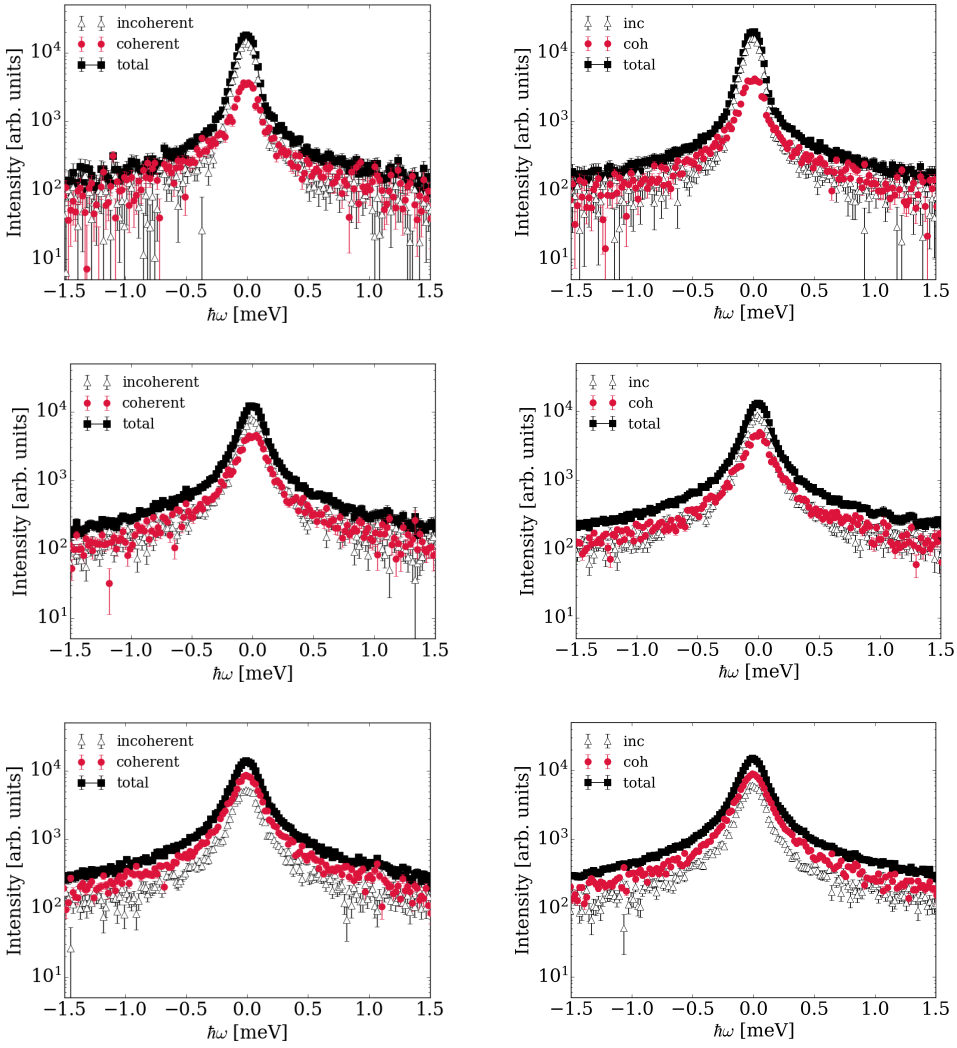

Figure S1: Comparison of the coherent (red circles), incoherent (empty triangles) and total (black squares) scattering functions measured on LET at T = 290 K and E_i= 3.84 meV for PCM in solvent (left column) and in 0.3 wt.% bis-urea gel (right column) at q = 1.0 Å^{-1} (top row), q = 1.6 Å^{-1} (middle row) and q = 1.9 Å^{-1} (bottom row). Error bars hidden beneath markers.

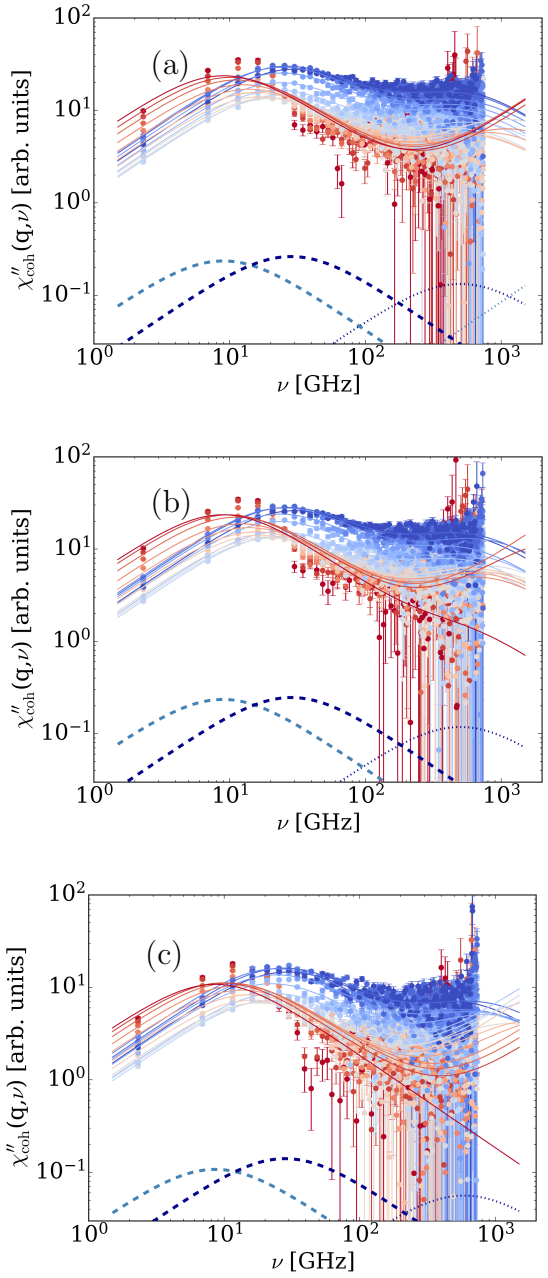

Figure S2: Imaginary part of the dynamical susceptibility for the coherent spectrum of D_2O/C_2H_5OD at 0.12 ethanol mole fraction recorded on LET at $E_i = 3.84$ meV, $T = 285$ K and $0.4\,\text{Å}^{-1} \leq q \leq 1.9\,\text{Å}^{-1}$ with (a) 0.3 wt.%, (b) 0.5 wt.% bis-urea gel and (c) without it. The solid lines stand for the fit according to eqn. 3 of the main text with blue dashed and dotted lines depicting the main and the second Debye process (scaled by a factor 0.6 for visibility) respectively.

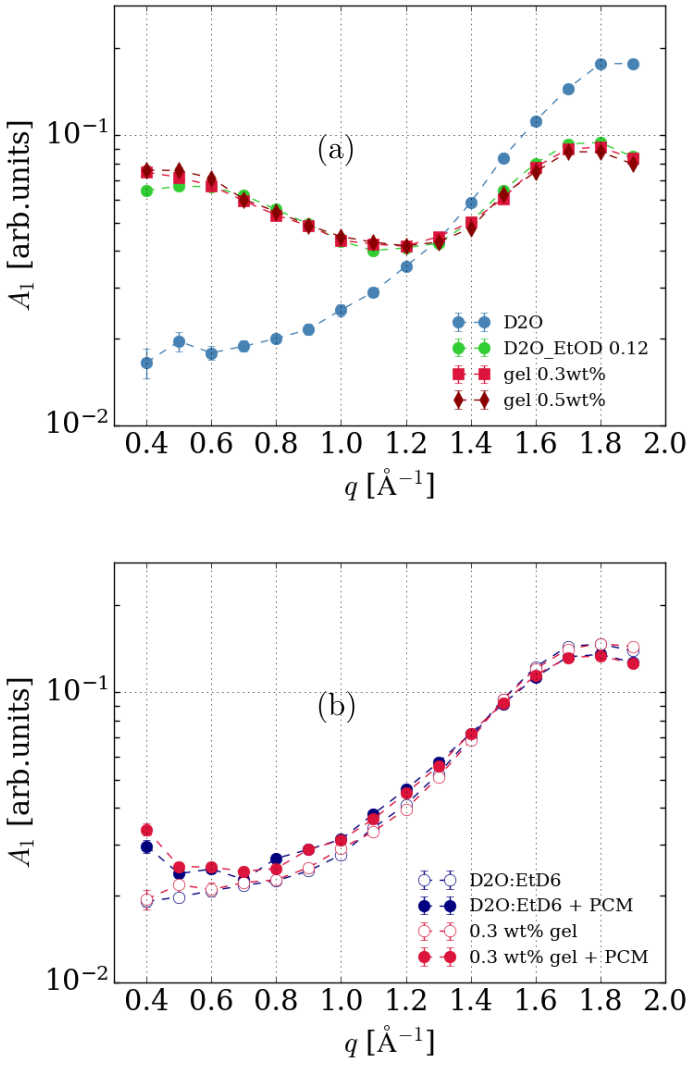

Figure S3: Amplitudes $A_1(q)$ of the main relaxation process of $\chi''_{\mathrm{coh}}(q,\nu)$ (eq.2) depending on q and incident energy $E_{\mathrm{i}} = 3.84$ meV. $\tau_1(q)$ was determined by the peak position $\nu_i^{\max} = (2\pi\tau_1)^{-1}$. (a) Comparison of the results for pure D_2O and for the partially deuterated D_2O : C_2H_5OD 7:3 *v:v* solvent mixture, corresponding to 0.12 ethanol mole fraction, at $T = 285$ K, in the absence of the bis-urea gelator as well as for 0.3 and 0.5 wt.% bis-urea gelator. (b) Comparison of the results in the presence (full symbols) and absence (open symbols) of PCM, for the pure fully deuterated water-ethanol solvent mixture and for the 0.3 wt.% bis-urea gel based on the same solvent at $T = 290$ K The lines are guides to the eye. Error bars hidden beneath markers.

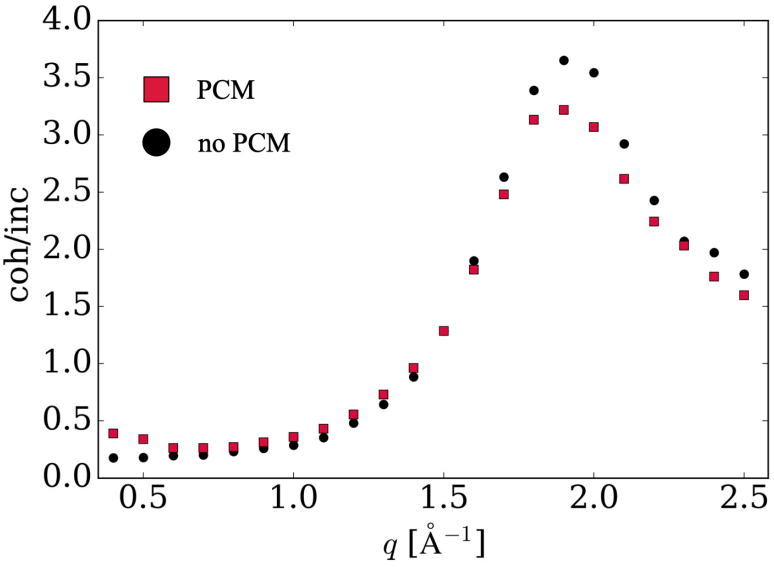

Figure S4: Intensity ratio between coherent and incoherent spectra for PCM loaded and unloaded D_2O-C_2D_5OD (0.12 ethanol mole fraction) at $T = 290K$.

Data accessibility

The neutron data are permanently curated by the ISIS facility and accessible via https://doi.org/10.5286/ISIS.E.RB1920548 and https://doi.org/10.5286/ISIS.E.RB2210240.

Bibliography

[1] Mathijs FJ Mabesoone, Anja RA Palmans, and EW Meijer. Solute–solvent interactions in modern physical organic chemistry: Supramolecular polymers as a muse. *Journal of the American Chemical Society*, 142(47):19781–19798, 2020.

[2] Angshuman Maitra and Sanjib Bagchi. Study of solute–solvent and solvent–solvent interactions in pure and mixed binary solvents. *Journal of Molecular Liquids*, 137(1-3):131–137, 2008.

[3] Alexander Ya Malkin, Svetlana R Derkach, and Valery G Kulichikhin. Rheology of gels and yielding liquids. *Gels*, 9(9):715, 2023.

[4] Pierre Terech and Richard G Weiss. Low molecular mass gelators of organic liquids and the properties of their gels. *Chemical reviews*, 97(8):3133–3160, 1997.

[5] William Edwards, Cecile A Lagadec, and David K Smith. Solvent–gelator interactions—using empirical solvent parameters to better understand the self-assembly of gel-phase materials. *Soft Matter*, 7(1):110–117, 2011.

[6] Jaclyn Raeburn, Cristina Mendoza-Cuenca, Beatrice N Cattoz, Marc A Little, Ann E Terry, Andre Zamith Cardoso, Peter C Griffiths, and Dave J Adams. The effect of solvent choice on the gelation and final hydrogel properties of fmoc–diphenylalanine. *Soft matter*, 11(5):927–935, 2015.

[7] Sylvie Spagnoli, Isabelle Morfin, Miguel A Gonzalez, Pierre Carcabal, and Marie Plazanet. Solvent contribution to the stability of a physical gel

characterized by quasi-elastic neutron scattering. *Langmuir*, 31(8):2554–2560, 2015.

[8] Tilo Seydel, Robert M Edkins, Christopher D Jones, Jonathan A Foster, Robert Bewley, Juan A Aguilar, and Katharina Edkins. Increased rate of solvent diffusion in a prototypical supramolecular gel measured on the picosecond timescale. *Chemical Communications*, 54(49):6340–6343, 2018.

[9] Kathryn J Skilling, Francesca Citossi, Tracey D Bradshaw, Marianne Ashford, Barrie Kellam, and Maria Marlow. Insights into low molecular mass organic gelators: a focus on drug delivery and tissue engineering applications. *Soft matter*, 10(2):237–256, 2014.

[10] Lamisse H El-Qarra, Niccolo Cosottini, Chayanan Tangsombun, and David K Smith. Formulation and release of active pharmaceutical ingredients using a supramolecular self-healing two-component gel. *Chemistry–A European Journal*, page e202402530, 2024.

[11] Robert M Edkins, Markus Appel, Tilo Seydel, and Katharina Edkins. The modifying effect of supramolecular gel fibres on the diffusion of paracetamol and ibuprofen sodium on the picosecond timescale. *Phys. Chem. Chem. Phys.*, 22(19):10838–10844, 2020.

[12] Tilo Seydel, Robert M Edkins, and Katharina Edkins. Picosecond self-diffusion in ethanol-water mixtures. *Phys. Chem. Chem. Phys.*, 21(18):9547–9552, 2019.

[13] RI Bewley, JW Taylor, and SM Bennington. Let, a cold neutron multidisk chopper spectrometer at isis. *Nucl. Instrum. Methods A*, 637(1):128–134, 2011.

[14] GJ Nilsen, J Košata, M Devonport, P Galsworthy, RI Bewley, DJ Voneshen, R Dalgliesh, and JR Stewart. Polarisation analysis on the let time-of-flight spectrometer. *Journal of Physics: Conference Series*, 862(1):012019, 2017.

[15] Arantxa Arbe, Gøran J Nilsen, J Ross Stewart, Fernando Alvarez, Victoria García Sakai, and Juan Colmenero. Coherent structural relaxation of water from meso- to intermolecular scales measured using neutron spectroscopy with polarization analysis. *Phys. Rev. Research*, 2(2):022015, 2020.

[16] Fernando Alvarez, Arantxa Arbe, and Juan Colmenero. Understanding the coherent dynamic structure factor of liquid water measured by neutron spectroscopy with polarization analysis: a molecular dynamics simulations study. In *EPJ Web of Conf.*, volume 272, page 01011. EDP Sciences, 2022.

[17] Riccardo Morbidini, Robert M Edkins, Mark Devonport, Gøran Nilsen, Tilo Seydel, and Katharina Edkins. Molecular structural dynamics in water–ethanol mixtures: Spectroscopy with polarized neutrons simultaneously accessing collective and self-diffusion. *The Journal of Chemical Physics*, 159(22), 2023.

[18] Gareth O Lloyd, Marc-Oliver M Piepenbrock, Jonathan A Foster, Nigel Clarke, and Jonathan W Steed. Anion tuning of chiral bis (urea) low molecular weight gels. *Soft Matter*, 8(1):204–216, 2012.

[19] P.G. De Gennes. Liquid dynamics and inelastic scattering of neutrons. *Physica*, 25(7):825–839, 1959.

[20] VN Novikov, Kenneth S Schweizer, and Alexei P Sokolov. Coherent neutron scattering and collective dynamics on mesoscale. *J. Chem. Phys.*, 138(16):164508, 2013.

[21] C. E. Bertrand, J. L. Self, J. R. D. Copley, and A. Faraone. Nanoscopic length scale dependence of hydrogen bonded molecular associates' dynamics in methanol. *J. Chem. Phys.*, 146(19):194501, 2017.

[22] Antonio Faraone, Kunlun Hong, Larry R. Kneller, Michael Ohl, and John R. D. Copley. Coherent dynamics of meta-toluidine investigated by quasielastic neutron scattering. *J. Chem. Phys.*, 136(10):104502, 2012.

[23] Tatsiana Burankova, Rolf Hempelmann, Andrew Wildes, and Jan P. Embs. Collective ion diffusion and localized single particle dynamics in pyridinium-based ionic liquids. *J. Phys. Chem. B*, 118(49):14452–14460, 2014.

[24] Kurt Sköld. Small energy transfer scattering of cold neutrons from liquid argon. *Phys. Rev. Lett.*, 19:1023–1025, Oct 1967.

[25] S Marčelja. Structural contribution to solute-solute interaction. *Croatica Chemica Acta*, 49(2):347–358, 1977.

[26] Deepa Subramanian, Christopher T Boughter, Jeffery B Klauda, Boualem Hammouda, and Mikhail A Anisimov. Mesoscale inhomogeneities in aqueous solutions of small amphiphilic molecules. *Faraday discussions*, 167:217–238, 2013.

[27] Kirill Nemkovski, Robert Bewley, Victoria García Sakai, Gøran Jan Nilsen, Adrien Perrichon, and Ian Silverwood. Sherpa: A spectrometer with high energy resolution and polarisation analysis. In *EPJ Web of Conferences*, volume 272, page 02004. EDP Sciences, 2022.

Chapter 7

Conclusions and future perspectives

Many biologic and chemotherapeutic drugs require parenteral administration, with subcutaneous injection being preferred for balancing bioavailability and patient tolerance.[1] However, challenges such as rapid uptake and poor localization persist. Matrix-based drug delivery systems, particularly hydrogels, provide solutions by enabling sustained, localized release while minimizing off-target effects. Supramolecular gels are especially promising, offering high biocompatibility, responsiveness to a range of physical stimuli, and tunability through subtle modifications of the gelator molecule. Their shear-thinning behavior further enables on-demand, injectable delivery. Despite their advantages, current drug release studies often rely on bulk dissolution techniques like UV-Vis spectroscopy, which oversimplify the complexity of drug-gel interactions by primarily viewing the gel as a steric barrier.[2, 3] As a result, crucial microscopic factors, such as gel fiber chemistry and non-steric interactions, are often overlooked. This project hypothesizes that understanding drug diffusion at the microscopic scale, independent of steric effects, is essential for accurately predicting and controlling macroscopic drug release. Using QENS, this study isolates the hydrodynamic and non-steric influences of the gel network on drug diffusion at the ps/ns time scale.

The primary finding of this project is the significant role of gel surface chemistry and specific drug-gel affinity in determining drug diffusion. This was demonstrated by measuring ibuprofen sodium diffusion in an FmocFF hydrogel and comparing it with previous results on a bis-urea-based system, which features distinct solvent properties and gel surface chemistry. Ibuprofen sodium shows a strong affinity for the gel fibers of FmocFF which leads at a retention at microscopic level, in contrast with its faster diffusion in bis urea gel. Notably, the strong interaction between ibuprofen sodium and the FmocFF gel, observed through QENS, is not evident in longer timescale release experiments such as SCISSOR. Moreover, our results highlight a broader phenomenon: the absence of correlation between microscopic drug diffusion and macroscopic release profiles. This discrepancy is evident not only for ibuprofen sodium but also for biologics such as lysozyme and insulin. While the FmocFF gel gener-

ally slows drug diffusion across both picosecond and hour-long timescales, the degree of hindrance is inconsistent between these scales and deviates from a straightforward Stokes-Einstein relationship with drug size. This work represents an important proof-of-concept that highlights the limitations of relying on a single experimental method, demonstrating that a multi-technique approach is essential for understanding drug release mechanisms. While QENS provides valuable insights into hydrodynamic interactions at the molecular level, SCISSOR captures macroscopic effects relevant to pharmaceutical drug delivery, such as membrane permeation and solution mixing. The combination of these techniques offers a comprehensive view of drug diffusion that neither method could achieve alone.

Building on this observation, the investigation of Doxorubicin diffusion in electrostatically modified peptide-based hydrogels highlights the advantage of focusing on a single drug while systematically tuning the gel fiber chemistry, using gels with more clearly defined hydrophobic and hydrophilic domains, compared to the more heterogeneous FmocFF surface chemistry. This approach demonstrates how short- and long-timescale dynamics can be aligned to uncover critical insights into drug-fiber interactions. By modifying terminal lysines in the peptide sequence, we identified a direct correlation between cation–π binding strength and both short-term diffusion coefficients and long-term release profiles. While the higher DOX concentrations used in QENS experiments posed challenges to full comparison with drug release studies, they also revealed additional factors influencing DOX self-diffusion, such as aggregation and hydrophilic structuring, which contribute to drug retention. This work not only demonstrates the ability to tune hydrogel properties via non-steric surface effects but also introduces the potential for high drug loading without gel degradation at acidic pH, reducing off-target toxicity and enhancing DOX efficacy by sustaining release at the tumor site to overcome cancer resistance.[4]

Finally, the investigation of diffusion in the bis-urea gel, considering the role of

the solvent, reveals that the assumption of an equivalence between the solution and solvent state is an approximation. Through the newly established sub-meV resolution polarization analysis, combined with selective solvent deuteration, QENS spectrometers are now capable of distinguishing between the incoherent and coherent components of the spectrum. This enabled the pioneering observation of water hydrogen bond network structural relaxation at the picosecond time scale.[5] In this thesis, this observation in pure water has been expanded by perturbing the network with ethanol, specifically at the mole fraction range where bis-urea gelation occurs. The study reveals that the structural relaxation slows down and the network becomes more rigid, potentially due to mesoscopic transient ethanol clusters. This increased rigidity is further enhanced by the dissolution of paracetamol, even though to a lower extent compared to ethanol, but still within the range detectable by polarized QENS. Surprisingly, the addition of bis-urea LMWG, while resulting in macroscopic gel formation, does not alter the behavior of structural relaxation. Despite the limitations of a newly developed method, this observation provides evidence that the structural networks of the solvent and solution states differ from a dynamic perspective. Although this approach is still in its early stages, it holds significant potential for expansion, starting with simpler systems where the coherent signal can predominantly be attributed to the solvent rather than the solute. This would include the investigation of small drugs in solution with varying hydrophilic and hydrophobic properties (like Doxorubicin). Along these lines, it would be of fundamental interest to apply this experimental protocol to investigate the mechanism of hydrotropes as solubility enhancers, particularly their role in water structuring, which is not yet fully understood.[6] Another promising direction involves extending the study of water-alcohol mixtures to other monohydroxy alcohols, such as methanol, propanol, butanol, and octanol. This would allow for experimental validation of whether the length of their carbon chains contributes to the stabilization of transient cluster-like structures.[7]

Limitations of the current studies

Overall, this thesis provides a proof-of-concept to look at the different mechanisms governing diffusion at microscopic scale in supramolecular gels but it also shows the fundamental challenges for advancing these materials toward practical applications. Despite significant progress in hydrogel research, the clinical translation of these systems remains highly complex, primarily due to regulatory hurdles. The approval process for drug-encapsulating hydrogels is costly and time-intensive, often requiring up to a decade for commercialization. Addressing key weaknesses in hydrogel systems is, therefore, essential for streamlining efforts and achieving success. One major challenge faced by supramolecular hydrogels is scalability, which is hindered by substantial batch-to-batch variability and poor reproducibility from preparation protocol. For example, in preparing FmocFF hydrogels, extensive sonication and vortexing to solubilize the hydrophobic gelator were needed, despite these methods not being recommended in standard protocols. Similarly, the standard protocol for the modified gels (F8, FK, KF8K) recommends a pH of 7, but in our experiments, the gelator precipitated at this pH. These gels were found to be more stable at a more acidic pH, further highlighting the variability in preparation protocols. Such inconsistencies reflect broader issues already noted in the literature: the influence of boundary conditions, including solvent choice, gelator concentration, temperature, pH, mixing techniques, and container properties, on the self-assembly process.[8, 9] These factors must be thoroughly characterized and standardized to ensure reproducibility and scalability in supramolecular gel production.

The inherent heterogeneity and variability of supramolecular gels also present significant challenges in studying drug diffusion. While this project demonstrated the potential of using quasi-elastic neutron scattering (QENS) to probe hydrodynamic, non-steric interactions between drugs and the gelator network, correlating these findings with bulk release data remains difficult. Drug loading limitations in QENS studies, where higher drug concentrations are typically used, can diverge from the conditions of bulk release experiments. Moreover,

the analysis and interpretation of QENS data, together with its accessibility (less convenient than tabletop methods) poses additional barrier that limits its widespread to systematic comparison with drug delivery studies. Even in the hypothetical case where QENS became widely accessible, this method inherently has its limitations, as it provides ensemble-average diffusion measurements, making it difficult to resolve multiple populations within a heterogeneous system like a gel (e.g., molecules near the fibers versus those in the pore center). For future studies, coupling QENS with direct single-particle tracking methods, such as fluorescence microscopy, could offer a complementary approach. While labeling introduces perturbations, it enables the visualization of individual molecule trajectories, potentially identifying distinct populations within the gel matrix and hints of anomalous diffusion.[10]

From a translational perspective, addressing in vivo variability remains a significant gap in hydrogel drug delivery research. Existing protocols often poorly represent key biological factors, such as molecular crowding, when using simplified buffer systems. Developing experimental protocols that better mimic in vivo conditions will be critical for advancing the predictive power of hydrogel systems in clinical applications. In this regard future work should prioritize a systematic investigation of a single hydrogel system. The family of β-sheet-forming peptide hydrogels presented in this thesis are an excellent candidate due to their stability, high drug-loading capacity, shape recovery, and tunability through modifications of the 20 naturally occurring amino acids. Systematic studies could explore how positional and chemical variations in these modifications influence final drug-retention properties. Such a framework could focus initially on a model drug, such as Doxorubicin, and systematically expand to other compounds with varying molecular size and chemical properties. Controlled release experiments at a larger scale could benefit from using standardized tools like SCISSOR, which limit variability across experimental setups and provide precise control over environmental parameters. While SCISSOR offers a more reproducible platform for in vitro release studies, gaps remain in mimicking in vivo conditions, particularly in representing molecular crowding effects.

Developing predictive models will be essential for future hydrogel research, helping to reduce the dependence on expensive experimental clinical trials. While traditional theoretical models may not immediately account for the observed complexities, machine-learning approaches hold significant promise. For example, using databases of release profiles, computational methods such as Principal Component Analysis (PCA) could be employed to reconstruct and predict release curves based on predictors such as solution pH or drug molecular weight.[11] These tools, already explored for monoclonal antibody formulations,[12] could shift hydrogel drug delivery studies from descriptive methods to predictive, data-driven approaches, ultimately enhancing bioavailability predictions and optimizing hydrogel design. By addressing these challenges with emerging technologies, the field can progress toward the rational design of hydrogels for drug delivery, bridging the gap between fundamental research and clinical translation.

Bibliography

[1] Lorenzo Tomasini, Marianne Ferrere, and Julien Nicolas. Subcutaneous drug delivery from nanoscale systems. *Nature Reviews Bioengineering*, pages 1–20, 2024.

[2] Jianyu Li and David J Mooney. Designing hydrogels for controlled drug delivery. *Nature Reviews Materials*, 1(12):1–17, 2016.

[3] Carlos BP Oliveira, Valéria Gomes, Paula MT Ferreira, José A Martins, and Peter J Jervis. Peptide-based supramolecular hydrogels as drug delivery agents: recent advances. *Gels*, 8(11):706, 2022.

[4] Chunbao Zang, Yu Tian, Yujing Tang, Min Tang, Dingyi Yang, Fangfang Chen, Mohammadreza Ghaffarlou, Yanyang Tu, Milad Ashrafizadeh, and Yan Li. Hydrogel-based platforms for site-specific doxorubicin release in cancer therapy. *Journal of Translational Medicine*, 22(1):879, 2024.

[5] Arantxa Arbe, Gøran J Nilsen, J Ross Stewart, Fernando Alvarez, Victoria García Sakai, and Juan Colmenero. Coherent structural relaxation of water from meso-to intermolecular scales measured using neutron spectroscopy with polarization analysis. *Physical Review Research*, 2(2):022015, 2020.

[6] Vividha Dhapte and Piyush Mehta. Advances in hydrotropic solutions: An updated review. *St. Petersburg Polytechnical University Journal: Physics and Mathematics*, 1(4):424–435, 2015.

[7] Seungeui Choi, Saravanan Parameswaran, and Jun-Ho Choi. Understanding alcohol aggregates and the water hydrogen bond network towards miscibility in alcohol solutions: graph theoretical analysis. *Physical Chemistry Chemical Physics*, 22(30):17181–17195, 2020.

[8] Dave J Adams. Personal perspective on understanding low molecular weight gels. *Journal of the American Chemical Society*, 144(25):11047–11053, 2022.

[9] Emily R Draper and Dave J Adams. Controlling supramolecular gels. *Nature Materials*, 23(1):13–15, 2024.

[10] Koen JA Martens, John Van Duynhoven, and Johannes Hohlbein. Spatiotemporal heterogeneity of κ-carrageenan gels investigated via single-particle-tracking fluorescence microscopy. *Langmuir*, 36(20):5502–5509, 2020.

[11] Adam J Gormley. Machine learning in drug delivery. *Journal of Controlled Release*, 373:23–30, 2024.

[12] Hao Lou and Michael J Hageman. Machine learning attempts for predicting human subcutaneous bioavailability of monoclonal antibodies. *Pharmaceutical Research*, 38:451–460, 2021.